Facultad de Ciencias

Departamento de Química Orgánica

Synthesis and properties of photo- and electroactive tetraazaporphyrins and their performance in dye-sensitized solar cells

Memoria presentada por

JAVIER FERNANDEZ ARIZA

Para optar al grado de

DOCTOR EN QUÍMICA ORGÁNICA

Madrid, 2016

La presente Tesis Doctoral ha sido realizada en el Departamento de Química Orgánica de la Universidad Autónoma de Madrid bajo la dirección del Profesor Tomás Torres Cebada y la Doctora M. Salomé Rodríguez Morgade.

Abbreviations and acronyms

We have used standard Organic Chemistry abbreviations and acronyms following the recommendation of the "guidelines for authors", *J. Org. Chem.* **2016**, which can be found in the journal webpage:
http://pubs.acs.org/paragonplus/submission/joceah/joceah_authguide.pdf

A	Acceptor
AcOH	Acetic acid
CB	Conduction band
CHENO	Chenodeoxycholic acid
CR	Charge recombination
CS	Charge separation
CSR	Charge separation rate
CSS	Charge separation state
CT	Charge transfer
CuTC	Copper(I) thiophene-2-carboxylate
D	Donor
DCTB	*trans*-2-[3-(4-*tert*-Butylphenyl)-2-methyl-2-propenylidene] malononitrile
DFT	Density functional theory
DMII	1,3-dimethylimidazolium iodide
DPV	Differential pulse voltammetry
DMAE	Dimethylaminoethanol
dppf	Diphenylphosphinoferrocene
DSSC	Dye-sensitized solar cell
ε	Molar extinction coefficient
EQE	External Quantum Efficiency
Fc	Ferrocene
FF	Fill factor
FTO	Fluorine-doped tin oxide

G	Guest
H	Host
HMDS	Hexamethyldisilazane
IPCE	Incident photon to current efficiency
ITO	Indium tin oxide
IVCT	Intervalence charge transfer
J_{SC}	Short-circuit current density
k_a	Association constant
λ	Wavelength
L	Linker
o-DCB	*o*-Dichlorobenzene
OTFT	Organic thin-film transistor
Φ	Quantum Yield
Pc	Phthalocyanine
PCE	Power conversion efficiency
PDA	Perylenedianhydride
PDI	Perylenediimide
PET	Photoelectron transfer
PSC	Perovskite solar cell
p-TSA	*para*-Toluensulfonic acid
Pz	Porphyrazine
η	Efficiency or Yield
SubPc	Subphthalocyanine
SubPz	Subporphyrazine
SWV	Square-wave voltammetry
τ	Lifetime
TCO	Transparent conductive oxide
$TBAPF_6$	Tetrabutylammonium hexafluorophosphate
TBP	*tert-B*utylpyridine
V_{OC}	Open-circuit voltage

Index

Introduction 1
Tetraazaporphyrin derivatives. Phthalocyanines and Porphyrazines 3
Synthesis of tetraazaporphyrins 7
Synthesis of phthalocyanines 7
Synthesis of porphyrazines 9
Synthesis of non-uniformly substituted porphyrazines 10
a) Synthesis of A_3B systems by statistical cyclotetramerization 10
b) Solid-phase synthesis 12
c) Ring expansion reaction 13
d) Synthesis of A_2B_2 by cross-condensation reactions 14
Applications of tetraazaporphyrins 15
General Objectives 19
Chapter 1 23
1.1 The Energy Problem 25
1.1.1 Photoinduced electron transfer (PET) in artificial systems 27
1.1.2 Organic synthetic artificial photosystems 29
1.1.3 Phthalocyanine-Perylenediimide as donor-acceptor systems 31
1.1.3.1 Intermolecular interactions between covalently linked Phthalocyanines and Perylenediimides 32
1.1.3.2 Intermolecular interactions between non-covalently linked Phthalocyanines and Perylenediimides 34
1.1.3.3 Inclusion of a secondary donor: Ferrocene 36
1.2 Specific objectives 39
1.3 Results and discussion 41
1.3.1 Synthesis and study of new Fc-Pc-PDI assemblies for artificial photosynthesis. 41
1.3.1.1 Synthesis of the ferrocenyl-substituted phthalocyanines 41
1.3.1.2 Synthesis of the perylenediimide derivatives 46
1.3.1.3 Assembly of RuPc-PDI-RuPc triads 49

1.3.1.4 Assembly of ZnPc-PDI dyads and triads in solution: ^{1}H-NMR studies 51
1.3.1.5 Calculation of the association constants 58
1.3.1.6 Electrochemical studies 64
1.3.1.7 Photophysical studies 68
1.3.2 Peripheral functionalization of SubPc with ferrocenes. 86
1.3.2.1 Synthesis of the ferrocenyl-substituted subphthalocyanines 86
1.3.2.2 Electrochemical studies 90
1.3.2.3 Assembly of ferrocenyl-substituted subphthalocyanine-C_{60} cocrystallates .93
1.3.2.4 Transient absorption spectroscopic studies 97
1.4 Summary and conclusions 99
1.5 Experimental section 101
1.5.1 Synthesis and study of new Fc-Pc-PDI assemblies for artificial photosynthesis. 103
1.5.1.1 Synthesis of the ferrocenyl-substituted phthalocyanines 103
1.5.1.2 Synthesis of the perylenediimide derivatives 109
1.5.1.3 Assembly of RuPc-PDI-RuPc triads 113
1.5.2.1 Synthesis of the ferrocenyl-substituted subphthalocyanines 115
Chapter 2 121
2.1 Photovoltaic devices 123
2.1.1 Inorganic solar cells 123
2.1.2 Organic solar cells 124
2.1.3 Hybrid solar cells 127
2.1.4 Characteristic parameters of solar cells 129
2.2 Dye sensitized solar cells 132
2.2.1 Structure and Operational Principle of Dye-Sensitized Solar Cells 132
2.2.2 Fundamental components of DSSCs 134
2.2.2.1 Electrodes 134
2.2.2.2 Electrolyte 135
2.2.2.3 Photosensitizer 138

2.3 Specific objectives 146
2.4 Results and discussion 147
2.4.1 Synthesis of ZnPz derivatives containing an isoindole-4-carboxylic unit 147
2.4.2 Synthesis of maleonitrile precursors 148
2.4.3 Synthesis of A_3B porphyrazines bearing an isoindole carboxylic function 152
2.4.4 Optical properties of Pzs 33-38 154
2.4.5 Electrochemical studies 156
2.4.6 Calculation of HOMO-LUMO levels 160
2.4.7 Photovoltaic performances in TiO_2-DSSC 165
2.4.7.1 Device fabrication 165
2.4.7.2 DSSC test results of sensitizers Pz 33-38 166
2.5 Synthesis of new Pzs by modification of the anchoring group 171
2.5.1 Synthesis of the maleonitrile precursors 172
2.5.2 Synthesis of the porphyrazines 174
2.5.3 Optical properties 177
2.5.4 Electrochemical studies 179
2.5.5 Calculation of HOMO-LUMO levels 179
2.5.6 Photovoltaic performances in TiO_2-DSSC 181
2.6 Summary and conclusions 182
2.7 Experimental section 183
2.7.1 Synthesis of ZnPz derivatives containing an isoindole-4-carboxylic unit 183
2.7.1.2 Synthesis of A_3B porphyrazines bearing an isoindole carboxylic function 189
2.7.2 Synthesis of new Pzs by modification of the anchoring group. 201
2.7.2.1 Synthesis of the precursors. 201
2.7.2.2 Synthesis of the porphyrazines 202
Resumen y Conclusiones 207

Introduction

Tetraazaporphyrin derivatives. Phthalocyanines and Porphyrazines

Tetrapyrrolic macrocycles[1] are a family of organic molecules which common structure consists of four pyrrole units forming an aromatic, planar structure linked through a *meso* atom (Figure 1). The electronic delocalization occurs preferably in the inner ring, being considered formally as an aromatic system formed by 16 atoms and 18 π electrons as can be observed in Figure 1c.[2] This family can be subdivided into two subgroups can be found as a function of the atom that occupies the *meso* position, namely porphyrins and tetraazaporphyrins. Porphyrins, which can be found in nature or laboratory synthesized, contain a carbon atom as the linkage. On the contrary, in tetraazaporphyrins, which are synthetic products, the pyrrole rings are linked through a nitrogen atom. The only presence of this nitrogen atom apparently produces discrete changes on the physicochemical properties of tetraazaporphyrins in comparison with porphyrins.[3] Phthalocyanines and porphyrazines represent the two cornerstones of tetraazaporphyrins. Phthalocyanines (Pcs) are a special case of tetraazaporphyrins comprising four benzene rings fused to the β-carbons of the pyrrole units. Therefore, they consist in porphyrinoids made up of four isoindole moieties attached through their 1,3-positions by aza linkages. Although, strictly speaking, Pcs are a class of porphyrazines from the structural point of view, they can be considered as a category themselves, based on the vast number of studies on these compounds and their numerous applications in different industrial fields. Therefore, we will reserve the term porphyrazine only when referred to macrocycles arranged by 1-4 pyrrole rings, and we will use the term "phthalocyanine" for macrocycles composed of four isoindole rings.

The main goal of this thesis relies on the synthesis of tetraazaporphyrin derivatives, and therefore we will not go into detail respecting other derivatives like the tripyrrolic subporphyrazines (SubPzs)[4] and subphthalocyanines (SubPcs),[5] even if a few examples of the latter will be discussed in section 1.3.2.

[1] H. Schultz, H. Lehmann, M. Rein, M. Hanack, *Structure and Bonding 74* (Ed. J. W. Buchler), Springer, Berlin, **1991**, pp. 41-146.
[2] a) E. Ortí, J. L. Brédas, *J. Chem. Phys.* **1988**, *89*, 1009; b) E. Ortí, J. L. Brédas, *Chem. Phys. Lett.* **1989**, *164*, 247.
[3] a) S.L. J. Michel, B. M. Hoffman, S. M. Baum, A. G. M. Barrett, *Prog. Inorg. Chem*. **2001,** *50***,** 473; b) Y. Rio, M. S. Rodríguez-Morgade, T. Torres, *Org. Biomol. Chem.* **2008**, *6*, 1877
[4] M. S. Rodríguez-Morgade, S. Esperanza, T. Torres, J. Barberá, *Chem. Eur. J*. **2005**, *11*, 35.
[5] C. G. Claessens, D. González-Rodríguez, M. S. Rodríguez-Morgade, A. Medina, T. Torres, *Chem. Rev.* **2014**, *114*, 2192.

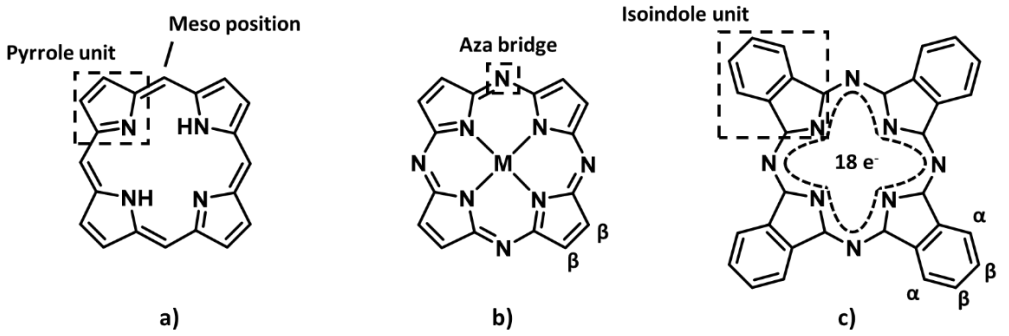

Figure 1. a) Free base porphyrin; b) metalloporphyrazine (MPz); c) main electronic delocalization mode in phthalocyanines.

Phthalocyanines[6] are the best-known class of tetraazaporphyrins. They were accidentally discovered at the beginning of the 20th century[7] and structurally characterized in the 1930s by Sir R. P. Linstead.[8] One of the most important characteristics of this kind of molecules is their high thermal and chemical stability, which is a common requirement for most technological applications. Unsubstituted Pcs are thermally and chemically stable (they can be heated up to 500 ^{o}C under high vacuum without decomposition and they resist non-oxidizing acids and bases) and optically stable, tolerating high intensity electromagnetic radiation. Nevertheless, their chemical versatility is by far the most remarkable feature that makes these molecules play an exceptional role in material science. The isoindolic hydrogen atoms of the central cavity can be replaced by more than 70 different elements of the periodic table, affording metallophthalocyanines (MPcs; Figure 2).[6a,b] However, as the coordination number of the macrocycle is four, according to the size and oxidation state of the metal, one or two ions (in the case of alkaline ions) can be inserted into the Pc core. When the metal demands a higher

[6] a) *Phthalocyanines. Properties and Applications* (Eds. C. C. Leznoff, A. B. P. Lever), VCH Publishers (LSK) Ltd., Cambridge, **1996**, vols. 1-4; b) *Phthalocyanine Materials. Synthesis, Structure and Function* (Ed. N. B. McKeown), Cambridge University Press, Cambridge, **1998**. c); N. B. McKeown in *Science of Synthesis* (*Houben-Weyl. Methods of Molecular Transformations*) (Ed. S. M. Weinreb), Georg Thieme Verlag, Stuttgart, **2004**, vol. 17, p. 1237 d) N. Kobayashi, *Curr. Opinion Solid-State Mater. Sci.* **1999**, *4*, 345; e) G. de la Torre, M. Nicolau, T. Torres, *Supramolecular Photosensitive and Electroactive Materials* (Ed. H. S. Nalwa), Academic Press, New York, **2001**, p. 1-111; f) K. M. Smith, R. Guilard in *The Porphyrin Handbook*, (Ed. K. M. Kadish), Academic Press, San Diego, **2003**, vols. 15-20; g) G. de la Torre, C. G. Claessens, T. Torres, *Chem. Comm*. **2007**, 2000; h) M. V. Martínez-Díaz, M. Quintiliani, T. Torres, *Synlett* **2008**, *1*, 1; i) C. G. Claessens, U. Hahn, T. Torres, *Chem. Record*. **2008**, 8, 75; j) M. V. Martínez-Díaz, T. Torres in *Handbook of Porphyrin Science,* (Eds. K. M. Kadish, R. Guilard, K. M. Smith), World Science Publishers, Singapore, **2010**, Vol. 10, Chapter 45, pp 141-181, k) *Structure and Bonding Vol. 135: Functional Phthalocyanine Molecular Materials* (Ed. D. M. P. Mingos), Springer, Berlin, **2010**; l) J. Mack, N. Kobayashi, *Chem. Rev.* **2011**, *111*, 281.

[7] A. Braun, J. Tscherniac, *Chem. Ber.* **1907**, *40*, 2709.

[8] a) R. P. Linstead, *J. Chem. Soc.* **1934**, 1022. b) C. E. Dent, R. P. Linstead, A. R. Lowe, *J. Chem. Soc.* **1934**, 1033. c) J. M. Robertson, R. P. Linstead, C. E. Dent, *Nature* **1935**, *135*, 506.

coordination number, one or two axial ligands are needed, resulting in pyramidal or octahedral structures (Figure 2).[9]

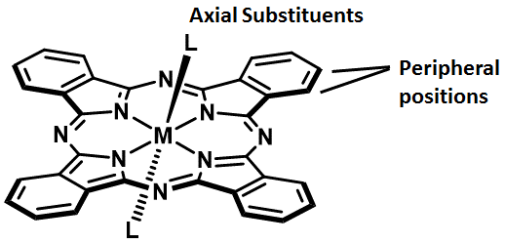

Figure 2. Schematic representation of possible functionalization in metallophthalocyanines.

Unsubstituted Pcs are highly insoluble in solvents other than aromatics with high boiling points such as quinoline, chlorobenzene, chloronaphthalene, nitrobenzene, or strong mineral acids, like sulfuric acid. In order to increase the solubility of Pcs in common organic solvents, or even in aqueous media, a wide variety of substituents can be attached at the axial positions and/or at the periphery.[10,6l] Some authors use the terms "non-peripheral" and "peripheral" positions to refer to the isoindole α and β positions, respectively (Figure 1).[11] In this report, we will use the term peripheral for all the isoindolic positions, namely "ortho" (4 and 7) and "meta"(5 and 6) positions. Axial and peripheral substitution also allow the modulation of the electronic structure of the macrocycle and constitutes an excellent strategy to tune their properties, as well as their organization both at supramolecular level and in the solid state.

Porphyrazines[12] were first synthesized and characterized by R. P. Linstead a few years after his first work on Pcs.[13] Although they are not as thermally stable as Pcs, their solubility is slightly higher than that observed in Pcs due to a reduction of the π-surface (there are no longer

[9] M. Hanack, S. Deger, A. Lange, *Coord. Chem. Rev.* **1988**, 115.
[10] V. N. Nemykin, E. A. Lukyanets, in *Handbook of Porphyrin Science,* (Eds. K. M. Kadish, R. Guilard, K. M. Smith), World Science Publishers, Singapore, **2010**, Vol. 3, pp 1-323.
[11] a) E. Sakamoto, T. Kato, M, J. Cook, *J. Porphyrins Phthalocyanines* **2001**, *05*, 742; b) A. N. Cammidge, C.-Hui Tseng, I. Chambrier, D. L. Hughes, M. J. Cook, *Tetrahedron Lett.* **2009**, *50*, 5254; c) A. N. Cammidge, I. Chambrier, M. J. Cook, D. L. Hughes, M. Rahman, L Sosa-Vargas, *Chem. Eur. J.* **2011**, *17*, 3136.
[12] a) P. A. Stuzhin, C. Ercolani, in *The Porphyrin Handbook* (Eds K. M. Kadish, K. M. Smith, R. Guilard) Academic Press, New York, **2003**, Vol. 15, p. 263; b) M. S. Rodriguez-Morgade, P. A. Stuzhin, *J. Porphyrins Phthalocyanines* **2004**, *8*, 1129; c) N. Kobayashi, in *The Porphyrin Handbook* (Eds K. M. Kadish, K. M. Smith, R. Guilard) Academic Press, New York, **1999**, Vol. 2, p. 301. d) M. J. Fuchter, C. Zhong, H. Zong, B. M. Hoffman, A. G. M. Barrett, *Aust. J. Chem.* **2008**, *61*, 235; e) K. Andersen, M. Anderson, O. P Anderson, S. Baum, T. F. Baumann, L. S. Beall, W. E. Broderick, A. S. Cook, D. M. Eichhorn, D. Goldberg, H. Hope, W. Jarrell, S. J. Lange, Q. J. McCubbin, N. S. Mani, T. Miller, A. Garrido Montalban, M. S. Rodriguez-Morgade, S. Lee, H. Nie, M. M. Olmstead, M. Sabat, J. W. Sibert, C. Stern, A. J. P White, D. B. G. Williams, D. J. Williams, A. G. M. Barrett, B. M. Hoffman, *J. Heterocyclic Chem.* **1998**, *35,* 1013.
[13] A. H. Cook, R. P. Linstead, *J. Chem. Soc.* **1937**, 929.

benzene rings fused to the pyrroles), which implies a reduction of the aggregation processes of these large planar aromatic systems.

The properties of Pzs can be modulated by introducing ions of different nature in the core cavity, axial substituents, and/or different substitution patterns at the peripheral positions. In the case of Pzs, only the β-positions of the pyrrole moiety are available for chemical modification. However, despite this apparent limitation, the effect of peripheral functionalization on the macrocycle is far stronger than in the case of Pcs due to a direct and effective electronic communication of the peripheral functions with the macrocyclic core.[3b,12b,e]

Both Pcs and Pzs strongly absorb radiation corresponding to visible light and have a high optical stability. This is the reason why Pcs have been traditionally used as dyes and pigments in textile industry and paintings. Moreover, as a consequence of their high extinction coefficient and the photophysical characteristics of their excited states, Pcs are continuously finding new applications in distinct applied fields. For example, during the last years, a huge effort has been devoted to the synthesis and study of water soluble compounds as photosensitizers in photodynamic therapy (PDT) for cancer.[14] Pzs, on the other hand, remain quite unexplored.

The electronic absorption spectrum of tetraazaporphyrins (Figure 3a) presents two main bands, the *Q*-band and the Soret or *B*-band. UV-Vis spectra of Pzs usually show *Q*- and *B*-bands with molar absorption coefficients (ε) of comparable intensity. On the contrary, Pcs show a *Q*-band which is usually much more intense than the Soret band. The former, which is responsible for the green or blue colour of these compounds, is often found for Pcs in the 620–700 nm region, while the *Q*-band in Pzs appears in the 530–620 nm region. The value of ε depends greatly on the substitution at the periphery, the central metal and the solvent, but in the case of Pzs often ranges from $5\cdot10^4$ to 10^5 $M^{-1}cm^{-1}$ and in the case of Pcs is a slightly higher, in the range of 10^5–$2\cdot10^5$ $M^{-1}cm^{-1}$.[3b,12b] The red shifted *Q*-band of Pcs is a consequence of the extended conjugation of the macrocycle over the fused benzene rings. The single *Q*-band is associated to π-π* HOMO-LUMO transitions from doubly degenerated orbitals (Figure 3b). In the case of metallomacrocycles MPcs and MPzs, displaying higher symmetry (D_{4h}), the LUMO is degenerated and a single band is observed. On the other hand, free base macrocycles show split *Q*-bands owing to their lower D_{2h} symmetry. Unsymmetrically substituted tetraazaporphyrins also display a reduction of the symmetry with respect to D_{4h} macrocycles, a fact that usually leads to splitting of the *Q*-band. The Soret band for both families appears at higher energies in

[14]a) U. Hahn, F. Setaro, X. Ragàs, A. Gray-Weale, S. Nonell, T. Torres, *Phys. Chem. Chem. Phys.*, **2011**,*13*, 3385; b) K. Ishii, *Coordination Chemistry Reviews*, **2012**, *256*, 1556

the spectrum, commonly around 350 nm, and is related to π-π* transitions from lower-energy molecular orbitals.

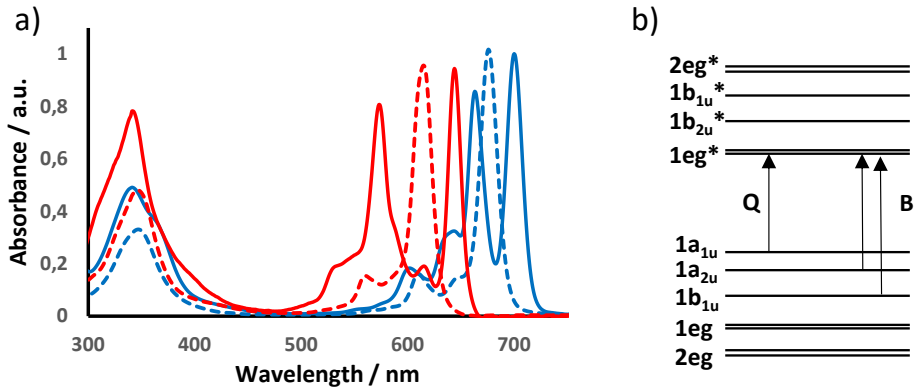

Figure 3. a) UV-Vis spectra of free-base PcH_2 (blue solid line) and PzH_2 (red solid line), and metallated MPc and MPz (blue and red dashed line, respectively); b) schematic representation of the energetic levels and transitions (*Q*- and *B*-band) of a metallophthalocyanine.

The photophysical properties of Pcs are strongly influenced by the presence and nature of the central atom, thus having an impact on their electronic absorption, fluorescence and phosphorescence spectra, as well as on the excited states.[3b,6l,15] Transition metal ions provide MPcs with short triplet lifetimes (in the nanosecond range), whereas closed-shell and diamagnetic metals, such as zinc, lead to dyes with high triplet state quantum yields. [16]

Synthesis of tetraazaporphyrins

Synthesis of phthalocyanines

The synthesis of symmetrically substituted Pcs (A_4), that is, bearing identical substituents at each of the four subunits (isoindole A), can be carried out by cyclotetramerization of suitable precursors (phthalonitriles or their 1,3-diiminoisoindolinederivatives), generally using a metal salt as a template. The most common synthetic methods are depicted in Scheme 1.

[15] a) E. Orti, M. C. Piqueras, R. Crespo, J. L. Brédas, *Chem. Mat*. **1990**, *2*, 110; b) E. Orti, R. Crespo, M. C. Piqueras, F. Tomas, *J. Mater. Chem*. **1996**, *6*, 1751; c) X. F. Zhang, X. Shao, H. Tian, X. Sun, K. Han, *Dyes Pigm*. **2013**, *99*, 480.
[16] H. Ali, J. E. van Lier, *Chem. Rev.* **1999**, *99*, 2379.

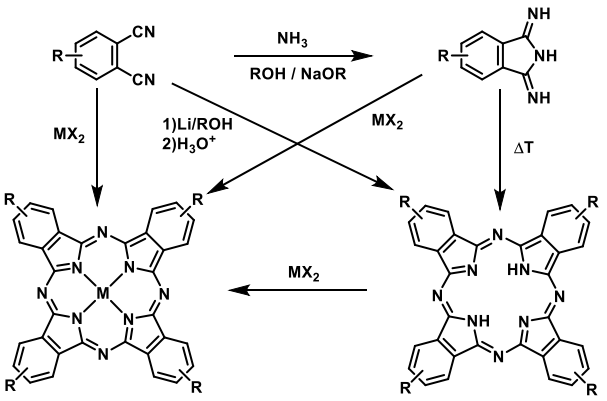

Scheme 1. . Common synthetic procedure to obtain Pcs.

The most employed method to prepare MPcs consists in a metal templated reaction in which the phthalonitrile and the metal salt are heated to reflux in a high boiling point solvent (DMAE, DMF, *o*-DCB, *etc*.). On the other hand, the synthesis of metal-free Pcs is usually carried out either employing 1,3-diiminoisoindolines as precursors in the above mentioned reaction conditions, or phthalonitriles and a basic catalyst (DBU) in the presence of alcohols, such as DMAE or 1-pentanol.[17] Lithium and magnesium alkoxides are also used as templates, giving rise to the corresponding MPcs that can be easily demetallated to afford the corresponding free base macrocycle by treatment with a mineral[18] or organic acid (AcOH, TFA), respectively.

Moreover, new methods that enable the preparation of Pcs in higher yields under milder conditions have also been described. For instance, treatment of phthalic anhydrides and phthalimides with metal salts and hexamethyldisilazane in DMF,[19] a double-addition of oximes to phthalonitriles,[20] or the use of microwave radiations[21] constitute alternative procedures.

When non symmetric phthalonitriles are used as starting materials, the resulting Pcs are obtained as mixtures of four structural isomers with C_{4h}, D_{2h}, C_{2v} and C_{2s} symmetries (see example in Figure 4).[22] These regioisomers have been separated in a few cases by chromatographic techniques.[23] Alternatively, some regioselective methods have been reported

[17]H. Tomoda, S. Saito, S. Ogawa, S. Shiraishi, *Chem. Lett*. **1980**, *9*, 1277.
[18]C. C. Leznoff, M. Hu, K. J. M. Nolan, *Chem. Comm.* **1996**, 1245.
[19] H. Uchida, H. Tanaka, H. Yoshiyama, P. Y. Reddy, S. Nakamura, T. Toru, *Synlett* **2002**, 1649.
[20] M. N. Kopylovich, V. Y. Kukushkin, M. Haukka, K. V. Luzyanin, A. J. L. Pombeiro, *J. Am. Chem. Soc.* **2004**, *126*, 15040.
[21] a) A. Loupy, D. Bogdal, A. Petit, *Tetrahedron*, **2005**, *61*, 179; b) I. Acar, H. Kantekin, Z. Biyikliouglu, *J. Organomet. Chem.* **2010**, *695*, 151; c) A. Was, E. Kaya, C. Elif, H. Kantekin, A. Soeknen, X. Cakir, *J. Organomet. Chem.* **2011**, *696*, 1659; c*) Dyes and Pigments*, **2007**, *74*, 279.
[22] M. Sommerauer, C. Rager, M. Hanack, *J. Am. Chem. Soc.* **1996**, *118*, 10085.
[23] a) G. Schmid, M. Sommerauer, M. Hanack, *Angew. Chem. Int. Ed.* **1993**, *32*, 1422; b) M. S. Rodríguez-Morgade, M. Hanack, *Chem. Eur. J.* **1997**, *3*, 1042

for the synthesis of C_{4h} and C_{2v} Pcs.[24] The synthesis of the former implies the use of bulky substituents[24f] and/or low temperatures[24g] while the latter involves the use of dimeric phthalonitriles[24h] or diiminoisoindolines.[24i]

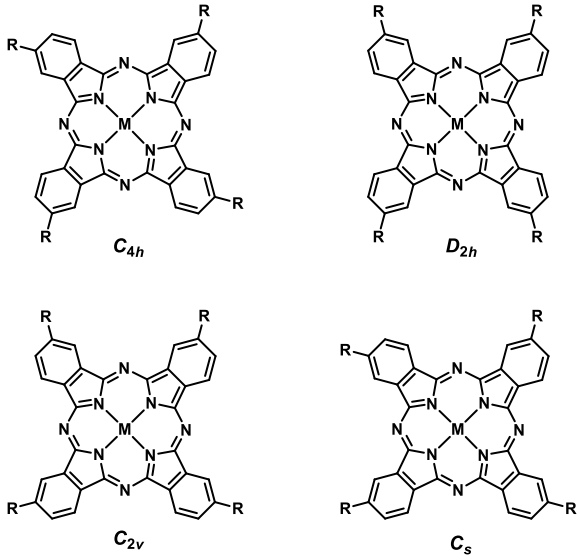

Figure 4. Structures of the constitutional isomers of 2(3)-tetrasubstituted MPcs.

Synthesis of porphyrazines

Linstead and coworkers described more than 50 years ago a synthetic method to obtain Pzs that it is still the most widely used and, for that reason, this system is called "Linstead macrocyclization" (Scheme 2).[25] Regardless of whether a maleonitrile or a 1,3-diiminopyrroline is used, the cyclotetramerization reaction is always templated by magnesium alkoxides, *i.e.* propoxide or butoxide. Further treatment with TFA or AcOH affords the free base Pz. The metallated macrocycle is generated by refluxing free base Pzs in the presence of a metal salt.

[24] a) N. Kobayashi, Y. Kobayashi, T. Osa*, J. Am. Chem. Soc.* **1993**, *115*, 10994; b) D. M. Drew, C. C. Leznoff, *Can. J. Chem.* **1996**, *74*, 307; c) M. Brewis, G. J. Clarkson, P. Humberstone, S. Makhseed, N. B. McKeown, *Chem. Eur. J.* **1998**, *4*, 1633; d) C. C. Leznoff, Z. Li, H. Isago, A. M. D'Ascanio, D. S. Terekhov, *J. Porphyrins Phthalocyanines* **1999**, *3*, 406; e) N. Iida, K. Tanaka, E. Tokunaga, H. Takahashi, N. Shibata, *ChemistryOpen* **2015**, *4*, 102; f) J. Ranta, T. Kumpulainen, H. Lemmetyinen, A. Efimov, *J. Org. Chem.* **2010**, *75*, 5178; g)C. C. Leznoff, M. Hu, K. J. M. Nolan, *Chem. Commun.* **1996**, *10*, 1245; h) D. M. Drew, C. C. Leznoff, *Synlett* **1994**, 623; i) W. Lv, X. Zhang, J. Lu, Y. Zhang, X. Li, J. Jiang, *Eur. J. Inorg. Chem*. **2008**, 4255.
[25] R. P. Linstead, M. Whalley, *J. Chem. Soc* **1952**, 4839.

Most of the reported Pzs are symmetric, probably owing to the challenge of synthesizing monosubstituted precursor. The separation of Pz regioisomers is so far unreported.

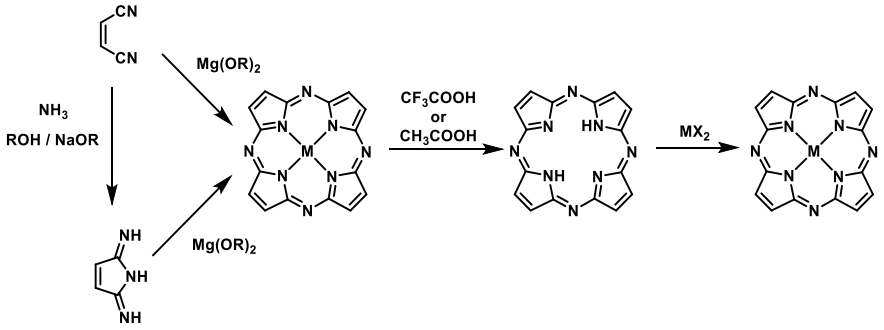

Scheme 2. Common synthetic procedure to obtain Pzs.

Synthesis of non-uniformly substituted porphyrazines

The synthesis of tetraazaporphyrins with two different substitution patterns at the pyrrole units (A and B) is a challenging task, and the methodology employed is chosen depending on the kind of substituents required and on their relative distribution in the final macrocycle (A_3B, A_2B_2 or ABAB).[26] A brief description of the most important methods is described.

a) Synthesis of A_3B systems by statistical cyclotetramerization[26a,b,c]

Due to its simplicity, statistical cyclotetramerization is by far the most broadly used methodology to prepare non-uniformly substituted tetraazaporphyrins. This method is based on the crossover condensation of two different dinitriles or their 1,3-diimino derivatives (A and B) to afford a mixture of macrocycles (Pcs, Pzs, hybrids… Figure 5) that, in a second step are separated by column chromatography. This approach is widely used to prepare A_3B derivatives, since A_2B_2 compounds are difficult to isolate by chromatographic techniques. In a condensation of two A and B phthalonitriles with equal reactivity in a 1:1 ratio, a purely statistic mixture would be obtained (see percentages in Figure 5). In order to optimize the reaction conditions and maximize the yield of the A_3B derivative, there are several variables to take into account: a) the relative reactivity of A and B; b) the steric effect of the substituents in any of the dinitriles, which has a direct influence on the reactivity; and c) the molar ratio between A and B. Assuming that

[26] T. Torres, *J. Porphyrins Phthalocyanines* **2000**, *4*, 325; b) G. de la Torre, C. G. Claessens, T. Torres, *Eur. J. Org. Chem*. **2000**, 2821; c) G. de la Torre, T. Torres, *J. Porphyrins Phthalocyanines* **2002**, *6*, 274; d) E. Fazio, J. Jaramillo-García, G. de la Torre, T. Torres, *Org. Lett*. **2014**, *16*, 4706; e) A. Wang, L. Long, C. Zhang, *Tetrahedron* **2012**, *68*, 2433.

the reactivity of A is equal to the reactivity of B, the yields of different products formed will be only governed by statistics, and the optimal stoichiometry should be 3:1. In this case, the A_3B macrocycle should be the major compound, with a theoretical yield of 42.2%. However, since A and B usually show different reactivity, sometimes the optimal ratio of precursors can be different to 3:1.

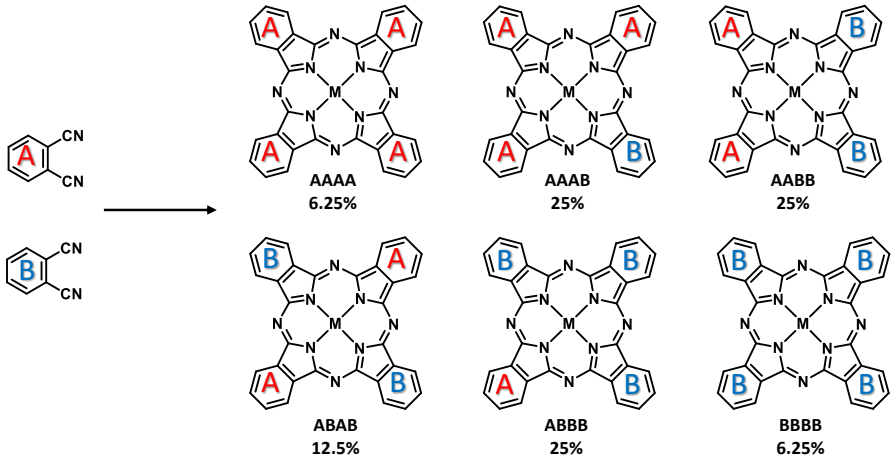

Figure 5. Mixture of phthalocyanines obtained *via* statistical cyclotetramerization of two differently functionalized phthalonitriles or diiminoisoindolines, A and B in a 1:1 ratio.

Concerning the mechanism of formation of Pcs, several pathways have been proposed. There are, however, some common features to all these mechanistic proposals.[27] In general, the macrocyclization in the presence of sodium or lithium alkoxide starts with the formation of the corresponding salt of 1-imido-3-alkoxyindoline (Scheme 3A). The next step in the reaction sequence is the nucleophilic attack of this intermediate to the nitrile group of another phthalonitrile molecule. A dimer is then formed (Scheme 3B), which can now either react with another phthalonitrile unit in the same way and form a trimer (Scheme 3C), or undergo condensation with another dimer present in the reaction media (Scheme 3D).

An alternative pathway consists in the metal-mediated formation of the Pc ring, that is, a metal cation acts as a template to which the reacting phthalonitriles coordinate during the macrocyclization.[28]

[27] a) C. R. Rager, G. Schmid, M. Hanack, *Chem. Eur. J.* **1999**, *5*, 280; b) S. W. Oliver, T. D. Smith, *J. Chem. Soc. Perkin Trans. II* **1987**, 1579.
[28] a) V. W. Day, T. J. Marks, W. A. Wachter, *J. Am. Chem. Soc*. **1975**, *97*, 4519; b) D. Bush, N. Stephenson, *Coord. Chem. Rev*. **1990**, *100*, 119.

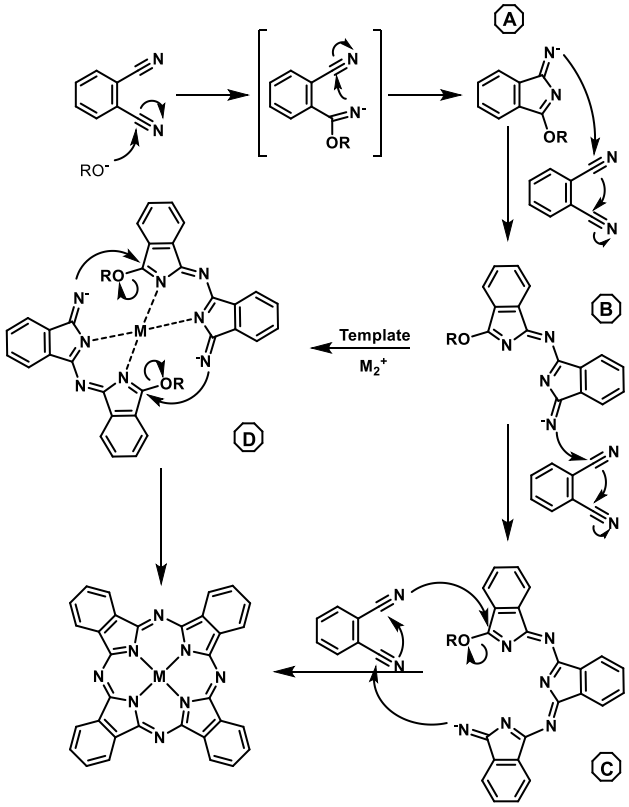

Scheme 3. Proposed mechanisms for the synthesis of metallophthalocyanines by cyclotetramerization of phthalonitriles in the presence of a metal salt.

b) Solid-phase synthesis[29]

In 1982 Leznoff and co-workers developed a method in which a phthalonitrile or diiminoisoindoline (B) is linked to an insoluble polymer or resin, and then is made to react with excess of a differently functionalized phthalonitrile or diiminoisoindoline (A). In a second step, the A_3B formed phthalocyanine is cleaved from the solid support (Scheme 4). However, preparation of asymmetric Pcs and Pzs using this method remains still largely unexplored and, so far, yields are similar those obtained through statistical synthesis. The restraints on what substituents can be used also constitute a serious drawback.

[29] a) C. C. Leznoff, T. W. Hall, *Tetrahedron Lett.* **1982**, *23*, 3023; b) A. Hirth, A. K. Sobbi, D. Wohrle, *J. Porphyrins Phthalocyanines* **1997**, *1*, 275; c) S. S. Erdem, I. V. Nesterova, S. A. Soper, R. P. Hammer, *J. Org. Chem.* **2008**, *73*, 5003; d) M. Mudyina, N. M. Ndingury, A. S. Steven, P. R. Hammer, *J. Porphyrins Phthalocyanines* **2010**, *14*, 891

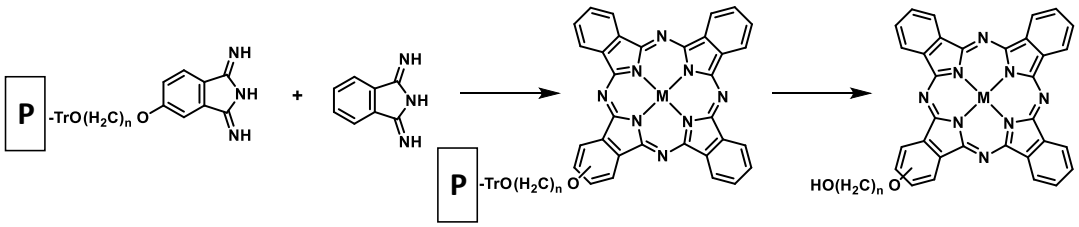

Scheme 4. Example of solid-phase synthesis of A_3B Pcs

c) Ring expansion reaction[30]

In 1990 Kobayashi described an elegant methodology for the synthesis of asymmetric A_3B Pcs by ring expansion of subphthalocyanines, by reacting these trimeric systems with phthalonitriles or diiminoisoindolines (Scheme 5). At first sight this is a very promising process since it avoids the tedious purification of the Pcs' mixture obtained when the statistical cyclotetramerization is used.

Several research groups have determined that its efficiency strongly depends on the nature of the SubPc and diiminoisoindolines peripheral substituents, the solvent and the temperature of the reaction.[31] Due to the potential of this method, there is still large room for research in order to optimize the reaction conditions.[32]

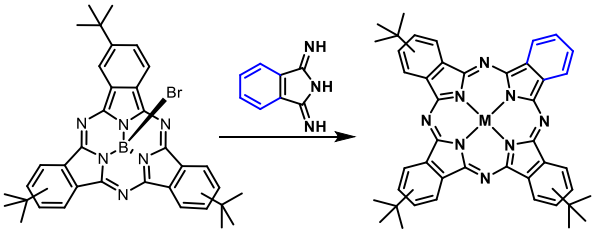

Scheme 5. Example of ring expansion reaction.

[30] a) N. Kobayashi, R. Kondo, S. –I. Nakajima, T. Osa, *J. Am. Chem. Soc.* **1990**, *112*, 9640

[31] a) E. Musluoglu, A. Gürek, V. Ahsen, A. Gül,. Ö. Bekaroğlu, *Chem. Ber*. **1992**, *125*, 2337; b) A. Weitemeyer, H. Kliesch, D. Wöhrle, *J. Org. Chem.* **1995**, *60*, 4900; c) A. Sastre, T. Torres, M. Hanack, *Tetrahedron Lett.* **1995**, *35*, 8501; d) S. Kudrevich, N. Brasseur, C. La Madeleine, S. Gilbert, J. E. van Lier, *J. Med. Chem.* **1997**, *40*, 3897.

[32] a) P. Matlaba, T. Nyokong, *Polyhedron* **2002**, *21*, 2463; b) K. Padmaja, W. J. Youngblood, L. Wei, D. F. Bocian, J. S. Lindsey, *Inorg. Chem.* **2006**, *45*, 5479; c) S. M. S. Chauhan, P. Kumari, *Tetrahedron* **2009**, *65*, 2518; d) T. C. Tempesti, M. G. Alvarez, E. N. Durantini, *Dyes Pigm.* **2011**, *91*, 6; e) A. L. Ochoa, T. C. Tempesti, M. B. Spesia, M. E. Milanesio, E. N. Durantini, *Eur. J. Med. Chem.* **2012**, *50*, 280.

Regarding Pzs, there is only one example in the literature, a patent, in which a SubPz is used for ring expansion reactions, [33] and a few in which diiminopyrrolines are used with SubPcs to form Pc-Pz hybrids. [30,34]

d) Synthesis of A_2B_2 by cross-condensation reactions

A_2B_2 macrocycles can be classified in two categories, the *cis* or AABB-type, and the *trans* or ABAB-type (see Figure 5 above). The separation of both isomers is usually difficult or not feasible since they show similar solubility and chemical polarity. Thus, specific synthetic strategies have been developed to prepare a single regioisomer.

The synthetic protocols that enable preparation of AABB-type tetraazaporphyrins involve the use of preformed dimers such as that depicted in Scheme 6a, or bisphthalonitrile bisdiiminoisoindoline derivatives (Scheme 6b) in crossover cyclotetramerizations with other phthalonitrile derivatives.[24h,i,35]

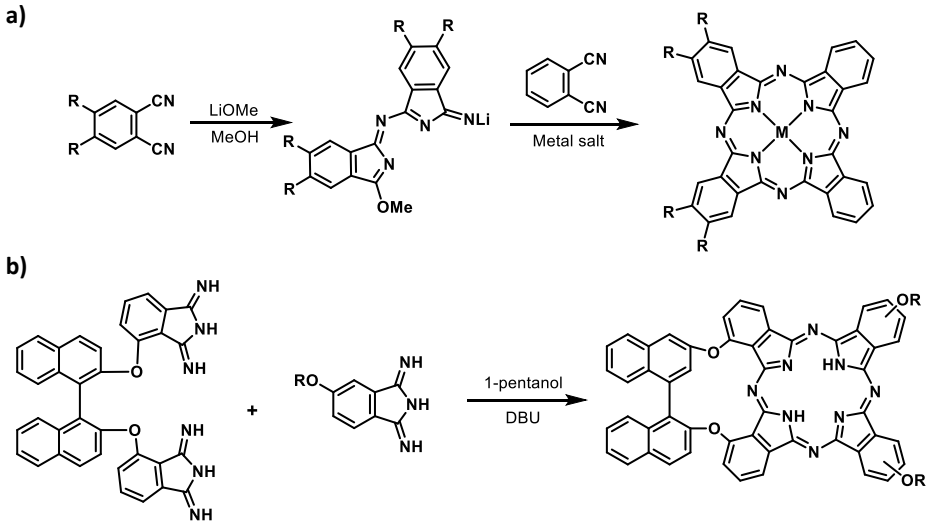

Scheme 6. Synthesis of AABB macrocycles.

[33] S. Nakajima, Jap. Pat, JP2009108249, **2009**.
[34] N. Kobayashi, T. Ishizaki, K. Ishii, H. Konami, *J. Am. Chem. Soc.* **1999**, *121*, 9096.
[35] a) K. J. M. Nolan, M. Hu, C. C. Leznoff, *Synlett* **1997**, 593 ; b) N. Kobayashi, *Chem. Comm.* **1998**, 487 ; c) H. Miwa, N. Kobayashi, *Chem. Lett.* **1999**, 1303; d) N. Kobayashi, H. Miwa, H. Isago, T. Tomura, *Inorg. Chem.* **1999**, *38*, 479; e) I. Seotsanyana-Mokhosi, T. Nyokong, *J. Porphyrins Phthalocyanines* **2004**, *8*, 1214; f) A. L Lyubimtsev, I. E Nifant'ev,.Russ.Chem.Bull.2**004**, *53*, **346**.

The specific synthesis of ABAB tetraazaporphyrins requires the use precursors that cannot self-condense.[36] Among them, 1,1,3-trichloroisoindolenines (Scheme 7) are the most important. In addition, phthalonitriles or diiminoisoindolines bearing bulky substituents at the 3- and 6-positions of the benzene ring have been reported to selectively yield ABAB macrocycles in crossover cyclotetramerizations with other phthalonitrile derivatives.[26d]
Both methods have been applied to the preparation of ABAB-type Pcs and Pzs, although the latter seems to be particularly useful within the Pz family.[37]

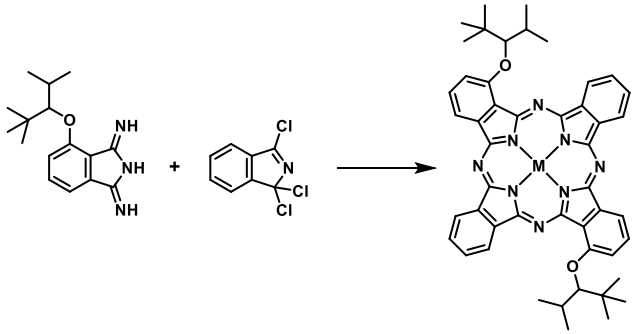

Scheme 7. Synthesis of an ABAB macrocycle.

Applications of tetraazaporphyrins

Since their first synthesis, early in the 20th century, Pcs have established themselves as blue and green dyestuff par excellence. They are an important industrial commodity, used primarily in inks (especially ballpoint pens), colouring for plastics and metal surfaces, and dyes for jeans and other clothing. More recently, and due to their outstanding properties such as high chemical, thermal and optical stability, semiconductivity and excellent photophysical features, there is a growing interest in the use of Pcs in many high technology fields (Figure 6),[6l,38] including

[36] a) J. G. Young, W. Onyebuagu, *J. Org. Chem.* **1990**, *55*, 2155; b) N. Kobayashi, T. Ashida, T. Osa, *Chem. Lett.* **1992**, 2031; c) S. Dabak, Ö. Bekaroğlu, *New J. Chem.* **1997**, *21*, 267; d) M. Hanack, P. Stihler, *Eur. J. Org. Chem.* **2000**, 303; e) J-. D. Wang, M-. J. Lin, S-. F. Wu, Y. Lin, *J. Organomet. Chem.* **2006**, *691*, 5074.
[37] T. P. Forsyth, D. B. G. Williams, A. G. Montalban, C. L. Stern, A. G. M. Barrett, B. M. Hoffman, *J. Org. Chem.* **1998**, 331; b) L. A. Ehrlich, P. J. Skrdla, W. K. Jarrell, J. W. Sibert, N. R. Armstrong, S. S. Saavedra, A. G. M. Barrett, B. M. Hoffman, *Inorganic Chemistry* **2000**, *39*, 3963; c) S. Lee, A. J. P. White, D. J. Williams, A. G. M. Barrett, B. M. Hoffman, *J. Org. Chem.* **2001**, 461.
[38] a) N. R. Armstrong, *J. Porphyrins Phthalocyanines* **2000**, *4*, 414; b) P. Gregory, *J. Porphyrins Phthalocyanines* **2000**, *4*, 432, c) S. M. O'Flaherty, S. V. Hold, M. J. Cook, T. Torres, Y. Chen, M. Hanack, W. J. Blau, *Adv. Mater.* **2003**, *15*, 19.

photovoltaic and solar cells,[39] molecular electronics and photonics,[40] electrochromism in display devices,[41] liquid crystals,[42] nonlinear optics,[43] (electro-)catalysis,[44] and photodynamic therapy (PDT).[45]

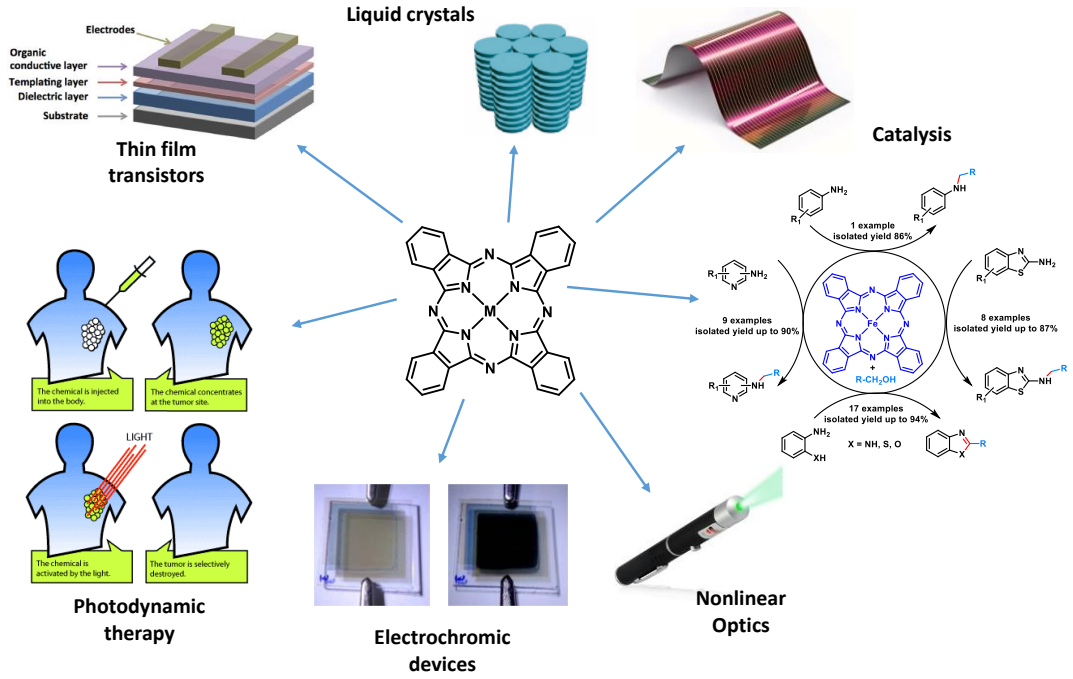

Figure 6. Examples of some of the most important applications of Pcs.

[39] a) J. Rostalki, D. Meissner *Sol. Energy Mater. Sol. Cells* **2000**, *63*, 37; b) B. E. Hardin, E. T. Hoke, P. B. Armstrong, J. H. Yum, P. Comte, T. Torres, J. M. J. Fréchet, M. K. Nazeeruddin, M. Grätzel, M. l. D. McGehee, *Nat. Photonics* **2009**, *3*, 406; c) M.-E. Ragoussi, M. Ince, T. Torres, *Eur. J. Org. Chem*. **2013**, *29,* 6475.

[40] a) B. Simic-Glavaski in *Phthalocyanine. Properties and Applications*, (Ed. C. C. Leznoff, A. B. P. Lever) VCH Publications: New York, **1993**; Vol. III, p 119; c) J. Jiang, K. Kasuga, D. P. Arnold, In *Supramolecular Photosensitive and Electroactive Materials*, (Ed. H. S. Nalwa) Academic Press: New York, **2001**; p 113; d) J. Jiang, W. Liu, D. P. Arnold, *J. Porphyrins Phthalocyanines* **2003**, *7*, 459; e) Y. Chen, W. Su, M. Bai, J. Jiang, X. Li, Y. Liu, L. Wang, S. Wang, *J. Am. Chem. Soc.* **2005**, *127*, 15700.

[41] M. M. Nicholson, *Phthalocyanine. Properties and Applications*, (Ed. C. C. Leznoff, A. B. P. Lever) VCH Publications: New York, **1993**; Vol. III, p 71.

[42] a) J. Simon, P. Bassoul, .in Phthalocyanine. *Properties and Applications*, (Ed. C. C. Leznoff, A. B. P. Lever) VCH Publications: New York, **1993**; Vol. II, p 223; b) J. A. Duro, G. de la Torre, J. Barberá, J. L. Serrano, T. Torres, *Chem. Mater.* **1996**, *8*, 1061, c) M. Kimura, H. Ueki, K. Ohta, H. Shirai, N. Kobayashi, *Langmuir* **2006**, *22*, 5051.

[43] a) S. R. Flom, S. R. in *The Porphyrin Handbook* (Eds K. M. Kadish, K. M. Smith, R. Guilard) Academic Press, New York, **2003**, Vol. 19, p. 179; b) G. de la Torre, P. Vázquez, F. Agulló-López, T. Torres, *Chem. Rev.* **2004**, *104*, 3723.

[44] M. Bala, P. K. Verma, U. Sharma, N. Kumarb, B. Singh, *Green Chem*. **2013**, *15*, 1687.

[45] a) E. Ben Hur, W.-S Chan, in The Porphyrin Handbook (Eds K. M. Kadish, K. M. Smith, R. Guilard) Academic Press, New York, **2003**, Vol. 19, p. 1; b) K. Ishii, *Coord. Chem. Rev.* **2012***, 256,* 1556.

They also play an important role in organic semiconductors.[46] For example, MPc-based organic thin film transistors (OTFTs)[47] have even been used for gas sensors (Figure 7).[48] The detection of the analytes occurs when they either interact with the surface or diffuse into the organic layer, producing a change in hole mobility (μ_h) (Figure 7). Zhang *et al.* used a CuPc OTFT to detect H_2S in dry air.[49a] When the concentration of H_2S increases, the oxygen adsorbed on the surface of the MPc film is displaced, and the reducing gas injects electrons into the *p*-type material, eliminating holes and decreasing the current. The authors tested the specificity of the sensor finding a moderate response to SO_2 and minor response to CH_4, H_2 and CO_2. In order to increase the amounts of analytes detected, Katz *et al*. combined de CuPc transistor with another two.[49b] This device could distinguish eight analytes, including water, acetone, hexane, hydrogen peroxide, and toluene, by analysing the direction and magnitude of response for each OTFT upon exposure.

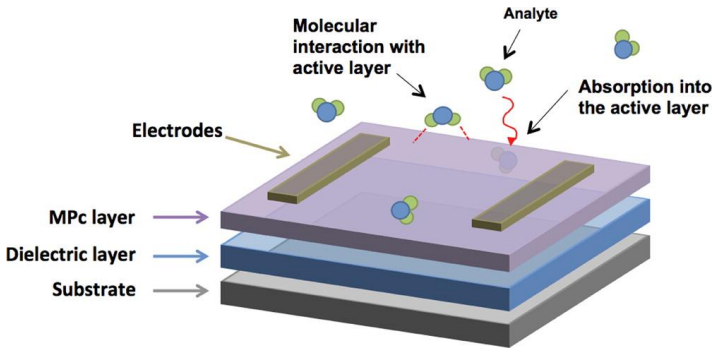

Figure 7. Gas sensors based on OTFT diagram.

With respect to Pzs, they can be envisioned as strong candidates in different technological and applied fields but, despite their potential, this area still remains barely explored. Nevertheless, Pzs have recently emerged as a useful class of tetrapyrroles in the biomedical field.[50] For

[46]a) B. M. Hoffman, J. A. Ibers, *Acc. Chem. Res.* **1983**, *16*, 15; b) J. Simon, In *Molecular Semiconductors*; (Ed. J. J. Andre), Springer, Berlin, **1985**, p 73 c) I. Muzikante, E. Fonavs, E. Silinsh, C. Fretigny, M. Bouvet, J. Simon, S. Spirkovitch, *Mol. Cryst. Liq. Cryst. Sci. Technol., Sect.C* **1998**, *9*, 301;d) M. Hanack, D. Dini, in *The Porphyrin Handbook* (Eds K. M. Kadish, K. M. Smith, R. Guilard) Academic Press, New York, **2003**, Vol. 18, p. 251 e) Bouvet, M. in *The Porphyrin Handbook* (Eds K. M. Kadish, K. M. Smith, R. Guilard) Academic Press, New York, **2003**, Vol. 19, p. 37.

[47] O. A. Melville, B. H. Lessard, T. P. Bender, *Appl. Mater. Interfaces* **2015**, *7*, 13105.

[48] a) A. W. Snow, W. R. Barger in Phthalocyanine. *Properties and Applications*, (Ed. C. C. Leznoff, A. B. P. Lever) VCH Publications: New York, **1989**; Vol. I, p 341; b) G. Guillaud, J. Simon, J. P. Germain, Coord. Chem. Rev. 1998, 178-180, 1433; c) P. Lin, F. Yan, *Adv. Mater*. **2012**, *24*, 34.

[49] a) X. Li, Y. Jiang, G. Xie, H. Tai, P. Sun, *Detection. Sens. Actuators, B* **2013**, *176*, 1191; b) W. Huang, J. Sinha, M.L. Yeh, J. F. M. Hardigree, R. LeCover, K. Besar, A. M. Rule, P. N. Breysse, H. E. Katz, *Adv. Funct. Mater*. **2013**, *23*, 4094.

[50] a) E. R. Trivedi, B. J. Vesper, H. Weitman, B. Ehrenberg, A. G.M. Barrett, J. A. Radosevich, B. M. Hoffman, *Photochem. Photobiol.* **2010**, *86*, 410; b) E. R. Trivedi, C. M. Blumenfeld, T. Wielgos, S. Pokropinski, P. Dande, T. T. Hai, A. G.M. Barrett,

example, Hoffman *et al.* have described a family of chiral oxygen atom-appended Pzs as biomedical optical agents that present absorption and emission in the near-IR range. The most promising Pz, namely H_2[Pz(*trans*-A_2B_2)] (Figure 8a) does not exhibit emission and has a negligible quantum yield for singlet oxygen generation (Φ_Δ = 0.074 in methanol), but when it is situated in the nonpolar environment of a liposome, it displays strong near-IR emission (λ_{max}= 705 nm, Φ_f= 0.087) and an extremely high oxygen quantum yield ($\Phi_\Delta \approx 1$). The molecule presents no evidence of dark toxicity, but it does show significant photoinduced toxicity, suggesting that this Pz is a promise as a "therasnostic" optical agent, which can be visualized with fluorescence imaging (Figure 8b) while acting as a sensitizer for PDT.

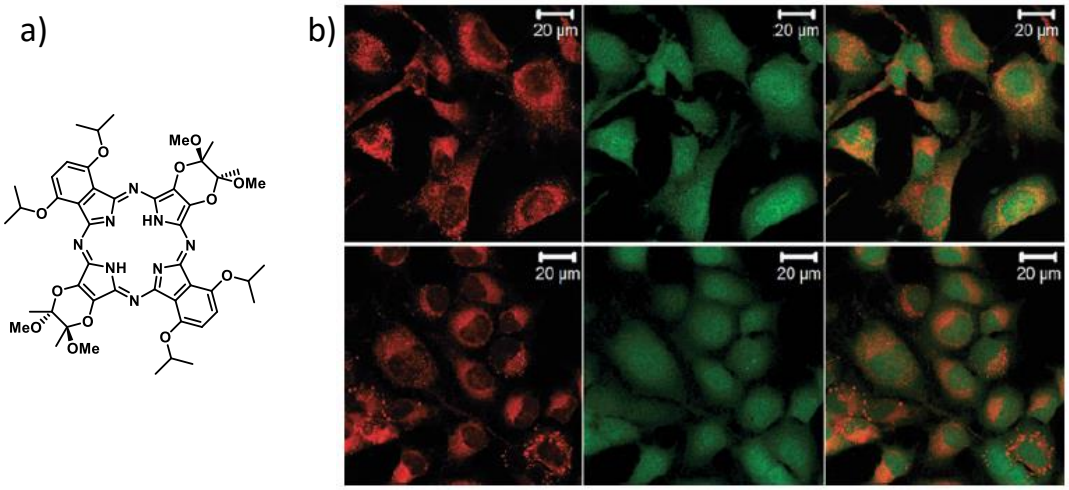

Figure 8. a) Chemical structure of H_2[Pz(*trans*-A_2B_2)]. b) A549 (upper) and WI-38 VA13 (lower) cells treated with 50 µMM Pz, and CellTracker Green™ to outline cells. Emission observed by confocal fluorescence microscopy for Pz (left), CellTracker Green™ (middle) and overlay (right).

B.M. Hoffman, *Tetrahedron Lett*, **2012**, *53*, 5475; c) M. A. Izquierdo, A. Vysniauskas, S. A. Lermontova, I. S. Grigoryev, N. Y. Shilyagina, I. V. Balalaeva, L. G. Klapshina M. K. Kuimova , *J. Mater. Chem. B* **2015**, *3*, 1089.

General Objectives

The aim of this Thesis is the preparation of new electron donor ligands and their complexes based on tetraazaporphyrin derivatives for their application in solar technologies.

Chapter 1 is devoted to the introduction of metallocene units at the periphery of Pcs and their contracted analogues, SubPcs, as a means to enhance their electron-donor ability. Those ferrocene-containing macrocycles will be assembled to an electron-acceptor chromophore, *i.e.* perylenediimide (PDI), and comparatively studied in terms of their ability to generate long-lived charge separated states. This is possible due to the presence of a second donor unit (the metallocene, specifically ferrocene), able to reduce the generated phthalocyanine radical cation through a subsequent electron shift, that should stabilize charge separation. The effect of introducing a different number of ferrocene units at the peripheral positions of the macrocycles (4 or 8 units) will also be investigated.

In addition, tri- and hexaferrocene substituted subphthalocyanines will be prepared. We aim at enhancing the reducing ability of SubPcs and study their assembly with complementary curved electron acceptors such as fullerene C_{60}.

The aim of **Chapter 2** is the synthesis of new electron donor ligands based on porphyrazine derivatives for their application in dye sensitized solar cells (DSSCs). These Pzs should be able to sensitize the injection of electrons into the conduction band of nanocrystalline semiconductors such as TiO_2 or ZnO, pursuing the fabrication of solar cells. These Pzs should have the following structural features:

1. They should contain functional groups that enable their anchoring to the oxide nanoparticles.
2. HOMO and LUMO orbitals of appropriate energy for the efficient electron injection from the Pz excited states to the conduction band of the metal oxide, as well as “in situ” regeneration by the electrolyte.
3. They should show little or no aggregation.

Specific objectives to be met in the research will be listed in each chapter.

Chapter 1

Attachment of ferrocene subunits to the periphery of Pcs and SubPcs

1.1 The Energy Problem

Ever since the Industrial Revolution, mankind has developed a strong dependence on fossil fuels to reach the energy required to cover its needs. In 2011, the annual worldwide consumption rate was approximately 15 TW ($15 \cdot 10^9$ W),[51] and as energy expenses are growing, it has been estimated that the world's energy consumption will reach 28 TW by 2050.[52] Approximately, 85% of this energy is coming from fossil fuels, which produce large quantities of greenhouse gases triggering global warming. As a matter of fact, the globally averaged combined land and ocean surface temperature has increased approximately 1 ^{o}C during the last century.[53] Humanity is then facing a dilemma: maintaining its actual welfare and promoting further economic development entails an increase of the energy consumption. On the other side of the coin are pollution and the predicted exhaustion of fossil energy resources. There is wide agreement that renewable energy sources can be the solution to all these problems as they will play an essential role in the sustainable progress of economy, society and environment.

Solar, wind, hydropower, tidal, geothermal and biomass are renewable energies that may be able to completely substitute or, at least, complement fossil fuels to fulfil these energy demands. Among those, sunlight is the most abundant and sustainable source of energy available. Earth receives approximately 120000 TW per year in a very distributed fashion, around 8000 times the annual consumption rate. Sunlight can be transformed into electricity either thermodynamically or electronically. The first method, the solar thermal energy, is focused on generating electricity by heating a fluid to drive a turbine connected to an electrical generator.[54] The second method converts the solar energy into electricity by opto-electronic devices, called solar cells. This method will be widely discussed in the second chapter of this thesis.

The main drawback of using sunlight to generate electricity is that it cannot be directly stored, and it must be converted to some other form of energy, such as the electrochemical energy of a battery or the kinetic energy of a flywheel.[52a] There is yet another way to store the energy coming from sunlight, and that is in the form of chemical bonds.

Natural photosynthetic organisms convert solar light into chemical fuel in the form of carbohydrates and molecular oxygen from CO_2 and H_2O at an optimal efficiency of roughly

[51] R. E. Blankenship, D. M. Tiede, J. Barber, G. W. Brudvig, G. Fleming, M. Ghirardi, M. R. Gunner, W. Junge, D. M. Kramer, A. Melis, T. A. Moore, C. C. Moser, D. G. Nocera, A. J. Nozik, D. R. Ort, W. W. Parson, R. C. Prince, R. T. Sayre, *Science* **2011**, *332*, 805

[52] a) R. F. Service, *Science* **2005**, *309*, 548; b) J. Potocnik, *Science* **2007**, *315*, 810.

[53] IPCC **2013** Work group I Chapter 2, p 161.

[54] B. Norton, *Harnessing Solar Heat*, Lecture in Energy 18, Springer, Dordrecht, **2014**.

25%.[55] Antennas and pigments are responsible of the absorption of photons that induce charge separation and migration in the reaction centre, generating spatially separated oxidizing and reducing equivalents. The conversion of solar energy into this electrochemical energy is followed by the production of oxygen from water at the oxygen evolving complex, the generation of NADPH, and creation of a proton gradient across the thylakoid membrane. ATP is then obtained by dissipation of this proton motive force through the membrane *via* ATP synthase (Figure 9). ATP and NADPH are the cell fuels to power the reactions of the Calvin-Benson cycle where the CO_2 fixation takes place.[56]

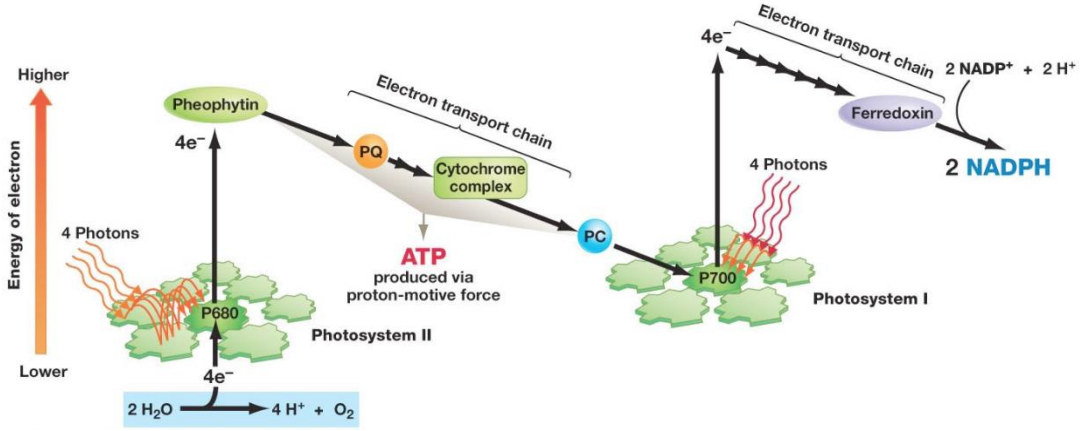

Figure 9. Photosynthetic process of ATP and NADPH generation.

Artificial photosynthesis seeks to mimic the natural process. Owing to its intrinsic complexity, a modular approach is often applied.[57] This approach consists in constructing multicomponent artificial arrays able to carry out each of the natural photosynthetic key steps, such as capture of visible light and/or electron transfer, to afford energetic oxidizing and reducing equivalents with long lifetimes of approximately 1 s, as in natural photosynthesis. These kind of structures are useful not only in artificial photosynthesis but also in photovoltaic and opto-electronic devices.

[55] a) R. E. Blankenship, in *Molecular Mechanisms of Photosynthesis*, Blackwell Science, Oxford, UK, **2002**; b) J. P. McEvoy, G. W. Brudvig, *Chem. Rev*. **2006**, *106*, 4455.
[56] a) *The photosynthetic Reaction Center*, (Eds. J. Deisenhoifer, J. R. Norris), Academic Press, New York, **1993**; b) B. D. Sherman, M. D. Vaughn, J. J., Bergkamp, D. Gust, A. L. Moore, T. A. Moore, *Photosynth Res* **2014**, *120*, 59.
[57] a) R. Eisenberg, D. G. Nocera, Inorg. Chem., 2005, 44, 6799; b) Artificial Mimicry of Photosynthesis *in Photosynth. Res.*, (Ed. S. Thayyumanavan), **2006**, vol. 87, *1*, p. 150; (c) I. McConnell, G. Li, G. W. Brudvig, *Chem. Biol* **2010**, *17*, 434.

1.1.1 Photoinduced electron transfer (PET) in artificial systems

In their most simple version, artificial photosystems are constituted by an electron donor unit (D) connected to an electron acceptor moiety (A) through a linker (L). This linker can connect both units either by covalent or supramolecular interactions (Figure 10).

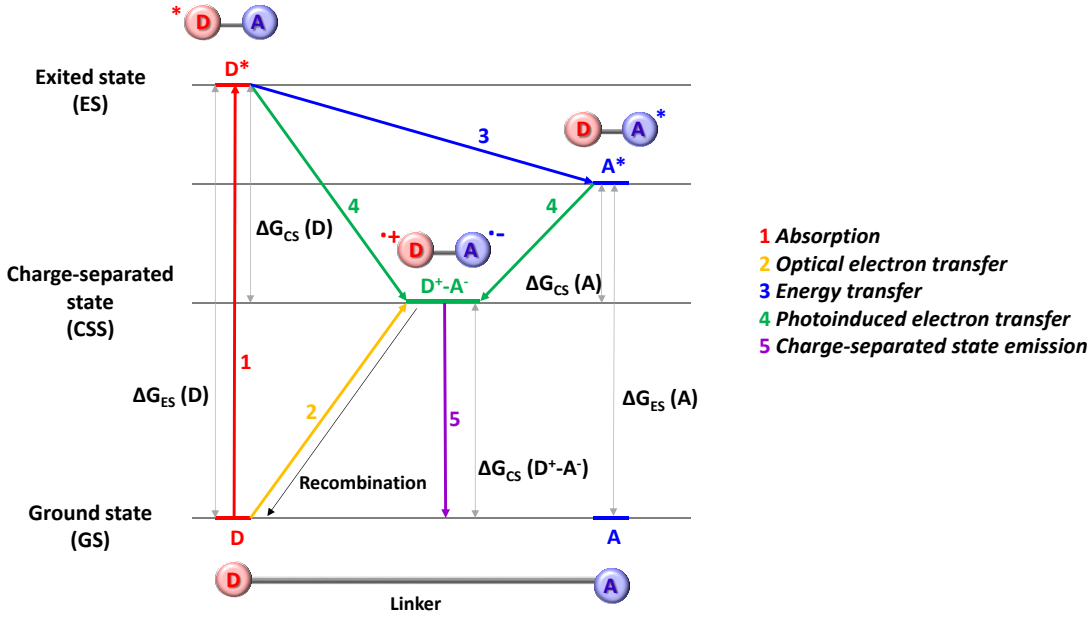

Figure 10. Representation of the photoinduced electron transfer between a donor and an acceptor connected through a linker.

Photoinduced electron transfer (PET) is a process by which an excited electron is transferred from a donor to an acceptor, and in can take place in two different ways.[58] If the electron donor is photoexcited, an electron will be promoted from its highest occupied molecular orbital (HOMO) to its lowest unoccupied molecular orbital (LUMO) and then, it will be transferred to the energetically lower-lying LUMO of the electron acceptor (Figure 11a). On the other hand, if the electron acceptor is the part of the molecule being photoexcited, a hole will appear in its HOMO, which is filled with an electron originating from the higher-lying HOMO of the electron donor (Figure 11b). Both possibilities lead to the formation of an ion-pair or charged separated state (CSS) which will subsequently recombine to the electronic ground state. ***One of the most important objectives of this field of study is to understand how can some factors (nature,***

[58] a) *Photoinduced Electron Transfer*, (Eds. M. A. Fox, M. Chanon), Elsevier, Amsterdam, **1988**; b) S. Speiser, *Chem. Rev.* **1996**, *96*, 1953; c) *Electron Tranfer in Chemistry* Vol I-IV (Ed. V. Balzani), Wiley-VCH, Weinheim, **2001**; d) U. E. Steiner, in *Photodynamic Therapy - From Theory to Application*,(Ed. M. H. Abdel-Kader), Springer, **2014**, Ch 2, p 25.

electronic coupling or structural arrangement of the components) be optimized[51,56b,59] to be used in molecular devices that transform solar energy into any other kind of energy (chemical, electrical…).[60]

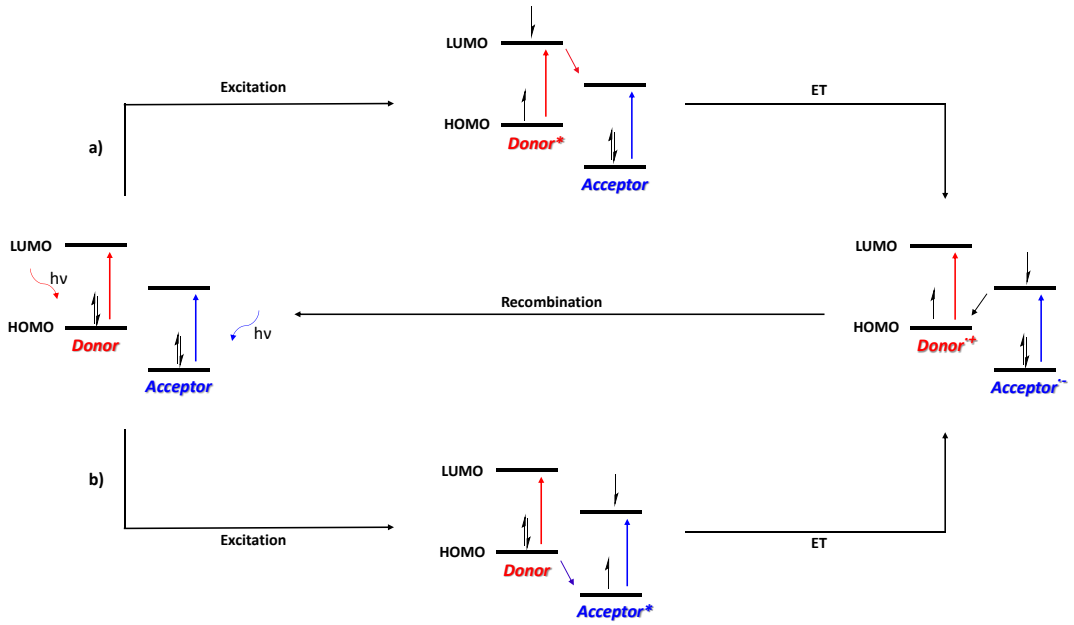

Figure 11. Possible pathways for PET reactions: a) photoexcitation of the donor; b) photoexcitation of the acceptor.

Within this context, the molecular or supramolecular systems must fulfil several requirements regarding PET:

- High extinction coefficients in the visible range of the spectrum.
- The charge separation processes quantum yield must be close to 1, so there are no losses of the excitation energy.
- The energetic level of the CSS must be high and close to the energy level of the initial excited state, to minimize de energy loss.
- Recombination kinetics must be as slow as possible so the CSS lifetime is as high as possible.

[59] a) M. R. Wasielewski, *Chem. Rev.* **1992**, *92*, 435; b) D. Gust, T. A. Moore, A. L. Moore, *Acc. Chem. Res*. **2001**, *34*, 40; c) H. Imahori, S. Fukuzumi, *Adv. Funct. Mater.* **2004**, *14*, 525; d) M. R. Wasielewski, *J. Org. Chem.* **2006**, *71*, 5051; e) M. R. Wasielewski, *Acc. Chem. Res.*, **2009**, *42*, 1910; f) S. Fukuzumi, K. Ohkubo, *J. Mater. Chem* **2012**, *22*, 4575 g) S. Fukuzumi, K. Ohkubo, T. Suenobu, *Acc. Chem. Res.* **2014**, *47*, 1455.
[60] *Acc. Chem. Res.* **2009**, *42*, 1859 (special issue).

1.1.2 Organic synthetic artificial photosystems

Extensive studies have been carried out during the past decades to construct artificial photosynthetic centres. Porphyrinoids,[61] especially porphyrins and phthalocyanines, have been widely used as chromophores, usually as the donor, in this kind of systems. The advantages of these macrocycles over other types of molecules arise from their 18 π-electron aromatic structure that provides them with high molar absorption coefficients and fast energy and/or electron transfer abilities. In addition, the small reorganization energies of electron transfer exhibited, provides them with fast charge separation (CS) and slow charge recombination (CR) rates.

During a long period of time, the acceptor moiety was predominantly based on **quinones**,[59d] owing to their well-known role in nature photosynthesis. A large number of studies regarding porphyrin-quinone systems have been carried out, measuring the effect that varying the number of quinone units, the type of linker, the distance or the relative position between the porphyrin and the quinone would have on the photosystem (Figure 12).[62] Quinones present a reversible two-electron redox process, and both the oxidized and the reduced forms are very stable under physiological conditions. The main drawback in the use of quinones is that their anion radicals are not easily identified by transient spectroscopy compared to other acceptors like fullerene or aromatic diimides.[62]

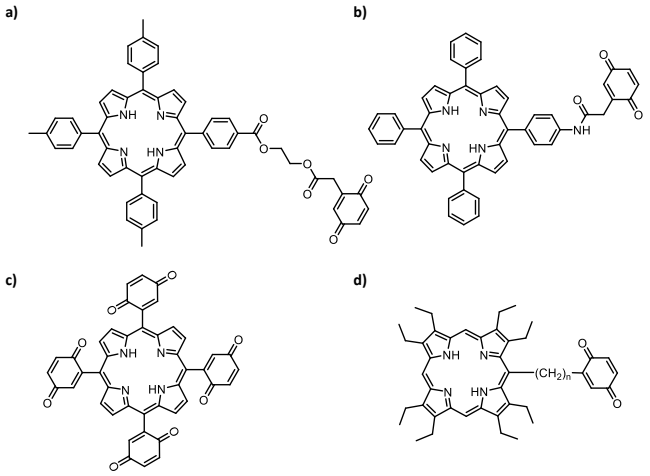

Figure 12. Examples of porphyrin-quinone photosynthetic systems.

[61] D. Gust, *Nature* **1997**, *386*, 21; b) F. D'Souza, O. Ito, *Chem. Commun.* **2009**, 4913; c) Y. Nakamura, N. Aratani, A. Osuka, *Chem. Soc. Rev.* **2007**, *36*, 831; d) A. Tebo, C. Herrero, A. Aukauloo, in *Handbook of Porphyrin Science*, (Eds. K. M. Kadish, K. M. Smith, R. Guilard, Roger), World Scientific Publishing, Singapur, **2014**, v *34*, 195.
[62] T. Nagata, *Res. Chem. Intermed.* **2014**, *40*, 3183 (and references therein).

The introduction of a **fullerene** electron-accepting unit in place of quinones improved the performance of the artificial reaction centres. Fullerenes present small solvent and internal reorganizational energies upon reduction and relative insensitivity to solvent dielectric constant compared to quinones.[59c,63] In comparison with systems employing quinones, those with fullerene acceptor moieties in general show more rapid photoinduced charge separation and slower charge recombination, rendering them as more suitable candidates. But fullerene C_{60} is not the only allotropic form of carbon being widely studied nowadays, carbon nanotubes (CNTs) and graphene, also have extraordinary electrical properties, namely, the ballistic transport of electrons along the main axis of CNTs, and the extraordinarily high mobility of charges in atomically flat graphene. The major downside of this family of compounds is their intrinsic low solubility, which requires functionalization of the sp^2 networks. Sometimes this functionalization has been performed using directly chromophores such as phthalocyanines yielding hybrid photoactive systems (Figure 13).[64]

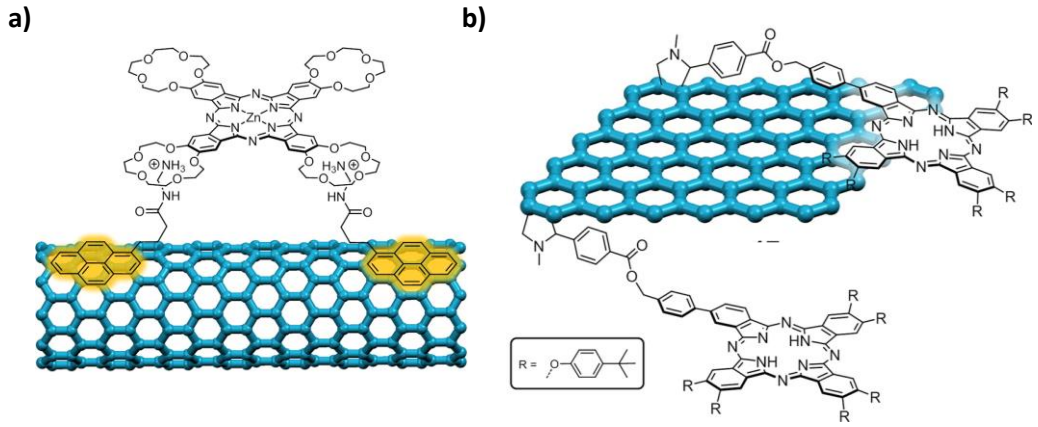

Figure 13. a) Molecular structure of a supramolecular Pc−SWCNT assembly. b) Molecular structure of a covalent Pc−graphene assembly.

The extremely challenging design and synthesis of triads, tetrads and pentads by the inclusion of additional donor or acceptors has led to the generation of long distance charge separations (Figure 14).[59b,65] This is possible because charge separation rates are much higher than charge

[63] a) P. A. Liddell, J. P. Sumida, A. N. Macpherson, *Photochem Photobiol* **1994**, *60*, 537; b) H. Imahori, K. Hagiwara, M. Aoki, *J Am Chem Soc* **1996**, *118*, 11771; c) V. Sgobba, D. M. Guldi, *Chem. Soc. Rev*. **2009**, *38*, 165; d) G. Bottari, G. de la Torre, D. M. Guldi, T. Torres, *Chem. Rev.* **2010**, *110*, 6768.

[64] G. Bottari, G. De la Torre, T. Torres, *Acc. Chem. Res*. **2015**, *48*, 900.

[65] a) P. A. Liddell, D. Kuciauskas, J. P. Sumida, B. Nash, D. Nguyen, A. L. Moore, T. A. Moore, D. Gust, *J. Am. Chem. Soc.* **1997**, *119*, 1400; b) H. Imahori , K. Tamaki , D. M. Guldi , C. Luo , M. Fujitsuka , O. Ito, Y. Sakata , S. Fukuzumi, *J. Am. Chem. Soc.* **2001**,

recombination rates, resulting in a multistep electron transfer system. The pentad depicted in Figure 14b presents a CS lifetime of 0.53 s at 163 K which is comparable to that observed in bacterial photosynthetic reaction center.[65b]

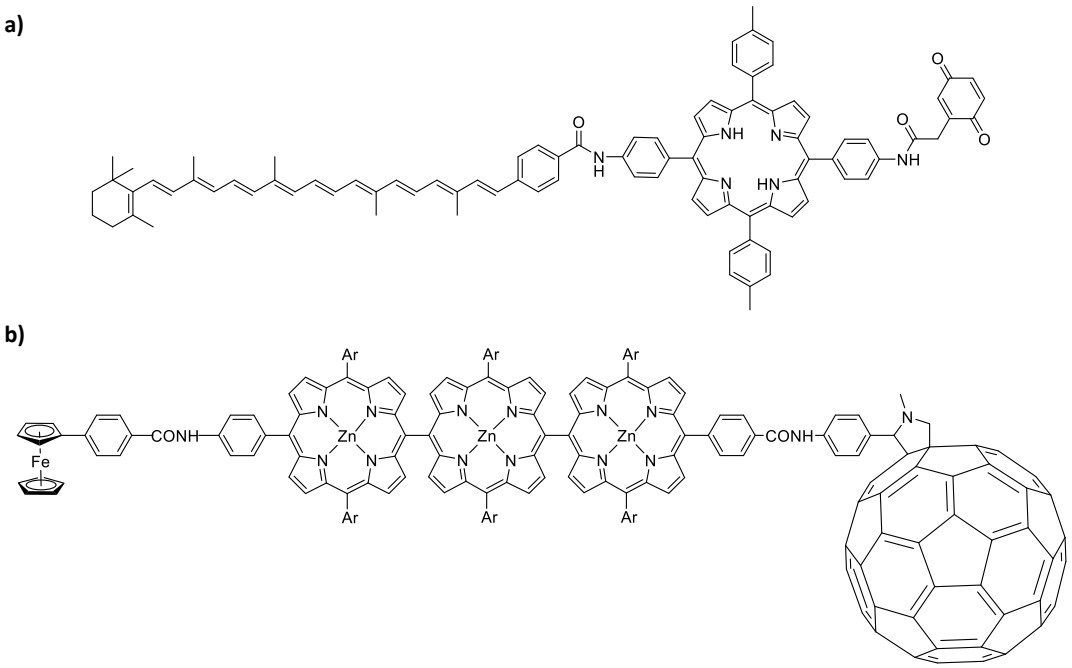

Figure 14. a) Example of a photosystem formed by a quinone as the final acceptor, a porphyrin as antenna and donor and a carotenoid as second donor. b) Example of a Ferrocene–(Zn porphyrin)$_3$–fullerene pentad mimicking multistep photosynthetic reaction centre.

Since the list of donor and acceptor moieties is large, their combination into donor-acceptor systems is too ample to be overviewed in this introduction. Therefore, we are going to focus only on related systems to those studied throughout this thesis, which are based on phthalocyanines as donors, perylenediimide as acceptors, and ferrocene units as secondary donor moieties.

1.1.3 Phthalocyanine-Perylenediimide as donor-acceptor systems

Among porphyrin analogues, phthalocyanines possess excellent light harvesting capabilities over a wide range of the solar light spectrum, with a maximum around 700 nm, where the

123, 2607; c) H. Imahori, Y. Sekiguchi, Y. Kashiwagi, T. Sato, Y. Araki, O. Ito, H. Yamada, S. Fukuzumi, *Chem. Eur. J.* **2004**, *10*, 3184

maximum of the solar photon flux occurs.[63d] This is a great advantage compared with porphyrins, which present their maximum of absorption around 400 nm. In addition, Pcs present higher thermal and photochemical stability than porphyrins, making them optimal candidates for the preparation of D-A ensembles to be used in optoelectronic devices. They have been successfully paired with nanocarbon structures like fullerenes, CNTs, and graphene showing promising results.[64]

On the other hand, perylenediimides (PDIs, Figure 15a)[66] are thermally, chemically and photochemically stable electron acceptors that present a strong absorption with its maximum at ~525 nm (Figure 15b), functioning as well as an antenna that compliments the Pcs absorption. A most important characteristic of this dyes is their mirror fluorescence with fluorescence quantum yield of or close to unity. All these features, along with small reorganization energies upon reduction, make PDIs suitable complementary oxidizing moieties to Pcs in D-A systems.

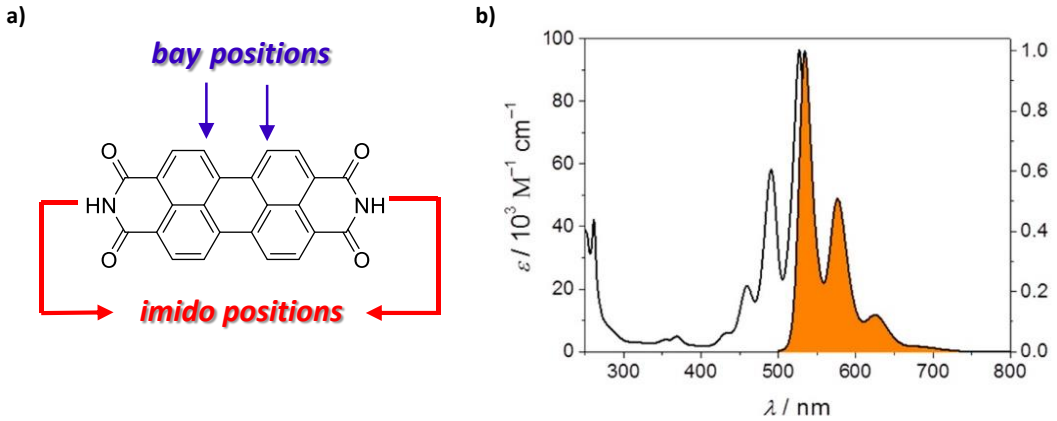

Figure 15. a) Chemical structure of PDI. b) Absorption and fluorescence spectra of PDI.

1.1.3.1 Intermolecular interactions between covalently linked Phthalocyanines and Perylenediimides

In 1998 Liu *et al*. described the first Pc-PDI-Pc triad in which the PDI was connected to the β-position of the phthalocyanine through the imidic nitrogen atom. Its photophysical properties were not studied until 2007 by Zhang and co-workers, who estimated a CSS lifetime of around

[66] a) F. Würthner, A. Sautter, D. Schmid, P. J. A. Weber, *Chem. Eur. J.* **2001**, *7*, 894; b)F. Würthner, C. R. Saha-Möller, B. Fimmel, S. Ogi, P. Leowanawat, D. Schmidt, *Chem. Rev.* Article ASAP, DOI**:** 10.1021/acs.chemrev.5b00188.

20 ns when exciting the PDI unit exclusively.[67] Several referable systems have been studied since then.[68]

In 2004, Wasielesky and co-workers described a tetrakis(perylenediimide)-tetraimideZnPc with a benzene spacer situated between chromophores (Figure 16a).[68a] This system showed a strong tendency to form H-aggregates and the formation of supramolecular fibers was described. Moreover, they studied the interaction at the excited state and when exciting the PDI, no electron but only energy transfer from the PDI to the Pc was observed, which is assigned to the acceptor character of both chromophores. A few years later, Sastre-Santos and co-workers reported a similar pentad, in which the Pc was directly substituted with four PDIs through the N at the imido position. CS was observed in this system with a lifetime of τ = 26 ps.[68c] Furthermore, they also described that the addition of a Mg^{2+} salt to the solution elongates the CS lifetimes up to τ = 480 μs, due to the stabilization of the $PDI^{\cdot-}$ at the CSS by the strong binding of the cation.[68b,c] Finally, in another work, they found a lifetime of 260 μs, the best so far without the addition of Mg^{2+} salts, by fusing both chromophores into a fully conjugated system (Figure 16b).[68e]

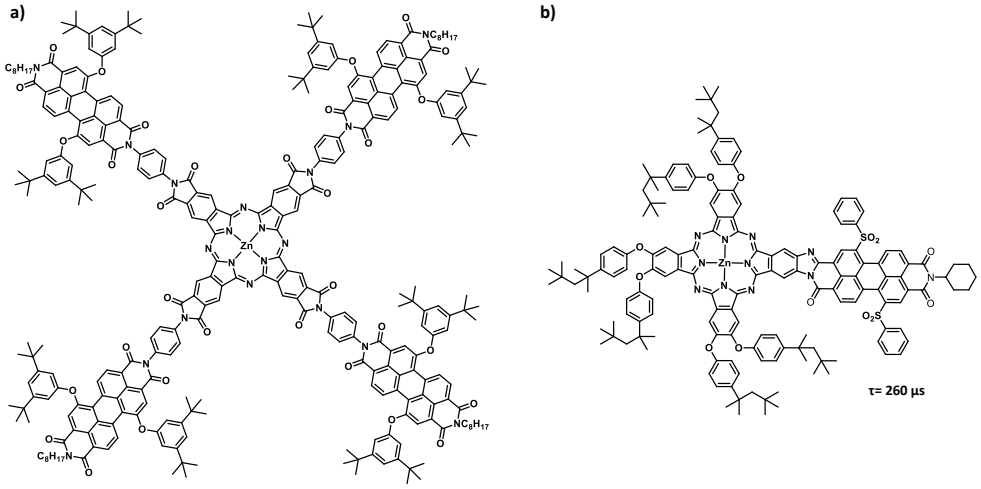

Figure 16.a) Structure of a Pc-PDI pentad. b) Structure of a fused Pc-PDI dyad.

[67]a) S. –G. Liu, Y. –Q. Liu, Y. Xu, X. –Z. Jiang, D. –B. Zhu, *Tetrahedron Lett.* **1998**, *39*, 4271; b) Y. Chen, Y. Lin, M. E. EI-Khouly, X. Zhuang, Y. Araki, O. Ito, W. Zhang, *J. Phys. Chem. C* **2007***, 111,* 16096.

[68]a) X. Li, Sinks, L. E. B. Rybtchinski and M. R. Wasielewski, *J.Am. Chem. Soc*. **2004**, *126*, 10810; b) S. Fukuzumi, K. Ohkubo, J. Ortiz, A. M. Gutierrez, F. Fernandez-Lazaro and A. Sastre-Santos, *Chem. Commun.* **2005**, 3814; c) F. J. Cespedes-Guirao, K. Ohkubo, S. Fukuzumi, A. Sastre-Santos and F. Fernandez-Lazaro, J. Org. Chem. **2009**, *74*, 5871; d) V. Blas-Ferrando, J. Ortiz, L. Bouissane, K. Ohkubo, S. Fukuzumi, F. Fernández-Lázaro and A. Sastre-Santos, *Chem. Commun.* **2012**, *48*, 6241; e) V. M. Blas-Ferrando, J. Ortiz, K. Ohkubo, S. Fukuzumi, F. Fernández-Lázaro, A. Sastre-Santos *Chem. Sci.* **2014**, *5*, 4785.

The connection of the PDI to Pcs *via* the bay positions of the PDI is synthetically challenging, and only a few examples have been described.[69] In our research group, a Pc-PDI-Pc triad linked through acetylene bridges was synthesized and a CSS with a lifetime in the order of hundreds of ps was obtained.[69a] Furthermore, a comparative study between two Pc-PDI dyads, linked through an acetylene and a *trans*-platinum(II) diacetylene bridge respectively, was carried out (Figure 17).[69b] The investigation showed that while in the former a strong coupling between both chromophores is observed in the ground state, the platinum disrupts the electronic communication. Nonetheless, the inclusion of Pt^{II} impacts the results in a longer-lived $Pc^{\bullet+}/PDI^{\bullet-}$ radical ion-pair state.

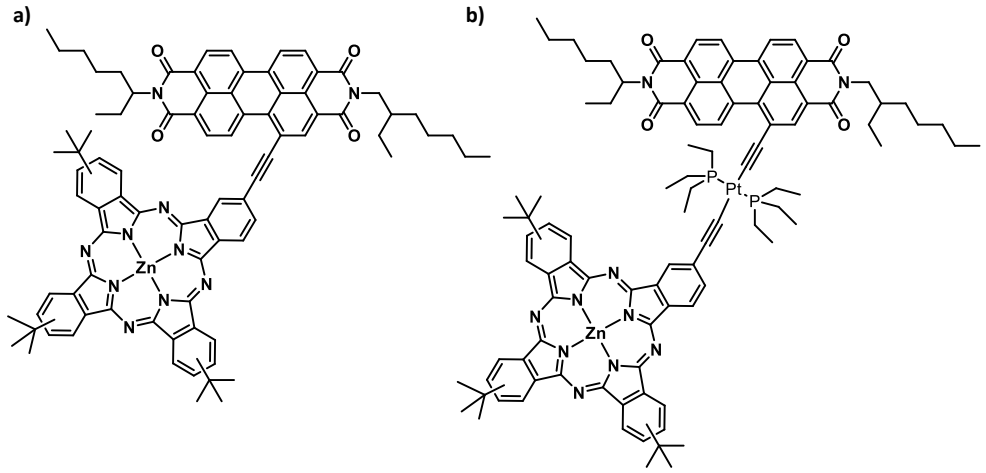

Figure 17.a) Structure of a Pc-PDI dyad linked through an acetylene bridge. b) Structure of a Pc-PDI dyad linked through a *trans*-platinum(II) diacetylene bridge.

1.1.3.2 Intermolecular interactions between non-covalently linked Phthalocyanines and Perylenediimides

Natural photosynthetic reaction centres are based on highly organized supramolecular ensembles that allow to obtain long charge separation lifetimes. With this goal in mind, our research group has synthesized new supramolecular systems employing Watson-Crick H-bonding and coordination chemistry.

Complementary hydrogen bonding interactions are suitable for the assembly of well-defined nanostructures, due to their specificity and directionality. The preparation of Pcs bearing a

[69]a) Á. J. Jimenez, F. Spänig, M. S. Rodríguez -Morgade, K. Ohkubo, S. Fukuzumi, D. M. Guldi, T. Torres, *Org. Lett*. **2007**, *9*, 2481; b) Á. J. Jiménez, M. Sekita, E. Caballero, M. L. Marcos, M. S. Rodríguez-Morgade, D. M. Guldi, T. Torres, *Chem. Eur. J.* **2013**, *19*, 14506; c) X. Sun, W. Qiu, D. Wei, M. Tang, L. Guo, *RSC Adv*. **2014**, *4*, 25616.

diaminotriazine moiety has led to the self-assembling process with a PDI by means of a triple hydrogen bonding. Based on this, two different systems have been studied. In the first one, the tri-*tert*-butyl substituted Pc and the triazine are connected through an acetylene spacer (Figure 18a).[70a] In this case, photoexcitation of the PDI led only to energy transfer to the Pc. On the second system, the melamine is directly linked to an asymmetric hexakis-hexylthio-Pc through an aminic N (Figure 18b).[70b] Photoexciting the PDI afforded a several nanosecond lived $Pc^{\bullet+}/PDI^{\bullet-}$ radical ion-pair state. On the other hand, photoexcitation of the Pc was only followed by an ordinary intersystem crossing to yield the triplet excited state of the Pc.

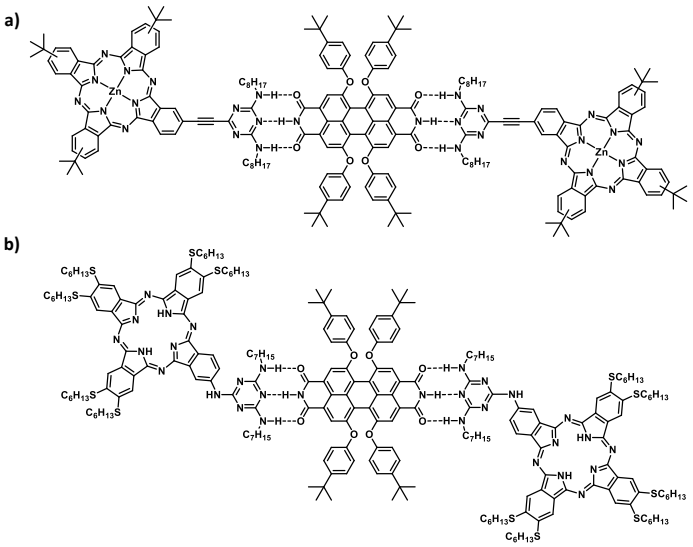

Figure 18. Example structures of two H-bonding based supramolecular Pc-PDI systems.

Ruthenium phthalocyanines tend to form stable and rigid architectures through metal coordination of nitrogen-based ligands.[71] On this basis, two systems were constructed utilizing the strongly coordinating pyridine as the linker between the PDI and Pc units. First, a Pc-PDI-Pc triad was obtained by assembly of a PDI bearing two 4-pyridyl substituents, one at each imido position, with two Ru(CO)tetra*tert*-butylphthalocyanines (Figure 19a).[72] The resulting array displayed an orthogonal geometry with diminished electronic coupling[73] and, consequently, slow charge recombination kinetics. Ultrafast and fast time-resolved techniques unveiled a

[70]a) W. Seitz, A. J. Jiménez, E. Carbonell, B. Grimm, M. S. Rodríguez-Morgade, D. M. Guldi,T. Torres, *Chem. Commun*. **2010**, *46*, 127; b) A. J. Jiménez, R. M. Krick-Calderón, M. S. Rodríguez-Morgade, D. M. Guldi, T. Torres, *Chem. Sci.* **2013**, *4*, 1064.
[71] T. Rawling, A. McDonagh, *Coord. Chem. Rev*. **2007**, *251*, 1128.
[72]M. S. Rodríguez-Morgade, T. Torres, C. Atienza Castellanos, D. M. Guldi, *J. Am. Chem. Soc.* **2006**, *128*, 15145
[73] R. Mercadante, M. Trsic, J. Duff, R. Aroca, *THEOCHEM* **1997**, *394*, 215.

remarkable stabilization of the radical ion pair, with a lifetime of approximately 115 ns. Two referable dyads were described in 2012 by Sastre-Santos and co-workers in which two different PDIs were axially coordinated to a Zn-naphthalocyanine.[74] In the second system, four pyridyl substituents located at the bay positions of the perylene coordinate to four Ru(CO) phthalocyanines (Figure 19b).[75] In this case, strong electronic coupling between the donors (*i.e.*, RuPc) and the acceptor ($PDIPy_4$) is observed in both the ground and excited states. Photoexcitation of either units produces a CSS which rapidly recombines through the Pc excited triplet state, and hence is short-lived (several hundred picoseconds).

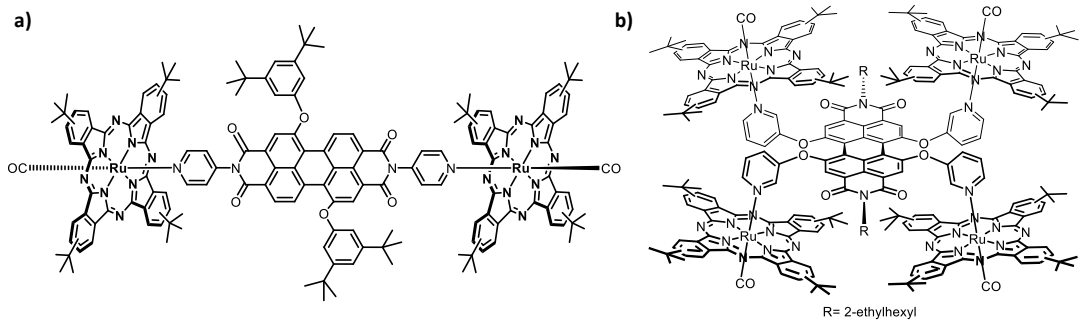

Figure 19. a) Structure of a metallosupramolecular triad *via* PDI imido positions. b) Structure of a metallosupramolecular pentad *via* PDI bay positions.

1.1.3.3 Inclusion of a secondary donor: Ferrocene

The presence of secondary donors in the artificial photosystems derives in the generation of longer lived CSS by a hole migration mechanism. Ferrocene (Fc), which has already a long history in combination with porphyrinoids,[76] has been widely used for this purpose due to its outstanding electrochemical properties, which arises from the reversibility of the Fc/Fc^+ couple.[77] Ferrocene is also able to deactivate the singlet excited state of the porphyrinoid

[74]M. E. El-Khouly, A. M. Gutierrez, A. Sastre-Santos, F. Fernandez-Lazaro, Shunichi Fukuzumi *Phys. Chem. Chem. Phys.* **2012**, *14*, 3612.
[75] A. J. Jiménez, B. Grimm, V. L. Gunderson, M. T. Vagnini, S. K. Calderón, M. S. Rodríguez-Morgade, M. R. Wasielewski, D. M. Guldi, T. Torres, *Chem. Eur. J.* **2011**, *17*, 5024.
[76] A. Vecchi, P. Galloni, B. Floris, S. V. Dudkin, V. N. Nemykin, *Coord. Chem. Rev.* **2015**, *291*, 95.
[77] a) S. Fery-Forgues, B. Delavaux-Nicot, *J. Photochem. Photobiol. A* **2000**, *132*, 137; b) K. Heinze, H. Lang, *Organometallics*, **2013**, *32*, 5623 (special issue).

derivatives, leading to a quenching of the fluorescence of the macrocycles due to intersystem crossing processes.[78] The emission reappears if the Fc unit is oxidised from Fe^{2+} to Fe^{3+}.[79]

A number of ferrocene containing triads, tetrads and pentads have been synthesized, usually utilizing C_{60} as the acceptor and a number of (metallo)porphyrins as the chromophore (see Figure 14b on page 31).[65c,80] Other acceptors rather than C_{60} have also been tested. In 2007 Fukuzumi *et al.* prepared a triad consisting of a Fc unit linked to a zinc triarylporphyrin through a benzo-amido-benzo spacer, and a 4-pyridylnaftalnediimide axially coordinated to the zinc atom of the porphyrin, measuring a charge separation lifetime of 320 μs (Figure 20).

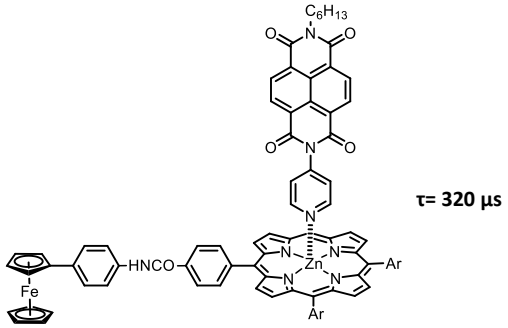

Figure 20. Structure of a Ferrocene-Porphyrin-Perylenediimide triad.

Multiple Fc-Pc arrays have been described, and usually the connection of both chromophores is done through different spacers. From all of these, only one example, described by Leznoff and co-workers, relates the synthesis of a free base Pc bearing four Fc units directly attached at the periphery.[81] However and to date, no Fc-Pc arrays have been reported as a part of artificial photosynthetic systems.

On the other hand, there are several examples of Fc-SubPc artificial systems, since SubPcs, the lower analogues of Pcs, act as the acceptor and antenna. One of the advantages SubPcs is that they usually possess higher fluorescence quantum yields and smaller reorganization energies than porphyrins.[82] The synthesis of a Fc-SubPc-C_{60} triad (Figure 21), which presented a long-lived

[78]a) M. Kubo, Y. Mori, M. Otani, M. Murakami, Y. Ishibashi, M. Yasuda, K. Hosomizu, H. Miyasaka, H. Imahori, S. Nakashima, *Chem. Phys. Lett*. **2006**, *429*, 91; b) M. Kubo, Y. Mori, M. Otani, M. Murakami, Y. Ishibashi, M. Yasuda, K. Hosomizu, H. Miyasaka, H. Imahori, S. Nakashima, *J. Phys. Chem*. *A* **2007**, *111*, 5136.
[79]J. Rochford, A. D. Rooney, M.T. Pryce, *Inorg. Chem*. **2007**, *46,* 7247.
[80]a) H. Imahori, K. Tamaki, H. Yamada, K. Yamada, Y. Sakata, Y. Nishimura, I.Yamazaki, M. Fujitsuka, O. Ito, *Carbon* **2000**, *38*, 1599; b) H. Imahori, K. Tamaki, D. M. Guldi, C. Luo, M. Fujitsuka, O. Ito, Y. Sakata, S.Fukuzumi, J. Am. Chem. Soc. 2001, 123, 2607.
[81] Z. Jin, K. Nolan, C. R. McArthur, A. B. P. Lever, C. C. Leznoff, *J. Organomet. Chem.* **1994**, *468*, 205.
[82]a) R. A. Kipp, J. A. Simon, M. Beggs, H. E. Ensley and R. H. Schmehl, *J. Phys. Chem. A* **1998**, *102*, 5659; b) A. Medina, C. G. Claessens, G. M. A. Rahman, A. M. Lamsabhi, O. Mo, M. Yañez, D. M. Guldi, T. Torres, *Chem. Commun*. **2008**, 1759.

charge separation state of 230 μs, was described by our research group.[83] Lately, Nemykin and co-workers have studied the effect of modifying the length and nature of the spacer between the boron atom and the ferrocene unit on the photophysical properties of the SubPc-Fc systems, concluding that the shorter the spacers, the faster the charge recombination occurs.[84]

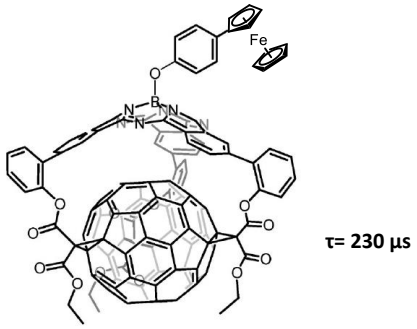

Figure 21. Structure of Fc-SubPc-C_{60} trimer

[83] a) D. González-Rodríguez, T. Torres, M. M. Olmstead, J. Rivera, M. Angeles Herranz, L. Echegoyen, C. Atienza Castellanos, D.M. Guldi, *J. Am. Chem. Soc*. **2006**, *128*, 10680; b) D. González-Rodríguez, E. Carbonell, G. M. Rojas, C. Atienza Castellanos, D. M. Guldi, T. Torres, *J. Am. Chem. Soc*. **2010**, *132*, 16488.

[84] a) P. V. Solntsev, K. L. Spurgin, J. R. Sabin, A. A. Heikal, V. N. Nemykin, *Inorg. Chem*. **2012**, *51*, 6537; b) E. Maligaspe, M. R. Hauwiller, Y. V. Zatsikha, J. A. Hinke, P. V. Solntsev, D. A. Blank, V. N. Nemykin, *Inorg. Chem*. **2014**, *53*, 9336.

1.2 Specific objectives

In the first part of this chapter, we aimed at optimizing the photophysical response of [Ru(CO)Pc]-[BPyPDI]-[Ru(CO)Pc] (Figure 19, *vide supra*) by the preparation of new cart-wheel-type hybrids from new modified phthalocyanines.

Within this model, phthalocyanines bearing different metal ions should render electron donor-acceptor conjugates connected with different linkage strengths. Weaker electron donor-acceptor associations could slow down the charge recombination process by dissociation after electron transfer. In this respect, we expected different behaviour for ZnPc and RuPc complexes, as components of cart-wheel systems (**18** and **19**, Figure 25, *vide infra*) based, on one hand, on the different strength of the pyridyl Ru and pyridyl Zn coordination bonds and, on the other hand, on their different ability to stabilize triplet excited states.

A potent strategy for the design of electron donating Pcs entails their peripheral functionalization with, for example, metallocenes, such as ferrocene. Ferrocenes interact with -conjugated systems both through the cyclopentadienyl anion and through the metal orbitals, and this should enrich the phthalocyanine with further redox processes. The role of these secondary electron donors is to reduce the generated phthalocyanine radical cation through a subsequent electron shift and thus, to stabilize charge separation.

The goal of this section is the synthesis and photophysical characterization of Ru(II) and Zn(II)phthalocyanines bearing four and eight ferrocenes directly attached to the periphery. In a second stage, these Pcs are assembled into the corresponding cart-wheel Pc-PDI-Pc hybrids of different nature, and comparatively studied in terms of their ability to generate long lived charge separated states. The specific objectives of this section are:

- Synthesis and characterization of the tetraferrocenyl phthalocyanines.
- Synthesis and characterization of the octaferrocenyl phthalocyanines.
- Assembly of the RuPc-PDI-RuPc complexes.
- Assembly of ZnPc-PDI-ZnPc complexes.
- Electrochemical and photophysical characterization of the systems both in the ground and excited states.

In the second part of this Chapter, we aimed at studying peripheral ferrocene substitution on subphthalocyanines. The introduction of 3 and 6 metallocene units should enhance the reducing ability of this macrocycles, which are acceptors related to Pcs. The large π-conjugated curvature of SubPcs will be used in a second step for convex-concave interaction with a C_{60} molecule, for the formation of donor-acceptor cocrystallates. Specific objectives of this section are:

- Synthesis and characterization of triferrocenylsubphthalocyanines.
- Synthesis and characterization of hexaferrocenylsubphthalocyanines.
- Electrochemical and photophysical characterization of the systems both in the ground and excited states.
- Studies on the formation of concave-convex supramolecular arrays with C_{60} both in solution and in the solid phase.

1.3 Results and discussion

1.3.1 Synthesis and study of new Fc-Pc-PDI assemblies for artificial photosynthesis.

1.3.1.1 Synthesis of the ferrocenyl-substituted phthalocyanines

A widely extended method to obtain new phthalocyanine derivatives relies on the employment of palladium catalysed cross-coupling reactions (such as Suzuki, Heck, Stille, Sonogashira, etc.).[85] On this regard, two different strategies that differ from each other on whether the coupling reaction takes place before (**route a**, Scheme 8) or after (**route b**, Scheme 8) the macrocyclization reaction, can be followed

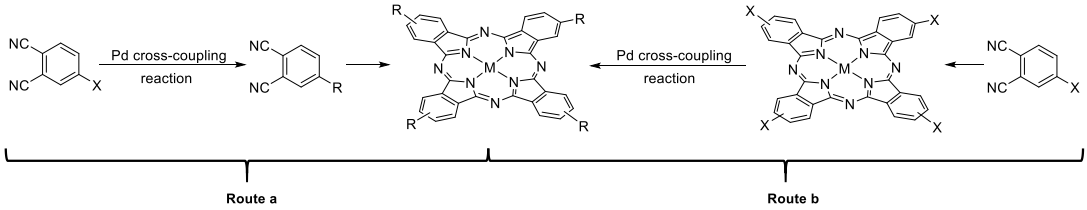

Scheme 8. Synthetic alternatives to prepare phthalocyanines using Pd cross-coupled reactions.

Both strategies have been successfully used in the literature. Route **a** was followed by Leznoff and co-workers to synthesize a tetraferrocenyl substituted free-base phthalocyanine. First, they prepared the 4-ferrocenylphthalonitrile by reaction of ferricenium chloride with 4-diazoniumphthalonitrile bisulphate in 45% yield (Scheme 9).[81] Cyclotetramerization of the former phthalonitrile in boiling amyl alcohol in the presence of the corresponding lithium alkoxide generated the dilithium phthalocyanine which, after treatment with diluted HCl, yielded the corresponding free base Pc.

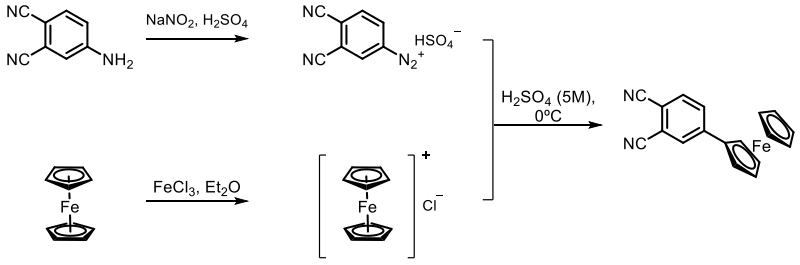

Scheme 9. Synthesis of 4-ferrocenylphthalonitrile by Leznoff and co-workers

[85] *Metal-Catalyzed Cross-Coupling Reactions*; 2nd Edition, (Eds, A. de Meijere, F. Diederich); WILEY-VCH: Weinheim, Germany, **2004**.

As an example of **route b**, Sugimoto *et al* have recently described the preparation of *meso*-tris(4-ferrocenylphenyl)subporphyrin in moderate yields through a Suzuki coupling of ferroceneboronic acid and the corresponding tribromosubporphyrin (Scheme 10).[86]

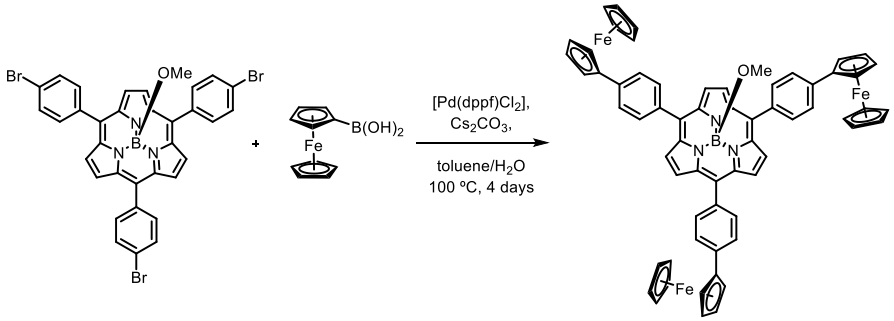

Scheme 10. Synthesis of *meso*-Tris(4-ferrocenylphenyl)subporphyrin.

We tackled the synthesis of ferrocene Pcs following **route a**. 4-ferrocenylphthalonitrile **1** and 4,5-bisferrocenylphthalonitrile **2** were prepared from the corresponding iododerivatives in good yields (70-80 %) by palladium catalysed crossed-coupling reaction of the corresponding iodo-derivative in a degassed 1:1 mixture of water and toluene for 18 h (Scheme 11).[87]

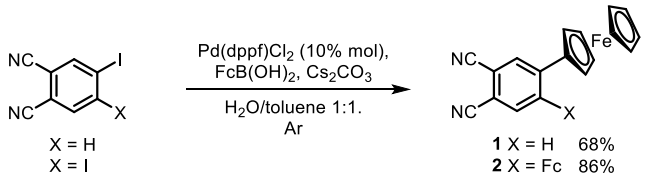

Scheme 11. Synthesis of **1** and **2**.

Next, $ZnFc_4Pc$ **3** was obtained by cyclotetramerization reaction of phthalonitrile **1** in refluxing DMAE, in the presence of $Zn(OAc)_2$ as a template (Scheme 12). In the case of RuPcs, the synthetic conditions depend on the axial substitution desired for the resulting Pc.[71] In our particular case, we blocked one of the two Ru axial positions in order to avoid supramolecular polymerization processes when coordinating a bidentate PDI ligand. Thus, single ligation at the Ru(II) centre of the Pc is assured by placing a strongly ligating, σ-donor *π*-acceptor carbonyl ligand at one of the two axial Ru(II) coordination sites. These complexes were obtained by metallation of free base Pc **4**, which was prepared by the cyclotetramerization reaction of phthalonitrile **1** using lithium

[86] H. Sugimoto, T. Tanaka, A. Osuka, *Chem. Lett.* ***2011****,* 40*, 629.*

[87] a) H. Lam, S.M. Marcuccio, P. I. Svirskaya, S. Greenberg, A. B. P., Lever, C. C. Leznoff, R. L. Cerby, *Can. J. Chem*. **1989**, *67*, 1087; b) D. S. Terekhov, K. J. M. Nolan, C. R. McArthur, C. C. Leznoff, *J. Org. Chem*. **1996**, *61*, 3034.

pentanolate as the metal template. Further treatment with $Ru_3(CO)_{12}$ in refluxing phenol afforded $RuFc_4Pc$ **5** in 24% yield overall.

Both $ZnFc_4Pc$ **3** and $RuFc_4Pc$ **5** were obtained as a mixture of the four C_{4h}, D_{2h}, C_{2v} and C_{2s} regioisomers and showed low solubility in common organic solvents. Therefore, they displayed in ^{1}H-NMR broad signals corresponding to the isoindole protons at 9.2 and 8.2 ppm ($ZnFc_4Pc$ **3**) and 9.45, 9.30 and 8.83 ppm ($RuFc_4Pc$ **5**), while signals at 4.6 and 4.2 ppm account for the ferrocene subunits.

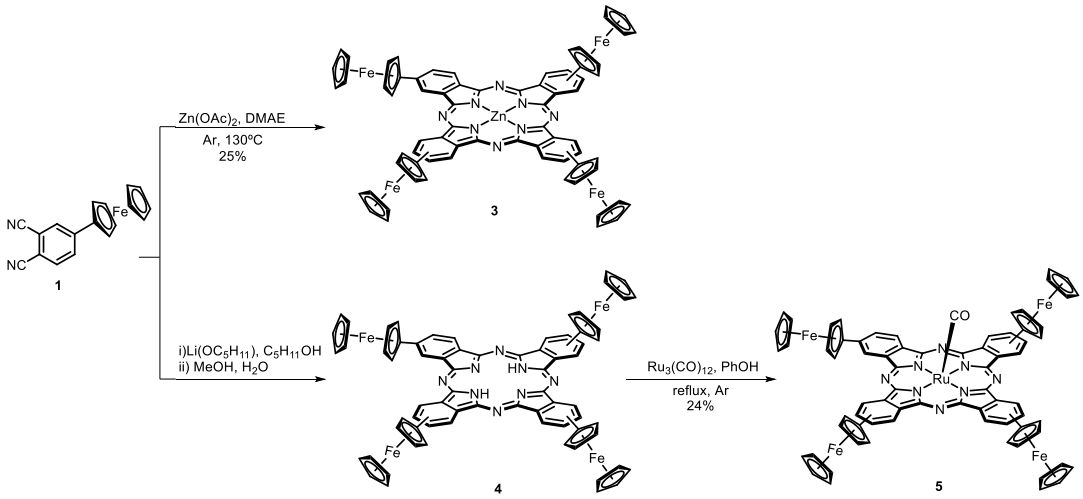

Scheme 12. Synthesis of ZnPc **3** and RuPc **5**.

Attempts to prepare the octasubstituted derivatives using the previous conditions were not successful. We attribute the failure to a sharp decrease of the phthalonitrile reactivity owing to the electron-donating groups at the *para* positions of the nitrile functions, which led to a minor electrophility thereof. In fact, the low 25 % yield reported for the formation of $ZnFc_4Pc$ **3** in comparison with other A_4 Pcs found in the literature can also be related to a lower reactivity of this phthalonitrile.

Therefore, the corresponding 1,3-diiminoisoindoline derivative **6** was prepared, following the typical procedure, by treating **2** with NH_3 gas in the presence of NaOMe, in refluxing methanol (Scheme 13). Diiminoisoindolines are more reactive than their phthalonitriles analogues. Indeed they are postulated as intermediate compounds in the formation of Pcs. Thus, they usually cyclotetramerize just by heating in solution, even without metal templates.

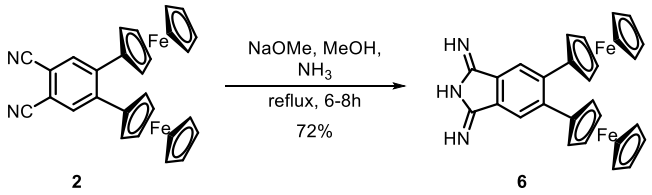

2 6

Scheme 13. Synthesis of **6**.

The first attempts to synthesize the free-base Pc by refluxing **6** in DMAE (b.p. 133 °C), 1-pentanol (*b.p*. 139 °C) and 1-octanol (*b.p*. 195 °C) were unsuccessful even in the presence of DBU as a basic catalyst. Further efforts to obtain the macrocycle using microwave techniques led only to decomposition of the starting material. We attempted then a templated macrocyclization by refluxing **6** in the presence of freshly prepared magnesium propoxide and butoxide. Under these conditions, we did observe formation of $MgFc_8Pc$ **7**, but after demetallation with TFA, free-base Pc **8** was obtained with only marginal yields (2 % overall, Scheme 14a).

Next, we turned to a less common synthetic procedure, consisting in refluxing **6** and $MgCl_2$ in dry DMF using hexamethyldisilazane (HMDS) and *para*-toluensulfonic acid (*p*-TSA) as catalysts (Scheme 14b).[19] HMDS has been postulated to behave as nucleophilic reagent and source of nitrogen, activating phthalonitriles, phthalimides or phthalic anhydrides by converting them into diiminoisoindoline derivatives, which, in turn, undergo intermolecular condensation. In our case, even if our starting material was already a diiminoisoindoline, this strategy led us to obtain H_2Fc_8Pc **8** in 21 % yield after demetallation with TFA. $ZnFc_8Pc$ **9** was synthesized under the same conditions but using $Zn(OAc)_2$ as the metal template (Scheme 14c). $RuFc_8Pc$ derivative **10** was obtained from the free base ZnPc **8** by metalation with $Ru_3(CO)_{12}$ (Figure 22). The solubility of this family of compounds is slightly higher but not enough to record ^{13}C-NMR spectra.

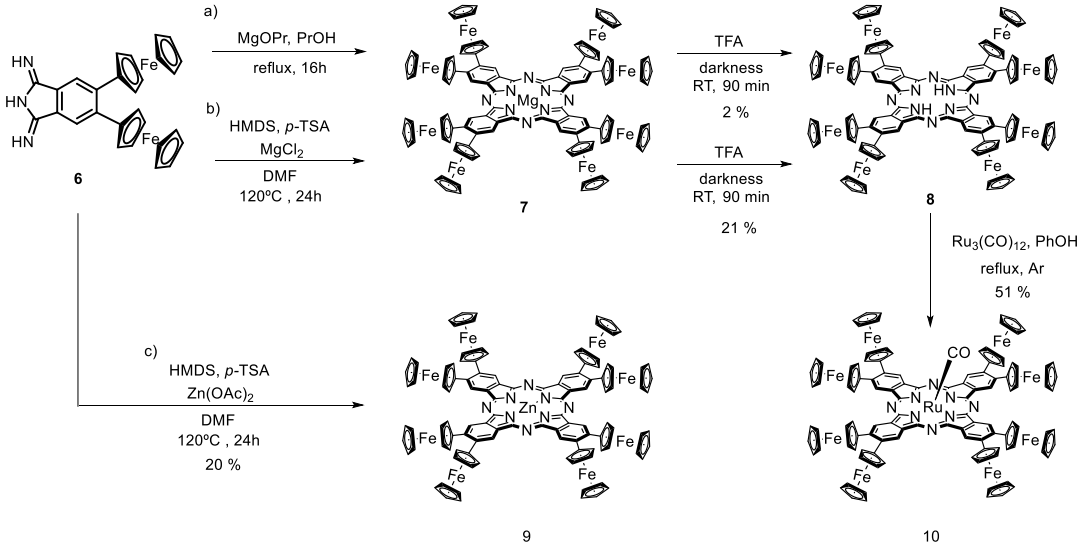

Scheme 14. Synthesis of $ZnFc_8Pc$ **9** and $RuFc_8Pc$ **10.**

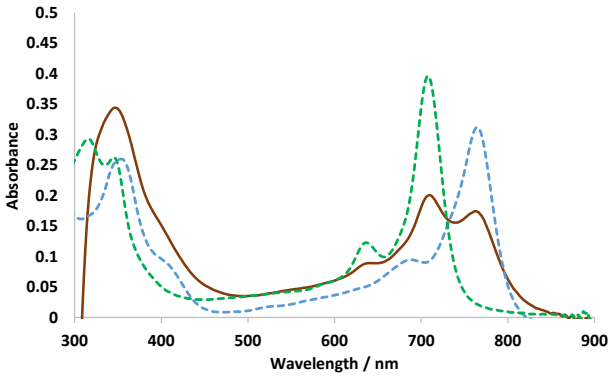

Figure 22. UV-vis spectra of H_2Pc **8** (blue dashed line), $RuFc_8Pc$ **10** (green dashed line) and of an aliquot of the metalation reaction from H_2Pc **8** to $RuFc_8Pc$ **10** (brown solid line).

The structure of the Pcs was established on the basis of their spectroscopic features, namely, ^{1}H-NMR, ^{13}C-NMR, FT-IR, UV-Vis and MS. Comparing the ^{1}H-NMR spectra of the $RuFc_4Pcs$ **5** and **10** (Figure 23), the main differences between a regioisomeric mixture of tetrasubstituted Pcs and a monoisomeric octasubstituted Pc can be easily spotted. While $RuFc_8Pc$ **10** (top part of Figure 23) presents one singlet corresponding to the signal of the aromatic proton of the macrocycle, $RuFc_4Pc$ **5** presents three sets of broad signals between 8 and 10 ppm. H_α of the phthalocyanines always appear at lower field than H_β due to the anisotropic current of the

macrocycle. The sharpness of the Pc H_α signal in the octasubstituted Pc spectrum indicates little aggregation in solution. The broader signals of $RuFc_4Pc$ **5** can be explained as an effect of the lower solubility of the tetrasubstituted macrocycles.

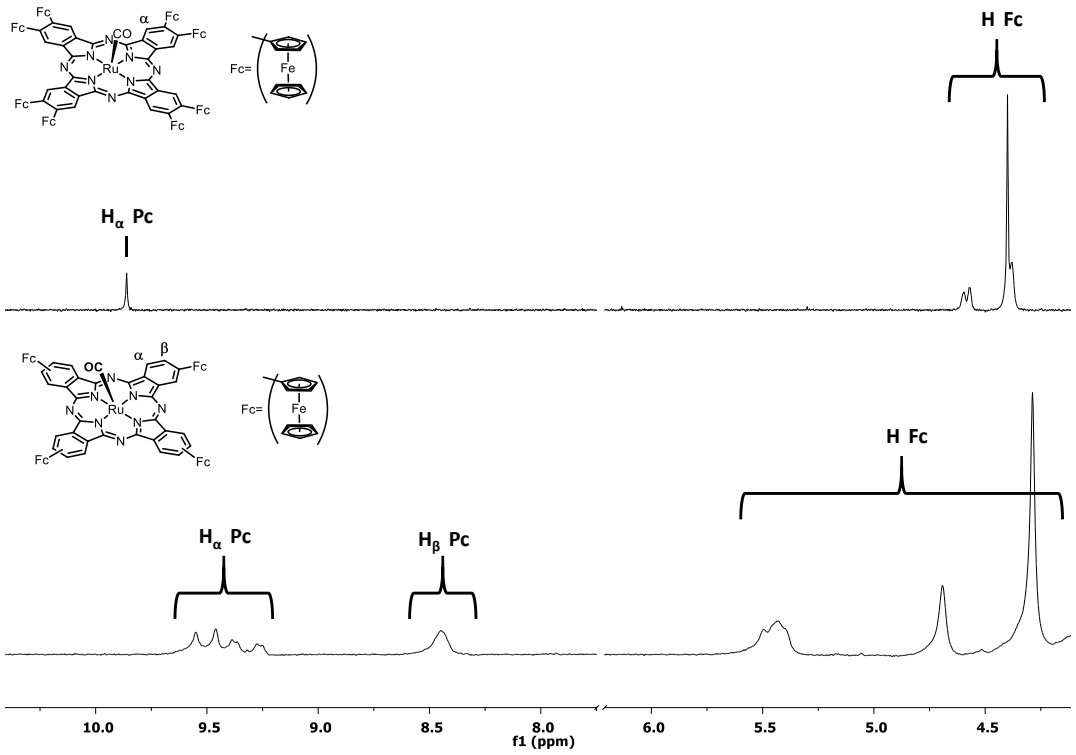

Figure 23. Top: ^{1}H-NMR spectrum of $RuFc_8Pc$ **10** in $CDCl_3$. Down: ^{1}H-NMR spectrum of $RuFc_4Pc$ **5** in DMSO-d_6

1.3.1.2 Synthesis of the perylenediimide derivatives

In order to study the assembly of Pc and PDI, a simpler monotopic PDI (**11**) was synthesized bearing at one imido position diisopropylphenyl and a 4-pyridyl group at the other one. In order to form the 1:2 complexes, the symmetric PDI **12** bearing two 4-pyridyl groups was also synthesized. Both **11** and **12** were prepared from PDA **16**.

Perylenedianhydride (PDA) **16** was prepared in four steps (Scheme 15), starting with chlorination of the bay positions of the commercially available perylene dianhydride, to afford PDA **13**.[88] Next, PDA **13** was converted into a diimide in order to increase to increase its

[88] M. Sadrai, L. Hadel, R. R. Sauers, S. Husain, K. Krogh-Jespersen, J. D. Westbrook, G. R. Bird, *J. Phys. Chem*. **1992**, *96*, 7988.

solubility. **14** was prepared in 88 % yield by refluxing perylenedianhydride **13** with *n*-butylamine in propionic acid.[89] Subsequently, *tert*-butylphenoxy groups were introduced at the bay positions through aromatic nucleophilic substitution, leading to PDI **15** in 96 % yield.[89] These bulky aromatic substituents produce a twist in the planar structure of the PDI, hampering the π-π interactions and, therefore, the π-π stacking, thus increasing notably the solubility of the PDI.[90] The last step in the synthesis of **16** was the hydrolysis of the imido functions to the dianhydride moieties by refluxing **15** in the presence of KOH.[91]

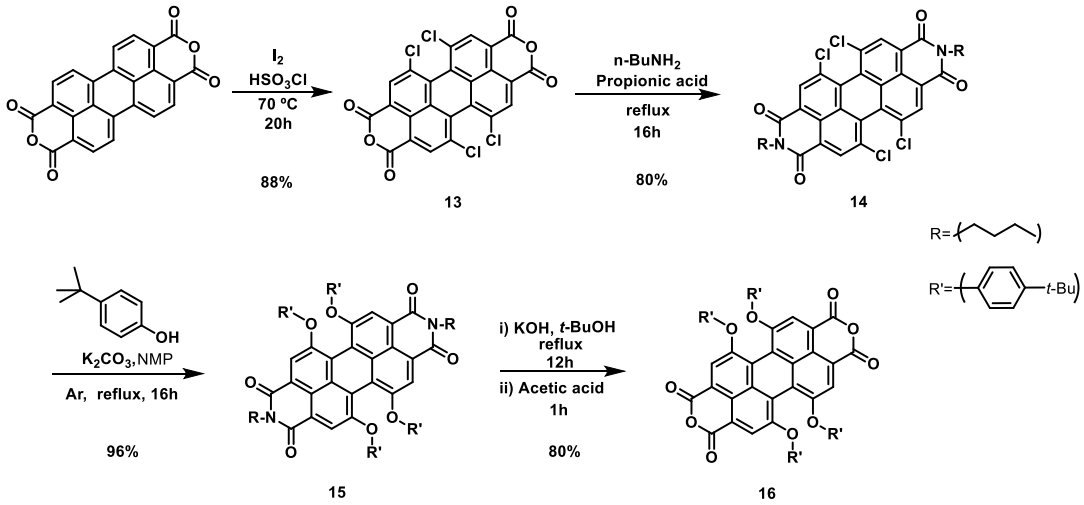

Scheme 15. Common synthetic pathway of PDIs **11** and **12**.

Symmetric PDI **12** was obtained directly by heating a solution of **16** and 4-aminopyridine in quinoline at 180 °C (Scheme 16). The synthesis of the asymmetric PDI **11** was not straightforward and it could be achieved in at least two ways, either stepwise, or in one step by mixing both at the same time to obtain a statistical mixture of compounds. We decided to introduce first the 4-aminopyridine unit as the foreseeable side product of the reaction would be **12**. Thus, **16** was reacted with 4-aminopyridine affording perylenemonoimide **17**. Further reaction of **17** with 2,6-diisopropylaniline led to the desired unsymmetrical PDI **11** (Scheme 16).[92] Both PDIs **11** and **12** were highly soluble in organic solvents and were purified by column chromatography on silica gel.

[89] F. Würthner, A. Sautter, J. Schilling, *J. Org. Chem.* **2002**, *67*, 3037.
[90] C. Kohl, T. Weil, J. Qu, K. Müllen, *Chem. Eur. J.* **2004**, *10*, 5297.
[91] D. K. Panda, F. S. Goodson, S. Ray, R. Lowell, S. Saha, *Chem. Commun.* **2012**, *48*, 8775.
[92] M. Lederer, U. Hahn, J. Fernández-Ariza, O. Trukhina, M. S. Rodríguez-Morgade, C. Dammann, T. Drewello, T. Torres, D. M. Guldi, *Chem. Eur. J.*, **2015** ,*21*, 5916

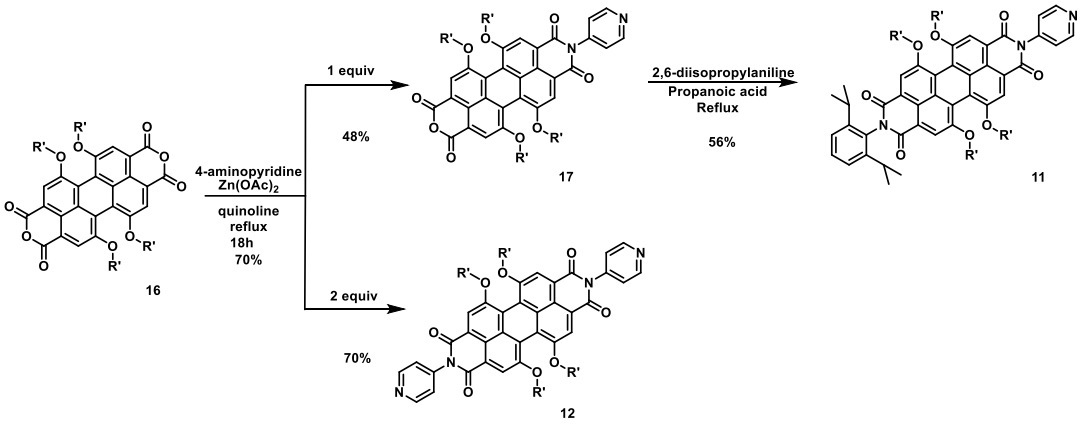

Scheme 16. Synthesis of PDI **11** and PDI **12** from PDI **16**.

A comparative study of the NMR spectra of PDIs **11** and **12** shows the effects of the reduced symmetry of the perylenediimide unit in **11** due to the effect of the different substituents at the imido positions (Figure 24). This is reflected by splitting of the signals of the PDI core.

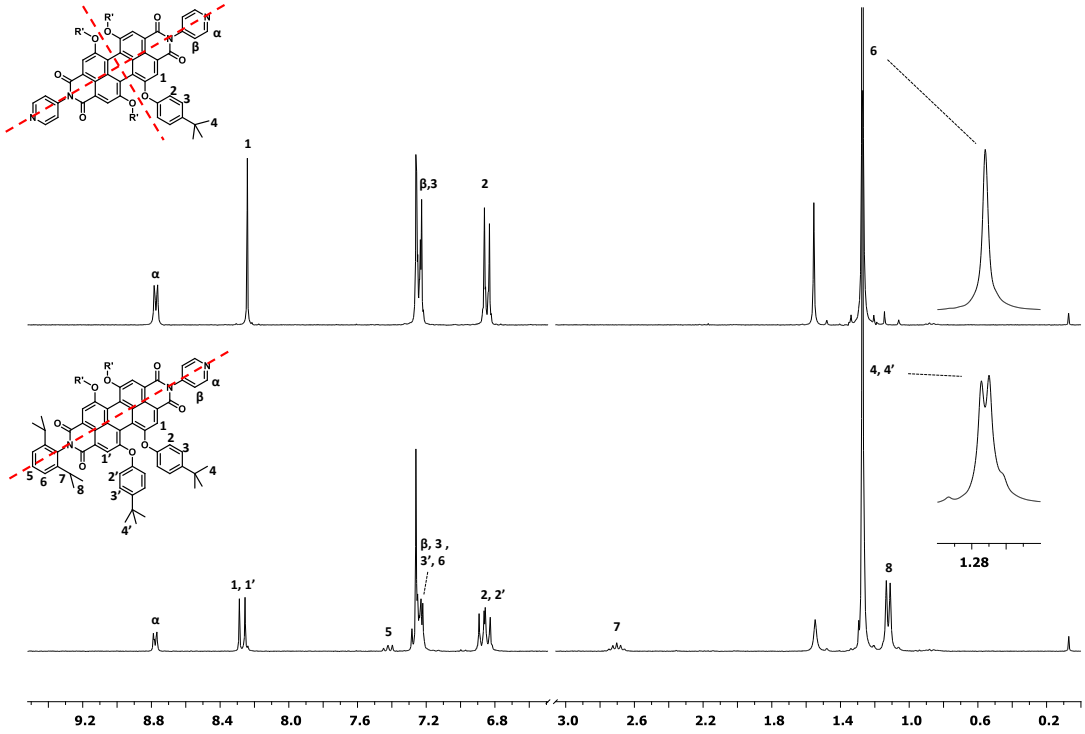

Figure 24. Top: ^{1}H-NMR spectrum of PDI **12** in $CDCl_3$. Down: ^{1}H-NMR spectrum of PDI **11** in $CDCl_3$. Red dashed lines indicate planes of symmetry.

1.3.1.3 Assembly of RuPc-PDI-RuPc triads

The assembly of the two supramolecular arrays **18a** and **19a** was carried out by treating two equivalents of the corresponding RuPcs **5** and **10** with one equivalent of BPyPDI **12** at room temperature. Purification by size exclusion chromatography yielded triads **18a** and **19a** in good yields (58 and 68 % respectively, Figure 25).

For comparison, triad **21a** was also prepared by treating tetra-*tert*-butylRuPc **20** with BPyPDI **12**. This compound differs from the one previously described in the number and the substitution of the phenoxy groups at the bay positions of the PDI.[72]

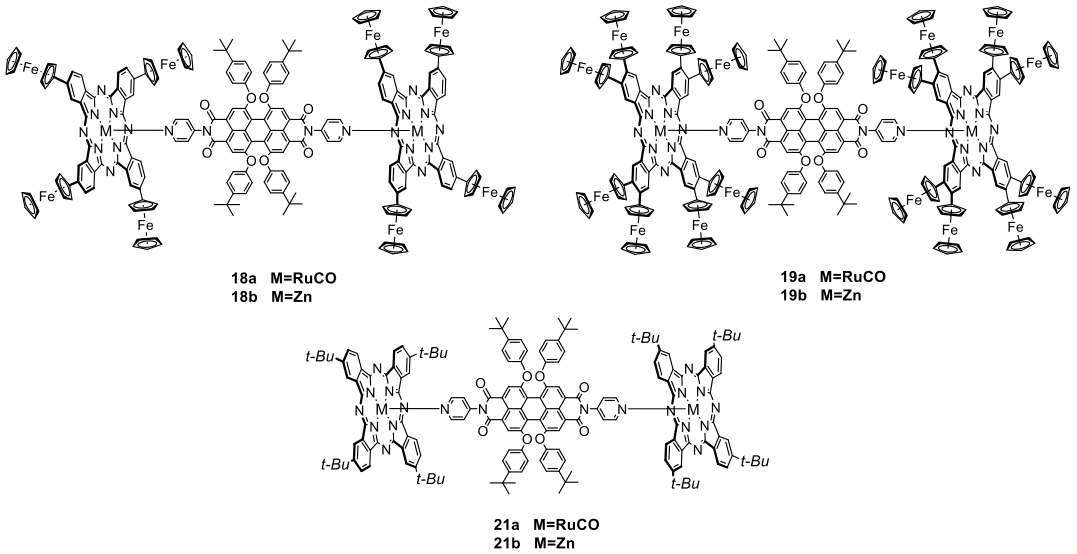

Figure 25. Chemical structure of triads **18**, **19** and **21**.

The structure of the triads **18a**, **19a** and **21a** was established on the basis of its spectroscopic features, namely, ^{1}H-NMR, ^{13}C-NMR, FT-IR and UV-Vis. Several attempts were made to obtain suitable mass spectra using FAB, ES and MALDI techniques, but usually the signals observed corresponded to the uncoordinated Pcs and the PDI. Only once, in the case of triad **19a**, we were able to observe a peak in MALDI-TOF, using DCTB as the matrix, which corresponds to [M-2CO-4-*t*-BuPhO]$^{+}$ (Figure 26). Any other attempt to extend this conditions for triads **18a** and **21a** was fruitless.

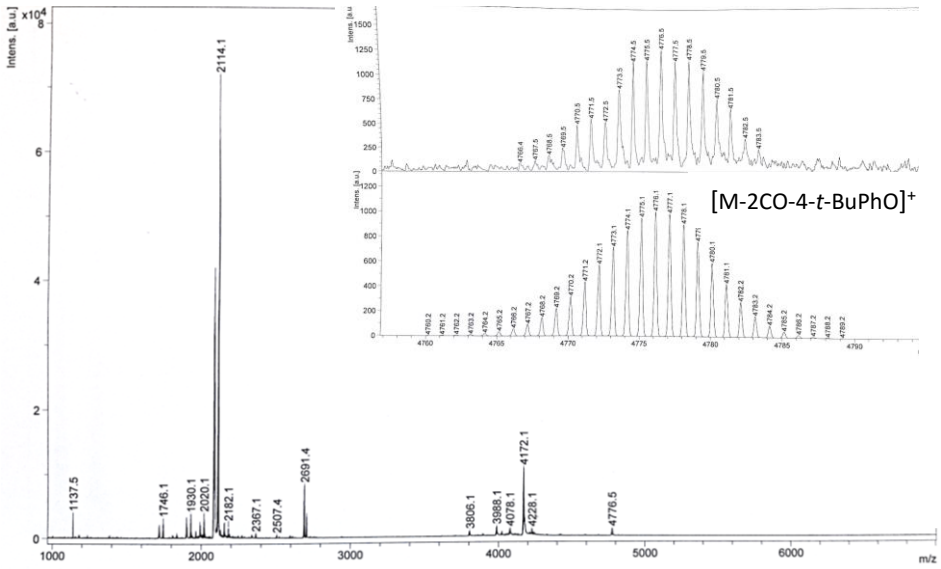

Figure 26. MS spectrum showing a peak corresponding to triad **19a** at m/z = 4776.5 Da ($[M\text{-}2CO\text{-}4(C_{10}H_{13})]^+$).

The most significant features of [Ru(CO)Pc]–[BPyPDI]–[Ru(CO)Pc] triads in IR spectroscopy are metal–carbonyl stretching bands at 1979, 1967 and 1961 cm^{-1} (for **18a**, **19a** and **21a** respectively), in addition to two bands at 1712, 1683 (for **18a**), 1711, 1680 (for **19a**) and 1710, 1681 (for **21a**) corresponding to the PDI imido functions.[72]

Figure 27 represents a comparison between ^{1}H-NMR spectra of BPyPDI **12** and triads **18a**, **19a** and **21a**. In the triads, BPyPDI **12** is situated between the two phthalocyanine rings, experiencing the influence of their diamagnetic ring currents, in the shielding cone. As a result, all PDI signals are upfield shifted, and the effect decreases with the distance between a given proton and the Pc core. Hence, the effect is maximum for the pyridyl substituents. Hereby, $H^{2''}$ shows in all cases an upfield shift of $\Delta\delta \approx 2$ ppm upon coordination, while pyridyl $H^{3''}$ displays the largest shift of $\Delta\delta \approx 6.5$ ppm. The shielding effect is more intense for triad **21a** than for the ferrocenyl substituted triads, and larger in the case of the tetraferrocenyl triad than in the octaferrocenyl one. This means that the PDI is closer to the Pc core in the case of triad **21a**. This could be rationalized by a larger steric hindrance and the donor capacity of the ferrocene units, which would also explain the less intense shielding effect observed in triad **19a** related to triad **18a**.

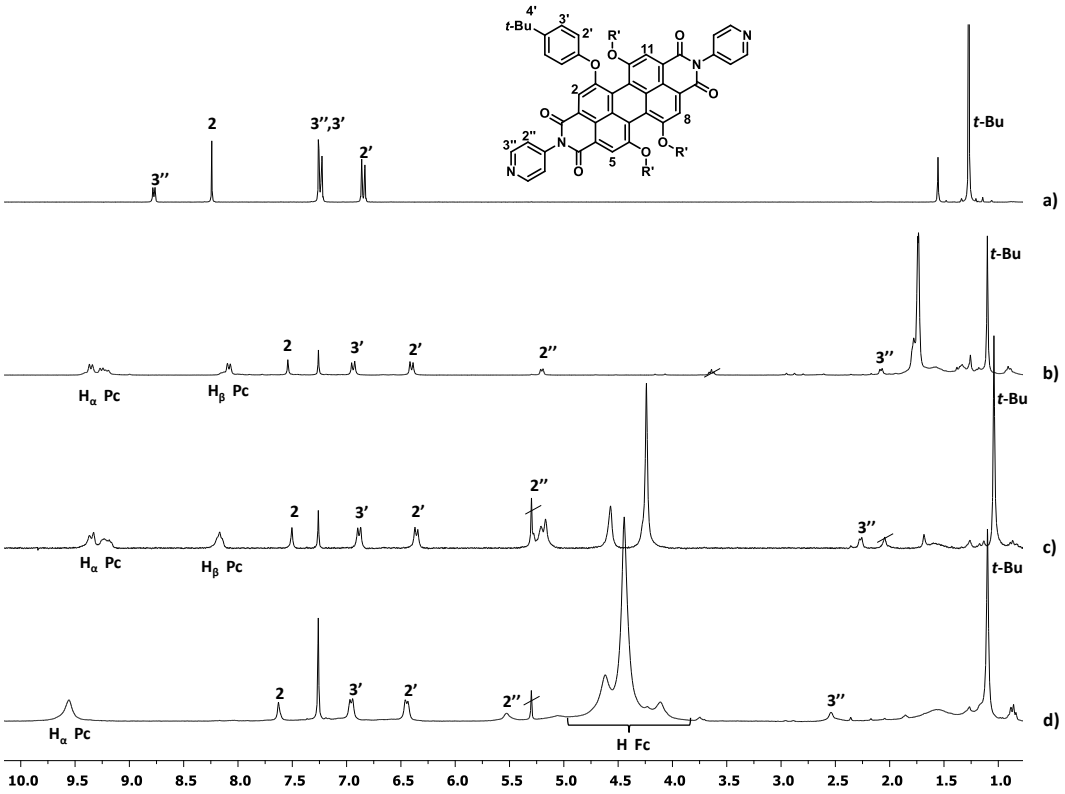

Figure 27. ^{1}H-NMR spectra in $CDCl_3$ of a) BPyPDI derivative **12**. b) [Ru(CO)Pc(*t*-Bu)$_4$-BPyPDI-Ru(CO)Pc(*t*-Bu)$_4$] **21a**. c) [Ru(CO)PcFc$_4$-BPyPDI-Ru(CO)PcFc$_4$] **18a**. d)[Ru(CO)PcFc$_8$-BPyPDI-Ru(CO)PcFc$_8$] **19a**.

As expected, the insertion of the PDI between the two Pcs resulted in a notable increase of the solubility. Even so, after a whole night performing ^{13}C-NMR experiments, we were only able to attain DEPT 135 spectra of triad **18a** and triad **19a**, but that was enough to be able to assign the aromatic -CH proton signals of the PDI and the Pc units, including the characteristic ferrocene signals around 70 ppm. On the contrary, it was possible to analyse triad **21a** by standard ^{13}C-NMR, since it is by far the most soluble compound.

1.3.1.4 Assembly of ZnPc-PDI dyads and triads in solution: ^{1}H-NMR studies

As the Zn—pyridine interaction is not as strong as the Ru-pyridine bond, these arrays are assembled in solution and were not isolated. For both ZnPcs **3** and **9**, two different titrations were carried out for each molecule, one with monodentate PDI (PyPDI **11**) to obtain the 1:1 complexes ZnFc$_4$Pc—PyPDI **22** and ZnFc$_8$Pc—PyPDI **23** (Figure 28), and another with bidentate BPyPDI **12** to study the 1:2 system.

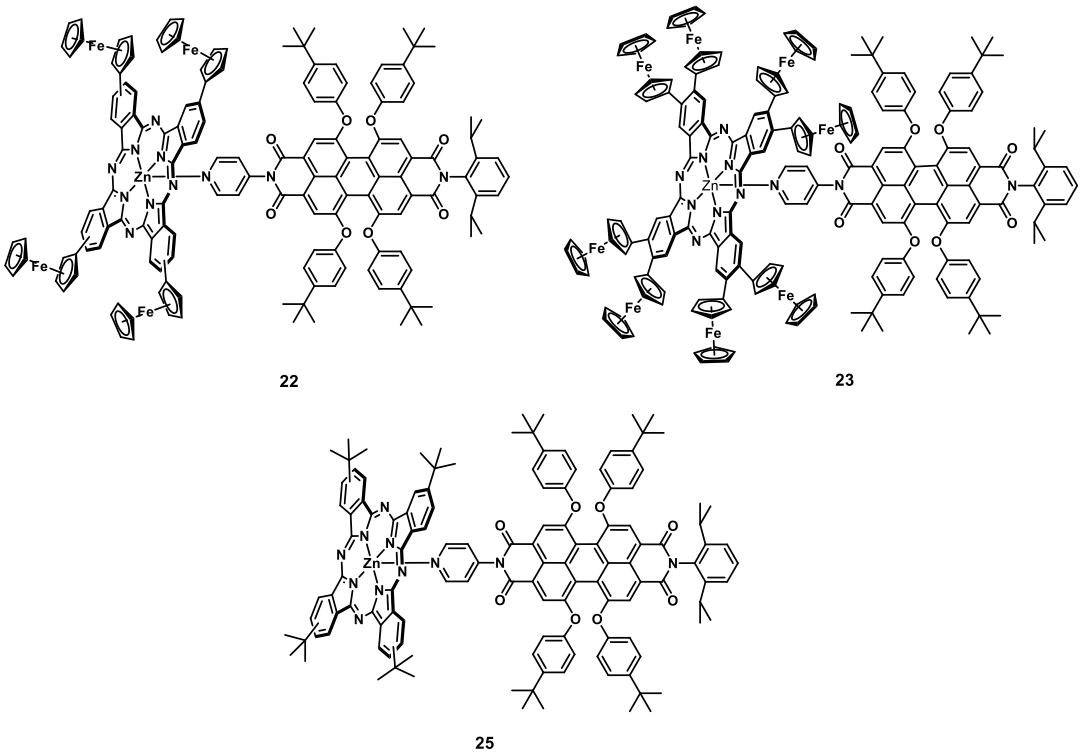

Figure 28. Structures of ZnPc-PDI 1:1 complexes.

All the titration experiments were done in $CDCl_3$ at 20 ^oC, keeping a constant concentration of 6 $\times$ 10^{-3} M of PDIs **11** or **12** (host) and slowly adding the corresponding Pc (guest). If a supramolecular interaction between the components was to happen, there were two possibilities[93]:

1) If the equilibrium is slower than ^{1}H-NMR spectroscopy timescale, then each spectrum should show the signals of the free host and guest, as well as the signals of all the complexes formed (1:1 and/or 1:2). As the complexation process advances with the titration, we should observe a change in the proportion of the integrals of the different species present in the reaction media (Figure 29a).
2) If the equilibrium process is faster than the ^{1}H-NMR spectroscopy timescale, then we should observe a single signal that appears at the averaged shift between the free and the bound species (Figure 29b).

[93]K. Hirose, *J. Incl. Phenom. Macrocycl. Chem.* **2001**, *34*, 193.

The titrations of PDIs with PCs were performed with the following purposes:

1) To demonstrate that the metallosupramolecular complexes are formed.

2) To calculate the stoichiometry of such complexes.

3) To measure, if possible, the association constants (k_a) of the complexation processes and the chemical shifts of the 1:1 and 1:2 species (δ_x).

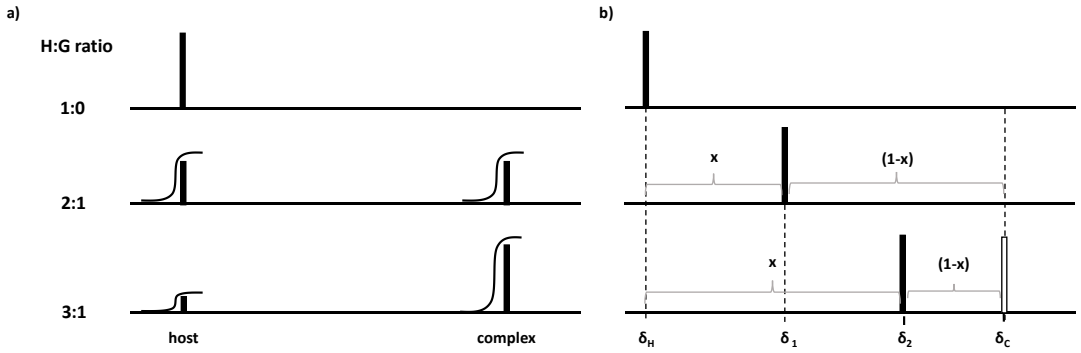

Figure 29. a) Representative NMR spectra for a slow exchange of the complexation equilibrium. b) Representative NMR spectra for a fast exchange of the complexation equilibrium.

The titrations of the monodentate PyPDI **11** with ZnPcs **3** and **9** to afford complexes **22** and **23** are represented in Figures 30 and 31, respectively. The saturation point appears around 1.4 eq. of added ZnPc. Upon addition of ZnPc **9**, the PDI proton signal shift towards upper fields, indicating that complexation between the chromophores takes place. As for the ruthenium complexes, the closer the protons are to the Pc core, the more affected they are by the aromatic current. In fact, the signal corresponding to $H^{3''}$ of the pyridine (Figure 29, blue dot) broadens rapidly and disappears. Even though the signal corresponding to $H^{2''}$ (green dot) is also broadened, it was possible to study its evolution.

Figures 32 and 33 show the titration experiments of BPyPDI **12** with ZnPcs **3** and **9**. In this case, the total complexation of PDI **12** was achieved after addition of approximately 2.2 equivalents, reflecting a stronger host guest interaction. After the saturation point, the signals sharpened and recovered their multiplicity, allowing us to assign the NMR signals. For the titration of BPyPDI **12**—$ZnFc_8Pc$ **9**, the pyridine $H^{3''}$ was assigned based on a COSY NMR, owing to its intense correlation with the well-defined pyridine $H^{2''}$ signal (Figure 34). Hence, $H^{3''}$ appear shielded at δ = 4.3 ppm and masked under the ferrocene cyclopentadienyl signal.

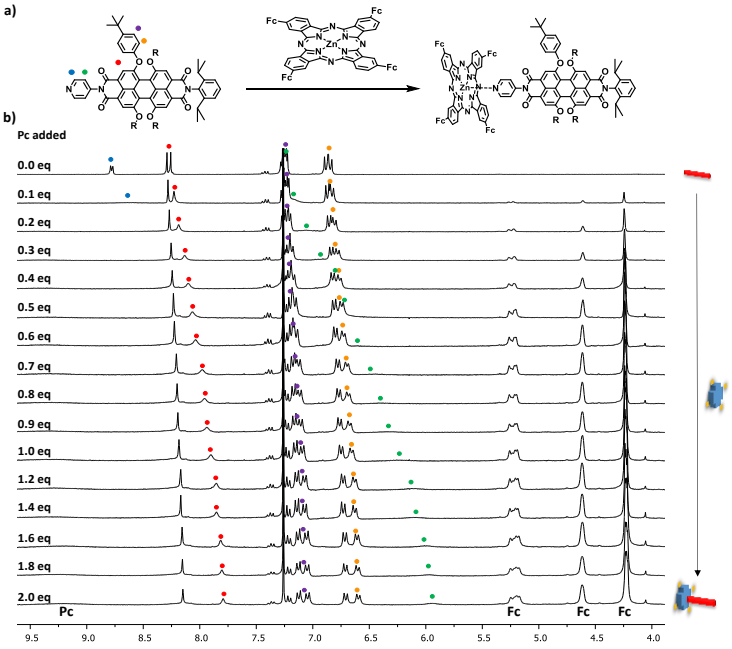

Figure 30. a) Coordination of PyPDI **11** to ZnPc **3**. b) ^{1}H-NMR titration of PyPDI **11** with $ZnFc_4Pc$ **3** in $CDCl_3$.

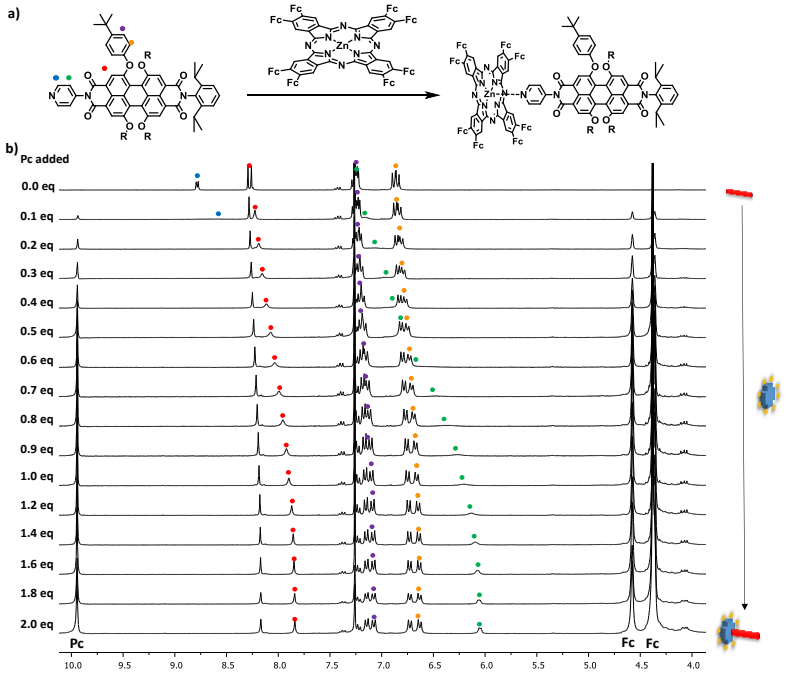

Figure 31. a) Coordination of PyPDI **11** to ZnPc **9**. b) ^{1}H-NMR titration of PyPDI **11** with $ZnFc_8Pc$ **9** in $CDCl_3$.

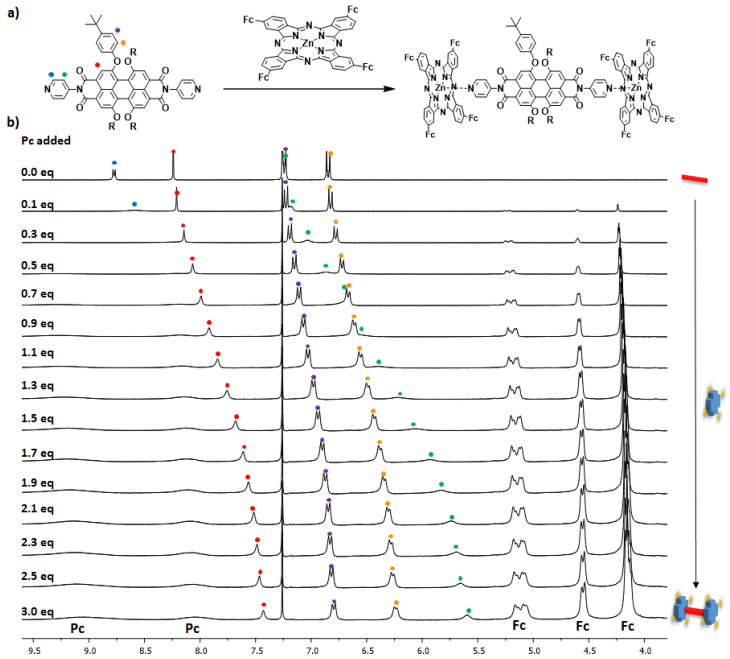

Figure 32. a) Coordination of BPyPDI **12** to ZnPc **3**. b) ^{1}H-NMR titration of BPyPDI **12** with ZnFc$_4$Pc **3** in CDCl$_3$.

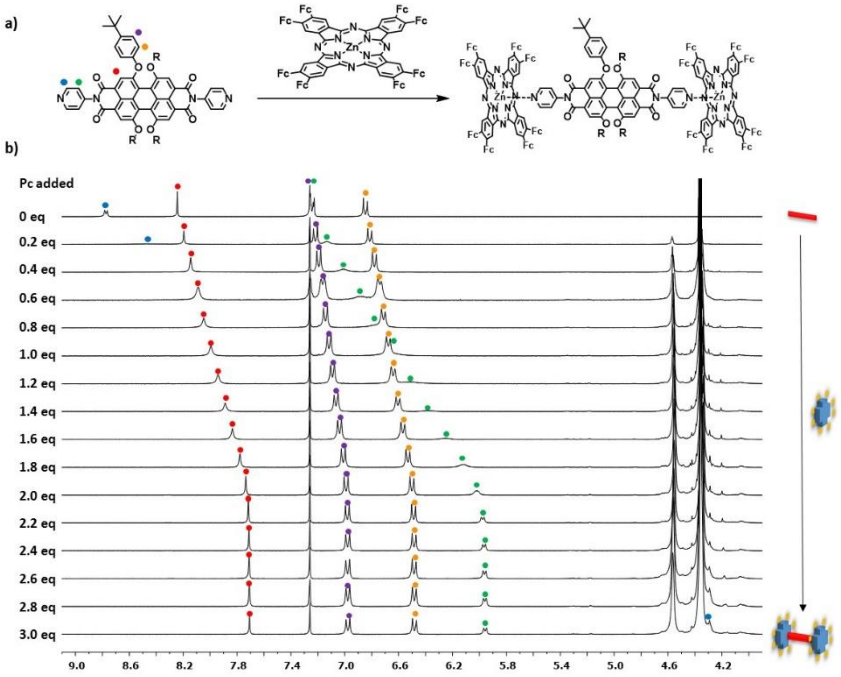

Figure 33. a) Coordination of BPyPDI **12** to ZnPc **9**. b) ^{1}H-NMR titration of BPyPDI **12** with ZnFc$_8$Pc **9** in CDCl$_3$.

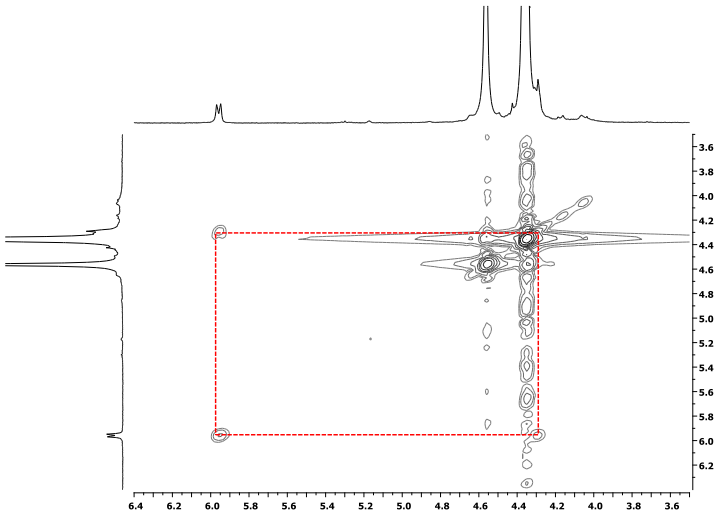

Figure 34. COSY NMR spectrum in the 3.5—6.5 ppm range showing the correlation between the signals of the pyridine $H^{3''}$ and $H^{2''}$ protons.

There is a noticeable 1.7 ppm shielding of the $H^{3''}$ pyridine protons in the ruthenium complex **19a** (Figure 27) related to the corresponding signal in the zinc complex **23** (Figure 33). This can be rationalized in terms of the weaker and larger Zn—pyridine bond related to the Ru—pyridine bond.

To summarize and make comparison easier, Figure 35 shows the initial and last spectra of each titration performed. To PyPDI **11**, up to two equivalents of Pc were added, and up to three were added to the BPyPDI **12**. Comparison between dyads and triads reveals a stronger upfield shift for the protons of the latter. For example, the perylene proton (red dot, Figure 29c) shows a $\Delta\delta$ ≈ 0.5 ppm when assembling a 1:1 complex and $\Delta\delta$ ≈ 0.7 ppm when the 2:1 complex is formed (red dot, Figure 29d). The same behaviour is observed with the pyridinic $H^{2''}$ signal (green dot). Chemical shifts vary from $\Delta\delta$ ≈ 1.3 ppm in the dyad to $\Delta\delta$ ≈ 1.7 ppm in the 2:1 complex. In addition, octaferrocenyl derivatives, show sharper signals, and smaller upfield shifts (comparing $H^{2''}$, green dot, between Figure 29a and c, and Figure29b and d). This behaviour is in agreement with that observed before for triads **18a** and **19a**, and suggests longer Zn—pyridyl bonds for $ZnFc_8Pc$ related to $ZnFc_4Pc$.

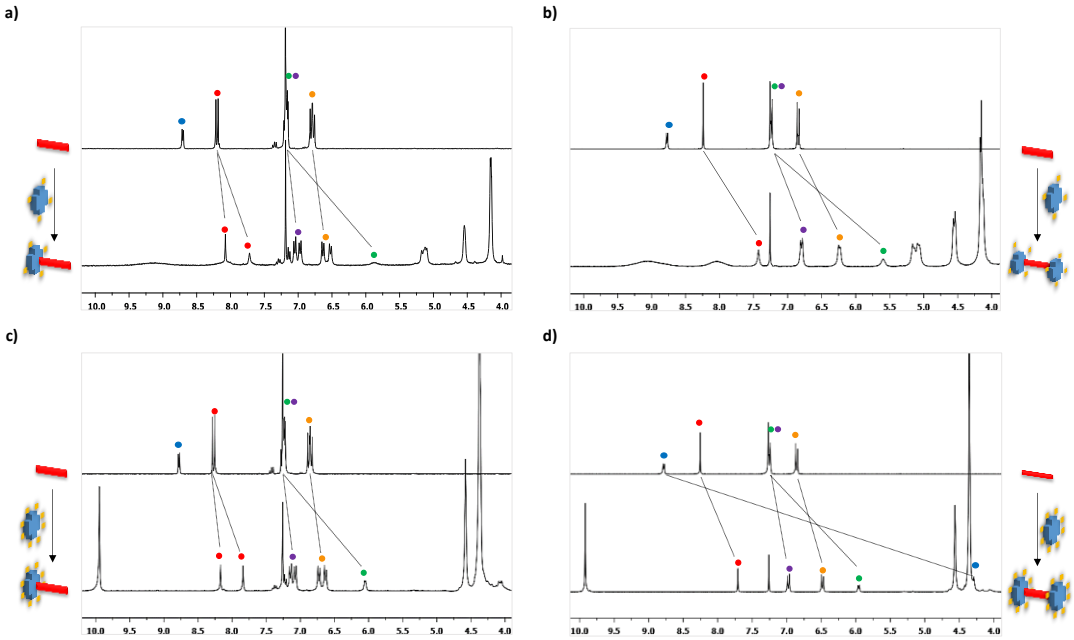

Figure 35. First and last spectra of the titrations carried out between PDIs **11** and **12** and ZnPcs **3** and **9**.

The stoichiometry of the complexes was calculated using the mole ratio method.[94] This method uses a binding isotherm where the concentration of host is fixed and the concentration of guest is varied, representing the chemical shift of a proton *versus* the concentration of guest. The break point coming from the extrapolation of the apparently linear points at the beginning and the end of the curve corresponds to the guest/host stoichiometric ratio (Figure 36). By applying this method, the titrations with PyPDI **11** confirmed a 1:1 stoichiometry, and the titrations with BPyPDI **12** a 2:1 stoichiometry.

[94] a) H. Tsukube, H. Furuta, A. Odani, Y. Takeda, Y. Kudo, Y. Inoue, Y. Liu, H. Sakamoto and K. Kimura, in Comprehensive Supramolecular Chemistry, (eds. J. L. Atwood, J. E. D. Davies, D. D. MacNicol and F. Vögtle), Pergamon, Oxford, **1996**, vol. 8, ch. 10, pp. 425; b) P. Thordarson, *Chem. Soc Rev.* **2011**, *40*, 1305.

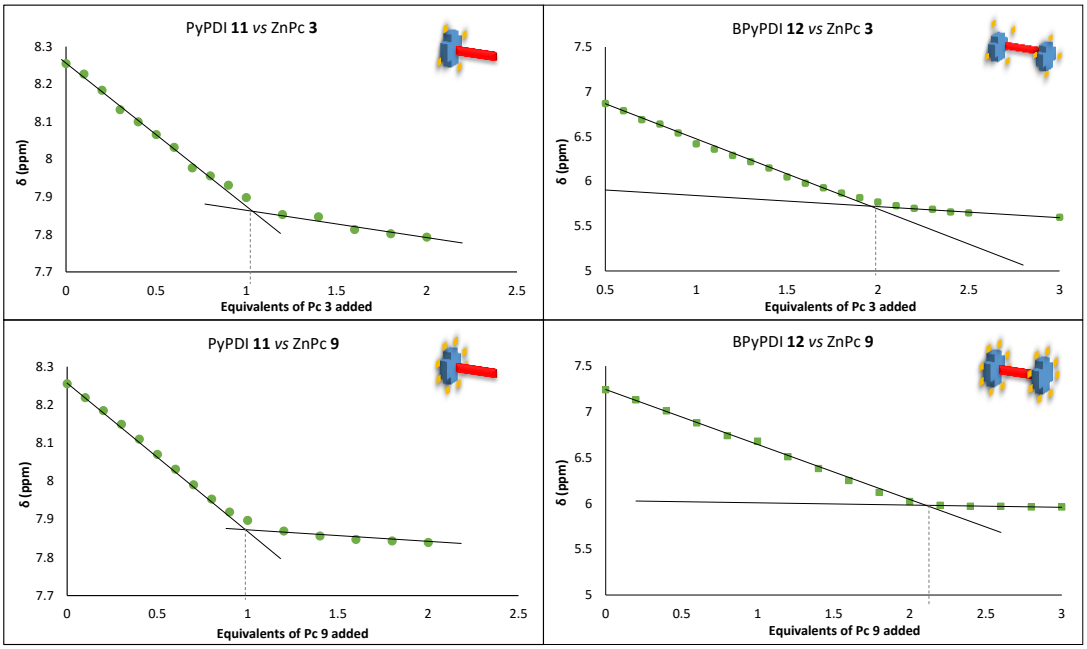

Figure 36. Plots of ^{1}H NMR titrations of PyPDI **11** and BPyPDI **12** with ZnPcs **3** and **9**, showing the changes in the chemical shifts of the H^2 PDI protons (top left and down left), and the $H^{2''}$ pyridyl protons (top right and downright). The apparently linear portions at the beginning and the end of the curve are extrapolated to find a break point, corresponding to the ZnPc/PDI stoichiometric ratio.

1.3.1.5 Calculation of the association constants

The data retrieved from the titrations was then used to calculate the association constants between the chromophores, so we could further analyse these systems. The association constant is the equilibrium constant of the formation of a complex, just as in any other chemical reaction (Figure 37). The thermodynamic association constant *K* is related to the kinetics of the system, so that $K_a = K_1/K_{-1}$, with K_1 and K_{-1} being the forward and backward rate constants for the equilibria.[94b]

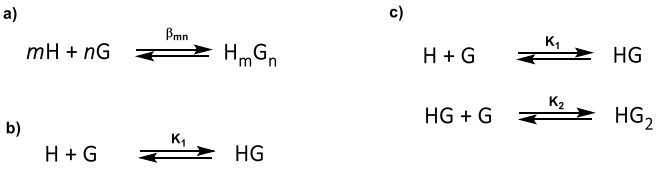

Figure 37. Three supramolecular equilibria: a) General *m:n* system; b) 1:1 system; c) 1:2 system.

The general equation for the formation of any supramolecular complex is represented in Equation 1.

$$\beta_{mn} = \frac{[\mathrm{H_mG_n}]}{[\mathrm{H}]^{\mathrm{m}}[\mathrm{G}]^{\mathrm{n}}} \qquad \text{(Eqn. } \mathbf{1}\text{)}$$

This can be easily converted to the specific equations for 1:1 stoichiometries, (*m* and *n* = 1, Equation 2).

$$K_1 = \frac{[\mathrm{HG}]}{[\mathrm{H}][\mathrm{G}]} \qquad \text{(Eqn. } \mathbf{2}\text{)}$$

Complexation to afford the 1:2 systems is most likely to occur in two steps. Hence, two association constants are described, one for each step depicted in Figure 33c above. The first step relates to the formation of a 1:1 system, while the second can be calculated in Equation 3.

$$K_2 = \frac{[\mathrm{HG_2}]}{[\mathrm{HG}][G]} \qquad \text{(Eqn. } \mathbf{3}\text{)}$$

First, we are going to focus on the development of the more simple 1:1 system. As a clarification, a concentration written as [A] represents the concentration of A at a certain moment of the titration, while $[A]_o$ represents the total concentration of A added.

The application of Equation 2 would be direct if we were able to directly measure the concentration of the complex [HG] or the host [H] or the guest [G]. If only one of those could be measured, the other could be determined by the mass balance equations as described by Equations 4 and 5:

$$[H]_o = [H] + [HG] \qquad \text{(Eqn. } \mathbf{4}\text{)}$$

$$[G]_o = [G] + [HG] \qquad \text{(Eqn. } \mathbf{5}\text{)}$$

For NMR titrations it could be possible to obtain the concentrations by integration if the equilibria occur in the slow regions. The main limitation to this strategy is the inaccuracy of the integration in NMR experiments.

In general, the association constants are obtained by monitoring a physical change (*Δ*Y), for example an NMR shift or a change in UV-Vis absorbance of the system, and this change is then plotted as a function of guest added to host. The resulting curve is known as binding isotherm and can be fitted to a mathematical model based on the assumed equilibria to obtain the association constant. In NMR, the physical change (Y) can be described as the aggregate of the individual components, as a function of mole fractions f_x (defined as $f_x = [X]/[X]_o$), according to Equation 6.

$$Y = Y_H f_H + Y_G f_G + Y_{HG} f_{HG} \quad \text{(Eqn. 6)}$$

Combining the concept of mole fraction with the mass balance (Equations 4 and 5), and with the definition of the association constant in Equation 2, we obtain Equation 7.

$$f_{HG} = \frac{K_a[G]}{1+K_a[G]} \quad \text{(Eqn. 7)}$$

This equation describes the general binding isotherm for a 1:1 system as a hyperbolic relationship between molar fraction f_{HG} and [G] but, once again, the free guest concentration [G] cannot be measured directly, so two different approaches are required to solve this problem. The first approach is based on the fact that as f_{HG} = $[HG]/[H]_o$, Equation 7 can also be written as $[HG] = [H]_o K_a[G]/(1 + K_a[G])$ which, after insertion of Equation 5 yields $[G]_o = [G] + H_o K_a[G]/(1 + K_a[G])$. Rearranging this equation yields the quadratic Equation 8, which has only one real solution according to Equation 9.

$$[G]^2 - [G]\left([G]_o - [H]_o - \frac{1}{K_a}\right) - \frac{[G]_o}{K_a} = 0 \quad \text{(Eqn. 8)}$$

$$[G] = \frac{1}{2}\left\{\left([G]_o + [H]_o - \frac{1}{K_a}\right) + \sqrt{\left([G]_o + [H]_o + \frac{1}{K_a}\right)^2 + 4\frac{[G]_o}{K_a}}\right\} \quad \text{(Eqn. 9)}$$

Alternatively, we can isolate [H] and [G] in Equations 4 and 5 and then insert them into Equation 2 to obtain then K_a = [HG] / (($[H]_o$ – [HG]) ($[G]_o$ – [HG])) which, after expanding the right-hand denominator and rearranging yields the quadratic Equation 10 and its corresponding solution in Equation 11.

$$[HG]^2 - [HG]\left([G]_o + [H]_o + \frac{1}{K_a}\right) + [H]_o[G]_o = 0 \quad \text{(Eqn. 10)}$$

$$[HG] = \frac{1}{2}\left\{\left([G]_o + [H]_o + \frac{1}{K_a}\right) - \sqrt{\left([G]_o + [H]_o + \frac{1}{K_a}\right)^2 - 4[H]_o[G]_o}\right\} \quad \text{(Eqn. 11)}$$

Equations 9 and 11 allow to find solutions for Equation 6 that only require the knowledge of the total (or initial) concentrations of the host $[H]_o$ and the guest $[G]_o$ in addition to the association constant K_a and the change in the physical properties measured during the titration.

If one of the components is silent, *e.g.* the guest [G] (as happens in our case with signals of added Pc, the chemical shift will be the weighted average between the shift of the free PDI and the Pc-PDI complex), Equation 6 can be simplified and, applying that [H] = $[H]_o$ – [HG] and f_{HG} = $[HG]/[H]_o$, we obtain $Y = Y_H + ([HG]/[H]_o)(Y_{HG} - Y_H)$, which can be further developed to yield Equation 12.

$$\Delta Y = Y_{\Delta HG}\left(\frac{[HG]}{[H]_o}\right) \quad \text{(Eqn. 12)}$$

Which in the case of NMR titrations equals to Equation 13.

$$\Delta\delta = \delta_{\Delta HG}\left(\frac{[HG]}{[H]_o}\right) \quad \text{(Eqn. 13)}$$

Using [HG] from Equation 11, we can now describe the expected changes from a supramolecular NMR titration from the known $[H]_o$ and $[G]_o$ and the unknown K_a and $\delta_{\Delta HG}$ (which correspond to the chemical shift of the complexed species) which will be obtained by non-linear regression of the data obtained.

The derivation of the equations for the 1:2 equilibria is similar to that detailed here for the 1:1 system.[94a] Once again we assume that the guest is silent, $Y_G = 0$. Then, the expression for free guest concentration is:

$$[G]^3(A) + [G]^2(AB) + [G](C) - [G]_o = 0 \quad \text{(Eqn. 14)}$$

with:

$$A = K_1K_2$$

$$B = K_1(2K_2[H]_o - K_2[H][G]_o + 1)$$

$$C = K_1([H]_o - [G]_o) + 1$$

And Equations 15 and 16, analogous to Equations 12 and 13, show the dependence of the change of the physical proportion up on titration.

$$\Delta Y = \left(\frac{Y_{\Delta HG}K_1[G] + Y_{\Delta HG}K_1K_2[G]^2}{1 + K_1[G] + K_1K_2[G]^2}\right) \quad \text{(Eqn. 15)}$$

That for NMR titrations equals:

$$\Delta\delta = \left(\frac{\delta_{\Delta HG}K_1[G] + \delta_{\Delta HG_2}K_1K_2[G]^2}{1 + K_1[G] + K_1K_2[G]^2}\right) \quad \text{(Eqn. 16)}$$

The data can now be fitted by non-linear regression to Equation 14 and 16 to obtain the unknown parameters K_1, K_2, $\delta_{\Delta HG}$ and $\delta_{\Delta HG2}$.

The experimental data obtained from the NMR titrations were fitted with two different softwares, namely *fittingprogram*[94b] and *Equilibria.*[95] *Fittingprogram* offers the possibility of performing a global fitting, in addition to fitting for every individual binding isotherm, and this reduces the overall error.[96] In *fittingprogram* the uncertainties associated to the binding

[95] P.G. Young, K. A. Jolliffe, *Organic & Biomolecular Chemistry* **2012**, *10*, 2664.
[96] A. J. Lowe, F. M. Pfeffer, P. Thordarson, Supramol. Chem. **2012**, *24*, 585.

constants are expressed as the expanded uncertainty at the 95% confidence interval. Moreover, *Equilibria* uses r^2 as an estimate of the good fit.

Tables 1 and 2 summarize the results obtained from fitting the chemical shifts of the signals corresponding to four different protons in the 1:1 titration data of PyPDI **11** with ZnPcs **3** and **9** respectively. The local fitting of each proton was carried out employing both software. Additionally, we performed the global fitting with *fittingprogram*.

Table 1. Calculated binding constants K_a for 1:1 binding equilibria and expanded uncertainties at the 95% confidence intervals (%) from ^{1}H-NMR titration in $CDCl_3$ at 293K of PyPDI **11** with $ZnFc_4Pc$ **3**.

11 *vs* **3**					
EQUILIBRIA	**H_1**	**H_2**	**H_3**	**H_4**	**Global fit**
K_a / M^{-1}	784	931	714	693	-
r^2	0.9939	0.995	0.9924	0.9929	
Fittingprogram					
K_a / M^{-1}	776 ± 65%	925 ± 60%	707 ± 72%	704 ± 67%	853 ± 29%

Table 2. Calculated binding constants K_a for 1:1 binding equilibria and expanded uncertainties at the 95% confidence intervals (%) from ^{1}H-NMR titration in $CDCl_3$ at 293K of PyPDI **11** with $ZnFc_8Pc$ **9**.

11 *vs* **9**					
EQUILIBRIA	**H_1**	**H_2**	**H_3**	**H_4**	**Global fit**
K_a / M^{-1}	8561	6625	8879	6066	-
r^2	0.9963	0.9962	0.9952	0.9941	
Fittingprogram					
K_a / M^{-1}	8466 ± 90%	6602 ± 83%	8695 ± 103%	6006 ± 98%	6759 ± 40%

The values obtained for each binding isotherm match, independently of which program was used to fit the data. Furthermore, comparing the information of both titrations, we can conclude that the association constant governing the formation of 1:1 complex **23** process is approximately one order of magnitude higher ($K_a \approx 6.7 \cdot 10^3$ M^{-1}) than the association constant for the complex **22** ($K_a \approx 8.5 \cdot 10^2$ M^{-1}).

The r^2 values in *Equilibria* are close to one, this meaning that the fitting is good. The values of the uncertainty in *fittingprogram* are high, especially in the titration with $ZnFc_8Pc$ **9**, but the global fitting decreases the uncertainty percentage greatly, reaching more reasonable values.[96]

Figure 38 shows the four sets of data analysed by *fittingprogram* in the global fit for each titration. The asterisks represent the experimental data of the shift of the corresponding signals, and the lines the non-linear regression fitting carried out by the program.

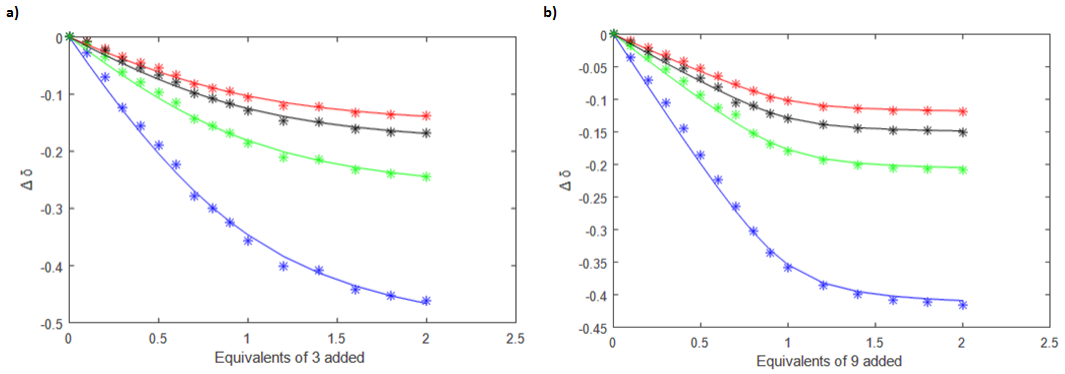

Figure 38. Non-linear regression fitting of the experimental shifts of the PDI protons (H^1 in blue, $H^{1'}$ in green, H^2 in black, $H^{2'}$ in red) upon addition of $ZnFc_4Pc$ **3** (a), and $ZnFc_8Pc$ **9**.

Regrettably, all our efforts to obtain the association constants k_1 and k_2 for the 1:2 systems were unsuccessful since the calculations did not converge. *Equilibria* cannot calculate 1:2 systems, and *fittingprogram* was not able to produce a good fit in our hands. We also tried to employ *WINEQNMR* software, but again no reasonable solution was found.

For example, the global fitting with *fittingprogram* using 4 signals of the titration of BPyPDI **12** with $ZnFc_8Pc$ **9** yielded k_1 = 3263 ± 183 % and k_2 = 54742 ± 132 %. Even if the values could be reasonable, the uncertainties are too high for even take them into consideration. Table 3 represents the k_a, $\delta_{\Delta HG}$ and $\delta_{\Delta HG2}$ for 1:2 binding equilibria calculated for the four PDI protons. While $\delta_{\Delta HG2}$ have little uncertainties (1 % approximately), $\delta_{\Delta HG}$ are higher than 45 %. In the titration of BPyPDI **12** with $ZnFc_4Pc$ **3**, k_2 = 1555 ± 32 %, while $k_1 = 1.05 \cdot 10^9$ ± 1432 %, value that makes no sense. We concluded that the software was having issues calculating the parameters for the more complex 1:2 systems.

Table 3. Calculated binding constants K_a, $\delta_{\Delta HG}$ and $\delta_{\Delta HG2}$ for 1:2 binding equilibria and expanded uncertainties at the 95% confidence intervals (%) from ^{1}H-NMR titration in $CDCl_3$ at 293K of BPyPDI **12** with ZnPcs **3** and **9**.

	K_1	K_2	H_1		H_2		H_3		H_4	
			$\delta_{\Delta HG}$	$\delta_{\Delta HG2}$	$\delta_{\Delta HG}$	$\delta_{\Delta HG2}$	$\delta_{\Delta HG}$	$\delta_{\Delta HG2}$	$\delta_{\Delta HG}$	$\delta_{\Delta HG2}$
12 vs 3										
Global fit	1,05E+09	1,56E+03	-0,36	-0,85	-0,19	-0,46	-0,26	-0,63	-0,78	-1,75
% uncertainty	1433	32	-2	-3	-3	-3	-2	-3	-1	-3
12 vs 9										
Global fit	3,26E+03	5,47E+04	-0,15	-0,53	-0,08	-0,26	-0,07	-0,18	-0,11	-0,36
% uncertainty	184	132	-93	-1	-71	-1	-46	-1	-81	-1

1.3.1.6 Electrochemical studies

Electrochemical experiments were conducted to investigate the influence of the ferrocene functionalization on the redox properties of the phthalocyanines and therefore, on the Pc-PDI complexes. The measurements were carried out using a three electrode cell in Ar saturated DCM solution containing 0.1 M tetrabutylammonium hexafluorophosphate (TBAF) supporting electrolyte. We used a glassy carbon working electrode, a Pt wire as counterelectode and $Ag/AgNO_3$ as reference electrode. Fc was used as an external standard. All data are represented vs Fc/Fc^+.

Cyclic voltammetry (CV) and square wave voltammetry (SWV) experiments were performed to investigate the phthalocyanine units (Figure 39). Ru- and Zn-tetra-*tert*-butylphthalocyanines **20** and **24**[97] were employed as reference compounds in the electrochemical studies of Pcs.

When comparing the ferrocenyl substituted Pcs to the reference phthalocyanines Zn(*t*-Bu)$_4$Pc **24** and Ru(*t*-Bu)$_4$Pc **20**, an additional oxidation wave appears around 0.0 V that is attributed to the Fc units. In all cases, this wave presents a strong adsorption on the electrode, which is more intense for the octasubstituted Pcs **9** and **10** (Figures 39c and f, respectively). Regarding the tetrasubstituted Pcs **3** and **5**, the separation between the cathodic and the anodic wave ΔE (> 100 mV) hints the presence of different Fc-centred processes and indicates the long range metal-metal coupling between the different pyrrolic units. When lowering the temperature to 273 K, in $ZnFc_4Pc$ **3** square wave, the ferrocene oxidation broadens remarkably and a multiple Gaussian fit reveals two subsequent oxidation processes at +0.01 and +0.06 V *vs* Fc/Fc^+ respectively, indicating electronic communication of one ferrocene unit with another one across the phthalocyanine core (Figure 40). This effect is even clearer in the case of the octaferrocenyl substituted Pcs **9** and **10** (Figure 39c and f). In this case there are two units of Fc at the same isoindole ring and the coupling is therefore stronger. Here, the first is separated from the rest of the Fc-centred processes by *ca*. 80 mV.

The same trend can be observed for triads **18a** and **19a**. **18a** presents a wide single wave at 0.04 V, while **19a** displays three different processes related to the Fc oxidations (green line, Figure 41).

[97] J. U. Lee, Y. D. Kim, J. W. Jo, J. P. Kim and W. H. Jo, *J. Mater. Chem.*, 2011, **21**, 17209.

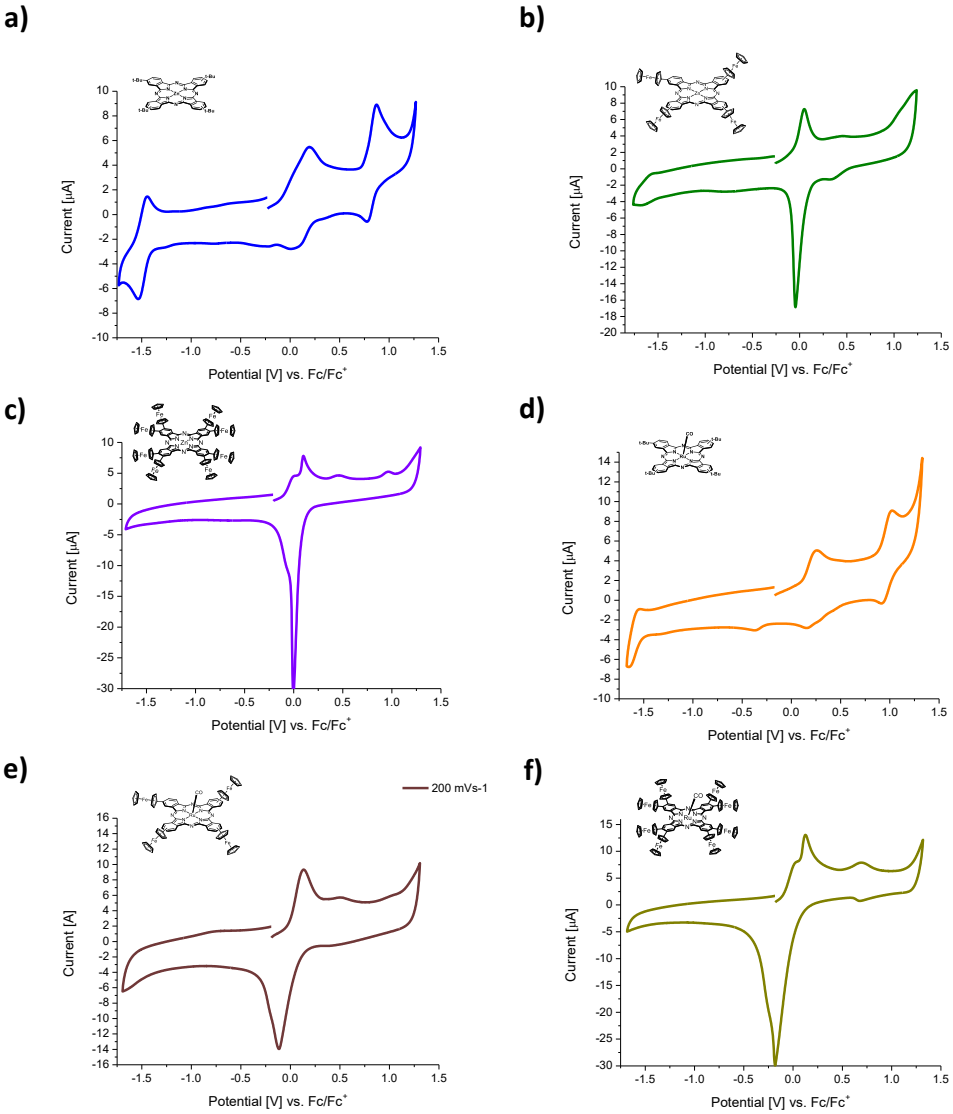

Figure 39. Cyclic voltammograms of **24** (a), **3** (b), **9** (c), **20** (d), **5** (e) and **10** (f) in DCM (0.1 M $TBAPF_6$) at room temperature using a glassy carbon electrode measured at 200 mV s^{-1}. Potentials *vs* Fc/Fc^+.

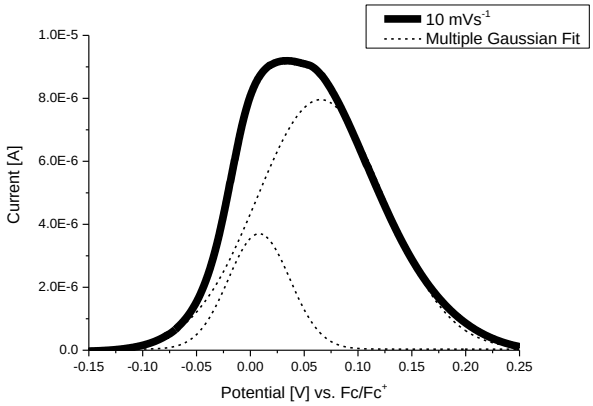

Figure 40. Square wave voltammogram of **3** (black line) and corresponding Gaussian fit (dashed lines) in DCM (0.1 M $TBAPF_6$) at 273 K using a glassy carbon electrode. Scan direction from —0.15 to +0.25 V. Potentials vs. Fc/Fc^+.

Any other wave observed was attributed to processes centred on the Pc ligand. In every case, the first oxidation wave that corresponds to the phthalocyanine is shifted towards higher potentials (around 0.45 V for **3** and **9**, and 0.6 V for **5** and **10**), showing a clear tendency in that direction with the addition of ferrocene units to the macrocyclic core. The first reduction wave of **3** and **5** also shifts but in the opposite direction, that is, towards lower potentials compared to references **24** and **20**. All the data are summarized in Table 4.

BPyPDI **12** shows the typical two one-electron reduction waves at —1.1 and —1.2 V, characteristic of perylenediimides. These processes did not change when the PDI was integrating the 2:1 complexes **18a** and **19a** [E^1_{red} (**12**) = —1.07 V, E^1_{red} (**18a**) = —1.06 V, E^1_{red} (**19a**) = —1.07 V, Figure 37 and Table 4]. This is in agreement with an impeded electronic communication of the imido substituents with the perylene core owing to the presence of nodes on the imido nitrogens.[73]

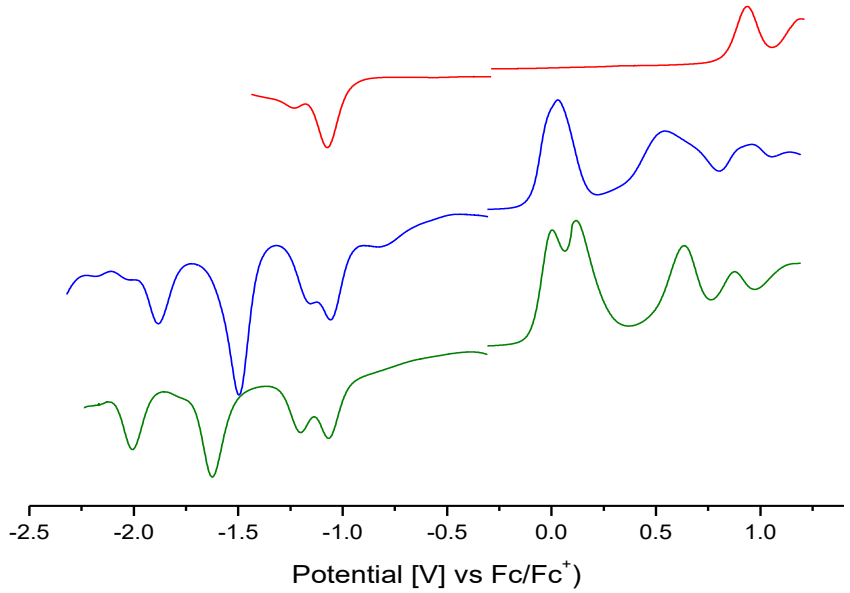

Figure 37. Square wave voltammograms of BPyPDI **12** (red), [($RuFc_4Pc$)—BPyPDI—($RuFc_4Pc$)] **18a** (blue), [($RuFc_8Pc$)—BPyPDI—($RuFc_8Pc$)] **19a** (green), in DCM (0.1 M $TBAPF_6$) at room temperature using a glassy carbon electrode. Potentials *vs*. Fc/Fc^+.

Table 4. Redox potentials ($E_{1/2}$ in V) *vs*. Fc/Fc^+ in DCM (0.1 M $TBAPF_6$) at room temperature using a glassy carbon electrode.

	E_{red4}	E_{red3}	E_{red2}	E_{red1}	E_{ox1}	E_{ox2}	E_{ox3}	E_{ox4}
Zn(*t*-Bu)$_4$Pc 24	-	-	-	—1.47	0.10	0.83	-	-
ZnFc$_4$Pc 3	-	-	-	—1.61[b]	0.02[a]	0.44	-	-
ZnFc$_8$Pc 9	-	-	-	-	—0.03[a]	0.05[a]	0.46[b]	0.94[b]
Ru(*t*-Bu)$_4$Pc 20	-	—1.59	—1.33[b]	—0.36[b]	0.21	0.49[b]	0.97	-
RuFc$_4$Pc 5	-	-	—1.56[b]	—0.78[b]	0.04[a]	0.59	1.06[b]	-
RuFc$_8$Pc 10	-	-	-		—0.09[a]	0.00[a]	0.61[b]	-
BPyPDI 12	-	-	—1.24	—1.07	0.94	1.07[b]	-	-
[(RuFc$_4$Pc)$_2$—BPyPDI] 18a	—1.91	—1.51	—1.19	—1.06	0.03[a]	0.54[b]	0.93[b]	-
[(RuFc$_8$Pc)$_2$—BPyPDI] 19a	—2.00	—1.62	—1.20	—1.07	0.00[a]	0.12[a]	0.64[b]	0.88[b]

[a] Signal with strong adsorption. [b] Irreversible.

1.3.1.7 Photophysical studies

The photophysical studies of this chapter were carried out during a predoctoral stay in the laboratory of Prof. Dirk Guldi at the Friederich-Alexander University in Erlangen, Germany.

1.3.1.7.1 Steady State

PDIs **11** and **12** display similar absorption spectra in chlorobenzene, with the typical PDI absorption features spanning from around 400 to 650 nm and the most prominent maxima at 545 and 585 nm, respectively. Fluorescence emission maximizes for both compound at 613 nm with a shoulder around 670 nm (Figure 42).

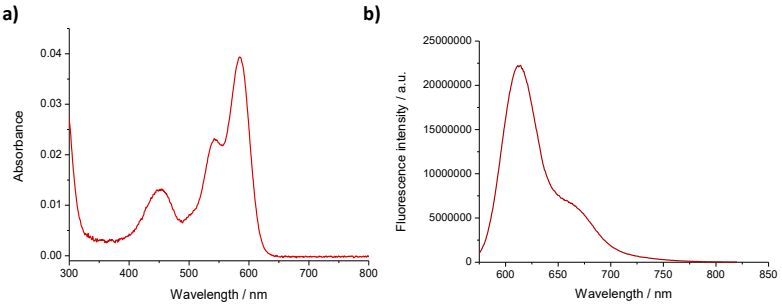

Figure 42. Absorption (left) and emission (λ_{ex} = 570 nm, right) spectra of **11** (10^{-6} M) in chlorobenzene.

Regarding the Pcs, Zn(*t*-Bu)$_4$Pc **24** shows the typical ZnPc absorption features with a *Q*-band maximizing at 680 nm and fluorescence spanning from ~685 to 800 nm. In ferrocene substituted ZnPcs **3** and **9** absorption features are strongly red shifted, the corresponding *Q*-band maxima appearing at 720 and 750 nm, respectively. Furthermore, both molecules display a broad absorption feature in the visible around 560 nm and a weaker feature at 860 and 910 nm, respectively (Figures 43a and b), which we assign to intervalent charge transfer (IVCT),[98] typical of aromatic macrocycles bearing more than one unit of ferrocene.[76] These IVCT bands observed are in agreement with metal-metal coupling effects observed in the electrochemical studies. Neither ZnPc **3** nor ZnPc **9** show any fluorescence due to fast intersystem crossing processes from the singlet to triplet excited state owing to the presence of ferrocenes.[78]

[98] V.N. Nemykin, G.T. Rohde, C.D. Barrett, R.G. Hadt, C. Bizzarri, P. Galloni, B. Floris, I. Nowik, R.H. Herber, A.G. Marrani, R. Zanoni, N.M. Loim, *J. Am. Chem. Soc.* **2009**, *131*, 14969.

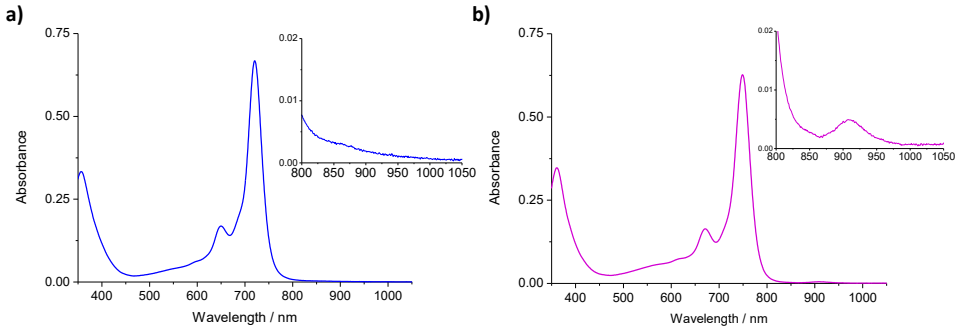

Figure 43. Absorption spectra of $ZnFc_4Pc$ **3** (a) and $ZnFc_8Pc$ **9** (b) in chlorobenzene. Inset: Zoom in into the NIR zone showing the IVCT absorption band.

Ruthenium phthalocyanines **5** and **10** exhibit absorption spectra showing broader and red-shifted Soret- and *Q*-band features compared to Ru(*t*-Bu)$_4$Pc reference **20** (Figure 44). Furthermore, ferrocene functionalization leads to the formation of a broad absorption band in the visible region from 350 to 600 nm, making both compounds panchromatic light absorbers from below 300 nm to above 850 nm. No IVCT bands were observed in the NIR for the ferrocenyl-RuPcs.

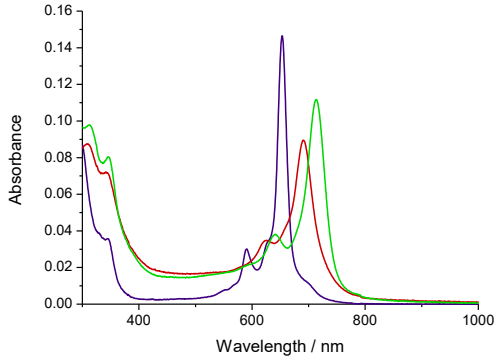

Figure 44. Absorption spectra of $RuFc_4Pc$ **5** (red), $RuFc_8Pc$ **10** (blue) and Ru(*t*-Bu)$_4$Pc **20** (1.0×10^{-6}M) in chlorobenzene.

Figure 45 shows the spectra of the four ferrocenyl Pcs (ZnPcs **3** and **9** in blue and pink, respectively, and RuPcs in **5** and **10** in orange and green respectively) in chloroform. When going from tetra- to octasubstituted Pcs, the Soret and the *Q*-bands are red shifted and the value of the molar extinction coefficient (ε) increases. On the other hand, the change of Zn by Ru produces the opposite effect: an hypsochromic shift of the bands and a reduction of ε.

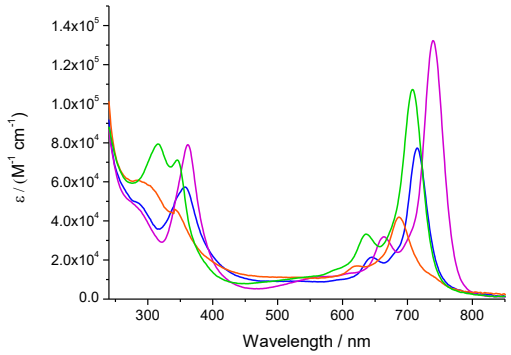

Figure 45. Absorption spectra of $ZnFc_4Pc$ **3** (blue), $RuFc_4Pc$ **5** (orange), $ZnFc_8Pc$ **9** (pink), and $RuFc_8Pc$ **10** (green) in chloroform.

Several titration experiments were carried out in order to study the interaction of the different species in solution. For example, when adding PDIs **11** or **12** to a solution of Zn(*t*-Bu)$_4$Pc **24** in chlorobenzene, no considerable ground state interactions were observed. The absorption spectra resemble the superimposition of the according PDI and ZnPc absorptions (Figure 46a). Proof for complexation and electronic interaction came from fluorescence titrations. Then, upon addition of either PDI, the Zn(*t*-Bu)$_4$Pc **24** fluorescence is strongly quenched (Figure 46b).

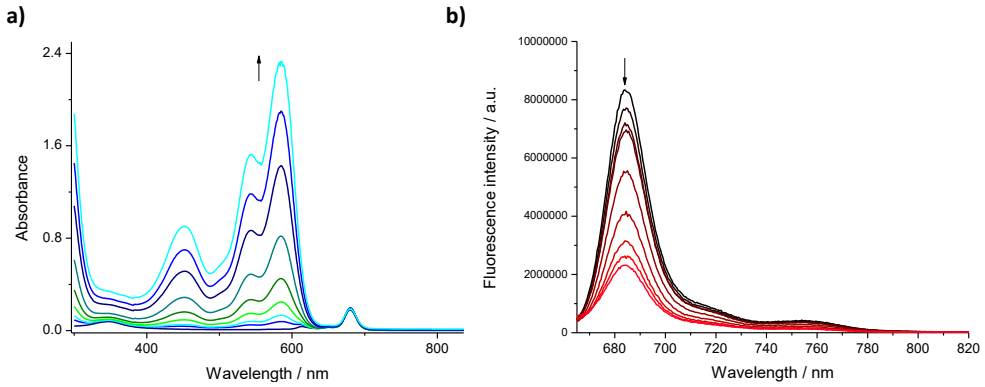

Figure 46. a) Absorption and b) emission spectra (λex = 660 nm) of Zn(*t*-Bu)$_4$Pc **24** (1.0 x 10-^{6}M) upon addition of different concentrations of PDI **11** (up to 50 equivalents) in chlorobenzene.

When treating ferrocene-substituted ZnPcs **3** and **9** similarly, the absorption spectra show some ground state interactions. Here, the ZnPc Soret band features are shifted bathochromically upon PDI addition. Additionally, the *Q*-band region is shifted hypsochromically (Figures 47a and 47b).

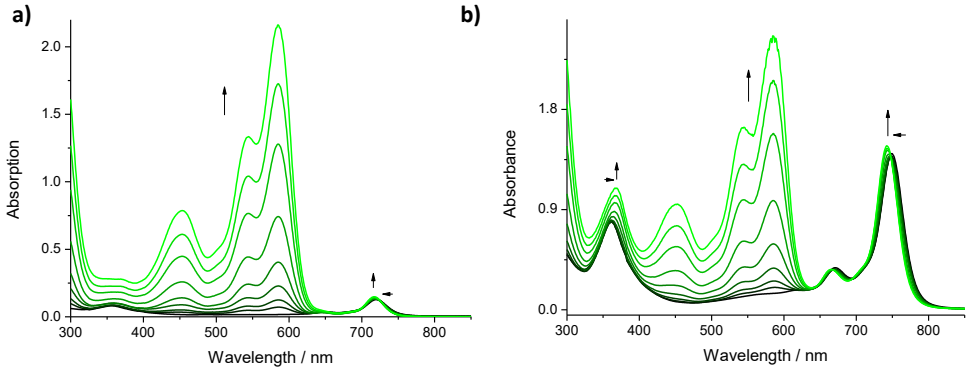

Figure 47. a) Absorption spectra of $ZnFc_4Pc$ **3** (1.0 x 10^{-6}M) upon addition of different concentrations of BPyPDI **12** (up to 50 equivalents) in chlorobenzene. b) Absorption of $ZnFc_8Pc$ **9** (1.0 x 10^{-5}M) upon addition of different concentrations of PyPDI **11** (up to 5 equivalents) in chlorobenzene.

On the other hand, when titrating in the reverse direction, *i.e.* adding the ZnPcs **3**, **9**, and **24** to solutions of PDIs **11** and **12**, respectively, it is hard to observe any interaction in the ground state since they are masked by the intense absorption features of the Pcs. Nevertheless, PDI fluorescence is strongly quenched in all cases (Figure 48).

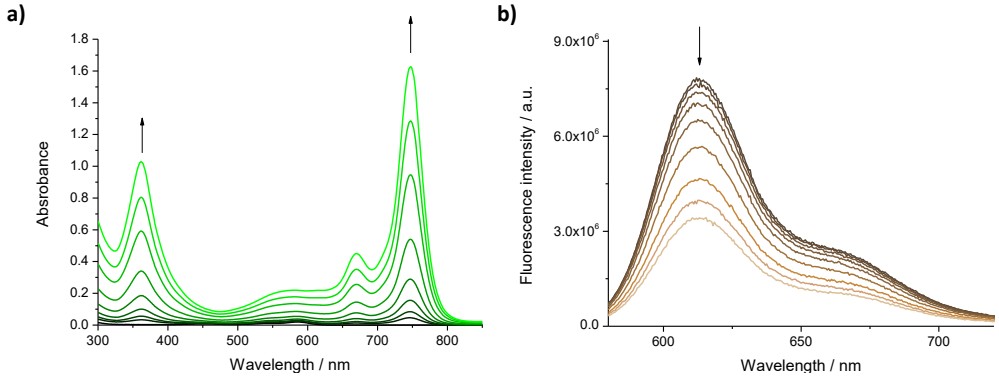

Figure 48. a) Absorption and b) emission spectra (λ_{ex} = 570 nm) of BPyPDI **12** (2.0 x 10^{-7}M) upon addition of different concentrations of $ZnFc_8Pc$ **9** (up to 60 equivalents) in chlorobenzene.

When compared to the monomeric building blocks, the PDI-$(RuPc)_2$ triads **18a**, **19a**, and reference **21a**, show changes in the absorption spectra: the PDI centred features are red shifted and the Pc *Q*-band shifts towards the blue region (Figure 49). These changes are attributed to the strong coordinative binding and the resulting ground state interactions, *i.e.* a shift of electron density from the electron donating Pc to the electron accepting PDI.

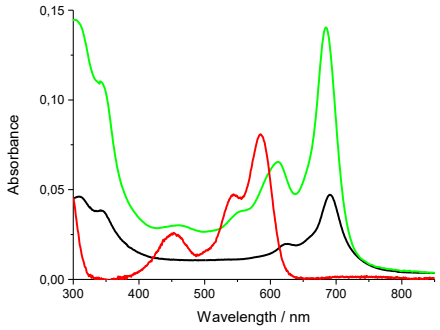

Figure 49. Absorption spectra of 1.0 x 10^{-6}M solutions of $RuFc_4Pc$ **5** (black line), BPyPDI **12** (red line) and triad **18a** (green line) in chlorobenzene.

Upon photoexcitation at 650 nm, Ru(*t*-Bu)$_4$Pc **20** shows the typical Pc emission, with a maximum at 704 nm, that is dramatically quenched in triad **21a** (Figure 50a). RuPcs **5** and **10** do not show any emission upon photoexcitation. This is rationalized by the presence of the ferrocene moieties. Excitation of the PDI units showed that their centred fluorescence is dramatically quenched in **18a**, **19a** and **21a** (Figure 50b).

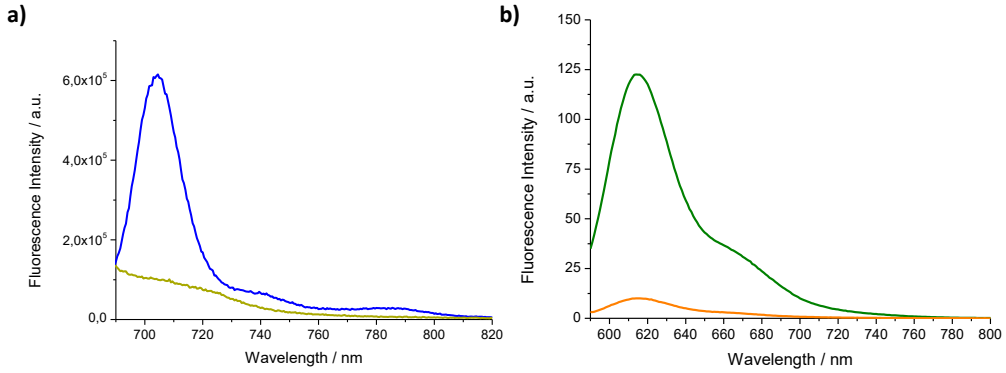

Figure 50. Emission spectra of 1.0 x 10^{-6}M solutions of: a) reference compounds Ru(*t*-Bu)$_4$Pc **20** (blue) and triad **21a** (yellow) upon 650 nm photoexcitation in chlorobenzene, and b) BPyPDI **12** (green) and triad **18a** (orange) upon 570 nm photoexcitation in chlorobenzene.

Subsequently, similar titrations to the previously described for the ZnPcs-PDI systems were carried out with RuPcs **5** and **10** (Figure 51). Upon addition of PDI over RuPcs no interaction in the ground state was observed. Nevertheless, when titrating in the opposite direction the PDI fluorescence is completely quenched after the addition of less than 10 equivalents, whereas ZnPcs titrations never reached that point even after having added 50 equivalents. This difference remarks again the stronger metal-ligand interaction between RuPcs-PyPDIs compared to ZnPcs-PyPDIs.

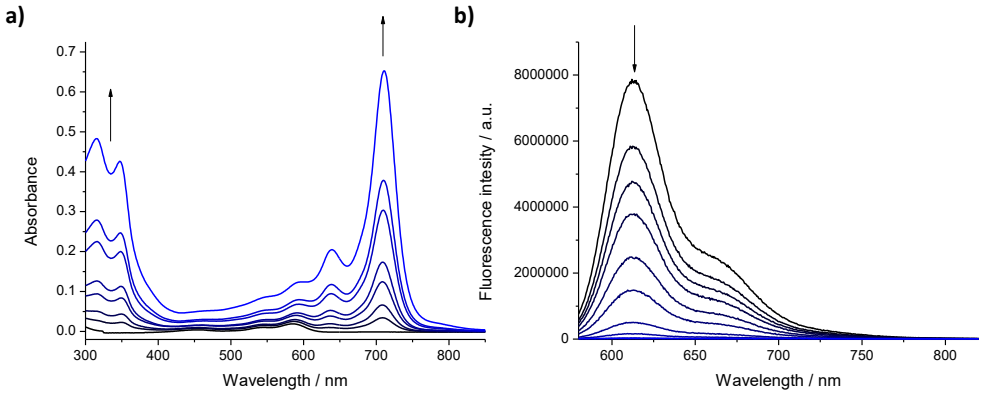

Figure 51. a) Absorption and b) emission spectra (λ_{ex} = 570 nm) of BPyPDI **12** (2.5 x 10^{-7}M) upon addition of different concentrations of $RuFc_8Pc$ **10** (up to 20 equivalents) in chlorobenzene.

Non-linear curve fitting of all spectroscopic changes allowed the determination of the association constants of the formation of Pc-PDI and Pc_2-PDI complexes using the ReactLab™ EQUILIBRIA software. The determined association constants are consistent with the experimental observations, that is, higher values of logk_a were found for the ruthenium complexes.

Quantitative analysis of solutions with optical density above 0.1 are subject to inner filter effects (IFEs). There exist two kinds of IFEs: the primary IFE is defined as the decrease in the intensity of the excitation beam at the point of observation because of the chromophore optical absorption in the excitation region, and the secondary IFE takes place when the fluorescence intensity decreases as a result of the chromophore absorption in the emission region.[99] To avoid this, all the fluorescence spectra were corrected according to Lakowicz equation:

$$F_{corr} = F_{obs} \times 10^{(Abs_{\lambda exc} + Abs_{\lambda emi})/2} \qquad \text{(Eqn 17)}$$

Where

F_{corr} = corrected fluorescence intensity

F_{obs} = observed fluorescence intensity

$Abs_{\lambda exc}$ = absorption at the excitation wavelength

$Abs_{\lambda emi}$ = absorption at the emission wavelength

[99] J. R. Miller, L. T. Calcaterra, G. L. Closs, *J. Am. Chem. Soc.* **1984**, *106*, 3047; b) J. R. Lakowicz,in *Principles of Fluorescence Spectroscopy;* 3. Ed.; Springer: **2002**.; c) Y.-L Wu,.P. D. Jarowski, W. B. Schweizer, F. Diederich, *Chem. Eur. J.* **2010**, *16*, 202.

Table 5. Association constants [M^{-1}] of phthalocyanines **3, 5, 9, 10** and **24** with PDIs **11** and **12** derived from fluorescence quenching titrations in chlorobenzene at 20 °C.

		pyPDI 11	bipyPDI 12	
		log K_{a1}	log K_{a1}	log K_{a2}
ZnPcs	**24**	4.9	6.0	5.5
	3	4.8	5.0	4.9
	9	4.7	5.0	4.0
RuPcs	**5**	6.6	7.1	6.3
	10	6.5	7.4	5.9

1.3.1.7.2 Transient Absorption

Femtosecond transient absorption spectroscopy is a method that allows the generation and investigation of ultra-short-lived species, *i.e.* transients of a molecule, and the corresponding electron dynamics *via* kinetic studies.[100]

In femtosecond transient absorption spectroscopy, the excitation of the sample is induced by ultra-short laser pulses on the femtosecond time-scale (10^{-15} s), which provides the opportunity of observing the temporal evolution of excited states.[101]

In principle, an intense, quasi monochromatic laser pulse – the pump pulse – transfers the sample from the electronic ground state into an excited state. A white-light probe pulse simultaneously monitors the induced optical changes *Δ*OD at time delays *Δt,* after the excitation according to Equation 18:

$$\Delta \mathrm{OD}(\lambda, \Delta t) = \log_{10} \frac{I(\lambda,\infty)}{I(\lambda,\Delta t)} \qquad \text{(Eqn. 18)}$$

where $I(\lambda, \infty)$ and $I(\lambda, \Delta t)$ are the spectral intensities of the probe pulse having passed through the sample, measured without any excitation and with a time delay Δt after excitation, respectively.[102] By recording *Δ*OD with different time delays *Δt* deactivation pathways of excited species with the corresponding kinetics can be resolved. A typical transient absorption system, as depicted in Figure 52, consists of a pulsed Titanium:sapphire laser with a pulse width of 150 fs and a wavelength of 775 nm. The pulsed beam from the laser light source is split up into a pump and a probe beam by a beam splitter.

[100] R. Berera, R. van Grondelle, J. T. M. Kennis, *Photosynth. Res*. **2009**; *101*, 105
[101] H. H. Telle, A. G. Urena, R. J. Donavan in *Laser Chemistry - Spectroscopy, Dynamics and Applications,* John Wiley & Sons, Chichester, **2007**.
[102] A. Maciejewski, R. Naskrecki, M. Lorenc, M Ziolek, J. Karolczak, J. Kubicki, M. Matysiak, M. Szymanski, *J. Mol. Struct.* **2000**, *555*, 1.

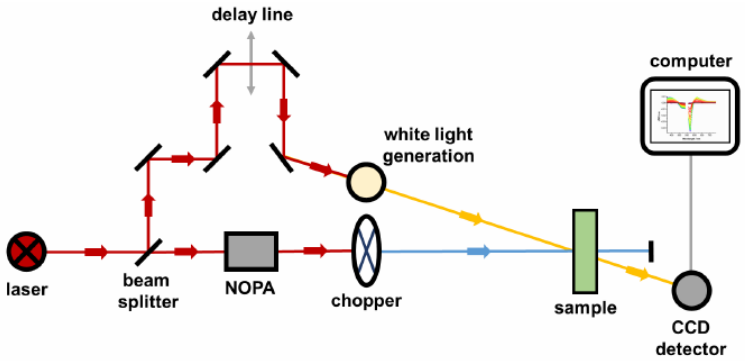

Figure 52. Schematic setup of a femtosecond transient absorption pump/probe system.

In order to obtain different wavelengths of the pump pulse, second harmonic (SHG) or third harmonic generation (THG) are utilized, leading to excitation wavelengths of 387 and 258 nm, respectively. Alternatively, with the help of a two stage non-collinear optical parametric amplifier (NOPA), the pump pulse can be tuned to excitation wavelengths between 470 and 1200 nm as well as to their second harmonics.

The probe beam, on the other hand, runs through a mirror system of variable path length along a delay line, is focused on a sapphire crystal to generate a continuum of white light and finally passes the sample. Since the speed of light is constant, the different path lengths Δx result in different time delays Δt of the probe and the pump pulse, which allows variable time delays between 0 and 8 ns. The probe pulse is subsequently detected by a CCD camera (Charge Coupled Device). The differential spectrum (ΔOD) is obtained by measuring the absorbance of the sample with and without excitation at given time delays, which is possible by means of a chopper wheel in the pump beam blocking every second excitation pulse. The excited state lifetime of a fluorophore is derived from the exponential decay of the intensity.

To shed light onto excited state interactions of the monomers, dyads and triads synthesized, transient absorption measurements were conducted. Right after conclusion of the 150 fs laser pulse (λ_{ex} = 676 nm) reference Zn(*t*-Bu)$_4$Pc **24** showed the typical transient absorption features of ZnPc in chlorobenzene (Figure 53). Namely, transient maxima at 454, 599, 637 and 829 nm accompanied by ground state bleaching around 616, 633 and 684 nm indicate excitation of the ZnPc singlet excited state (^{1*}**24**). These features deactivated *via* intersystem crossing within ~3 ns to the lower lying triplet excited state ^{3*}**24**, exhibiting a transient maximum at 494 nm. Nanosecond transient absorption measurements revealed a lifetime of the triplet excited state of 22.5 µs.

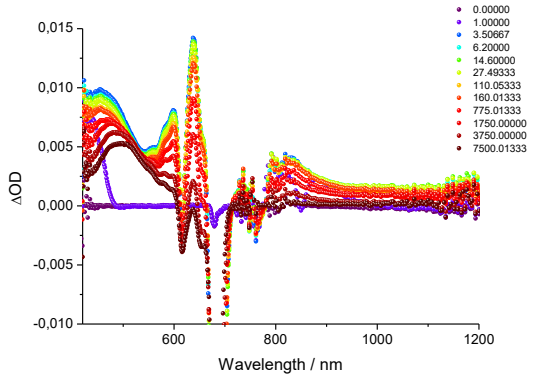

Figure 49. Transient absorption spectra of Zn(*t*-Bu)$_4$Pc **24** in argon saturated chlorobenzene upon 676 nm photoexcitation.

After photoexcitation, ZnFc$_4$Pc **3** showed similar transients with maxima at 477, 622 and 853 nm accompanied by corresponding ground state bleaching around 657 and 724 nm (Figure 54a). In contrast to Zn(*t*-Bu)$_4$Pc **24**, these singlet excited state features deactivated within 3.6 ps to yield the triplet excited state that was identified by transient maxima at 490, 524 and around 1100 nm. The deactivation to the ground state took place within 3.0 ns after excitation. A similar picture was presented when exciting ZnFc$_8$Pc **9** (Figure 54b). Singlet features at 506, 648, 700 and 820 nm (with ground state bleach at 674 and 750 nm) deactivated within 4.4 ps to the triplet excited state. The triplet deactivated within 4.5 ns to the ground state. This very fast intersystem crossing and the subsequent deactivation to the ground state was rationalized by the presence of the 4 / 8 ferrocene units on the ZnPc periphery in **3** and **9**, respectively. This observation is well in line with the absence of fluorescence in emission experiments.

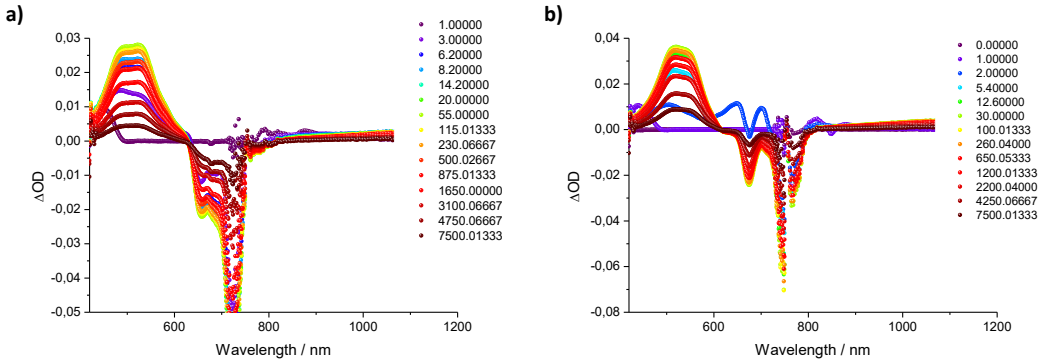

Figure 54. Transient absorption spectra of ZnFc$_4$Pc **3** (a) and ZnFc$_8$Pc **9** (b) in argon saturated chlorobenzene upon 676 nm photoexcitation.

Instantaneously after conclusion of the laser pulse, reference Ru(*t*-Bu)$_4$Pc **20** showed the typical transient features of the singlet excited state of RuPc in chlorobenzene, *i.e*. transient absorptions maximizing at 545, 586, 918 and around 1200 nm, accompanied by ground state bleaching minimizing at 634 and 677 nm (Figure 55). Within 9 ps, these singlet features deactivated to the RuPc triplet excited state identified by transient maxima at 514, 543, 664 and 952 nm. These long-lived features exceeded the limits of the experimental setup. Nanosecond transient absorption measurements revealed a lifetime of 6.9 µs for ^{3*}**20**.

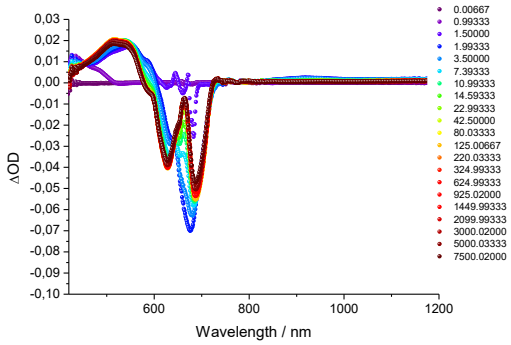

Figure 55. Transient absorption spectra of Ru(t-Bu)$_4$Pc **20** in argon saturated chlorobenzene upon 676 nm photoexcitation.

When exciting RuFc$_4$Pc **5**, the triplet excited state features appeared within the instrument response time (<1ps, Figure 56a). This acceleration was attributed to the presence of the four ferrocene units on the RuPc periphery. ^{3*}**5** deactivated within 209 ns to the electronic ground state. RuFc$_8$Pc **10** showed similar behaviour. However, the deactivation of ^{3*}**10** was further accelerated with a shorter triplet excited state lifetime of 1.6 ns (Figure 56b).

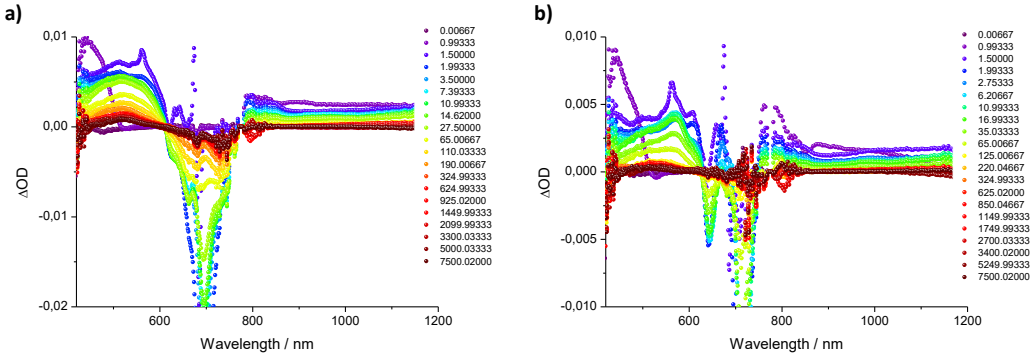

Figure 56. Transient absorption spectra of RuFc$_4$Pc **5** (a) and RuFc$_8$Pc **10** (b) in argon saturated chlorobenzene upon 676 nm photoexcitation.

Regarding the PDI units, upon 568 nm photoexcitation, **11** and **12** showed the typical transient absorption features of PDIs around 710, 970 and 1045 nm and ground state bleaching at 460, 544, 598 and 670 nm (Figure 57). These features deactivated to the ground state within 5.8 ns. The kinetic data obtained so far is presented in Table 6.

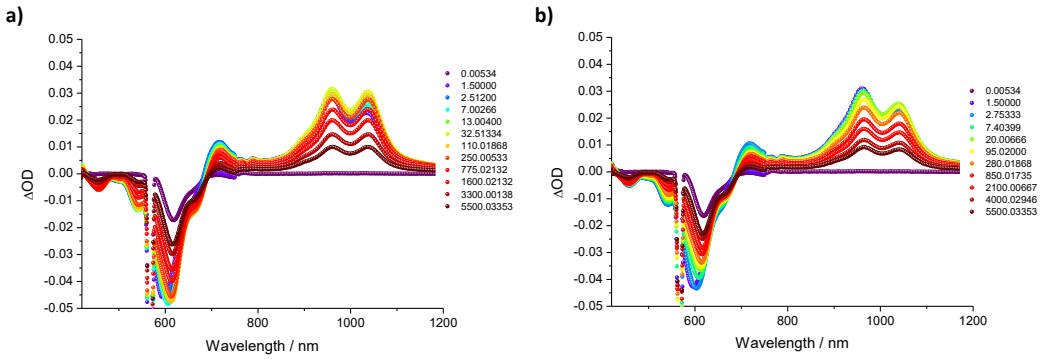

Figure 57. Transient absorption spectra of PDI **11** (a) and PDI **12** (b) in argon saturated chlorobenzene upon 568 nm photoexcitation.

Table 6. Singlet (S) and triplet (T) excited state lifetimes of phthalocyanines **3, 5, 9, 10, 20** and **24** upon 676 nm and PDIs **10** and **11** upon 568 nm photoexcitation in chlorobenzene.

	τ (^{1}*S) / ps	τ (^{3}*T) / ns
Zn(*t*-Bu)$_4$Pc 24	2820	22500
ZnFc$_4$Pc 3	3.6	3.0
ZnFc$_8$Pc 9	4.4	4.5
Ru(*t*-Bu)$_4$Pc 20	9	6900
RuFc$_4$Pc 5	<1	209
RuFc$_8$Pc 10	<1	1.6
PyPDI 11	5795	-
BPyPDI 12	5753	-

Initially, when exciting the reference 1:1 complex **25** at 676 nm (which exclusively excites the Zn(*t*-Bu)$_4$Pc), ZnPc singlet excited state features were observed. Within 53 ps, these features depleted and the typical transient absorption features of the ZnPc radical cation (maximum at 846 nm) and the PDI radical anion (792, 987 and 1093 nm) aroused (Figure 58a), respectively.[68e,72] The charge separated state Zn(*t*-Bu)$_4$Pc **24**$^{\bullet+}$-PyPDI **11**$^{\bullet-}$ (CSS) recombined within 2050 ps to the triplet manifold of the ZnPc which subsequently deactivated to the ground state. The observations were very similar for 2:1 complex **21b** (Figure 58b). All kinetic data are presented in Table 7.

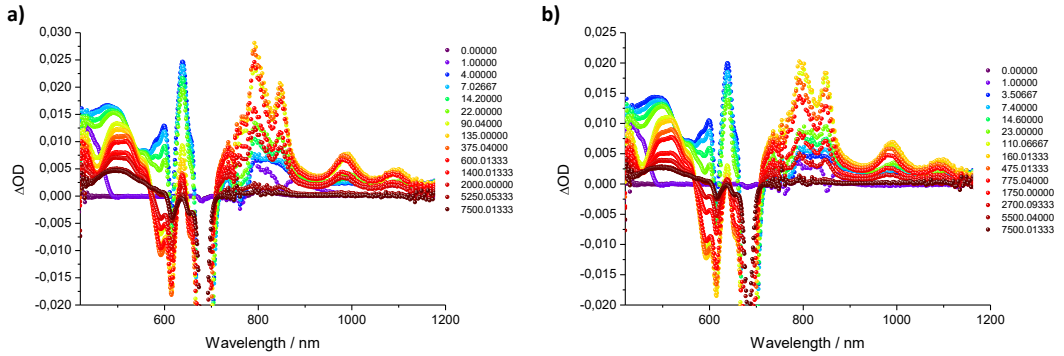

Figure 58. Transient absorption spectra of **25** (a) and **21b** (b) in argon saturated chlorobenzene upon 676 nm photoexcitation.

Excitation of 1:1 and 2:1 Zn complexes **25** and **21b** at 568 nm exclusively yielded the singlet excited state features of the PDI unit (Figures 59a and b). Subsequent electron transfer from the ground state ZnPc to the excited state PDI led to the formation of the charge separated states within 57 and 51 ps, respectively.

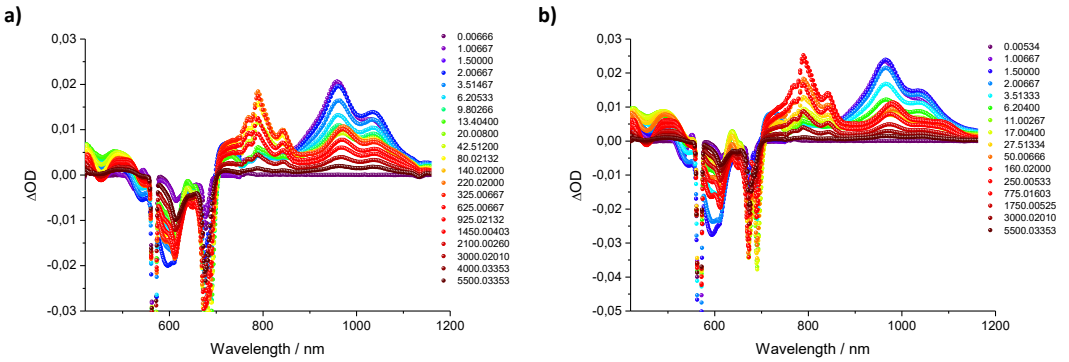

Figure 59. Transient absorption spectra of **25** (a) and **21b** (b) in argon saturated chlorobenzene upon 578 nm photoexcitation.

Table 7. Rate constants for charge separation (CS) and charge recombination (CR) and corresponding lifetimes of the charge separated states (CSS) $ZnPc^{\bullet+}$-$PDI^{\bullet-}$ upon 676 nm and 568 nm photoexcitation in chlorobenzene.

	λ_{ex} = 676 nm			λ_{ex} = 568 nm		
	CS / s^{-1}	CR / s^{-1}	τ (CSS) / ps	CS / s^{-1}	CR / s^{-1}	τ (CSS) / ps
1:1 complex 25	1.9×10^{10}	4.9×10^{8}	2050	1.7×10^{10}	4.3×10^{8}	2333
2:1 complex 21b	2.1×10^{10}	6.2×10^{8}	1613	2.0×10^{10}	6.0×10^{8}	1663

When exciting the ZnFcPc containing complexes **22**, **18b**, **23**, **19b** at 676 nm, only ZnPc centred transients are observed (Figures 60a-d). The singlet excited state deactivates rapidly to the triplet excited state, as seen for the monomeric $ZnFc_4Pc$ **3** and $ZnFc_8Pc$ **9**, which then yields the ZnPc ground state. We attribute this lack of electronic interaction between excited ZnPc and ground state PDI to the very fast deactivation of the ZnPc singlet excited state induced by the presence of the ferrocene units.

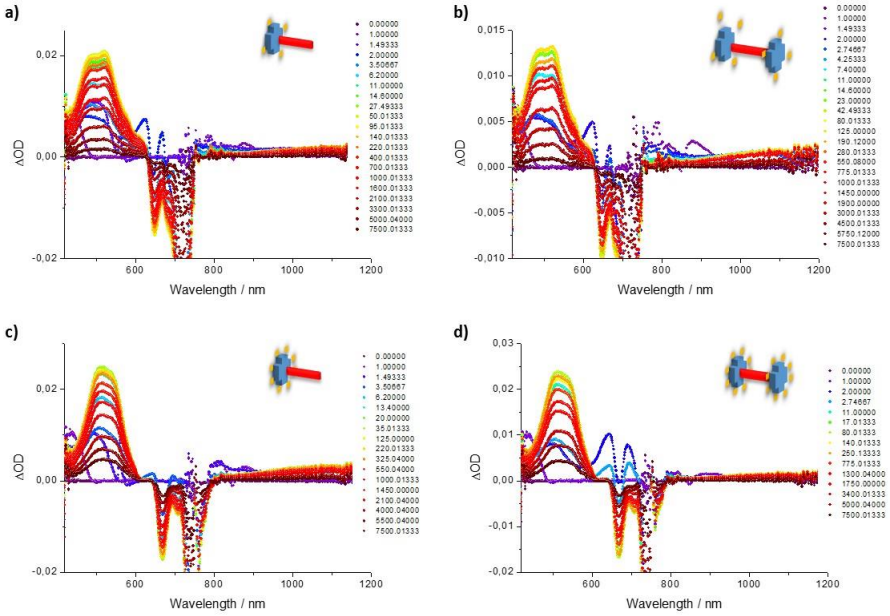

Figure 60. Transient absorption spectra of ZnFcPc containing complexes **22** (a), **18b** (b), **23** (c) and **19b** (d) in argon saturated chlorobenzene upon 676 nm photoexcitation.

Upon 568 nm photoexcitation of complexes **22**, **18b**, **23**, **19b**, singlet excited state features of PDI are visible. Within about 2-5 ps these features diminish, while ZnPc ground state bleaching is observed, accompanied by the typical transient features of ^{3*}ZnPc. A likely rationale for this observation is a fast energy transfer from the excited state PDI to the ground state ZnPc, populating ^{1*}ZnPc. As intersystem crossing in ZnPcs **3** and **9** takes place very quickly (~4 ps), the typical ^{1*}ZnPc transients are masked. ^{3*}ZnPc subsequently deactivates to the electronic ground state within several nanoseconds (Figures 61a-d). The kinetic data are presented in Table 8.

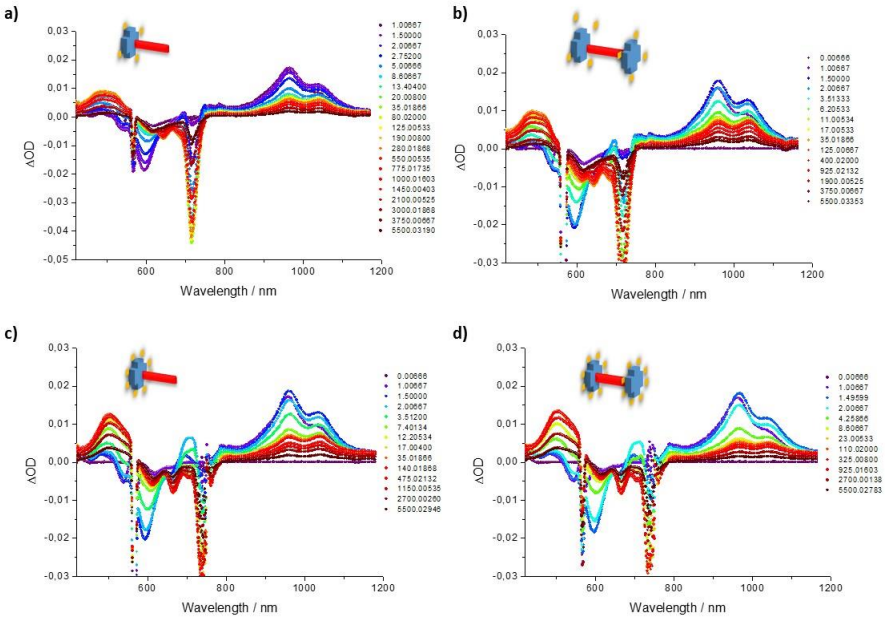

Figure 61. Transient absorption spectra of **22** (a), **18b** (b), **23** (c) and **19b** (d) in argon saturated chlorobenzene upon 578 nm photoexcitation.

Table 8. Rate constants for the energy transfer from PDI to ZnPc upon 568 nm photoexcitation in chlorobenzene.

λ_{ex} = 568 nm	
	k_{EnT} / s^{-1}
22	2.1 x 10^{11}
18b	4.5 x 10^{11}
23	2.6 x 10^{11}
19b	2.6 x 10^{11}

Regarding the RuPc-PDI complexes, upon 676 nm photoexcitation of triad **21a** in chlorobenzene, the former observed Ru(*t*-Bu)$_4$Pc **20** singlet excited state features deactivate within 5 ps to new transient features that were not detected in the monomers. A new transient maximizing around 730 nm resembles the radical cation of RuPc, whereas maxima at 795 and 995 and 1100 nm corroborate the formation of the PDI anion (Figure 62).[72] These features decay within 320 ns to the triplet excited state of RuPc, which is approximately 3 times larger than it was described,[72] probably owing to further stabilization due to the increased number of phenoxy groups at the bay positions

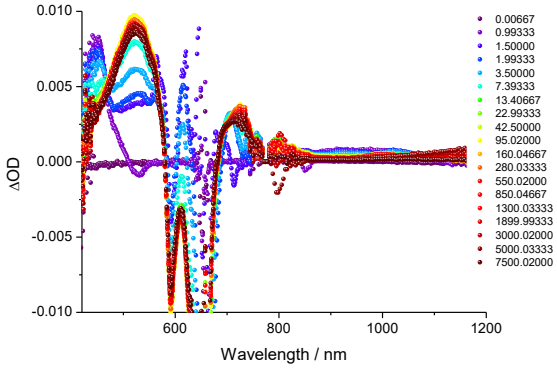

Figure 62. Transient absorption spectra of triad **21a** in argon saturated chlorobenzene upon 676 nm photoexcitation.

When exciting triads **18a** and **19a** at 676 nm, no evidence for electron transfer could be observed. Electronic interaction between the excited state RuPc and the PDI in the ground state is hindered by the fast singlet excited state deactivation induced by the ferrocene units in triad **18a**, which is even faster in the case of triad **19a** (Figures 63a and b).

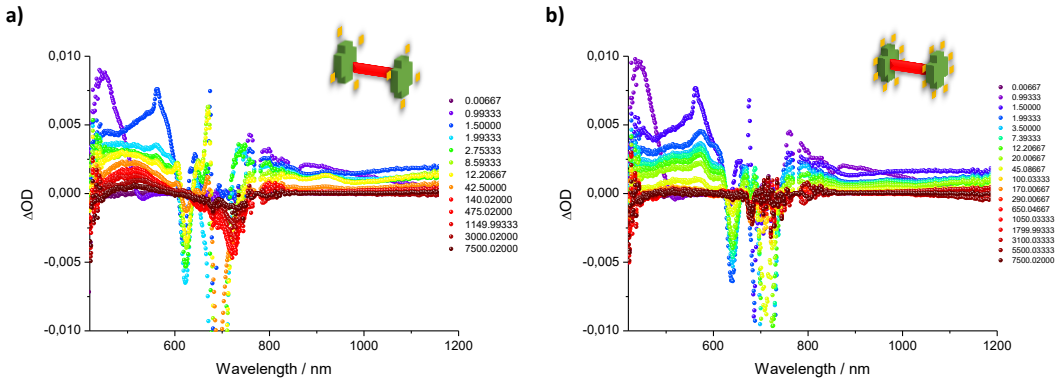

Figure 63. Transient absorption spectra of triads **18a** (a) and **19a** (b) in argon saturated chlorobenzene upon 676 nm photoexcitation.

Therefore, we turned to 568 nm excitation. Here, PDI is exclusively excited, and hence the influence of the ferrocene units on the excited state should be minimized. In chlorobenzene, for reference triad **21a**, a quick deactivation (9 ps) of the PDI singlet excited state, *e.g.* 980 nm, gives rise to the radical ion species' bands. A transient at 730 nm reflects the generation of the RuPc cation, transients at 795, 995, and 1100 nm the PDI anion (Figure 64).

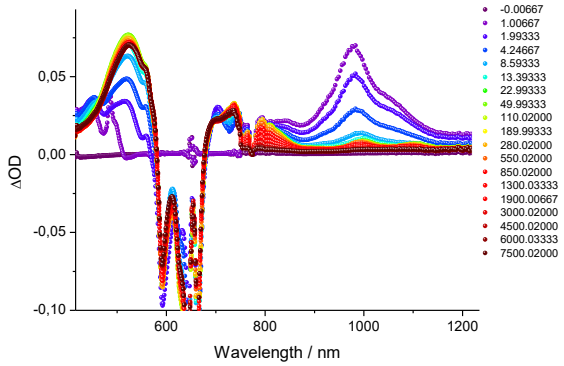

Figure 64. Transient absorption spectra of triad **21a** in argon saturated chlorobenzene upon 568 nm photoexcitation.

For triads **18a** and **19a**, charge separation is even faster (~1 ps). After photoexcitation of the PDI unit, the singlet excited state features quickly deactivate to the charge separated state that is identified by the RuPc radical cation band around 725 nm and the PDI radical anion bands around 795, 995 and 1100 nm (Figures 65a and b). The charge recombination takes place within 2.3 and 1.2 ns, for triads **18a** and **19a** respectively, to yield the RuPc triplet excited state (see Table 9).

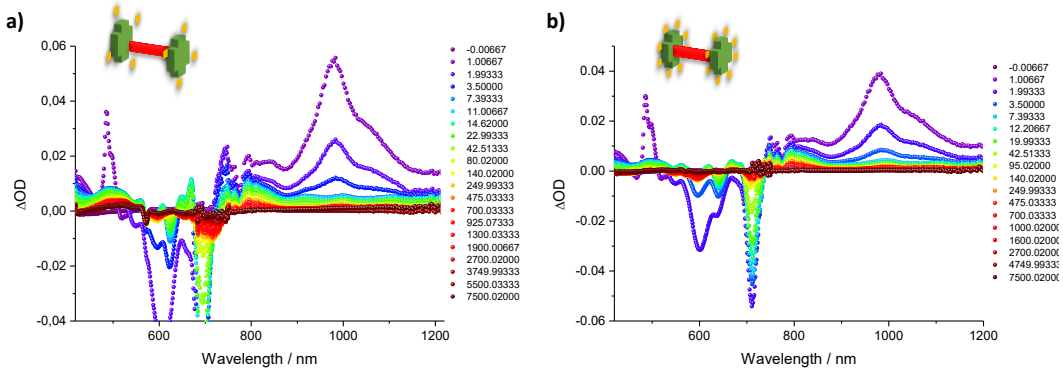

Figure 65. Transient absorption spectra of triads **18a** (a) and **19a** (b) in argon saturated chlorobenzene upon 568 nm photoexcitation.

Different solvents were then studied in order to observe their influence on the transient features. In less polar anisole similar observations with comparable rates for charge separation and recombination were made (Figure 66a and b).

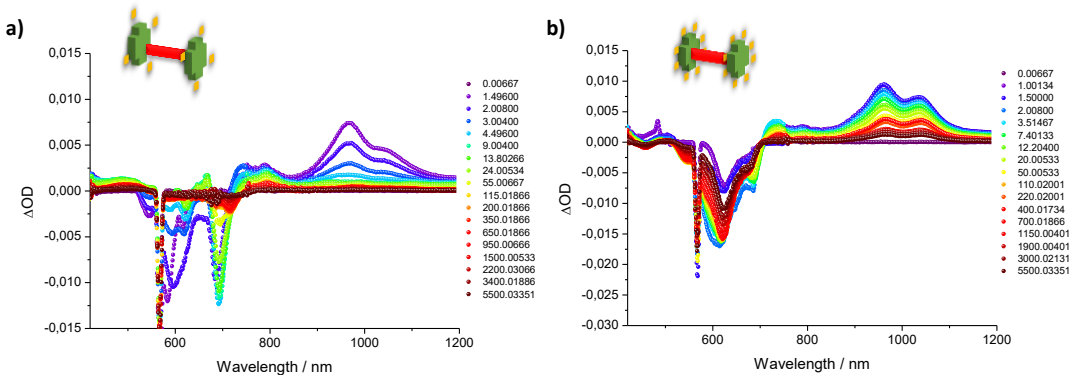

Figure 66. Transient absorption spectra of triads **18a** (a) and **19a** (b) in argon saturated anisole upon 568 nm photoexcitation.

In more polar benzonitrile (Figure 67a and b), charge separation is decelerated by approximately one order of magnitude. Charge recombination takes place with comparable rate constants. All kinetic data obtained are shown in Tables 9, 10 and 11.

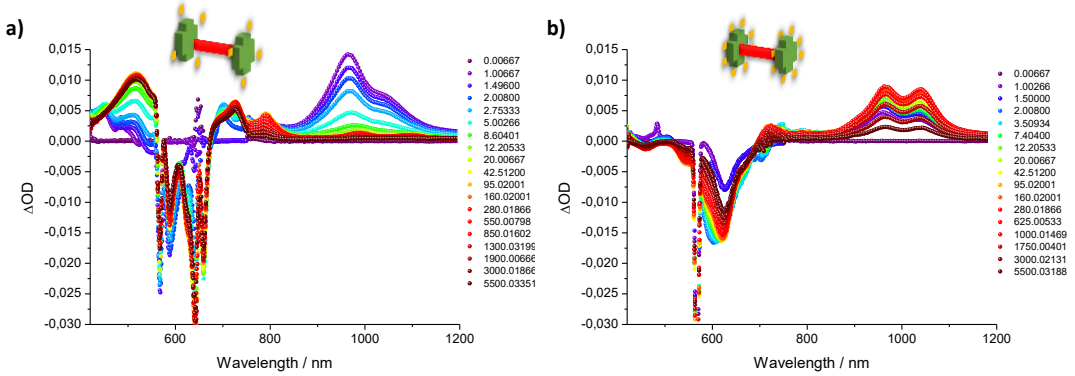

Figure 67. Transient absorption spectra of triads **18a** (a) and **19a** (b) in argon saturated benzonitrile upon 568 nm photoexcitation.

Table 9. Rate constants for charge separation (CS) and charge recombination (CR) and corresponding lifetimes of the charge separated states (CSS) $RuPc^{\bullet+}$-$PDI^{\bullet-}$ upon 676 nm and 568 nm photoexcitation in chlorobenzene.

Chlorobenzene			
	CS / s^{-1}	**CR / s^{-1}**	**τ (CSS) / ps**
21a (λ_{ex} = 676 nm)	2.0 x 10^{11}	3.1 x 10^{6}	320000
21a (λ_{ex} = 568 nm)	1.2 x 10^{11}	3.0 x 10^{6}	331000
18a (λ_{ex} = 568 nm)	7.6 x 10^{11}	4.3 x 10^{8}	2338
19a (λ_{ex} = 568 nm)	1.0 x 10^{12}	8.2 x 10^{8}	1225

Table 10. Rate constants for charge separation (CS) and charge recombination (CR) and corresponding lifetimes of the charge separated states (CSS) $RuPc^{\bullet+}$-$PDI^{\bullet-}$ upon 676 nm and 568 nm photoexcitation in anisole.

Anisole			
	CS / s^{-1}	**CR / s^{-1}**	**τ (CSS) / ps**
21a (λ_{ex} = 676 nm)	–	–	–
21a (λ_{ex} = 568 nm)	2.0×10^{11}	2.4×10^{6}	417000
18a (λ_{ex} = 568 nm)	8.3×10^{11}	5.0×10^{8}	2031
19a (λ_{ex} = 568 nm)	6.7×10^{11}	7.5×10^{8}	1340

Table 11. Rate constants for charge separation (CS) and charge recombination (CR) and corresponding lifetimes of the charge separated states (CSS) $RuPc^{\bullet+}$-$PDI^{\bullet-}$ upon 676 nm and 568 nm photoexcitation in benzonitrile.

Benzonitrile			
	CS / s^{-1}	**CR / s^{-1}**	**τ (CSS) / ps**
21a (λ_{ex} = 676 nm)	–	–	–
21a (λ_{ex} = 568 nm)	3.3×10^{10}	3.9×10^{6}	259300
18a (λ_{ex} = 568 nm)	4.4×10^{10}	2.8×10^{8}	3606
19a (λ_{ex} = 568 nm)	8.3×10^{10}	2.3×10^{8}	4315

1.3.2 Peripheral functionalization of SubPc with ferrocenes.

1.3.2.1 Synthesis of the ferrocenyl-substituted subphthalocyanines

Subphthalocyanines are aromatic macrocycles composed of three units of isoindole linked together through aza bridges that present a tetracoordinated boron atom in their central cavity.[5,103] They consist in aromatic system of 14 π-electrons mainly delocalized over the inner ring. Unlike Pcs, they possess a conical structure (determined by X-Ray diffraction) imposed by the tetrahedral geometry of the central boron atom, which always bears an axial ligand.

SubPcs are synthesized nowadays in high yields by cyclotrimerization reaction of the desired phthalonitrile in the presence of a Boron-derivative, usually a boron trihalide (BX_3), at high temperatures (140-200 ^oC) employing high boiling point solvents (*p*-xylene, naphthalene, etc.)[5,103](Scheme 17).

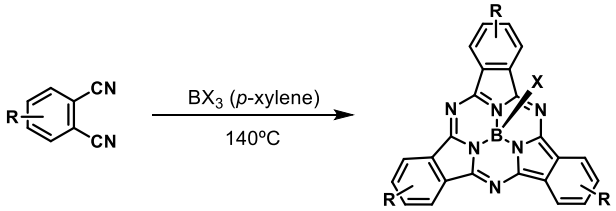

Scheme 17. General synthetic route for obtaining SubPcs.

Two possible synthetic routes to obtain the desired tri- and hexaferrocenylsubstituted SubPcs are envisioned:

1) Cyclotrimerization reaction of the previously prepared phthalonitriles **1** and **2** or
2) Pd catalysed Suzuki cross coupling reaction on the tri- or hexaiodo substituted SubPcs.

Treatment of phthalonitrile **1** with 1 M BCl_3 in refluxing *p*-xylene (Scheme 18), only led to decomposition of the starting material.

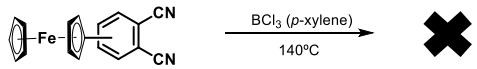

Scheme 18. Synthetic attempt to obtain triferrocenylSubPc.

In order to proceed with route 2, triiodoSubPc was prepared following Scheme 19 by refluxing a mixture of 4-iodophthalonitrile in 1 M BCl_3 in refluxing *p*-xylene (Scheme 19). This yielded

[103] a) C.G. Claessens, D. González-Rodríguez, T. Torres, *Chem. Rev.* **2002**, *102*, 835; b) M. Geyer, F. Plenzig, J. Rauschnabel, M. Hanack, B. del Rey, A. Sastre, T. Torres, *Synthesis* **1996**, 1139.

SubPc **26** which, after *in situ* treatment with *tert*-butylphenol, generated SubPc **24**. During the purification of **24** by column chromatography, C_1 and C_3 regioisomers were separated.[104]

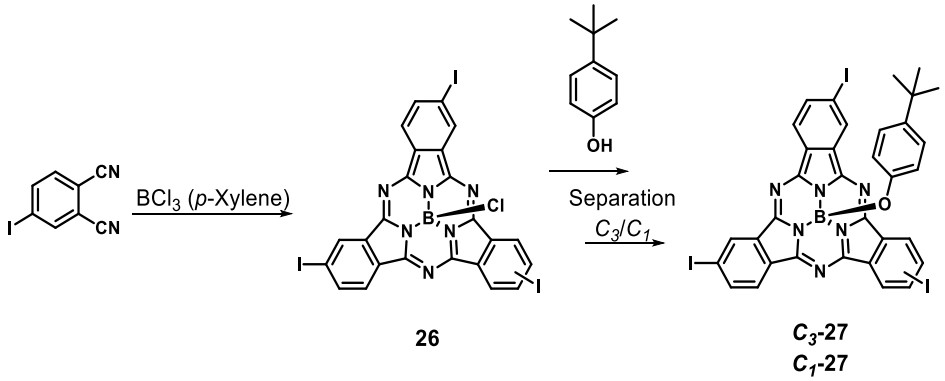

Scheme 19. Synthesis of SubPcs **26** and **27**.

Finally, refluxing the corresponding iodo-derivative with ferrocene boronic acid and the Pd catalyst, in a degassed 1:1 mixture of water and toluene for 18 h yielded, C_1- and C_3- SubPcs **28** as blue solids in good yields (Scheme 20).

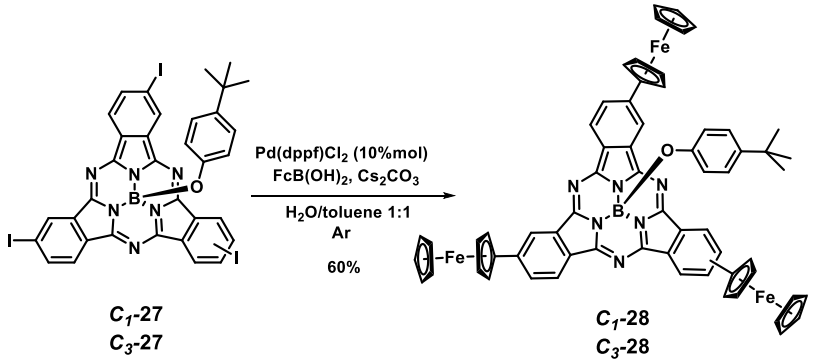

Scheme 20. Synthesis of SubPc **28**.

A similar synthetic approach was then followed to prepare the hexasubstituted derivative. This time, a solution of BBr_3 1 M in DCM was used to template the formation of SubPc **29** from diiodophthalonitrile (Scheme 21).[105] SubPc **29** was then transformed into SubPc **30** after exchanging the axial ligand through refluxing in toluene in the presence of *tert*-butylphenol. Finally, six ferrocene units where introduced by Pd catalysed cross coupling reaction conditions as before, affording SubPc **31** in moderate yields.

[104] C. G. Claessens, M. J. Vicente-Arana, T. Torres, *Chem. Commun*. **2008**, 6378.
[105] W. M. Sharman, J. E. van Lier, *J. Porphyrins Phthalocyanines* **2005**, *9*, 651.

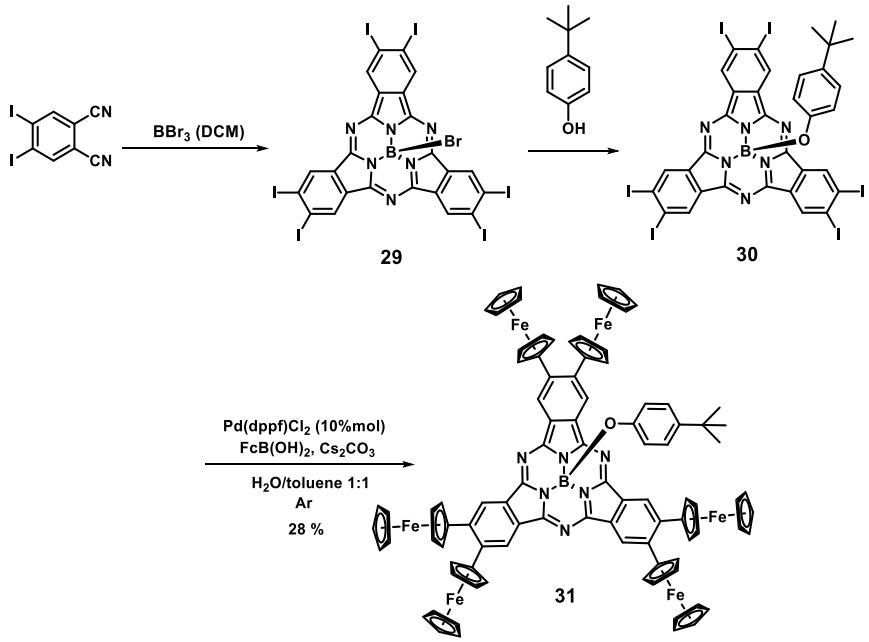

Scheme 21. Synthesis of SubPc **31**.

The structure of SubPcs was established on the basis of their spectroscopic features, namely, ^{1}H-NMR, ^{13}C-NMR, FT-IR, UV-Vis and MS.

The bulky *tert*-butylphenoxy group placed on the axial position excludes the formation of aggregates due to π-π interactions, thus providing better solubility and better resolved ^{1}H-NMR spectra than in the case of the planar Pcs (Figure 68). ^{1}H-NMR spectra of Fc_3SubPc **28**, and Fc_6SubPc **31** show similar patterns: the signals corresponding to the aromatic protons of the macrocycle appear between 8 and 9 ppm, whereas the phenoxy group show its signals at $\delta \approx$ 6.8 and 5.5 ppm. The latter appear strongly upfield shifted due to the SubPc anisotropic ring current. Finally, the ferrocene units display their protons between 4 and 5 ppm.

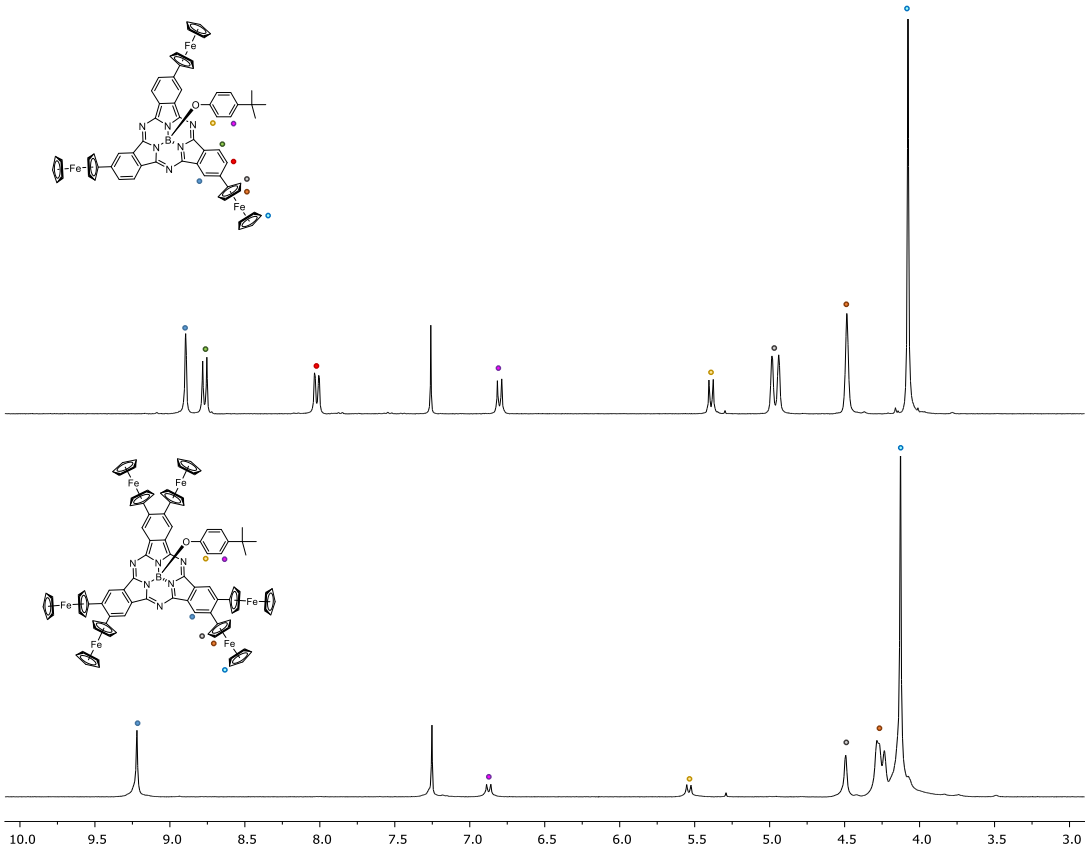

Figure 68. Aromatic region of the ^{1}H-NMR spectra of SubPcs ***C*$_{3}$-28** (top) and **31** (down).

Figure 69 shows the absorption and emission spectra of ***C*$_{1}$-28**, **30** and **31**. The introduction of the Fc substituents produces a bathocromic shift of the SubPc *Q*-band, which is larger as the number of ferrocene units increase. Conversely, no effect is observed on the molar extinction coefficient for SubPcs. Regarding the emission, once again, the introduction of ferrocenes quenches the fluorescence of these molecules (Figure 69b).

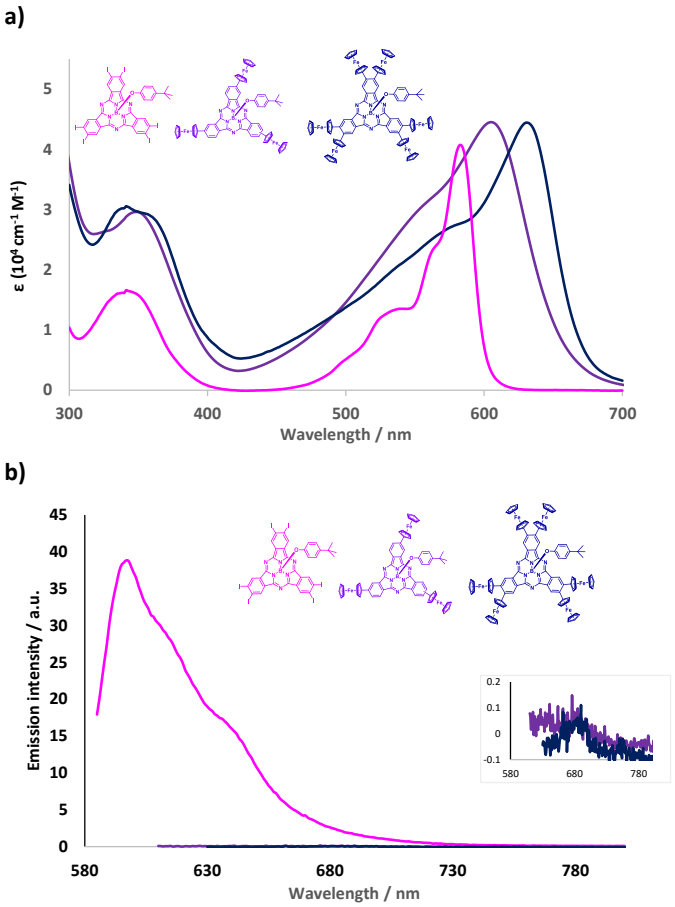

Figure 69. a) Absorption spectra of ***C*$_1$-28** (purple), **30** (pink), and **31** (blue) in toluene. b) Emission spectra of ***C*$_1$-28** (purple, λ_{exc} = 580 nm), **30** (pink, λ_{exc} = 600 nm), and **31** (blue, λ_{exc} = 620 nm) in toluene.

1.3.2.2 Electrochemical studies

As a general fact, both the first oxidative or reductive half-wave potentials of SubPcs are one electron processes.[5] The reduction is frequently reversible on the cyclic voltammetry time scale, while oxidation processes give rise to less stable charged species. Scanning at more positive or negative potentials typically reveals several redox events, some of them multielectronic, which are usually electrochemically irreversible or quasi-reversible. This irreversibility is thought to

arise from chemical transformations or to the deposition of the redox species on the electrode surfaces.[83a,106]

The first oxidative or reductive half-wave potential of SubPcs, and hence their electron-donor/acceptor ability, can be predictably tuned by the peripheral substitution pattern on the macrocycle (see Figure 65). For instance, the first reduction event is typically observed between —1.58 V tris(diphenylamino)phenoxySubPc and —0.82 V (hexakis(octylsulfonyl)phenoxySubPc, Figure 70 a and b,),[83a,106a] whereas first oxidative half-wave values were as high as +1.15 V (dodecafluorophenoxySubPc, Figure 70c) and as low as +0.37 V (tris(diphenylamino)phenoxySubPc, Figure 70a) vs the Fc/Fc^{+} internal reference.

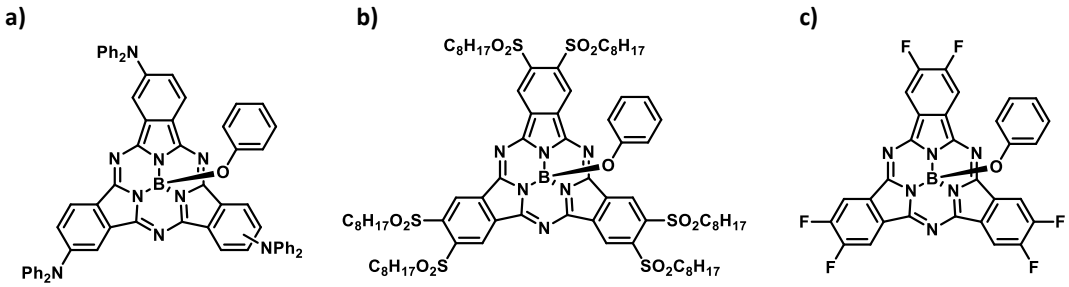

Figure 70. Chemical structure of the SubPcs with the highest and lowest oxidation and reduction potentials reported. The largest and the smallest oxidation and reduction values are highlighted.

The electrochemical properties of SubPcs **28** and **31** have been investigated by cyclic voltammetry and square wave voltammetry in dry DCM with a glassy carbon electrode as working electrode and using ferrocene as an external reference. A subphthalocyanine with no peripheral substituents and bearing a phenoxy group at the axial position was used as the reference (Figure 71).[107]

[106] a) D. González-Rodríguez, T. Torres, D. M. Guldi, J. Rivera, M. A. Herranz, L. Echegoyen, *J. Am. Chem. Soc.* **2004**, *126*, 6301; b) D. González-Rodríguez, T. Torres, M. A. Herranz, L. Echegoyen, E. Carbonell, D. M. Guldi, Chem. Eur. J. **2008**, *14*, 7670.
[107] E. Caballero, J. Fernández-Ariza, V. M. Lynch, C. Romero-Nieto, M. S. Rodríguez-Morgade, J. L. Sessler, D. M. Guldi, T. Torres, *Angew. Chem*. **2012**, *124*, 11499.

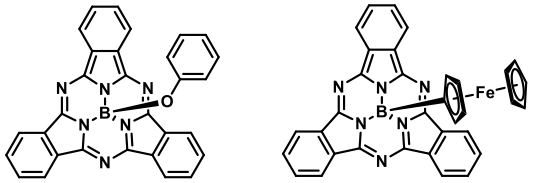

Figure 71. Chemical structure of references SubPc **32** and (Fc-B)SubPc.

Similarly to the corresponding FcPcs, the first oxidation waves that appear at 0.11 for Fc_3SubPc **28** and 0.02-0.18 V for Fc_6SubPc **31**, corresponding to the oxidation of the ferrocene units (Figure 72). Furthermore, electronic communication between ferrocene moieties is clearly observed for Fc_6SubPc **31** (Figure 72b) but not for Fc_3SubPc **28** (Figure 72a). These processes are fully reversible, although in the case of Fc_6SubPc **31**, a sharp cathodic peak appearing in the reverse scan that is assigned to adsorption on the working electrode.

The SubPc centred oxidation exhibit an irreversible wave and takes place at ~0.7 V, while the first reduction appears at -1.54 and -1.63 V for SubPcs **28** and **31**, respectively. Additionally, we carried out square wave voltammetry (Figure 73), which confirmed what had been observed in CV and also allowed us to observe a second reduction process for the SubPc core at -2 V approximately.

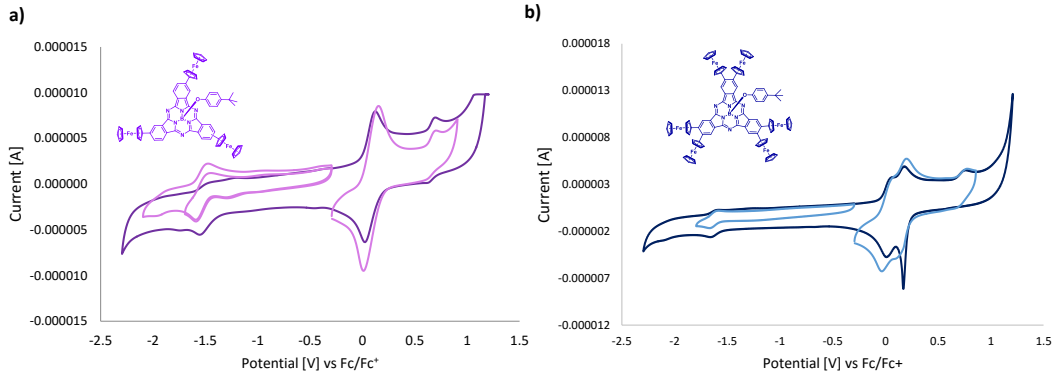

Figure 72.Cyclic voltammograms of Fc_3SubPc **28** (a) and Fc_6SubPc **31** (b) in DCM (0.1M $TBAPF_6$) at room temperature using a glassy carbon electrode. Potentials *vs* Fc/Fc^+.

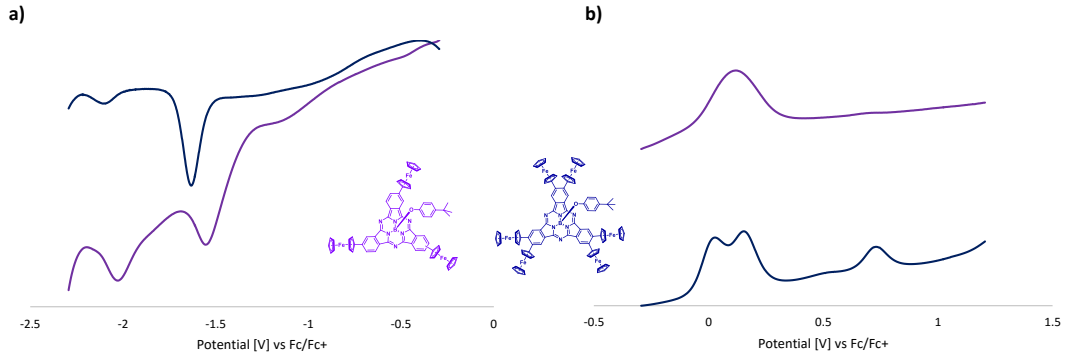

Figure 73 a)Reduction window and b) oxidation window of square wave voltammograms of Fc_3SubPc **28** (purple line) and Fc_6SubPc **31** (blue line) in DCM (0.1M $TBAPF_6$) at room temperature using a glassy carbon electrode. Potentials *vs* Fc/Fc^+.

Comparison of the first reduction potentials of Fc_3SubPc **28** and Fc_6SubPc **31** with the reference **32** reveals higher oxidizing ability for Fc-substituted SubPcs related to non-substituted macrocycles. Moreover, hexaferroceneSubPc **31** is 90 mV more difficult to reduce than **28** and reference **32** (Table 12).

When comparing the peripherally substituted ferrocenyl SubPcs **28** and **31** with axially ferrocenyl substituted (Fc-B)SubPc, no significant differences are observed in the oxidation features, although the Fc_6SubPc **31** shows again less reducing ability (Table 12).[83b] The counter-electrolyte used for the latter is tetrabutylammonium perchlorate (TBAP).

Table 12. Redox potentials of SubPcs **28**, **31** and **32** ($E_{1/2}$ in V) vs. Fc/Fc^+ in DCM (0.1 M $TBAPF_6$) at room temperature using a glassy carbon electrode.

	E_{red2}	E_{red1}	E_{ox1}	E_{ox2}	E_{ox3}
32	—2.05	—1.54	0.57	-	-
28	—2.16[b]	—1.54	0.12	0.70[b]	-
31	—2.10[b]	—1.63	0.03	0.15[a]	0.73[b]
(Fc-B)SubPc[c]	-	—1.58	0.02	0.75	-

[a] Signal with strong adsorption. [b] Irreversible. [c] In DCM (0.1 M TBAP).

1.3.2.3 Assembly of ferrocenyl-substituted subphthalocyanine-C_{60} cocrystallates

As it was stated in the general introduction of this chapter, fullerene and its derivatives are being widely used as active components in optoelectronic devices due to their outstanding

photophysical and electrochemical properties. The performance of the devices depend of their morphology, so great efforts have been made to study the interactions between the different components, in this case, between the fullerenes and the chromophores.[108] The basis to design new fullerene receptors is based on 3 principles: shape complementarity, electrostatic complementarity with the electron deficient fullerene and entropic factors such as the hydrophobic effect.[108a,109] SubPcs, with their bowl-shaped structure, present the adequate and complementary shapes to fullerenes. This has been confirmed by several theoretical studies, which show a high degree of complementarity between SubPc and C_{60}.[110] Several C_{60} and SubPc covalent dyads have been reported by our research group. These studies show that electronic communication between the units is strongly dependent on the distance between them.[83b,111] On the other hand, Ziessel *et al.* reported in 2009 a 1:1 SubPc/C_{60} complex in solution even if no quantitative data was reported.[112] Recently, our research group presented an extensive study of the interaction between SubPcs and fullerenes C_{60} and C_{70}, in which 1:1 and 2:1 SubPc/fullerene complexes were observed and their association constants quantified. Moreover, unidirectional energy transfer from the SubPc to the fullerene core was determined upon photoexcitation.[113]

In the solid state, Kobayashi and co-workers described in 2011 the 1:1 complex between fullerene and a π-extended subphthalocyanine and recently Konarev *et al.* have reported a 1:1 co-crystallized structure of a dimeric SubPc with a C_{60} in which the fullerene is surrounded by two SubPcs (Figure 69).[114]

[108] a) K. Tashiro, T. Aida, *Chem. Soc. Rev*. **2007**, *36*, 189; b) A. M. V. M. Pereira, A. R. M. Soares, A. Hausmann, M. G. P. M. S. Neves, A. C. Tomé, A. M. S. Silva, J. A. S. Cavaleiro, D. M. Guldi, T. Torres, *Phys. Chem. Chem. Phys*. **2011**, *13*, 11858; c) H. Imahori and Y. Sakata, *Adv. Mater*. **1997**, *9*, 537; d) P. D. W. Boyd and C. A. Reed, *Acc. Chem. Res*. **2005**, *38*, 235.

[109] a) E. M. Pérez, N. Martín, *Chem. Soc. Rev*. **2008**, 37, 1512; b) A. Sygula, F. R. Fronczek, R. Sygula, P. W. Rabideau, M. M. Olmstead, *J. Am. Chem. Soc.* **2007**, *129*, 3842; c) E. M. Pérez, L. Sánchez, G. Fernández and N. Martín, *J. Am. Chem. Soc*. **2006**, *128*, 7172

[110] a) P. A. Denis, *New J. Chem.* **2014**, *38*, 5608; b) P. A. Denis, M. Yanney, *Chem. Phys. Lett.* **2015**, *640*, 140.

[111] a) D. González-Rodríguez, T. Torres, D. M. Guldi, J. Rivera, M. A. Herranz, L. Echegoyen, *J. Am. Chem. Soc*. **2004**, *126*, 6301; b) D. González-Rodríguez, E. Carbonell, D. M. Guldi, T. Torres, *Angew. Chem.* **2009**, *48*, 8032; c) M. Rudolf, O. Trukhina, J. Perles, L. Feng, T. Akasaka, T.Torres, D. M. Guldi, Chem. Sci. **2015**, *6*, 4141.

[112] R. Ziessel, G. Ulrich, K. J. Elliott, A. Harriman, *Chem.–Eur. J.* **2009**, *15*, 4980.

[113] I. Sánchez-Molina, C. G. Claessens, B. Grimm, D. M. Guldi, T. Torres, *Chem. Sci.* **2013**, *4*, 1338.

[114] a) S. Shimizu, S. Nakano, T. Hosoya and N. Kobayashi, *Chem.Commun*. **2011**, *47*, 316; b) D. V. Konarev, S. I. Troyanov, R. N. Lyubovskaya, *CrystEngComm* **2015**, *17*, 3923.

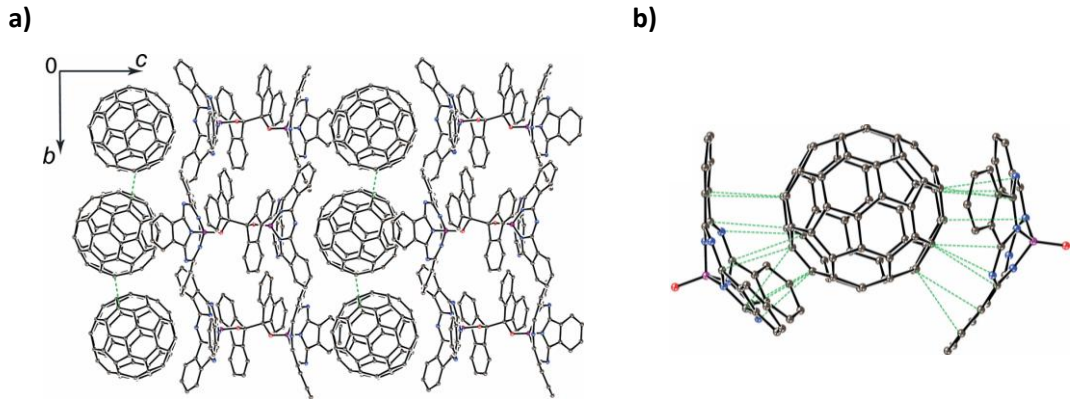

Figure 69. a) Crystal structure showing the π-π interactions between a dimeric SubPc and C_{60}. b) van der Waals contacts between SubPc fragments and C_{60}.

Tri- and hexaferrocenylSubPcs **25** and **28** meet at least two of the conditions described above to build a good fullerene receptor: the complementary concave π conjugated structure of the SubPc and the enhanced donor capability granted by the Fc moieties. First, we carried out the titrations of both ***C*$_3$-25** and **28**, adding up to 5 and 250 equivalents of C_{60} in toluene and chlorobenzene, respectively, but no isosbestic point appeared, meaning that no interaction takes place between the two molecules in the ground-state (Figure 70). Furthermore, since the SubPcs emission is completely quenched by the ferrocene units, and we cannot selectively excite the C_{60}, we could not perform reverse titrations to monitor the quenching of the fluorescence of the fullerene.

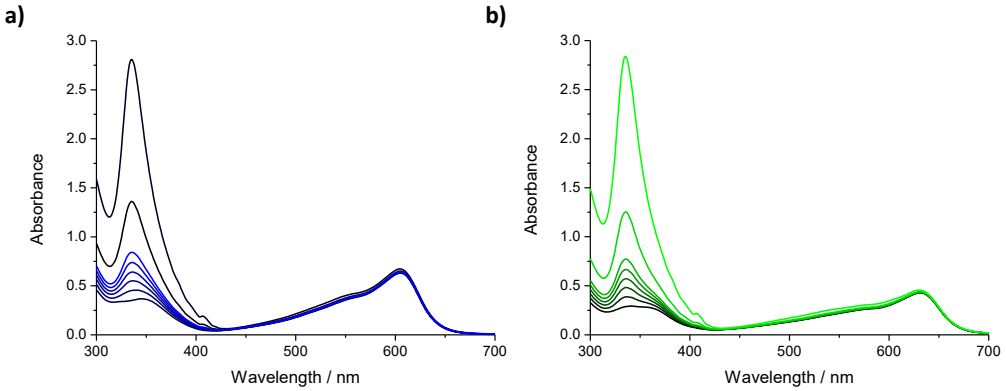

Figure 70. a) Absorption spectra of **25** (1.0×10^{-5} M) upon addition of different concentrations of C_{60} (up to 5 equivalents) in toluene. b) Absorption spectra of **28** (1.0×10^{-5} M) upon addition of different concentrations of C_{60} (up to 5 equivalents) in toluene.

We decided then to study if there was any interaction between the subphthalocyanines and the fullerenes in the solid-state. After several attempts of cocrystallization, monocrystals of SubPc **28** and C_{60} were obtained by slow diffusion of hexane in an equimolar solution of the compounds in toluene. The crystal structure is shown in Figure 71.

The X-ray structure of the SubPc/C_{60} cocrystallate show no deviation from the typical rigid cone-shaped geometry of the SubPc, characteristic of this kind of macrocycle. The B-O distance found in this work ($d_{(B\text{-}O)}$ = 1.450 Å) is similar to other B-OPh example reported ($d_{(B\text{-}O)}$ = 1.443 Å).[115] The C,N(SubPc **28**)···C(C_{60}) distances are 3.16-3.62 Å, which are shorter than those described for the system depicted in Figure 69 above (3.3-3.8 Å).[114b] This can be explained by a larger electrostatic interaction due to the stronger donor character of SubPc **28**. Besides, π-π interactions between the fullerene and the convex face of the contiguous SubPc are also observed. All the ferrocene units are situated approximately horizontal to the macrocycle except for one that is perpendicular to it. Also, one toluene molecule forms part of the crystal structure.

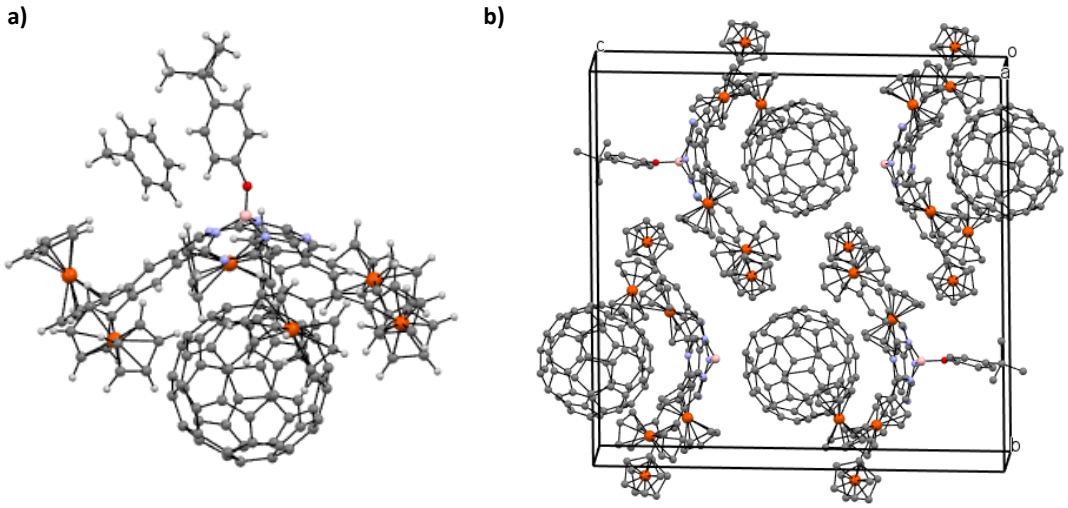

Figure 71. a) Molecular structure of the SubPc **28**-C_{60} assembly in the crystal as determined from X-ray diffraction analysis. b) View of the crystal unit cell. Hydrogens and some *t*-BuPhO groups have been omitted for the sake of clarity.

[115] A. S. Paton, G. E. Morse, A. J. Lough, T. P. Bender, *CrystEngComm* **2011**, *13*, 914

1.3.2.4 Transient absorption spectroscopic studies

Finally, in collaboration with the group of Professor Guldi in Erlangen, we studied the excited state properties of the SubPcs and the interactions between the chromophores and the fullerene unit.

The transient absorption features of the SubPc reference **32** after excitation at 530 nm infer its rapid singlet excited state formation with maxima at 430, 615, 630 and 695nm as well as minima at 510, and 566. The singlet excited state transforms into the corresponding triplet excited state, whose transient absorption spectrum maximizes at 457 and 670 nm and minimizes at 565 nm, within 1.9 ns (Figure 72).

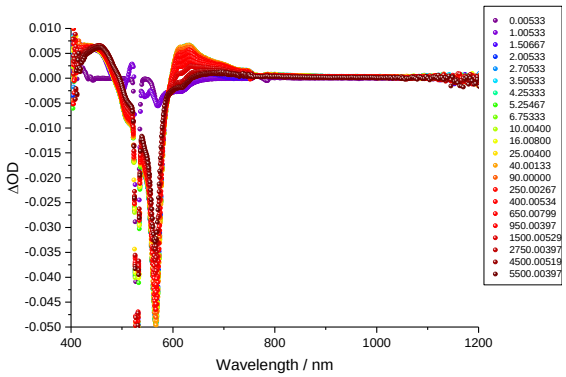

Figure 72. Transient absorption spectra of SubPc **32** in argon saturated chlorobenzene upon 530 nm photoexcitation.

Regioisomerically pure SubPcs ***C*$_1$-** and ***C*$_3$-28** presented the same behaviour but different to the reference. After photoexcitation they showed transients with maxima at 430, 580 and 660 nm accompanied by ground state bleaching around 470 and 610 nm, which corresponds to the formation of the singlet excited state. Right after, deactivation to the ground state takes place with two lifetime components (~2 and 30 ps, Figure 73).

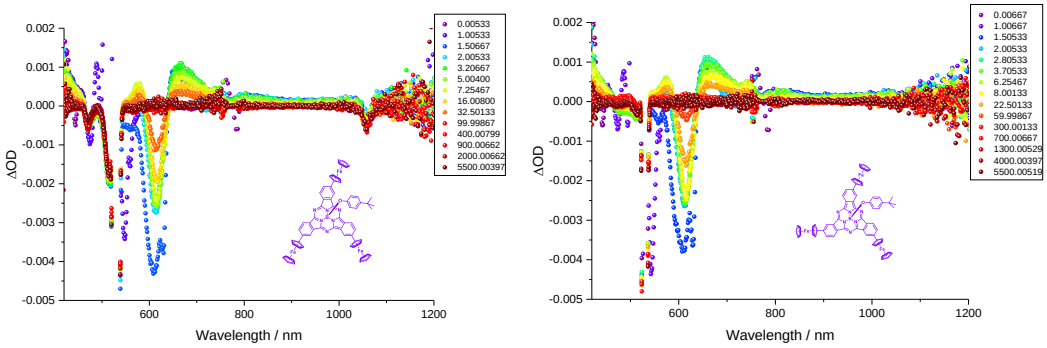

Figure 73. Transient absorption spectra of SubPcs ***C*$_1$**-(a) ***C*$_3$**-**28** (b) in argon saturated chlorobenzene upon 530 nm photoexcitation.

Hexaferrocenyl SubPc **31** showed a similar behaviour compared to the trisubstituted derivatives: instantaneously after conclusion of the laser pulse, singlet transient absorption features appeared maximizing at 430, 560, 605 and 690 nm, accompanied by ground state bleaching at ~650 nm. The excited state decays to the ground state even faster than **28** with two lifetime components (<1 and 29 ps, Figure 74).

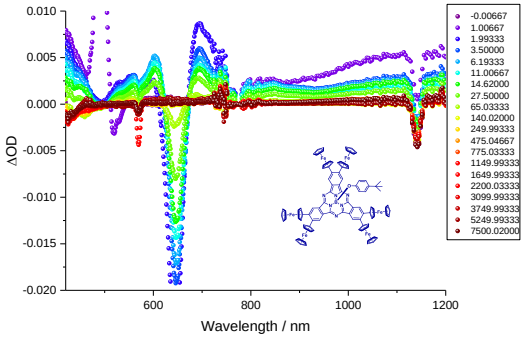

Figure 74. Transient absorption spectra of **31** in argon saturated chlorobenzene upon 568 nm photoexcitation.

Lastly, several mixtures with different proportions of SubPcs **28** and **31** with C_{60} were also measured photoexciting at the same wavelengths but no changes were found in the transient spectra obtained, which was expected after having observed such fast decays to the ground state of SubPcs **28** and **31**.

1.4 Summary and conclusions

In the first part of this Chapter, we synthesized and characterized new families of tetra- and octaferrocenyl phthalocyanines, bearing Zn(II) and Ru(II) in the central cavity of the macrocycles. The influence of the ferrocene units in the electronic properties of Pcs has been studied. Peripheral ferrocenyl substituents produce large bathochromic shifts and increase of the molar extinction coefficient of the *Q*-band. The extent of this red shift is of 8-9 nm per Fc unit. None of the FcPcs prepared showed any fluorescence emission. Contrary to what has been reported,[81] we have observed electronic communication between Fc units in the tetraferrocenylphthalocyanines despite the long distance between the two contiguous metallocenes (≥ 9 atoms separate from one another).

The ferrocenyl-substituted phthalocyanines have been assembled to perylenediimides bearing pyridyl groups at the imido positions by metal coordination to the Pc central metals. While RuPcs assemble into stable Pc-PDI complexes that were isolated, Zn complexes were assembled only in chloroform solution and showed K_a values of 8.5 x 10^2 M^{-1} ($ZnFc_4Pc$-PDI) and 6.8 x 10^3 M^{-1} ($ZnFc_8Pc$-PDI), that have been calculated through ^{1}NMR titrations. In chlorobenzene, the association constants calculated for 3 x 10^{-5} M solutions of PDI are in the order of 10^4 M^{-1} for ZnPc-PDI systems and 10^6 M^{-1} for RuPc-PDI systems, calculated by emission titrations.

FerrocenylPcs showed rapid intersystem crossing processes from the singlet to the triplet excited states within picoseconds, which deactivated to the electronic ground state within several nanoseconds. This behaviour can be explained by the presence of the ferrocene units directly linked to the macrocycle. Regarding the Pc-PDI complexes, in the case of the ZnPc-PDI-ZnPc, energy transfer processes were observed when exciting the PDI unit, while only deactivation to the ground state occurred when exciting the Pcs. On the other hand, RuPc-PDI-RuPc complexes showed, upon excitation of the PDI, a charge separation state with a lifetime of 1.2 and 2.3 nanoseconds, respectively. Although the presence of the peripheral ferrocenyl ligands increase the rates of CS by one order of magnitude, CR rates are also increased by two orders of magnitude. Therefore, no stabilization of the CSS is observed due to the peripheral Fcs.

On the second part of this Chapter, we synthesized and characterized tri- and hexaferrocenylsubstituted subphthalocyanines. Peripheral Fcs strongly interact with the SubPc π-system in the ground state, as was inferred from the large bathochromic shifts of the SubPc *Q*-bands (8-9 nm per Fc unit). Fc_3SubPc and Fc_6SubPc constitute new types of SubPc-based electron donors that form cocrystallates with C_{60}.

Transient absorption spectroscopic studies showed rapid conversion of the singlet excited state into the triplet excited state, followed by fast deactivation to the ground state due to the proximity of the Fc units, similarly to what was observed for the Pcs.

We attribute the fast deactivation of the excited states observed for Fc-Pcs and Fc-SubPcs to the direct attachment of ferrocene units to the macrocycles. As mentioned in the introduction, Fc units had been successfully used before as secondary donors in D-A assemblies, but in all the previously reported cases, metallocenes where separated from the macrocycles by some kind of linker.

1.5 Experimental section

Chemical reagents were purchased from Aldrich Chemical Co., Alfa Aesar, Acros Organics or Fluka Chemie and were used without further purification. “Synthetic grade” solvents were used for chemical reactions and column chromatography purifications and “anhydric grade” for reactions under dry conditions. Additionally, some solvents were further dried by distillation with Na/benzophenone (THF), or with previously activated molecular sieves (3 or 4 Å), or with a solvent purifying system by Innovative Technology Inc. MD-4-PS. Air- and moisture sensitive experiments were carried out using standard Schlenk line techniques.

The monitoring of the reactions has been carried out by thin layer chromatography (TLC), employing aluminium sheets coated with silica gel type 60 F254 (0.2 mm thick, E. Merck). The analysis of the TLCs was carried out with an UV lamp of 254 and 365 nm. Purification and separation of the synthesized products was performed by column chromatography, using silica gel (230-400 mesh, 0.040-0.063 mm, Merck). Eluents and relative proportions of the solvents is indicated for each particular case. Size exclusion chromatography was performed using Bio-Beads S-X1 (200-400 mesh, Bio-Rad).

Melting points (MP) were measured in open-end capillary tubes by using a Büchi 504392-S apparatus, and are uncorrected.

Nuclear magnetic resonance spectra (^{1}H NMR and ^{13}C NMR) were recorded on a Bruker AC-300 (300 MHz) or a Bruker XRD-500 (500 MHz) instruments either in the Organic Chemistry Department or in SIdI (Servicio Interdepartamental de Investigación, Interdepartmental Investigation Service). In each case, the deuterated solvent employed is indicated between brackets, and its residual peak was used to calibrate the spectra using literature reference δ ppm values.[116]

Mass spectra (MS) and high resolution spectra (HRMS) were recorded in SIdI, employing Electronic Impact (EI), Fast Atom Bombardment (FAB-MS) or Matrix Assisted Laser Desorption/Ionization-Time of Flight (MALDI-TOF), using a VG-AutoSpec spectrometer for EI and FAB-MS and a Bruker Reflex III spectrometer, with a nitrogen laser operating at 337 nm, for MALDI-TOF. The different matrixes employed are indicated for each spectrum. Mass spectrometry data are expressed in *m/z* units.

Ultraviolet and visible (UV-vis) spectra were recorded in the Organic Chemistry Department of UAM and in Friederich-Alexander University in Erlangen, employing a Hewlett-Packard 8453,

[116] G. R. Fulmer, A. J. M. Miller, N. H. Sherden, H. E. Gottlieb, A. Nudelman, B. M. Stoltz, J. E. Bercaw, K. I. Goldberg, *Organometallics* **2010**, *29*, 2176.

JASCO-V660 and Lambda 2 UV/Vis spectrophotometers. Fluorescence studies were carried out with a JASCO-V8600 and a Horiba FluoroMax3 fluorometers.

Femtosecond transient absorption studies were performed using 530 and 680 nm laser pulses (1 kHz, 150 fs pulse width) from an amplified Ti:sapphire laser system (Model CPA 2101, Clark-MXR Inc.). Nanosecond laser flash photolysis experiments were performed with 355 or 532 nm laser pulses from a Brilliant B Quantel Nd:YAG system (5 ns pulse width).

Infrared spectra were recorded in the Organic Chemistry Department on a Bruker Vector 22 spectrophotometer.

Electrochemical measurements were performed on an Autolab PGStat 30 equipment using a three electrode configuration system. The measurements were carried out using DCM solutions containing 0.1 M tetrabutylammonium hexafluorophosphate ($TBAPF_6$). A glassy carbon electrode (3 mm diameter) was used as the working electrode, and a platinum wire and an Ag/AgNO3 (in CH_3CN) electrode were employed as the counter and the reference electrodes, respectively. Ferrocene (Fc) was used as an external reference and all the potentials were given relative to the Fc/Fc^+ couple.

X-Ray diffraction spectra were done in SIdi with a Bruker KAPPA APEX II CCD goniometer with kappa geometry and Mo source (λ = 0.71073 Å). Data were collected at different temperatures, specified in each case, utilizing a system equipped with an Oxford Cryosystems dispositive. The distance between the sample and the detector is 3.5 cm. The data harvesting is done over 99% and the redundancy value is over 3. Data are corrected then with SADABS program. The intensities are calculated with SAINT program. Finally, the structures are resolved with SHELXS and refined with SHELXL.

1.5.1 Synthesis and study of new Fc-Pc-PDI assemblies for artificial photosynthesis.

1.5.1.1 Synthesis of the ferrocenyl-substituted phthalocyanines

4-Ferrocenylphthalonitrile (1)

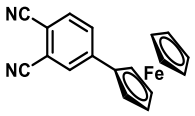

A 50 mL Schlenk flask was charged with 4-iodophthalonitrile[87a] (180 mg, 0.71 mmol), ferrocenylboronic acid (200 mg, 0.87 mmol), $Pd(dppf)Cl_2$ (55 mg, 0.067 mmol), Cs_2CO_3 (3.37 g, 10.3 mmol), toluene (12 mL) and H_2O (12 mL). The resulting solution was deoxygenated *via* three Freeze-Pump-Thaw cycles and then stirred at 100 °C for 18h under argon atmosphere. The organic phase was separated, washed with water, dried with $MgSO_4$ and then evaporated until dryness. The crude product was purified by column chromatography on silica gel (eluent: CH_2Cl_2) to afford 150 mg (68%) as an orange-reddish solid.

MP = 163.6-166.8 °C.
^{1}H-NMR (300 MHz, $CDCl_3$): δ (ppm) = 7.79 (dd, *J* = 1.8, 0.6 Hz), 7.72 (dd, *J* = 8.2, 1.8 Hz), 7.66 (dd, *J* = 8.2, 0.6 Hz), 4.72 (m, 2H) y 4.53 (m, 2H), 4.07 (s, 5H).
^{13}C-NMR (75.5 MHz, $CDCl_3$): δ (ppm) = 147.59, 133.43, 130.09, 129.44, 116.00, 115.94, 115.63, 111.34, 79.85, 71.22, 67.11, 70.17.
FT-IR (KBr): ν (cm^{-1}) = 3102.7, 3087.5, 3039.8, 2923.3, 2239.2, 2226.9, 1933.0, 1759.1, 1682.7, 1638.3, 1600.6, 1556.8, 1508.6, 1456.0, 1407.0, 1384.3, 1298.9, 1286.2, 1270.9, 1215.9, 1181.8, 1102.6, 1076.5, 1052.3, 1028.8, 1017.1, 996.9, 968.3, 916.6, 887.0, 839.8, 812.9, 801.4, 723.3, 666.5, 593.1, 551.3, 521.7, 481.8.
MS (GC-EI): *m/z* = 312.0 $[M]^+$.
HRMS: *m/z* Calcd for $[C_{18}H_{12}N_2Fe]$: 312.0350; Found: 312.0352.

4,5-Bisferrocenylphthalonitrile (2)

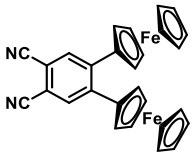

A 50 mL Schlenk flask was charged with 4,5-diiodophthalonitrile[87b] (200 mg, 0.53 mmol), ferrocenylboronic acid (200 mg, 1.22 mmol), $Pd(dppf)Cl_2$ (80 mg, 0.097 mmol), Cs_2CO_3 (5.0 g, 15.3 mmol), toluene (15 mL) and H_2O (15 mL). The resulting solution was deoxygenated *via* three Freeze-Pump-Thaw cycles and then stirred 100 °C for 18h under argon atmosphere. The organic phase was separated, washed with water, dried with $MgSO_4$ and then evaporated until dryness. The crude product was purified by column chromatography on silica gel (eluent: CH_2Cl_2) to give 224 mg (86%) as an orange-reddish solid.

MP = 203.2-205.4 °C.
^{1}H-NMR (300 MHz, $CDCl_3$): δ(ppm) = 8.08 (s, 2H), 4.29 (m, 4H) 4.17 (m, 4H), 4.05 (s, 5H).
^{13}C-NMR (75.5 MHz, $CDCl_3$): δ(ppm) = 144.3, 136.3, 116.0, 110, 83.3, 70.8, 69.0, 70.0.
FT-IR (KBr): ν (cm^{-1}) = 3086.3, 3061.5, 2922.5, 2852.2, 2573.2, 2257.5, 2227.5, 1638.2, 1589.2, 1530.8, 1499.3, 1471.1, 1412.9, 1380.9, 1322.3, 1304.6, 1266.8, 1246.1, 1205.8, 1128.3, 1106.3, 1090.8, 1065.3, 1050.2, 1031.3, 1000.9, 950.8, 928.8, 893.2, 810.7, 750.3, 729.5, 636.5, 588.1, 548.8, 508.9, 477.6, 462.1, 417.7.
MS (FAB; m-NBA): *m/z* = 496.0 $[M]^+$.
HRMS: *m/z* Calcd for $[C_{18}H_{12}N_2Fe_2]$: 496.0325; Found: 496.0338.

4,5-bisferrocenyldiiminoisoindoline (6)

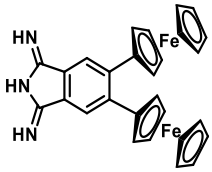

A 25 mL two-necked flask was charged with Na (8 mg, 0.34 mmol) and dry MeOH (10 mL) and the solution was stirred at room temperature under argon atmosphere until no more Na is observed. Phthalonitrile **2** was added (150 mg, 0.30 mmol) and a strong current of ammonia gas was bubbled through the solution for 10 minutes. Afterwards, the solution was refluxed for 6h, keeping a small ammonia current. The solvent was evaporated and the residue purified by column chromatography on silica gel (eluent CH_2Cl_2/MeOH 50:1 to 10:1) to yield 110 mg (72%) of **2** as a brown-reddish solid.

MP > 300 °C.
^{1}H-NMR (300 MHz, MeOD): δ(ppm) =8.33 (s, 2H), 4.29 (m, 4H) y 4.22 (m, 4H), 4.09 (s, 10H).
^{13}C-NMR (75.5 MHz, MeOD): δ(ppm) = 144.89, 132.04, 127.07, 119.26, 86.87, 71.96, 70.95, 69.65.
FT-IR (KBr), ν(cm^{-1}): 3087.5, 1766.3, 1718, 1619.2, 1537.9, 1485.3, 1451.9, 1406.7, 1326.7, 1289.2, 1248.3, 1156.6, 1105.4, 1058.7, 1029.2, 1001.4, 887.8, 819.8, 749.7, 655.6, 599.6, 530.8, 511.5, 491.8, 455.2, 428.5.
MS (MALDI-TOF, DCTB): *m/z* = 514.2 $[M+H]^+$.

[2,9(10),16(17),23(24)-tetrakis-ferrocenylphthalocyaninate]Zn(II) (3)

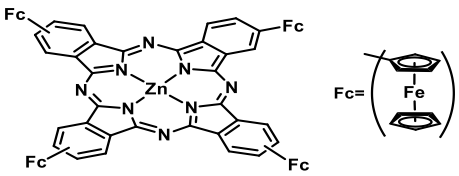

A 10 mL flask was charged with 4-ferrocenylphthalonitrile **1** (120 mg, 0.38 mmol), $Zn(OAc)_2$ (25 mg, 0.19 mmol) and DMAE (3 mL). The resulting solution was refluxed under argon atmosphere for 16h. After addition of water (15 mL), the solid was filtered and exhaustively washed with water, methanol, acetone and hexane until the washings were colorless. The compound was isolated as a dark blue solid (32 mg, 25%).

MP > 300 °C.
^{1}H-NMR (300 MHz, $C_2D_2Cl_4$): δ(ppm) = 9.22 (m-broad, 8H), 8.16 (m-broad, 4H), 4.59 (m, 8H), 4.17 (s, 28H).
FT-IR (KBr): ν(cm^{-1}) = 3092, 1767, 1728, 1607, 1512, 1485, 1404, 1337, 1310, 1269, 1188, 1134, 1107, 1053, 1026, 926, 874, 820, 752, 675, 530, 490, 424.
UV-vis ($CHCl_3$): λ_{max} (nm) (log ε (dm^3 mol^{-1} cm^{-1})) = 715 (4.89), 645 (4.34), 358 (4.76).
MS (MALDI-TOF, DCTB): *m/z* = 1308.1 $[M]^+$.
HRMS : *m/z* Calcd for $[C_{72}H_{48}Fe_4N_8Zn]$: 1308.0781; Found: 1308.0726.

2,9(10),16(17),23(24)-tetrakis-ferrocenylphthalocyanine (4)[81]

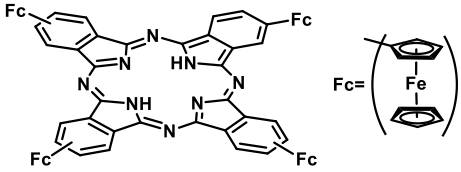

A suspension of Li (30 mg, 5 mmol) in dry pentanol (2 mL) was warmed to 145 °C and stirred until a turbid solution was observed. 4-ferrocenylphthalonitrile (**1**) (100 mg, 0.32 mmol) was then added and the mixture was heated to reflux for 16h. The solution was cooled down to room temperature and, subsequently, MeOH (10 mL) and HCl 1M (1 mL) were added. The precipitate was filtered and exhaustively washed with water, methanol, acetone and hexane until the washings were colorless. The compound was isolated as a dark blue solid (38 mg, 25%) without further purification. At this point, and due to the low solubility of the resulting compound, it could only be characterized by UV-vis spectroscopy.

UV-vis ($CHCl_3$): λ_{max} (nm) = 737, 671, 347, 297.

[Carbonyl-2,9(10),16(17),23(24)-tetrakis-ferrocenylphthalocyaninate]Ru(II) (5)

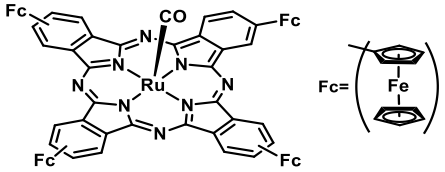

A solution of phthalocyanine **4** (35 mg, 0.028 mmol), $Ru_3(CO)_{12}$ (35 mg, 0.056 mmol) and phenol (3.3 g), was vigorously refluxed under argon atmosphere for 6h. The mixture was poured on a 1:1 solution of H_2O/MeOH (150 mL). The precipitate was filtered and exhaustively washed with water, methanol, acetone and hexane until the washings were colorless. The compound was isolated as a dark blue solid (23 mg, 60%).

MP > 300 °C.
^{1}H-NMR (300 MHz, DMSO-d_6): δ(ppm) = 9.47 (m-broad, 4H), 9.30 (m-broad, 4H), 8.43 (m-broad, 4H), 4.67 (m, 8H), 4.27 (s, 28H).
FT-IR (KBr): ν(cm^{-1}) = 3092, 3175, 2920, 2853, 2042, 1961(C=O), 1612, 1599, 1504, 1464, 1423, 1383, 1369, 1342, 1248, 1146, 1119, 1053, 1040, 1001, 881, 827, 762, 673, 530, 490, 428.
UV-vis ($CHCl_3$): λ_{max} (nm) (log ε(dm^3 mol^{-1} cm^{-1})) = 687 (4.62), 622 (4.23), 341 (4.66), 283 (4.78).
MS (MALDI-TOF, DCTB): *m/z* = 1372.0 $[M]^+$.
HRMS: *m/z* Calcd for $[C_{72}H_{48}Fe_4N_8{}^{96}Ru\ CO]$: 1372.0437; Found: 1372.0532.

[2,3,9,10,16,17,23,24-octakis-ferrocenylphthalocyaninate]Zn(II) (9)

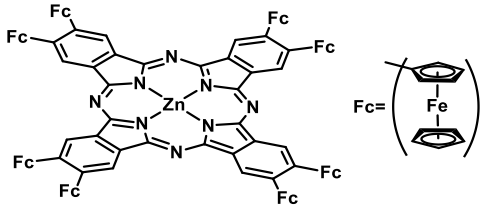

A sealed tube was charged with 4,5-bisferrocenyldiiminoisoindoline **6** (200 mg, 0.39 mmol), $Zn(OAc)_2$ (36.4 mg, 0.2 mmol), hexamethyldisilazane (250 mg, 1.55 mmol), *p*-toluenesulfonic acid (8.3 mg, 0.044 mmol) and dry DMF (0.2 mL). The resulting solution was stirred under argon atmosphere at 120 °C during 20h. The solvent was removed under reduced pressure, and the residue was suspended in MeOH and exhaustively washed with water, methanol, acetone and hexane until the washings were colorless. The residue was purified on a short pad of silica gel (eluent $CHCl_3$). The compound was isolated as a dark blue solid (16 mg, 20%).

MP > 300 °C.
^{1}H-NMR (300 MHz, $CDCl_3$): δ(ppm) = 9.95 (s, 8H), 4.60 (m, 16H), 4.38 (s, 56H).
FT-IR (KBr): ν(cm^{-1}) = 2930, 2860, 1645, 1111, 816, 473.
UV-vis ($CHCl_3$): λ_{max} (nm) (log ε(dm^3 mol^{-1} cm^{-1})) = 739 (5.12), 663 (4.50), 565 (4.05), 362 (4.90).

MS (MALDI-TOF, DCTB): *m/z* = 2044.0 $[M]^+$.
HRMS: *m/z* Calcd for $[C_{112}H_{80}Fe_8N_8Zn]$: 2044.0638; Found: 2044.0693.

2,3,9,10,16,17,23,24-octakis-ferrocenylphthalocyanine (8)

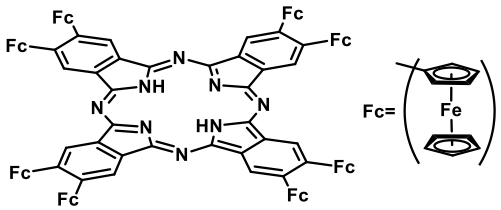

A sealed tube was charged with 4,5-bisferrocenyldiiminoisoindoline (**6**) (200 mg, 0.39 mmol), $MgCl_2$ (36.4 mg, 0.2 mmol), hexamethyldisilazane (250 mg, 1.55 mmol), *p*-toluenesulfonic acid (8.3 mg, 0.044 mmol) and dry DMF (0.2 mL). The resulting solution was stirred under argon atmosphere at 120 °C during 20h. The solvent was removed under reduced pressure and trifluoroacetic acid (5 mL) was added to the residue. The mixture was stirred for 90 min in the absence of light. Then, the green solution was poured over an ammonia solution (20 mL, 10%). The precipitate was filtered and exhaustively washed with water, methanol, acetone and hexane until the washings are colorless. The residue was purified on a short pad of silica gel (eluent $CHCl_3$). The compound was isolated as a blue-green solid (42 mg, 21%).

UV-vis ($CHCl_3$): λ_{max} (nm) = 764, 687, 405, 354.
MS (MALDI-TOF(ditranol)): *m/z* = 1982.0 $[M]^+$.

[Carbonyl-2,3,9,10,16,17,23,24-octakis-ferrocenylphthalocyaninate]Ru(II) (10)

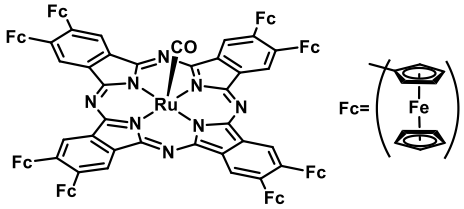

A solution of phthalocyanine **8** (25 mg, 0.012 mmol), $Ru_3(CO)_{12}$ (17 mg, 0.027 mmol) and phenol (2.3 g) was vigorously refluxed under argon atmosphere for 6h. The mixture was then poured over a solution of H_2O/MeOH 1:1 (100 mL). The solid was filtered and exhaustively washed with water, methanol, acetone and hexane until the washings are colorless. The residue was purified on a short pad of silica gel (eluent $CHCl_3$). The compound was isolated as a dark blue solid (13 mg, 51%).

MP > 300 °C.
^{1}H-NMR (300 MHz, $CDCl_3$): δ(ppm) = 9.86 (s, 8H), 4.59 (d, 16H), 4.40-4.38 (m, 56H).

FT-IR (KBr): ν(cm^{-1}) = 3088, 2961, 2926, 2856, 2359, 2347, 2058, 1963, 1626, 1497, 1416, 1404, 1393, 1358, 1300, 1242, 1196, 1122, 1095, 1001, 978, 885, 812, 762, 704, 669, 565, 503, 449.
UV-vis ($CHCl_3$): λ_{max} (nm) (log ε (dm^3 mol^{-1} cm^{-1})) = 708 (5.03), 636 (4.52), 345 (4.85), 316 (4.90).
MS (MALDI-TOF, DCTB): *m/z* = 2105.0 $[M]^+$.
HRMS: *m/z* Calcd for $[C_{112}H_{80}Fe_8N_8{}^{96}RuCO]$: 2105.0339; Found: 2105.0451.

2,9(10),16(17),23(24)-*tert*-butylphthalocyanine

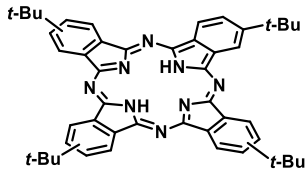

A suspension of Li (38 mg, 5.5 mmol) in dry pentanol (2 mL) was warmed to 145 °C and stirred until a turbid solution was observed. 4-*tert*butylphthalonitrile (500 mg, 2.71 mmol) was added and the mixture was heated at reflux temperature for 16h. The solution was cooled down to room temperature and, subsequently, MeOH (10 mL) and HCl 1M (1 mL) were added. The solid was filtered and exhaustively washed with water, methanol, acetone and hexane until the washings are colorless. The compound was isolated as a dark blue solid (38 mg, 25%).

^{1}H-NMR (300 MHz, DMSO): δ (ppm) = 9.41 – 9.02 (m-broad, 8H), 8.35 – 8.01 (m-broad, 4H), 1.72, 1.62, 1.59 (3 s, 36H).
UV-vis ($CHCl_3$): λ_{max} (nm) = 701, 663, 643, 602, 341.

[Carbonyl-2,9(10),16(17),23(24)-*tert*-butylphthalocyaninate]Ru(II) (20)[72]

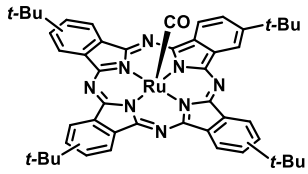

A mixture of free base tetra-*tert*-butylphthalocyanine (100 mg, 0.13 mmol), $Ru_3(CO)_{12}$ (173 mg, 0.27 mmol) and phenol (6 g) was heated at reflux temperature under argon for 8 h. The solution was allowed to cool to room temperature, and then it was dissolved in 50 mL of ethanol. After addition of water (200 mL) the resulting blue precipitate was filtered, washed with a 4:1 mixture of water and methanol, and dried. The crude was purified by column chromatography on silica gel using toluene and then chloroform as eluents. The solid was suspended in hexanes, filtered and washed with the same solvent, affording 96 mg (82%) of **20** as a deep blue solid.

^{1}H-NMR (300 MHz, DMSO): δ (ppm) = 9.41 – 9.02 (m-broad, 8H), 8.35 – 8.01 (m-broad, 4H), 1.72, 1.62, 1.59 (3 s, 36H).
UV-vis ($CHCl_3$): λ_{max} (nm) = 651, 628 (sh), 590, 344, 296.

[2,9(10),16(17),23(24)-*tert*-butylphthalocyaninate]Zn(II) (24)[97]

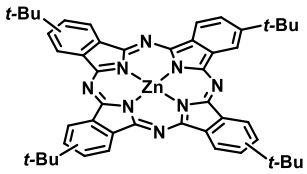

A 10 mL flask was charged with 4-*tert*-butylphthalonitrile (700 mg, 3.80 mmol), $Zn(OAc)_2$ (130 mg, 0.95 mmol) and DMAE (2 mL). The resulting solution was refluxed under argon atmosphere for 16h. After the reaction mixture was concentrated under reduced pressure, the blue solid was extracted with dichloromethane and then washed with water. Pc **24** was isolated as a dark blue solid (532 mg, 70 %).

^{1}H-NMR (300 MHz, $CDCl_3$): δ (ppm) = 9.14 – 9.06 (m, 4H), 8.90 – 8.61 (m, 4H), 8.12 – 8.01 (m- 4H), 1.92, 1.89, 1.88 (3 s, 36H).
UV-vis ($CHCl_3$): λ_{max} (nm) = 678, 650 (sh), 612, 348, 280.

1.5.1.2 Synthesis of the perylenediimide derivatives

1,6,7,12-tetrachloroperylene-3,4:9,10-tetracarboxilic dianhydride (13)[88]

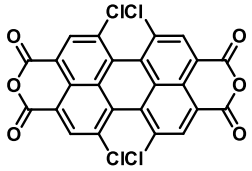

A mixture of perylene-3,4,9,10-tetracarboxylic dianhydride (3.3 g, 8.3 mmol), iodine (0.56 g, 2.2 mmol) and chlorosulphonic acid (20 mL) is stirred at 70 °C for 20h. The reaction mixture was then carefully poured over ice/water and the resulting solid was filtered. The desired product was purified by a Soxhlet extraction with $CHCl_3$ for 72h to yield **13** as a dark red solid (3.9 g, 88%). Due to its extremely low solubility, no characterization data could be obtained.

N,N'-Di(*n*-butyl)-1,6,7,12-tetrachloroperylene-3,4:9,10-bis(carboximide) (14)[89]

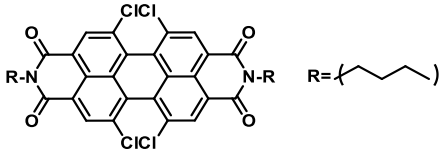

A 50 mL round bottom flask was charged with perylene **13** (1.2 g, 2.3 mmol), butylamine (1 mL, 10 mmol) and propionic acid (20 mL). The mixture was heated to reflux during 16h and it was then cooled down to RT. At this point MeOH was added (20 mL) and the precipitate was filtered.

Subsequently, it was purified by recrystallization from a CH_2Cl_2/MeOH mixture, affording **14** as a red solid (1.16 g, 80%).

^{1}H-NMR (300 MHz, $CDCl_3$): δ(ppm) = 7.26 (s, 4H), 4.08 (t, 4H), 1.63 (m, 4H), 1.37 (m, 4H), 0.93 (t, 6H).

N,N'-Di(*n*-butyl)-1,6,7,12-tetrakis(4'-*t*-butylphenoxy)perylene-3,4:9,10-bis(carboximide) (15)[89]

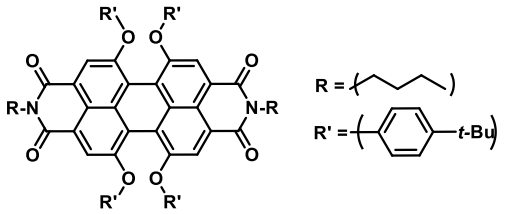

A mixture of perylenediimide **14** (1.16 g, 1.7 mmol), K_2CO_3 (1.23 g, 8.9 mmol), 4-*tert*-butylphenol (1.34 g, 8.9 mmol) and N-methylpyrrolidone (30 mL) was refluxed under Ar atmosphere for 16h. Then, water was added and the precipitate was filtered and washed with HCl 2 M (50 mL) and water. Recrystallization from a CH_2Cl_2/MeOH mixture, yielded **15** as a red solid (1.85 g, 96%).

^{1}H-NMR (300 MHz, $CDCl_3$): δ(ppm) = 8.22 (s, 4H), 7.26-7.21 (m, 8H), 6.85-6.81 (m, 8H), 4.08 (t, 4H), 1.63 (m, 4H), 1.37 (m, 4H), 1.29 (s, 36H), 0.93 (t, 6H).

1,6,7,12-tetrakis(4'-*t*-butylphenoxy)perylene-3,4:9,10-tetracarboxylic dianhydride (16)[91]

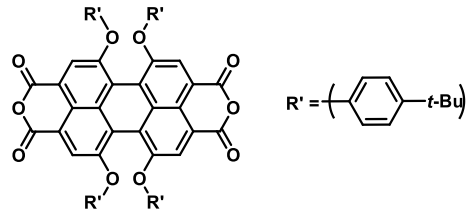

A mixture of perylenediimide **15** (1.85 g, 1.7 mmol), KOH (7.25 g, 129 mmol) and *tert*-butanol (175 mL) was heated to reflux for 12h. Afterwards, the mixture was poured over a 2% (v/v) HCl solution. The precipitate was filtered and washed with water. Then, the collected solid was dissolved in acetic acid (50 mL) and stirred at RT for 1h. Subsequently, this mixture was added to a 1M NaOH solution (30 mL), filtered and washed thoroughly with water. Recrystallization from a CH_2Cl_2/MeOH mixture, gave **16** as a red solid (1.2 g, 80%).

^{1}H-NMR (300 MHz, $CDCl_3$): δ(ppm) = 8.21 (s, 4H), 7.26-7.21 (m, 8H), 6.85-6.81 (m, 8H), 1.30 (s, 36H).

N-(4-pyridyl)-1,6,7,12-tetrakis(4'-*tert*-butylphenoxy)perylene-3,4-anhydride-9,10-carboximide (17)[91]

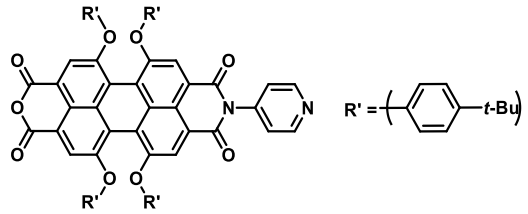

A solution of perylene **16** (224 mg, 0.22 mmol), $Zn(OAc)_2$ (14.5mg, 0.08 mmol), and 4-aminopyridine (10 mg, 0.11 mmol) in freshly distilled quinoline (20 mL) was stirred at 180 °C under Ar atmosphere overnight. Then, HCl 2M (10 mL) was added and the resulting solid was filtered and washed with HCl 2M (2 x 10 mL) and water (3 x 10 mL). The product was purified by column chromatography on silica gel (eluent CH_2Cl_2/MeOH; 50:1) to yield **17** as a red-purple solid (120 mg, 48%).

^{1}H-NMR (300 MHz, $CDCl_3$): δ (ppm) = 8.77 (m, 4H), 8.22 (s, 4H), 7.24 (m, 8H), 6.83 (m, 4H), 1.26 (d, 36H).

N-(4-pyridyl)-N'-(2,6-diisopropylphenyl)-1,6,7,12-tetrakis(4'-*t*-butylphenoxy)perylene-3,4:9,10-bis(dicarboximide) (11)[92]

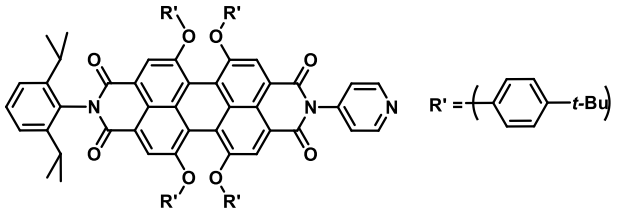

To a solution of PMI **17** (100 mg, 0.094 mmol) in refluxing propionic acid (5 mL), 2,6-diisopropylaniline (0.19 µl, 0.1 mmol) was added dropwise and the mixture was stirred for 14 h. Then, the reaction mixture was cooled down to room temperature and the solvent was evaporated under reduced pressure. The residue was extracted with $CHCl_3$ and washed with saturated $NaHCO_3$, H_2O and dried with $MgSO_4$. The product was purified by column chromatography on silica gel (eluent CH_2Cl_2 with 1% of MeOH), and then recrystallized from a CH_2Cl_2/MeOH mixture to yield **11** as a red powder (60 mg, 56% yield).

MP > 250 °C.

^{1}H-NMR (300 MHz, $CDCl_3$): δ (ppm) = 8.78 (d, 2H), 8.29 (s, 2H), 8.25 (s, 2H), 7.43 (m, 1H), 7.28-7.22 (m, 14H), 6.86 (m, 8H), 2.70 (sept, 2H), 1.27 (s, 36H), 1.12 (d, 12H).

^{13}C-NMR (75 MHz, $CDCl_3$): δ(ppm) = 163.30, 162.84, 156.23, 155.95, 152.78, 152.65, 151.00, 147.57, 147.47, 145.61, 143.17, 133.56, 133.16, 133.07, 130.65, 129.41, 126.71, 123.96, 123.88, 122.93, 121.86, 121.35, 120.39, 120.35, 120.06, 119.84, 119.31, 119.24, 34.38, 31.44, 31.42, 29.10, 24.01.
FT-IR (KBr): ν(cm^{-1}) = 3045, 2962, 2869, 1708, 1676, 1586, 1505, 1407, 1340, 1313, 1287, 1210, 1174, 1110, 1014, 961, 882, 836, 751, 557.

UV-vis ($CHCl_3$): λ_{max} (nm) (log ε (dm^3 mol^{-1} cm^{-1})) = 589 (4.50), 548 (4.27), 455 (4.05).
MS (MALDI-TOF, DCTB): *m/z* = 1219.6 $[M]^+$.

HRMS: *m/z* Calcd for $[C_{81}H_{77}N_3O_8]$: 1219.5722; Found: 1219.5705.

N,N'-Di(4-pyridyl)-1,6,7,12-tetrakis(4'-*t*-butylphenoxy)perylene-3,4:9,10-bis(dicarboximide) (12)[66a]

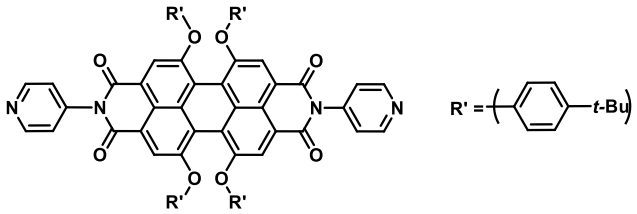

A solution of perylene **16** (560 mg, 0.56 mmol), $Zn(OAc)_2$ (36.4 mg, 0.2 mmol), and 4-aminopyridine (128.4 mg, 1.35 mmol) in freshly distilled quinoline (20 mL) was stirred at 180 °C under Ar atmosphere overnight. Then, HCl 2M (15 mL) was added and the resulting solid was filtered and washed with HCl 2M (2 x 15 mL) and water (3 x 10 mL). Afterwards, the product was purified by column chromatography on silica gel (eluent CH_2Cl_2/MeOH; 50:1) to yield **12** as a red-purple solid (440 mg, 70%).

^{1}H-NMR (300 MHz, $CDCl_3$): δ(ppm) = 8.77 (d, 2H) 8.24 (s, 4H), 7.26-7.21 (m, 10H), 6.87-6.83 (m, 8H), 1.27 (s, 36H).
UV-vis ($CHCl_3$): λ_{max} (nm) (log ε (dm^3 mol^{-1} cm^{-1})) = 593 (4.60), 550 (4.37), 458 (4.16).

1.5.1.3 Assembly of RuPc-PDI-RuPc triads

[Ru(CO)PcFc$_4$-BPyPDI-Ru(CO)PcFc$_4$] (18a)

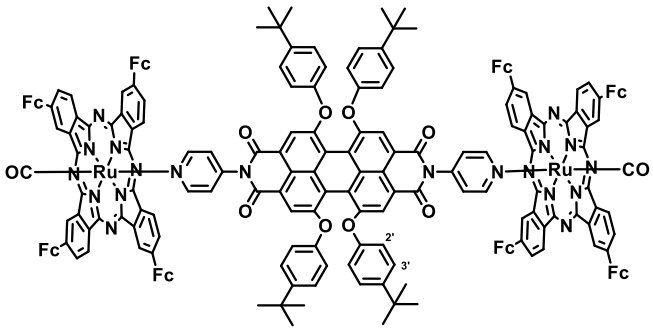

A mixture of PDI **12** (2 mg, 1.76 µmol) and Pc **5** (10 mg, 7.16 µmol) in $CHCl_3$ (2 mL) was stirred at RT protected from light. The progress of the reaction was monitored by ^{1}H-NMR until no free PDI or 1:1 complex was observed. Then, the solvent was removed under reduced pressure and the residue was purified by size-exclusion chromatography (Bio-Beads™) in toluene to yield **18a** as a blue solid (4 mg, 58%).

MP > 300 °C.
^{1}H-NMR (300 MHz, $CDCl_3$): δ(ppm) = 9.37 - 9.26 (m, 16H), 8.2 (m, 8H), 7.52 (s, 4H), 6.89 (m, 8H), 6.37 (m, 8H), 5.31 (d, 4H), 5.15 (d, 16H), 4.55 (m, 16), 4.23 (s, 40H), 2.28 (d, 2H), 1.04 (s, 36H).
DEPT 135 NMR (75.5 MHz, $CDCl_3$): δ(ppm) = 145.46, 126.89, 126.42, 123.25, 122.05, 119.65, 119.65, 119.16, 118.85, 70.05, 69.70, 67.44, 67.23, 31.24.
FT-IR (KBr): ν(cm^{-1}) = 3094, 2960, 2923, 2852, 2041, 1978, 1712, 1683, 1612, 1586, 1541, 1506, 1457, 1404, 1339, 1313, 1287, 1260, 1216, 1171, 1095, 1054, 1020, 881, 802, 761, 697.
UV-vis ($CHCl_3$): λ_{max} (logε) = 685 (5.15), 612 (4.82). 560 (4.59), 461 (4.49), 342 (5.05), 302 (5.16).

[Ru(CO)PcFc$_4$-BPyPDI-Ru(CO)PcFc$_4$] (19a)

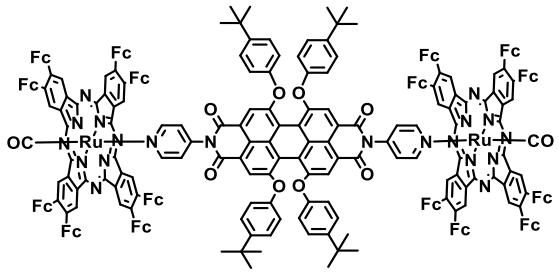

A mixture of PDI **12** (2 mg, 1.76 µmol) and RuPc **10** (16 mg, 7.16 µmol) in $CHCl_3$ (2 mL) was stirred at RT protected from light for 1h. The progress of the reaction was monitored by ^{1}H-NMR until no free PDI or 1:1 complex was observed. Then, the solvent was removed under reduced pressure and the

residue was purified by size-exclusion chromatography (Bio-Beads™) in toluene to yield **19a** as a blue solid (14 mg, 68%).

MP >300 °C.
^{1}H-NMR (300 MHz, $CDCl_3$): δ (ppm) = 9.74 (m, 16H), 8.2 (m, 8H), 7.62 (s, 4H), 6.5 (m, 8H), 6.43 (m, 8H), 5.54 (d, 4H), 4.51 (d, 32H), 4.41 (m, 32H), 4.38 (s, 80H), 2.58 (d, 2H), 1.08 (s, 36H).
DEPT 135 NMR (75.5 MHz, $CDCl_3$): δ (ppm) = 126.49, 124.96, 123.45, 123.36, 119.79, 118.91, 77.22, 71.99, 70.68, 68.37, 31.33.
FT-IR (KBr): ν (cm^{-1}) = 3092, 2957, 2926, 2863, 1967, 1711, 1680, 1597, 1502, 1400, 1340, 1291, 1201, 1170, 1127, 1077, 879, 819, 769, 578.
UV-vis ($CHCl_3$): λ_{max} (logε) = 704 (5.26), 630 (4.75), 602 (4.76), 564 (4.54), 467 (4.26), 347 (5.04), 315 (5.03).
MS (MALDI-TOF, DCTB): *m/z* = 4776.5 [M-2(CO)-4(*t*-BuPh)]$^+$.

[Ru(CO)Pc(*t*-Bu)$_4$-BPyPDI-Ru(CO)Pc(*t*-Bu)$_4$] (21a)

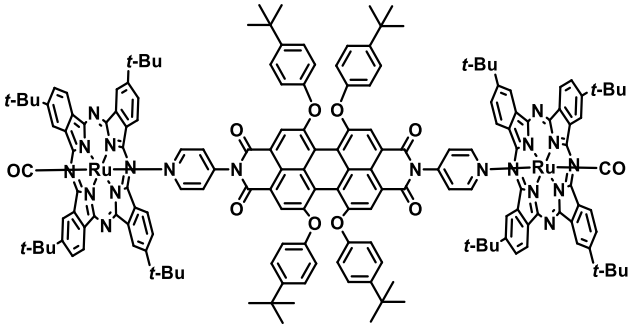

A mixture of PDI **12** (4 mg, 3.52 µmol) and RuPc **20** (6.2 mg, 7.2 µmol) in $CHCl_3$ (2 mL) was stirred at RT for 1h protected from light. The formation of the product was monitored by ^{1}H-NMR until no free PDI or 1:1 complex was observed. The solvent was removed under reduced pressure and the residue was purified by size-exclusion chromatography (Bio-Beads™) in toluene to yield **21a** as a blue solid (7.8 mg, 78%).

MP > 300 °C.
^{1}H-NMR (300 MHz, $CDCl_3$): δ (ppm) = 9.42 - 9.20 (m, 16H), 8.20 – 8.05 (m, 8H), 7.54 (s, 4H), 6.94 (m, 8H), 6.41 (m, 8H), 5.20 (d, 4H), 2.08 (d, 2H), 1.74 (br, s, 72H), 1.10 (s, 36H).
^{13}C-NMR (75.5 MHz, $CDCl_3$): δ (ppm) = 161.33, 155.77, 152.61, 152.25, 147.54, 145.40, 144.24, 142.17, 139.89, 139.80, 137.43, 132.64, 126.58, 123.19, 121.89, 121.04, 120.64, 119.80, 118.98, 118.75, 35.93, 35.89, 34.33, 32.17, 32.13, 31.39.
FT-IR (KBr): ν (cm^{-1}) = 2958, 2921, 2861, 1961, 1710, 1681, 1652, 1616, 1585, 1540, 1506, 1457, 1403, 1363, 1340, 1317, 1284, 1257, 1205, 1155, 1124, 1093, 1051, 939, 881, 831, 767, 755, 694.
UV-vis ($CHCl_3$): λ_{max} (logε) = 651 (5.41), 588 (4.90). 550 (4.47), 464 (4.15), 346 (4.77), 299 (5.17).

1.5.2.1 Synthesis of the ferrocenyl-substituted subphthalocyanines

Chloro-2,9(10),16(17)-triiodosubphthalocianinateboron(III) (26)[104]

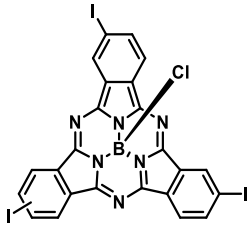

4-iodophthalonitrile[87a] (400 mg, 1.57 mmol) was placed in a round-bottom flask equipped with a reflux condenser and a magnetic stirrer under argon atmosphere. A 1 M solution of BCl_3 in *p*-xylene (0.8 mL, 0.8 mmol) was added through a syringe and the mixture refluxed for 2 h. The final purple mixture was flushed with an argon stream to remove volatiles and the solvent was evaporated under reduced pressure. The product was purified by column chromatography on silica gel (hexane / EtOAc 1:2) to afford **26** as a purple solid (272 mg, 63 %).

^{1}H-NMR (300 MHz, $CDCl_3$): δ (ppm) =9.25-9.21 (m, 3H), 8.60-8.54 (m, 3H), 8.27-8.21 (m, 3H).
UV-vis ($CHCl_3$): λ_{max} (nm) (log ε (dm^3 mol^{-1} cm^{-1})) = 570 (4.5), 520 (h), 303 (3.9), 270 (4.1).

(4-*tert*-butylphenoxy)-2,9(10),16(17)-triiodosubphthalocianinateboron(III) (27)[104]

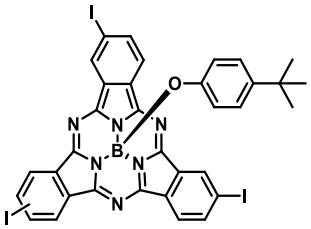

The crude of the previous reaction was dissolved in 0.75 mL of toluene and kept under argon atmosphere. A solution of 4-*tert*butylphenol (157 mg, 1 mmol) in 0.8 mL of THF and 80 µL of DBU were added, and the mixture was heated to reflux until completion. The solvent was then evaporated and the solid obtain was washed with a 1:1 water/MeOH mixture. The product was purified by column chromatography (toluene), and during the process the C_3 and C_1 regioisomers were separated. SubPc **25** was isolated as a purple solid (286 mg, 94%)

C_3-isomer

^{1}H-NMR (300 MHz, $CDCl_3$): δ (ppm) = 9.20 (s, 3H), 8.53 (d, 3H), 8.22 (d, 3H), 6.73 (m, *J* = 8.2 Hz, 2H), 5.24 (m, *J* = 8.2 Hz, 2H), 1.08 (s, 9H).

C_1-isomer

^{1}H-NMR (300 MHz, $CDCl_3$): δ (ppm) = 9.06 (d, 1H), 9.02 (s, 2H), 8.46 – 8.29 (m, 3H), 8.11 – 7.95 (m, 3H), 6.84 (m, *J* = 8.7 Hz, 2H), 5.41 (m, *J* = 8.7 Hz, 2H), 1.12 (s, 9H).

C$_3$-(4-*tert*-butylphenoxy)-2,9(10),16(17)-triferrocenesubphthalocianinateboron(III) (28)

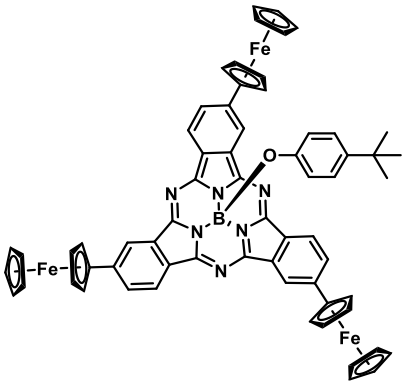

A 50 mL Schlenk flask was charged with *C*$_3$-triiodo-4-*tert*-butyloxysubphthalocyanine **27** (50 mg, 0.054 mmol), ferrocenylboronic acid (41 mg, 0.179 mmol), Pd(dppf)Cl_2 (8.2 mg, 0.01 mmol), Cs_2CO_3 (0.53 g, 1.63 mmol), toluene (4 mL) and H_2O (4 mL). The resulting solution was deoxygenated *via* three Freeze-Pump-Thaw cycles and stirred at 110 °C for 2h under argon atmosphere. The organic phase was retained, washed with brine, dried with $MgSO_4$ and then evaporated to dryness. The crude product was purified by column chromatography on silica gel (eluent: $CHCl_3$) to yield **28** as a purple solid (36 mg, 60%).

^{1}H-NMR (300 MHz, $CDCl_3$): δ (ppm) = 8.89 (s, 3H), 8.77 (d, J_o = 8.3 Hz, 3H), 8.02 (dd, J_o = 8.4, J_m = 1.5 Hz, 3H), 6.80 (d, J_o' = 8.7 Hz, 2H), 5.39 (d, J_o' = 8.7 Hz, 2H), 4.98-4.94 (d, 6H), 4.49 (s, 6H), 4.08 (s, 14H), 1.09 (s, 9H).

^{13}C-NMR (75.5 MHz, $CDCl_3$): δ (ppm) = 151.61, 151.55, 150.53, 143.50, 142.75, 131.83, 128.66, 127.91, 125.84, 122.10, 118.69, 117.72, 84.39, 70.20, 70.16, 70.09, 67.43, 67.12, 33.97, 31.49.

FT-IR (KBr): ν (cm^{-1}) = 3092.3, 2922.1, 2852.1, 2459.3, 2361.1, 2341.9, 1617.1, 1541.8, 1513.1, 1453.4, 1426.4, 1374.2, 1289.1, 1250.1, 1166.3, 1106.4, 1056.2, 940.9, 891.2, 816.9, 760.7, 733.0, 707.1, 643.9, 619.5, 448.6.

UV-vis (toluene): λ_{max} (nm) (log ε ($dm^3\ mol^{-1}\ cm^{-1}$)) = 605 (4.64), 555 (sh), 344 (4.47).

MS (MALDI-TOF, DCTB): *m/z* = 1096.2 $[M]^+$.

HRMS: *m/z* Calcd for $[C_{64}H_{49}BFe_3N_6O]$: 1096.2119; Found: 1096.2105.

(4-*tert*-butylphenoxy)-2,3,9,10,16,17-triiodosubphthalocianinateboron(III) (30)[105]

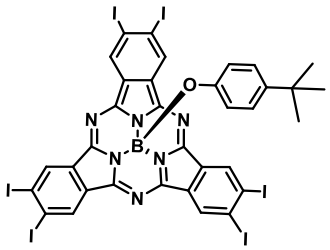

4,5-diiodophthalonitrile (785mg, 2 mmol) was placed in a round-bottom flask equipped with a reflux condenser and a magnetic stirrer under argon atmosphere. A 1 M solution of BBr_3 in DCM (0.8 mL, 0.8 mmol) was then added through a syringe and the mixture was refluxed for 2 h. The final purple mixture was flushed with an argon stream to remove volatiles and the solvent was evaporated under reduced pressure, affording SubPc **29**. Without any further purification, a solution of *tert*-butylphenol (3.1 g, 20 mmol) in a dry and degassed THF/toluene 1:1 mixture (4 mL) was added to the crude, and the reaction mixture was stirred at reflux of for 16 h. The reaction mixture was allowed to cool down to room temperature, the solvent was removed and the resulting purple solid was washed with methanol before being chromatographied on silica gel using ethyl toluene/hexane (3:2) as eluent. Subphthalocyanine **30** was collected as a purple solid (105 mg, 12% overall).

^{1}H-NMR (300 MHz, $CDCl_3$): δ (ppm) = 9.31 (s, 6H), 6.76 (m, J_o = 8.7 Hz, 2H), 5.25 (m, J_o = 8.7 Hz, 2H), 1.09 (s, 9H).

^{13}C-NMR (75.5 MHz, $CDCl_3$): δ (ppm) = 150.14, 149.31, 132.64, 130.98, 125.87, 122.95, 117.81, 109.91, 33.88, 31.29.

UV-vis (toluene): λ_{max} (nm) (log ε (dm^3 mol^{-1} cm^{-1})) = 583 (4.61), 561 (sh), 540 (4.13), 341 (4.22).

MS (MALDI-TOF, DCTB): *m/z* = 1299.6 $[M]^+$.

HRMS: *m/z* Calcd for $[C_{34}H_{19}BI_6N_6O]$: 1299.5982; Found: 1299.5978.

(4-*tert*-butylphenoxy)-2,3,9,10,16,17-triferrocenesubphthalocianinateboron(III) (31)

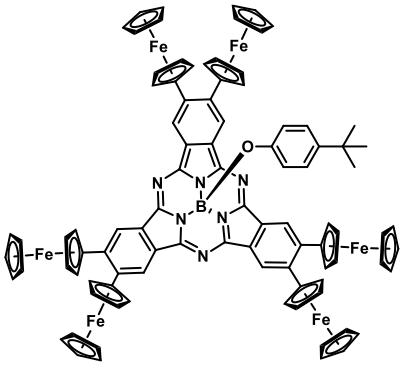

A 50 mL Schlenk flask was charged with subphthalocyanine **30** (50 mg, 0.038 mmol), ferrocenylboronic acid (58.3 mg, 0.254 mmol), $Pd(dppf)Cl_2$ (8.2 mg, 0.01 mmol), Cs_2CO_3 (0.38 g, 1.15 mmol), toluene (4 mL) and H_2O (4 mL). The resulting solution was deoxygenated *via* three Freeze-Pump-Thaw cycles and stirred at 110 °C for 2h under argon atmosphere. The organic phase was washed with brine, dried with $MgSO_4$ and then evaporated until dryness. The crude product was chromatographied on silica gel (eluent: CH_2Cl_2/Hexane; 1:1) to yield **31** as a purple solid (18 mg, 28%).

^{1}H-NMR (300 MHz, $CDCl_3$): δ (ppm) = 9.23 (s, 6H), 6.88 (d, J_o = 8.6 Hz, 2H), 5.55 (d, J_o = 8.5 Hz, 2H), 4.62 – 3.87 (m, 54H), 1.12 (s, 9H).

^{13}C-NMR (75.5 MHz, $CDCl_3$): δ (ppm) = 151.390, 140.488, 128.480, 125.786, 124.256, 117.839, 87.534, 71.360, 71.208, 69.851, 67.967, 31.403.

FT-IR (KBr): ν (cm^{-1}) = 3092.3, 2922.1, 2852.1, 2459.3, 2361.1, 1617.1, 1541.8, 1513.1, 1453.4, 1426.4, 1374.2, 1289.1, 1250.1, 1166.3, 1106.4, 1106.4, 1056.2, 940.9, 891.2, 816.9, 760.7, 733.0, 707.1, 643.9, 619.5, 448.6.

UV-vis (toluene): λ_{max} (nm) (log ε ($dm^3\ mol^{-1}\ cm^{-1}$)) = 632 (4.64), 576 (sh), 360 (sh), 341 (4.49).

MS (MALDI-TOF, DCTB): *m/z* = 1648.2 $[M]^+$.

HRMS: *m/z* Calcd for $[C_{94}H_{73}BFe_6N_6O]$: 1648.2063; Found: 1648.2017.

XRD: monocrystalls of a 1:1 SubPc **31**-C_{60} structure were obtained by slow diffusion of hexane in toluene. Crystallographic data and some refining details are summarized in the following table:

Formula	$C_{157.50}H_{77}BFe_6N_6O$
M	2415.16
Volume/ Å^3	11633.6(12)
Z	4
Density/ g cm^{-3}	1.379
Crystalline system	Monoclinic
Spatial group	P 1 21/c 1
a/ Å	18.5032(12)
b/ Å	24.5177(13)
c/ Å	26.9126(17)
α/ °	90°
β/ °	107.662(2)
γ/ °	90°
R	0.1730

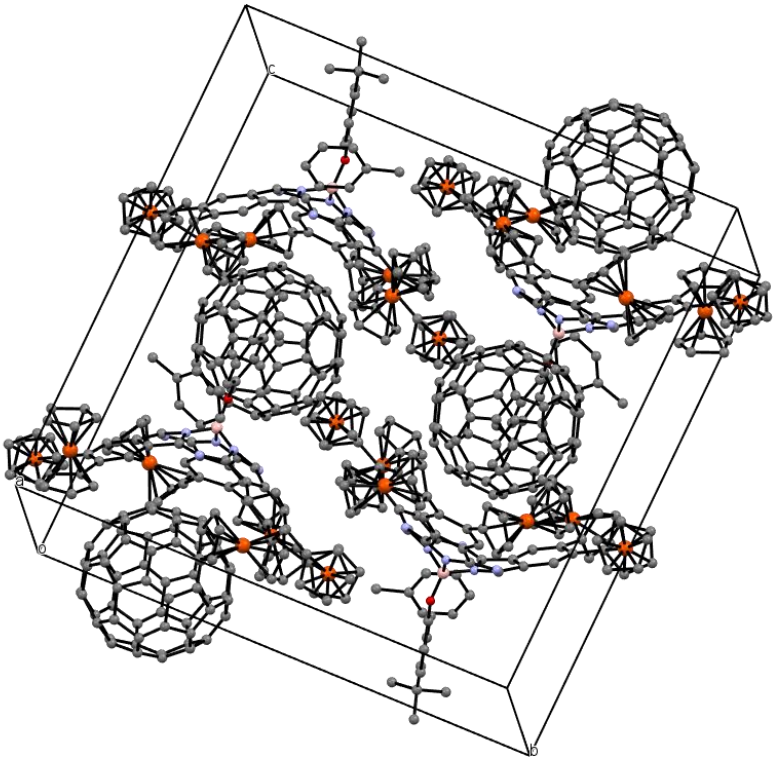

Figure 75. Unity cell and crystalline packing of 1:1 SubPc **31**-C_{60}.

Chloro-subphthalocianinateboron(III)[107]

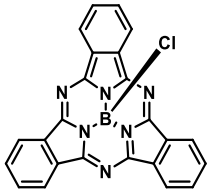

1,2-dicyanobenzene (1.28 g, 10 mmol) was placed in a round-bottom flask equipped with a refrigerant and a magnetic stirrer under argon atmosphere. A 1 M solution of BCl_3 in *p*-xylene (10 mL, 10 mmol) was then added through a syringe and the mixture was refluxed for 30 min. The final purple mixture was flushed with an argon stream to remove volatiles and hexane was added. The product was filtrated and washed exhaustively with hexane and methanol. The product wass obtained as a purple solid (830 mg, 58 %).

Phenoxy-subphthalocianinateboron(III) (32)[107]

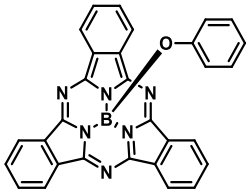

Cl-SubPc (830 mg, 1.93 mmol) obtained in the previous reaction was dissolved in 20 mL of toluene and kept under argon. A solution of phenol (1.27 g, 13.5 mmol) in 3 mL of THF was added, and the mixture was heated to reflux until completion. The solvent was evaporated and the solid obtain was washed with a 1:1 mixture of water/MeOH. The product was purified by column chromatography (toluene), affording SubPc **32** as a purple solid (848 mg, 90%).

^{1}H-NMR (300 MHz, $CDCl_3$): δ (ppm) = 8.85 (m, 6H), 7.89 (m, 8H), 6.76 (m, 2H), 6.65 (m, 1H), 5.30 (m, 2H).

Chapter 2

Design and synthesis of new porphyrazine derivatives as photosensitizers for DSSCs

2.1 Photovoltaic devices

The idea of artificial photosynthesis as a possible solution to the increasing energy demand and greenhouse gas emission problems has been developed in the previous Chapter. Throughout Chapter 2, direct light-to-electric energy conversion through solar cells will be discussed. (The record conversion efficiencies for the different technologies reported in this section are updated until December 2015).

2.1.1 Inorganic solar cells

Inspired by the use of silicon as semiconductor in the microelectronics industry, the first silicon solar cell was developed by the Bell Telephone Lab in 1954, showing an efficiency of 6%.[117] Much research followed due to the large abundance of silicon on Earth. Crystalline solar cells, either mono- or polycrystalline, are known as 1st generation solar cells. They currently dominate the photovoltaic market, with large efficiencies (over 25 % and 20 %, SunPower and Solibro, respectively) that are close to the Shockley-Queisser theoretical limit (~31 %, Figure 76).[118] Nevertheless, this type of solar cells presents an important drawback their elevated production cost. This is mainly due to the high and prolonged temperatures required to achieve large and ultrapure silicon single crystals, and it has promoted the seek for alternative, cheaper materials to use in photovoltaics.

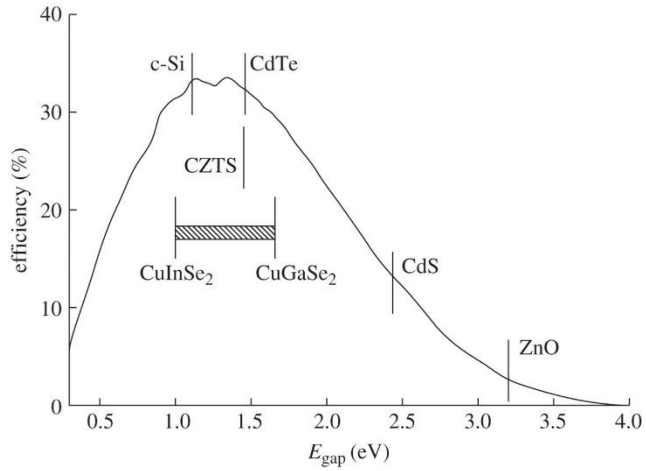

Figure 76. Maximum theoretical efficiency (Shockley–Queisser limit) for solar cells under AM1.5 illumination without concentration. Note that the bandgap of the CIGS system can be tuned by controlling the In/Ga ratio.

The second generation of solar cells is based on thin-film (≤1 μm) inorganic semiconductor materials such as cadmium telluride (21.5 %, First Solar), copper indium gallium selenide (21.7 %, ZSW) or amorphous silicon (13.6 %, AIST), appeared to overcome the high cost of silicon solar

[117] D. M. Chapin, C. S. Fuller, G. L. Pearson, *J. Appl. Phys*. **1954**, *25*, 676.
[118] W. Shockley, H. J. Queisser, *J. Appl. Phys*. **1961**, *32*, 510.

panels.[119] The main downsides of this second generation is the employment of hazardous toxic materials in the devices and the resource scarcity of the materials needed.

All this led to the third generation of photovoltaic cells, based on environmentally friendly materials that allow inexpensive solvent-based fabrication techniques. Leading examples are low-cost, thin-film solar cells based on novel concepts like hot carrier solar cells, multiple exciton generation, tandem or multijunction solar cells.[120] This generation has the aim of reducing production costs, as well as exceeding the Shockley and Queisser efficiency limit.[121]

2.1.2 Organic solar cells

Organic and hybrid solar cells, framed into the 3rd generation of solar devices, display promising characteristics as low cost, higher stability, processability and flexibility.[122] Research on organic photovoltaics started in the middle of the XX century, when simple organic dyes, like chlorophyll or magnesium phthalocyanines, were used to construct a monolayer solar cell, with reported power conversion efficiencies (PCE) not surpassing 0.1%.[123] This poor performance was attributed to the fact that excitons (localized and bound electron-hole pairs), formed upon light illumination, do not easily dissociate in most organic semiconductors, contrary to the case of inorganic derivatives.[122d,124] Hence, the main weakness of single-layer architectures was the extensive charge recombination. A milestone was achieved in 1986 when Tang used a two component, donor:acceptor active layer (planar bilayer heterojunction, PHJ, or p-n solar cell, Figure 77), consisting of a copper phthalocyanine (donor) and a perylene derivative (acceptor).[125] In this case, exciton dissociation at the heterojunction (interface) of the two molecules was favoured due to the substantially different electron affinities and ionisation potentials. Also, the separated charge transport layers ensure connectivity with the correct electrode and give the separated charge carriers only a small chance to recombine with their counterparts. A record, for the time, efficiency of 1% was reported. Nevertheless, only excitons formed very close to the interface between donor and acceptor layers are able to dissociate.

To overcome this structural problem, the concept of bulk-heterojunction (BHJ, Figure 77b) was introduced by Yu *et al.*,[126] in which a blend of a donor and an acceptor with a bicontinual phase separation is formed.[127] The advantage of this type of cell is the large interpenetrated area,

[119] a) H.W. Schock, *Appl. Surf. Sci*. **1996**, *92*, 606; b) L. M. Peter, *Phil. Trans. R. Soc. A* **2011**, *369*, 1840.
[120] M. A. Green, in *Third Generation Photovoltaics*, Springer-Verlag, Berlin, **2003**.
[121] a) M. A. Green, *Prog. Photovoltaics* **2001**, *9*, 123; b) C. A. Nelson, N. R. Monahan, X. –Y. Zhu, *Energy Environ. Sci*. **2013**, *6*, 3508
[122] a) F. G. Brunetti, R. Kumar, F. Wudl, *J. Mater. Chem*. **2010**, *20*, 2934; b) J. L. Delgado, P.-A. Bouit, S. Filippone, M. A. Herranz, N. Martin, *Chem. Comm*. **2010**, *46*, 4853; c) J. Yan, B. R. Saunders, *RSC Adv*. **2014**, *4*, 43286; d) K. A. Mazzio, C. K. Luscombe, *Chem. Soc. Rev*. **2015**, *44*, 78; e) M.-E. Ragoussi, T. Torres, *Chem. Commun*. **2015**, *51*, 3957.
[123] D. Kearns, M. J. Calvin, Chem. Phys., 1958, 29, 950.
[124] C. J. Brabec, N. S. Sariciftci, J. C. Hummelen, *Adv. Funct. Mater*. **2001**, *11*, 15.
[125] a) C. W. Tang, *Appl. Phys. Lett*. **1986**, *48*, 183; b) C. W. Tang, *US* Patent, 4, 164, 431, **1979**.
[126] G. Yu, J. Gao, J. C. Hummelen, F. Wudl, A. J. Heeger, *Science* **1995**, *270*, 1789.
[127] a) M. Hiramoto, H. Fujiwara, M. Yokoyama, *Appl. Phys. Lett*. **1991**, *58*, 1062; b) J. J. M. Halls, C. A. Walsh, N. C. Greenham, E. A. Marseglia, R. H. Friend, S. C. Moratti, A. B. Holmes, *Nature* **1995**, *376*, 498.

which results in a dramatic increase of the contact area, enhancing a more efficient charge separation.

A second approach to improve the single junction structure is called tandem solar cells (Figure 77c). The architecture of this device consists in the combination of two or more single junction cells (one on top of the other), absorbing at different wavelengths. This allows a large spectral coverage, which would be difficult to obtain with a PHJ.[128,129]

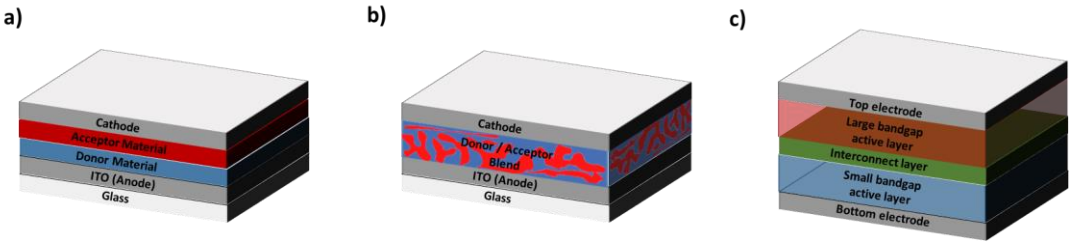

Figure 77. Schematic representation of a) PHJ solar cell; b) BHJ solar cell and c) tandem solar cell.

The configuration of a device involves a photoactive layer interposed between a modified indium tin oxide (ITO) bottom anode, and a low-work function metal cathode, such as Al, to collect holes and electrons (Figure 77). To a lesser extent, devices with an inverted structure, that is, with an ITO bottom cathode and a high-work function metal anode, have also been studied.[130]

Based on the donor photoactive material, organic solar cells can be divided in two different categories: polymer-based photoactive cells, also known as plastic solar cells;[131] and small molecule solar cells, in which discrete chromophores form the active layer.[132] For the acceptor counterpart, fullerene derivatives $PC_{61}BM$ and $PC_{71}BM$ (Figure 78) have been the most widely

[128] a) A. Hadipour, B. de Boer, P. W. M. Blom, *Adv. Funct. Mater*. **2008**, *18*, 169; b) T. Ameri, G. Dennler, C. Lungenschmied, C. J. Brabec, *Energy Environ. Sci*. **2009**, *2*, 347; c) M. Riede, C. Uhrich, J. Widmer, R. Timmreck, D. Wynands, G. Schwartz, W.-M. Gnehr, D. Hildebrandt, A. Weiss, J. Hwang, S. Sundarraj, P. Erk, M. Pfeiffer, K. Leo, *Adv. Funct. Mater*. **2011**, *21*, 3019; d) T. Ameri, N. Li, C. J. Brabec, *Energy Environ. Sci*. **2013**, *6*, 2390.

[129] a) J. Y. Kim, K. Lee, N. E. Coates, D. Moses, T.-Q. Nguyen, M. Dante, A. J. Heeger, *Science* **2007**, *317*, 222; b) S. Sista, Z. Hong, L.-M. Chen, Y. Yang, *Energy Environ. Sci*. **2011**, *4*, 1606; c) J. You, L. Dou, Z. Hong, G. Li, Y. Yang, *Prog. Polym. Sci*. **2013**, *38*, 1909; d) O. Adebanjo, B. Vaagensmith, Q. Qiao, *J. Mater. Chem. A* **2014**, *2*, 10331.

[130] T. Ameri, G. Dennler, C. Waldauf, H. Azimi, A. Seemann, K. Forberich, J. Hauch, M. Scharber, K. Hingerl and C. J. Brabec, *Adv. Funct. Mater*. **2010**, *20*, 1592.

[131] a) C. J. Brabec, N. S. Sariciftci, J. C. Hummelen, *Adv. Funct. Mat*. **2001**, *11*, 15; b) J. Peet, M. L. Senatore, A. J. Heeger, G. C. Bazan, *Adv. Mater*. **2009**, *21*, 1521; c) C. J. Brabec, S. Gowrisanker, J. J. M. Halls, D. Laird, S. Jia, S. P. Williams, *Adv. Mater*. **2010**, *22*, 3839; d) J. Peet, A. J. Heeger, G. C. Bazan, *Acc. Chem. Res*. **2009**, *42*, 1700; e) D. Gendron, M. Leclerc, *Energy Environ. Sci*. **2011**, *4*, 1225; f) L. Lu, T. Zheng, Q. Wu, A. M. Schneider, D. Zhao, L. Yu, *Chem. Rev.* **2015**, *115*, 12666.

[132] a) J. Roncali, P. Frere, P. Blanchard, R. de Bettignies, M. Turbiez, S. Roquet, P. Leriche, Y. Nicolas, *Thin Solid Films* **2006**, *511-512*, 567; b) B. Walker, C. Kim, T.-Q. Nguyen, *Chem. Mater*. **2011**, *23*, 470; c) A. Mishra, P. Bauerle, *Angew. Chem. Int. Ed*. **2012**, *51*, 2020; d) Y. Lin, Y. Li, X. Zhan, *Chem. Soc. Rev.* **2012**, *41*, 4245; e) W. Hu (ed.), Y. Lin, X. Zhan, *Organic Optoelectronics,* Wiley-VCH Verlag GmbH & Co. KGaA, Weinheim, Germany, **2013**, Chapter 18. *Organic Solar Cells Based on Small Molecules*; f) Y. Chen, X. Wan, G. Long, *Acc. Chem. Res*. **2013**, *46*, 2645; g) A. F. Eftaiha, J.-P. Sun, I. G. Hill, G. C. Welch, *J. Mater. Chem. A* **2014**, *2*, 1201; h) J. Roncali, P. Leriche, P. Blanchard, *Adv. Mater*. **2014**, *26*, 3821.

used units.[133] Furthermore, recently the indene-C_{60} bis-adduct (ICBA, Figure 78) reported by He *et al.* has been described to increase the efficiencies of the devices.[134] To overcome the scarce bandgap tunability of fullerene based acceptors, some research has also been carried out. For example, n-type organic molecules with strong absorption in the visible range and easy-to-modify structures and electronic levels, such as perylenediimides,[135] diketopyrrolopyrroles,[136] benzothiadiazoles,[137] and dicyanovinylenes[138] have been used. The performance of devices with this type of acceptors is poor (minor to 3%) except for the PDI units, that present efficiencies up to 6.1 %.[135c]

While polymeric tandem solar cells have reached a conversion efficiency of 10.6% (UCLA-Sumitomo Chem.), it is worth noting that the record in multi-junction architectures is currently held by Heliatek, which recently reported a tandem oligomer-based device with a certified power conversion efficiency of 12%. The best conversion efficiency for a single junction device has been achieved by Mitsubishi Chemical, reaching an 11.7% value.

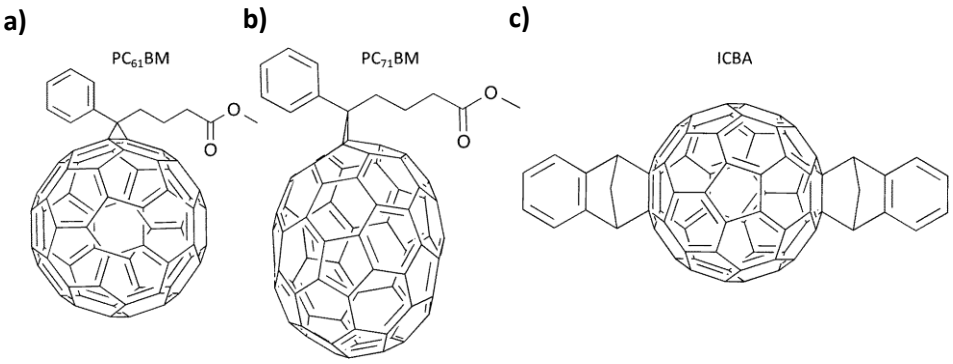

Figure 78. Structure of $PC_{61}BM$ (a), $PC_{71}BM$ (b) and ICBA (c)

[133] Y. He and Y. Li, *Phys. Chem. Chem. Phys*. **2011**, *13*, 1970.
[134] Y. He, H.-Y. Chen, J. Hou and Y. Li, *J. Am. Chem. Soc*. **2010**, *132*, 1377.
[135] a) E. Kozma, M. Catellani, *Dyes Pigments* **2013**, *98*, 160; b) Q. Yan, Y. Zhou, Y.-Q. Zheng, J. Pei, D. Zhao, *Chem. Sci*. **2013**, *4*, 4389; c) X. Zhang, C. Zhan, J. Yao, *Chem. Mater*. **2015**, *27*, 166.
[136] a) Y. Lin, Y. Li, X. Zhan, *Adv. Energy Mater*. **2013**, *3*, 724; b) H. Patil. W. X. Zu, A. Gupta, V. Chellappan, A. Bilic, P. Sonar, A. Rananaware, S. V. Bhosale, S. V. Bhosale, *Phys. Chem. Chem. Phys*. **2014**, *16*, 23837.
[137] J. T. Bloking, T. Giovenzana, A. T. Higgs, A. J. Ponec, E. T. Hoke, K. Vandewal, S. Ko, Z. Bao, A. Sellinger, M. D. McGehee, *Adv. Energy Mater*. **2014**, *4*, 1301426.
[137]a) T. Zhou, T. Jia, B. Kang, F. Li, M. Fahlman, Y. Wang, *Adv. Energy Mater*. **2011**, *1*, 431, b) Y. Fang, A. K. Pandey, A. M. Nardes, N. Kopidakis, P. L. Burn, P. Meredith, *Adv. Energy Mater*. **2013**, *3*, 54.
[138] J. You, L. Dou, K. Yoshimura, T. Kato, K. Ohya, T. Moriaty, K. Emery, C.-C. Chen, J. Gao, G. Li, Y. Yang, *Nat. Commun*. **2013**, *4*, 1446.

2.1.3 Hybrid solar cells

Organic—inorganic hybrid solar cells combine organic and inorganic particles, with the intent of incorporating the advantages associated with both material groups, *i.e.* the excellent transport properties of inorganic materials plus the high absorption coefficients and low cost processability of organic compounds, among others.[139] The appearance in the last decade of the XX century of dye-sensitized solar cells (DSSCs) meant the beginning of the development of cost-efficient devices functioning at the molecular and nanoscale levels.[140] The seminal paper by O'Regan and Grätzel in 1991[141] introduced a pioneering architecture, an n-type DSSC. In this kind of device, an organic light-absorbing dye is anchored to a mesoporous inorganic n-type semiconductor film (that operates as the photoanode) and it is filled in with a redox-active electrolyte. This type of DSSCs has shown a tremendous potential and nowadays is a real alternative to the standard silicon photovoltaics,[142] with the efficiencies growing from 7% in the seminal report,[141] using ruthenium complexes as the dye, to the current 13.0% employing porphyrins as sensitizers and eliminating the need for rare and costly, ruthenium-based sensitizers as a requirement for high efficiencies.[143] Recently, p-type DSSCs have also been explored, although they have not yet exhibited energy conversion values as high as conventional DSSCs. To date, there is just one example of comparable efficiency (2.51%).[144] Architectures and operational principles, as well as some approximation towards the optimization of DSSCs will be further analysed.

Within hybrid solar cells, quantum dot[145] and, specially, perovskite solar cells[146] (PSC) deserve a special mention. The latter stand out as promising candidates to contribute to a large scale solar energy production owing to their high efficiency (already over 20%) and compatibility with scalable processes. Perovskites have the general formula of ABX_3 (Figure 79) where A and B are monovalent and divalent ions, respectively, and X is O, C, N or a halogen.

---

[139] M. Wright, A. Uddin, *Sol. Energ. Mat. Sol. Cells* **2012**, *107*, 87.

[140] a) A. Hagfeldt, G. Boschloo, L. Sun, L. Kloo, H. Pettersson, *Chem. Rev*. **2010**, *110*, 6595; b) M. K. Nazeeruddin, E. Baranoff, M. Grätzel, *Solar Energy* **2011**, *85*, 1172; c) J. Albero, P. Atienzar, A. Corma, H. García, *Chem. Rec*. **2015**, *15*, 803.

[141] B. O'Regan, M. Grätzel, *Nature* **1991**, *353*, 737.

[142] H. S. Jung, J.-K. Lee, *J. Phys. Chem. Lett*. **2013**, *4*, 1682.

[143] S. Mathew, A. Yella, P. Gao, R. Humphry-Baker, B. F. E. Curchod, N. Ashari-Astani, I. Tavernelli, U. Rothlisberger, M. K. Nazeeruddin, M. Grätzel, *Nat. Chem*. **2014**, *6*, 242.

[144] I. R. Perera, T. Daeneke, S. Makuta, Z. Yu, Y. Tachibana, A. Mishra, P. Bauerle, C. A. Ohlin, U. Bach, L. Spiccia, *Angew. Chem. Int. Ed*. **2015**, *54*, 3758.

[145] a) M. A. Halim, *Nanomaterials* **2013**, *3*, 22; b) M. R. Kim, D. Ma, *J. Phys. Chem. Lett*. **2015**, *6*, 85.

[146] a) H. J. Snaith, *J. Phys. Chem. Lett*. **2013**, *4*, 3623; b) M. A. Loi, J. C. Hummelen, *Nat. Mater*. **2013**, *12*, 1087; c) S. Kazim, M. K. Nazeeruddin, M. Grätzel, S. Ahmad, *Angew. Chem. Int. Ed*. **2014**, *53*, 2812; d) M. He, D. Zheng, M. Wang, C. Lin, Z. Lin, *J. Mater. Chem. A* **2014**, *2*, 5994; e) P. Gao, M. Grätzel, M. K. Nazeeruddin, *Energy Environ. Sci.* **2014**, *7*, 2448; f) M. A. Green, A. Ho- Baillie, H. J. Snaith, *Nature Photon*. **2014**, *8*, 506; g) H.-S. Kim, S. H. Im, N.-G. Park, *J. Phys. Chem. C* **2014**, *118*, 5615; h) G. Giorgi, K. Yamashita, *J. Mater. Chem. A* **2015**, *3*, 8981; i) W.-J. Yin, J.-H. Yang, J. Kang, Y. Yan, S.-H. Wei, *J. Mater. Chem. A* **2015**, *3*, 8926.

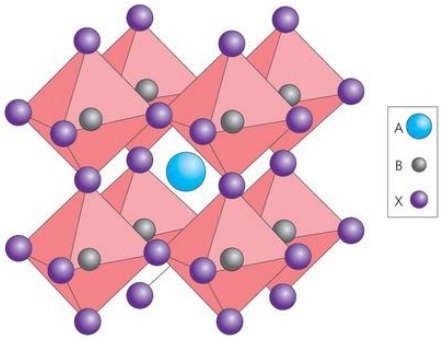

Figure 79. Cubic perovskite crystal structure. For photovoltaically interesting perovskites, the large cation A is usually the methylammonium ion (CH_3NH_3), the small cation B is Pb and the anion X is a halogen ion.

The field of perovskite-sensitized solar cells has grown exponentially since the first work about perovskite-sensitized solar cells. It was published in 2009 by Miyasaka and co-workers and a power conversion efficiency (PCE) of 3.81% was reported for the device employing $CH_3NH_3PbI_3$ as absorber and an iodide-based liquid electrolyte.[147] In 2012, Kim *et al.* substituted the liquid electrolyte with a solid-state hole transporting material, *spiro*-MEOTAD, obtaining a PCE of 9.7%.[148] One year later, a new sequential deposition method reported by Burschka *et al.* which permits a better control over the morphology raised the PCE up to 15%, beating already the best DSSC at the time (YD2-oC8, 12%).[149] Current progress in the area focuses mainly on the morphology optimization (thickness and homogeneity),[149] broadening the absorption and improving the stability.[150] The current record of PSC stands now at 20.1% (KRICT). Despite their indisputable leadership in terms of high-efficiency and low-cost production, PSC present two important drawbacks. The first one is environmental related, and is due to the toxicity of lead. The second one is the short-term stability due to high moisture-sensitivity of perovskites.

To sum up, Figure 80 shows a chart developed by the U.S. National Renewable Energy Laboratories that displays the evolution of the efficiencies of the different inorganic, organic and hybrid photovoltaic devices.

[147] A. Kojima, K. Teshima, Y. Shirai, T. Miyasaka, *J. Am. Chem. Soc*. **2009**, *131*, 6050.
[148] H.-S. Kim, C.-R. Lee, J.-H. Im, K.-B. Lee, T. Moehl, A. Marchioro, S.-J. Moon, R. Humphry-Baker, J.-H. Yum, J. E. Moser, M. Grätzel, N.-G. Park, *Sci Rep.* **2012**, *2*, 591.
[149] J. Burschka, N. Pellet, S.-J. Moon, R. Humphry-Baker, P. Gao, M. K. Nazeeruddin, M. Grätzel, *Nature* **2013**, *499*, 316.
[150] G. E. Eperon, S. D. Stranks, C. Menelaou, M. B. Johnston, L. M. Herz, H. J. Snaith, *Energy Environ. Sci*. **2014**, *7*, 982.

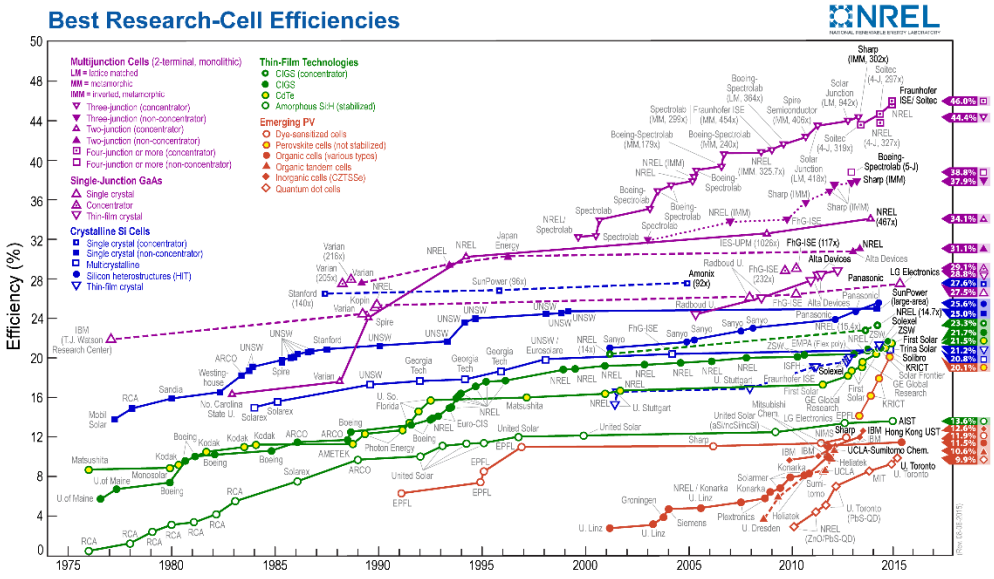

Figure 80. Efficiency of photovoltaic devices updated to December 2015.

2.1.4 Characteristic parameters of solar cells

The properties of photovoltaic devices can be characterized by plotting the measured current density output *J* of the cell versus the voltage output *V* of the cell (*J*-*V* graph, Figure 81). In the dark, this *J*-*V* curve passes through the origin, since at that moment no current is flowing through the device and no potential is present. By exposing the photovoltaic device to light, the *J*-*V* curve shifts downwards. The most important characteristic parameters of photovoltaic devices can be found on this *J*-*V* curve.

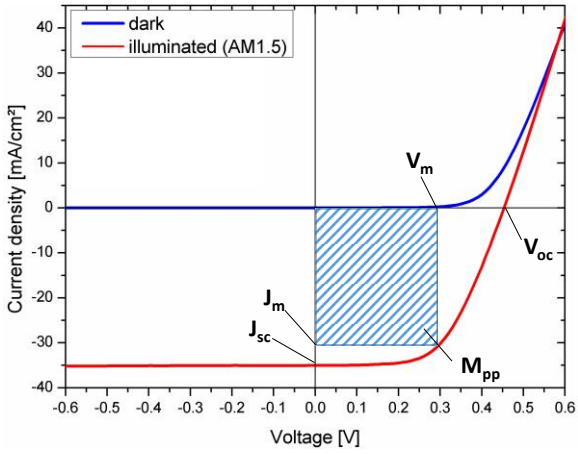

Figure 81. Typical *J*-*V* curve for any type of solar cell in the dark and under illumination (the most important photovoltaic parameters are indicated).

Open-circuit voltage (V_{OC}): It is the maximum possible voltage across a photovoltaic device. This is the voltage across the cell, under sunlight, when no current is flowing through the device. It is mainly defined by the difference in voltage between the Fermi level of the semiconductor and the reduction potential of the electrolyte redox pair.

Short-circuit current (I_{SC}): It is the current that flows through an illuminated solar cell when there is no external resistance *i.e.* when the electrodes are simply connected or short-circuited. I_{SC} is the maximum current that a photovoltaic device is able to produce. Under an external load, the current will always be less than I_{SC}. The short-circuit current depends on a number of factors, such as the area of the solar cell. To remove the dependence of the solar cell area, it is more common to list the short-circuit current density (J_{SC} in mA/cm^2), rather than the short circuit current (I_{SC} in mA).

Maximum power point (M_{pp}): It is the point (V_m, J_m) on the *J-V* curve at which the maximum power is produced. Power is the product of current I and voltage *V*. This is represented in Figure 26 as the area of the rectangle formed between a point on the *J-V* curve and the axes *J* and *V*. The maximum power point is that point on the I-V curve at which the area of the resulting rectangle, *J* x *V*, is largest.

Fill Factor (FF): It is the ratio of its actual maximum power output to its theoretical power output, if current and voltage would be at their maxima, J_{SC} and V_{OC}, respectively. This is a very important property used to measure photovoltaic device performance. It is a measure of the 'squareness' of the *J-V* curve. FF can be written down as follows:

$$FF = \frac{J_m \times V_m}{J_{sc} \times V_{oc}} \qquad \text{(Eqn. } \mathbf{19}\text{)}$$

Power Conversion Efficiency (PCE or η): It is the ratio of power output (P_{out}), to power input (P_{in}). PCE measures the amount of power produced by a photovoltaic device relative to the power available in the incident solar radiation. P_{in} is the sum over all wavelengths, which usually has a value of 100 mW/cm^2 when solar simulators are used. This is the most general way to define the efficiency of a photovoltaic device. PCE can be written down as follows:

$$PCE\ (\eta) = \frac{P_{out}}{P_{in}} = \frac{J_m \times V_m}{P_{in}} = \frac{J_{sc} \times V_{oc} \times FF}{P_{in}} \qquad \text{(Eqn. } \mathbf{20}\text{)}$$

PCE is one of the most important parameters to characterize solar cell performances. In order to compare results from various devices, regardless of the design and active material, photovoltaic cells are all subjected to the same standard test conditions.

The cells are typically illuminated at a constant density of roughly 100 mW/cm^2, which is defined as the standard '1 Sun' value, with a spectrum consistent to an air-mass global value of 1.5 (AM 1.5G), at a temperature of 25 ^{o}C. Air mass describes the spectrum of radiation and can be defined as the amount of atmosphere though which sunlight has to travel to reach the Earth's surface. This is abbreviated as AM x, in which x is the inverse of the cosine of the zenith angle of

the sun. The above mentioned AM1.5G conditions correspond to the spectrum and irradiance of sunlight incident with a zenith angle of 48.2° (Figure 82).

External Quantum Efficiency (EQE): Also known as Incident Photon to Current Efficiency (IPCE), is another important parameter for solar cell characterization. It is calculated by the number of electrons extracted in an external circuit divided by the number of incident photons at a certain wavelength under short-circuit condition. EQE can be written down as follows:

$$EQE\ (\lambda) = \frac{number\ of\ electrons}{number\ of\ incident\ photons} = \frac{J_{sc}\ (\lambda)/e}{P_{in}(\lambda)/(\frac{hc}{\lambda})} = \frac{J_{sc}\ (\lambda)\times hc}{P_{in}(\lambda)\times e\lambda} \qquad \text{(Eqn. 21)}$$

Where λ is the wavelength, e is the elementary charge, h is the Planck constant, and c is the speed of light in vacuum.

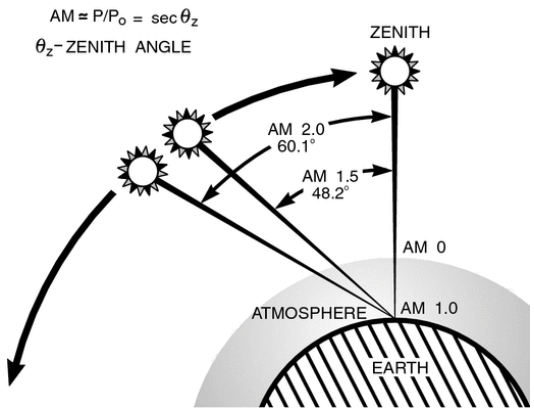

Figure 82. The air-mass value AM 0 equates to insolation at sea level with the Sun at its zenith.AM 1.0 represents sunlight with the Sun at zenith above the Earth's atmosphere. AM 1.5 is the same, but with the Sun at an oblique angle of 48.2°, which simulates a longer optical path through the Earth's atmosphere; AM 2.0 extends that oblique angle to 60.1°.

2.2 Dye sensitized solar cells

Nowadays, dye-sensitized solar cells offer a lower-cost alternative to silicon photovoltaics because they are based on cheap materials and inexpensive manufacturing technology. A dye-sensitized solar cell can be generally described as a photoelectrochemical cell where the working electrode consists of photon-absorbing dyes (sensitizers) anchored onto mesoporous surfaces of semiconducting nanoparticles.

Although at the present time, DSSCs have not reached efficiencies as high as silicon-based cells under standard conditions (1 sun, AM1.5G), they usually over perform by far under low-light intensities (0.1 sun), achieving similar or even higher efficiencies under these conditions. ***This constitutes a first great advantage for practical indoor application and during cloudy days***. Moreover, the possibility of designing devices with large and flexible shapes, colours and transparency, enables a wide range of commercial opportunities.

2.2.1 Structure and Operational Principle of Dye-Sensitized Solar Cells

The typical DSSC structure consists of the following elements: (a) a transparent glass sheet covered with a conductive fluorine-doped tin oxide (FTO, Figure 83) layer is used as anode substrate which allows light to pass through and electron transport; (b) a mesoporous oxide layer[151] deposited on the substrate to transfer electrons, composing with the FTO glass the photoanode; (c) a monomolecular layer of dye adsorbed on the surface of the mesoporous oxide layer to harvest incident sunlight, (d) a liquid or solid redox electrolyte[152] (usually a volatile organic solvent containing a redox mediator, such as iodide/triiodide couple) to regenerate the dye; (e) a counter electrode (cathode) made of an ITO or FTO conductive glass sheet coated with a catalyst (typically, Pt) to catalyse the redox couple regeneration reaction and collect electrons from the external circuit. A schematic representation, as well as the main processes occurring in a DSSC are shown in Figure 83.

[151] a) R. Jose, V. Thavasi, S. Ramakrishna, *J. Am. Ceram. Soc*. **2009**, *92*, 289; b) N. Sharifi, F. Tajabadi, N. Taghavinia, *ChemPhysChem* **2014**, *15*, 3902.
[152] J. Wu, Z. Lan, J. Lin, M. Huang, Y. Huang, L. Fan, G. Luo, *Chem. Rev*. **2015**, *115*, 2136.

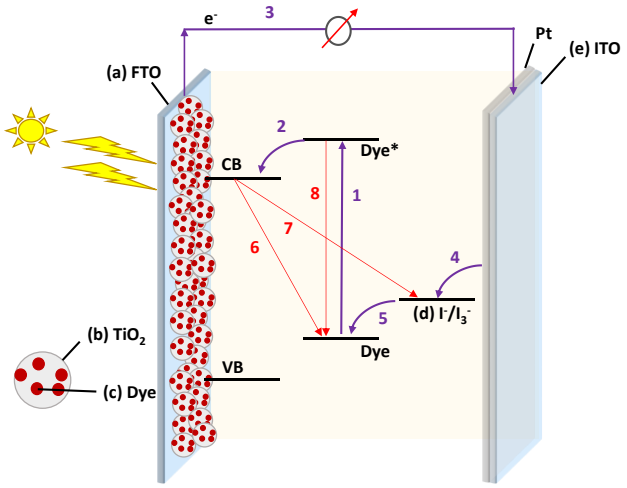

Figure 83. Schematic representation and main processes occurring in a DSSC.

Upon illumination, a photosensitizer molecule absorbs a photon and promotes an electron from its ground state to the excited state (process 1, Figure 83). This electron is subsequently injected into the conduction band (CB) of the semiconductor (process 2, Figure 83). The injected electrons diffuse through the photoanode and arrive at the back contact and then flow through an external circuit to reach the counter electrode (process 3, Figure 83). At the counter electrode, the electrons are transferred to the oxidized shuttle present in the electrolyte (regeneration of the oxidized shuttle: process 4, Figure 83). The most commonly used electrolyte contains the I^-/I_3^- redox couple. The oxidized dye is finally regenerated to its neutral form by the action of the redox couple of the electrolyte (process 5, Figure 83).

Some undesirable phenomena that affect its efficiency take place in the solar cell. These are the recombination of the injected electrons in the titanium oxide either with the oxidized dye (process 6, Figure 83), or with the redox couple (also known as dark current, process 7, Figure 83). Alternatively, the excited dye may also relax to its ground state by a non-radiative decay process (process 8 in Figure 83).

The processes taking place in the photovoltaic cell can be resumed as:

- Photoexcitation (process 1): Dye + $h\nu$ → Dye*
- Electron injection (process 2): Dye* → $Dye^+ + e^-_{TiO2}$
- Electrolyte regeneration (process 4): $I_3^- + 2\ e^-_{Pt} \rightarrow 3I^-$
- Dye regeneration (process 5): $3I^- + 2Dye^+ \rightarrow I_3^- + Dye$
- Back electron transfer (process 6): $e^-_{TiO2} + Dye^+ \rightarrow Dye$
- Electron recombination with the redox couple (process 7): $I_3^- + 2\ e^-_{TiO2} \rightarrow 3I^-$
- Dye excited state deactivation (process 8): Dye* → Dye

The recombination processes do not play a remarkable negative effect owing to their slower reactions ratio compared to the forward reactions (See Figure 84).[140,153]

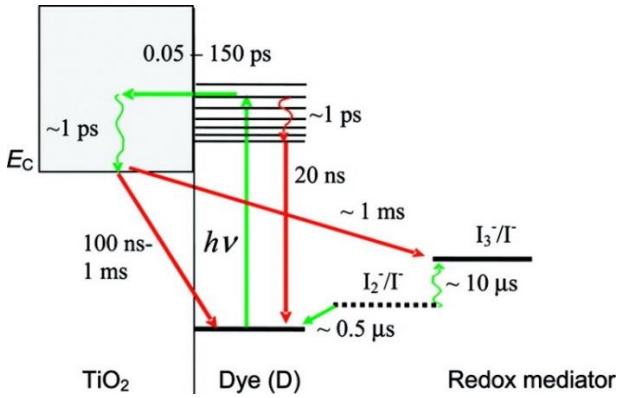

Figure 84. Kinetics of the *cis*-Ru(dcbpy)$_2$(NCS)$_2$-sensitized TiO_2 solar cell with I^-/I_3^- redox mediator. Typical time constants of the forward reactions (green) and recombination reactions (red) are indicated.[153c]

In order to optimize the performance of the DSSC, research focuses on tailoring the physicochemical properties of the components of the cell.[154]

2.2.2 Fundamental components of DSSCs

DSSCs are composed of multiple components, and their overall efficiency depends strongly on the individual properties of each constituent. Much effort has been spent on the optimisation of the materials used in the fabrication of solar cells, such as the semiconductor metal oxide, the photosensitizer, the electrolyte and the electrodes.

2.2.2.1 Electrodes

As it was mentioned before, the photoanode is composed of a mesoporous semiconductor attached to a transparent conductive oxide (TCO) coated with a thin layer of a transparent conductive material. In this type of devices, the most commonly used conductive material is FTO. In other devices, the material used is ITO that presents higher conductivities. However, thermal treatment to optimize the TiO_2 structure implies temperatures as high as 500 ^oC during the fabrication of photoanode, upon which ITO is unstable and hence strongly increases the resistance of the material. Furthermore, as indium is a scarce element, ITO is a more expensive material. Thus, FTO is nowadays preferred to ITO to fabricate DSSC devices.

[153] a) M. Grätzel, *Acc. Chem. Res*. **2009**, *42*, 1788; b) S. Ardo, G. J. Meyer, *Chem. Soc. Rev*. **2009**, *38*, 115; c) G. Boschloo, A. Hagfeldt, *Acc. Chem. Res*. **2009**, *42*, 1819.
[154] a) B. E. Hardin, H. J. Snaith and M. D. McGehee, *Nat. Photonics* **2012**, *6*, 162; b) V. Sugathan, E. John, K. Sudhakar, *Renew. Sust. Energ. Rev.* **2015**, *52*, 54.

The nanocrystalline semiconductor is one of the components that has been most widely studied.[154b] Anatase TiO_2 based photoanode is the most commonly used in DSSC, [155] as it is a stable, cheap and non-toxic oxide. However, it presents some limitations due to the presence of large number of grain boundaries that lead to electron recombination losses, and it also fails to achieve good efficiency in near infrared region. A number of other oxides, such as ZnO,[156] SnO_2,[157] and Nb_2O_5,[158] have been tested as alternatives, but TiO_2 has overall given by far the highest efficiencies, which is why it is still the most commonly used metal semiconductor. The use of 1D- and well-ordered TiO_2-nanomaterials[159] as photoanodes, such as nanowires,[160] nanorods,[161] nanotubes,[162] or nanobelt,[163] has received great attention since their apparition to reduce the recombination in the TiO_2/electrolyte interface.

The main inconvenient found for the platinum the counter electrode is its high cost due to the value of platinum. In order to reduce the device cost, the amount of Pt used is decreased by using various platinum composite materials. On the other hand, free-platinum conductive materials, such as carbon-based materials,[164] polymers[165] and other inorganic transition metal compounds[166] are being studied.

2.2.2.2 Electrolyte

The electrolyte is one of the most important components of DSSCs,[167] as it is responsible of charge carrier transport between electrodes and continuous regeneration of the dye and itself during DSSC operation. The efficiency of the device is determined by J_{sc}, V_{oc} and FF, and all three can be affected by the electrolyte.[152] For example, J_{sc} can be affected by the transport of the redox couple in the electrolyte. Furthermore, the diffusion of the charge carrier can affect the FF, and V_{oc} can be influenced by the redox potential of the electrolyte.

---

[155] a) P. M. Sommeling, B. C. O'Regan, R. R. Haswell, H. J. P. Smit, N. J. Bakker, J. J. T. Smits, J. M. Kroon, J. A. M. van Roosmalen, *J. Phys. Chem. B* **2006**, *110*, 19191; b) J. M. Kroon, N. J. Bakker, H. J. P. Smit, P. Liska, K. R. Thampi, P. Wang, S. M. Zakeeruddin, M. Grätzel, A. Hinsch, S. Hore, U. Wurfel, R. Sastrawan, J. R. Durrant, E. Palomares, H. Pettersson, T. Gruszecki, J. Walter, K. Skupien, G. E. Tulloch, *Prog. Photovoltaics* **2007**, *15*, 1.

[156] K. Keis, E. Magnusson, H. Lindstrom, S.-E. Lindquist, A. Hagfeldt, *Sol. Energy Mater. Sol.Cells* **2002**, *73*, 51; b) K. Keis, C. Bauer, G. Boschloo, A. Hagfeldt, K. Westermark, H. Rensmo, H. Siegbahn, *J. Photochem. Photobiol. A* **2002**, *148*, 57; c) Q. Zhang, C. S. Dandeneau, X. Zhou and G. Cao, *Adv. Mater*. **2009**, *21*, 4087.

[157] S. Ferrere, A. Zaban and B. A. Gregg, *J. Phys. Chem. B*, **1997**, *101*, 4490.

[158] P. Guo and M. A. Aegerter*, Thin Solid Films*, 1999, 290.

[159] Y. Bai, I. Mora-Sero, J. Nabiullun, F. De Angelis, J. Bisquert, P. Wang, *Chem. Rev.* **2014**, *114*, 10095.

[160] D. Jiang, Y. Hao, Y. Shen, S. Ghazarian, A. Ramos, F. Zhou, *ACS Appl. Mater. Interfaces* **2013**, *5*, 11906.

[161] W. Guo, C. Xu, X. Wang, S. Wang, C. Pan, C. Lin, Z. L. Wang, *J. Am. Chem. Soc.* **2012**, *134*, 4437.

[162] Q. Zheng, H. Kang, J. Yun, J. Lee, J. H. Park, S. Baik, *ACS Nano* **2011**, *5*, 5088.

[163] X. Wang, Z. Li, J. Shi, Y. Yu, *Chem. Rev.* **2014**,*114*, 9346.

[164] S. Ahmad, E. Guillen, L. Kavan, M. Grätzel, M. Nazeeruddin, *Energy Environ. Sci*. **2013**, *6*, 3439

[165] J. Wu, Q. Li, L. Fan, Z. Lan, P. Li, J. Lin, S. J. Hao, *Power Sources* **2008**, *181*, 172.

[166] G. Wang, D. Wang, S. Kuang, S. J. Zhuo, *Inorg. Mater*. **2013**, *28*, 907.

[167]L. Goncalves, V. Bermudez, H. Ribeiroa, A. Mendes, *Energy Environ. Sci.* **2008**, *1*, 655.

A suitable electrolyte must present several characteristics:

- It must provide good contact between the working and counter electrodes.
- It must be able to permit fast charge transport between the electrodes.
- Its redox potential must allow efficient and rapid dye regeneration to its ground state after electron injection into the CB.
- The electrolyte should neither degrade nor desorb the photosensitizer from the metal oxide surface.
- It should also be thermal, optical, chemical and electrochemically stable.

A large number of redox mediators and electrolyte systems have been explored, including I_3^-/I^- in either liquid or solid polymer,[168] gel,[169] ionic liquid[170] or plastic crystal[171] systems, solid inorganic materials,[172] Co(III)/Co(II),[171] $(SeCN)^{3-}/(SeCN)^-$ redox couples,[170] hole-conducting organic polymers[173] and small organic molecules.[174] To date, the best performances have been obtained with I_3^-/I^- and the Co(III)/Co(II) redox couples, being the latter the one utilized in the record DSSC with porphyrin SM315 as dye.[143] The main advantage that cobalt-based electrolyte presents is that its reduction potential lies lower than that of the iodide pair, and therefore, higher V_{oc} values can be obtained.[154] Nonetheless, cobalt electrolytes present recombination rates 10 times higher than the iodide electrolytes.

Liquid electrolytes have been the most widely used. Here, the redox pair is usually dissolved in organic solvents with high dielectric constants, such as acetonitrile, *N*-methylpyrrolidine and valeronitrile, or a combination of these solvents. Typically, iodine-based electrolytes are composed of iodine and lithium iodide, and others additives (*vide infra*) in AcCN,[175] which is considered the best electrolyte solvent for fundamental studies due to its low viscosity, good solubility, and excellent chemical stability (electrochemical window > 4V).[176] On the other hand, since Papageorgiou *et al.* first report in 1996, ionic liquids have also been widely utilized in DSSCs,[177] and that is due to their unique properties, such as chemical and thermal stability, tuneable viscosity, relative non-flammability, high ionic conductivity and broad electrochemical potential window, and more importantly, extremely low vapour pressure making less evaporation and leakage.[178] Nevertheless, the relatively high viscosity and low ion mobility of

[168] M.-S. Kang, J. H. Kim, J. Won, N.-G. Park, N.-G.; S. Kang, *Chem. Commun*. **2005**, 889.
[169] P. Wang, S. M. Zakeeruddin, J. E. Moser, M. K. Nazeeruddin, T. Sekiguchi, M. Grätzel, *Nat. Mater*. **2003**, *2*, 402.
[170] P. Wang, S. M. Zakeeruddin, J. E. Moser, R. Humphrey-Baker, M. Grätzel, *J. Am. Chem. Soc.* **2004**, *126*, 7164.
[171] H. Nusbaumer, S. M. Zakeeruddin, J. E. Moser, M. Grätzel, *Chem. Eur. J.* **2003**, *9*, 3756.
[172] P. Wang, Q. Dai, S. M. Zakeeruddin, M. Forsyth, D. R. MacFarlane, M. Grätzel, *J. Am.Chem. Soc*. **2004**, *126*, 13590.
[173] Y. Sato, T. Azechi, T. Kitamura, Y. Hasegawa, Y. Wada, S. Yanagida, *Coord. Chem. Rev.* **2004**, *248*, 1469.
[174] J. Krüger, R. Plass, L. Cevey, M. Piccirelli, M. Grätzel, U. Bach, *Appl. Phys. Lett.* **2001**, *79*, 2085.
[175] A. Hauch, A. Georg, *Electrochim. Acta* **2001**, *46*, 3457.
[176] A. Hagfeldt, M. Grätzel, *Acc. Chem. Res.* **2000**, *33*, 269.
[177] N. Papageorgiou, Y. Athanassov, M. Armand, P. Bonhote, H. Pettersson, A. Azam, M. Grätzel, *J. Electrochem. Soc.* **1996**, *143*, 3099.
[178] M. Gorlov, L. Kloo, *Dalton Trans.* **2008**, 2655.

pure ionic liquids limit the transportation of iodide/triiodide. In order to reduce these limitations, they are frequently diluted with organic solvents, such as AcCN.[178]

The use of liquid electrolytes produces practical problems, such as leakage and evaporation of solvent, photodegradation and desorption of dye, corrosion of counter electrode, and ineffective sealing of the cells for long-term applications. One way to solve these problems is using quasi-solid-state electrolytes. Although the efficiencies of the DSSCs with quasi-solid-state electrolytes are usually lower, they present improved stability and better sealing abiliy.[152] There exist two methods to prepare quasi-solid electrolyte from (ionic) liquid electrolytes: they can be either solidified by organic polymer gelators to form thermoplastic polymer electrolytes, or by inorganic gelators, such as SiO_2 or nanoclay powder, to form composite polymer electrolytes.[178,179]

The volatility of liquid electrolytes remains an issue for long term stability of DSSCs, which has prompted the development of all-solid electrolyte. Yet, the solid hole-conductors present several disadvantages: (i) the efficiencies of the DSSC remain constantly lower that those obtained with common iodine-based liquid electrolytes, (ii) surface wetting (percolation inside the nanoporous of the semiconductor oxide), (iii) moderate stability in air that requires a perfect sealing and encapsulation, (iv) partial absorption of light by the material acting as a filter for the sensitized films. The most common and efficient solid electrolyte used is spiro-OMeTAD.[180] Even though the efficiencies in DSSC are not yet so high, an all-solid-state solar cell using spiro-OMeTAD with an organolead halide perovskite achieved a conversion efficiency close to 20%.

In order to enhance the performance of DSSCs, additives are incorporated into the device. The main effect of these additives is the shift of the semiconductor conduction band, modulation of the redox couple potential, and surface blocking effects. Alkyl- or diakyl-imidazolium iodide such as 1,3-dimethylimidazolium iodide (DMII),[181] guanidinium thiocyanate,[182] and 4-*tert*butylpyridine (TBP)[140] are among the most commonly and widely used. In particular, TBP is known to modify the surface of the semiconductor by coordination to the defective sites of the surface where no dyes are adsorbed. This produces a reduction of the dark current (*i.e.* recombination e^-_{TiO2}/electrolyte) that improves the FF. The second effect of TBP is the upwards shift of the conduction band edges of the semiconductor, which enhance V_{OC}, but at the same time this shift also decreases the injection driving force, which may reduce the electron injection efficiency and hence the photocurrent of the cell.[183]

[179] S. Zakeeruddin, M. Grätzel, *Adv. Funct. Mater*. **2009**, *19*, 2187.
[180] a) U. Bach, D. Lupo, P. Comte, J. E. Moser, F. Weissortel, J. Salbeck, H. Spreitzer, M. Grätzel, *Nature* **1998**, *395*, 583; b) H. Snaith, A. Moule, C. Klein, K. Meerholz, R. Friend, M. Grätzel, M. *Nano Lett*. **2007**, *7*, 3372; c) J. Burschka, A. Dualeh, F. Kessler, E. Baranoff, N. Cevey, C. Yi, M. Nazeeruddin, M. Grätzel,. *J. Am. Chem. Soc*. **2011**, *133*, 18042.
[181] S. Zakeeruddin, M. Grätzel, *Adv. Funct. Mater*. **2009**, *19*, 2187.
[182] X. A. Jeanbourquin, X. Li, C. Law, P. R. F. Barnes, R. Humphry-Baker, P. Lund, M. I. Asghar, B. C. O'Regan, *J. Am. Chem. Soc.* **2014**, *136*, 7286.
[183] S. A. Haque, E. Palomares, B. M. Cho, A. N. M. Green, N. Hirata, D. R. Klug, J. R. Durrant, *J. Am. Chem. Soc.* **2005**, *127*, 3456.

Finally, in order to block the deactivation pathway caused by dye-aggregation and hence improve the performance of DSSC, many strategies have been successfully applied. One of the most commonly used is the incorporation of a coadsorbent in the dye solution during the fabrication of the device, such as cholic acids or salts,[184] which can improve simultaneously V_{OC}, J_{SC}, and FF. Chenodeoxycholic acid, abbreviated as "CDCA" or "CHENO", is one of the most commonly used.[185]

2.2.2.3 Photosensitizer

In order to be efficient in DSSCs, the sensitizer must meet a number of characteristics:

1- ***The sensitizer must absorb light across the widest portion of the visible spectrum, especially in the red and NIR region where the solar photon flux is maximum.*** Figure 85 represents the spectrum of solar irradiance in the visible and NIR region, being the 500−800 nm region the most photon-rich part of sunlight. Based on AM1.5G simulations, the expected current density between 400 and 900 nm is approximately 7 mA·cm^{-2} for every 100 nm, which constitutes a maximum cumulated J_{SC} value of around 35 mA·cm^{-2} for an ideal dye that would harvest whole sunlight in this region. Therefore, most efforts to improve the efficiency of DSSCs are focused on obtaining compounds that display strong absorption in the red and/or NIR region of the solar spectrum.[140c]

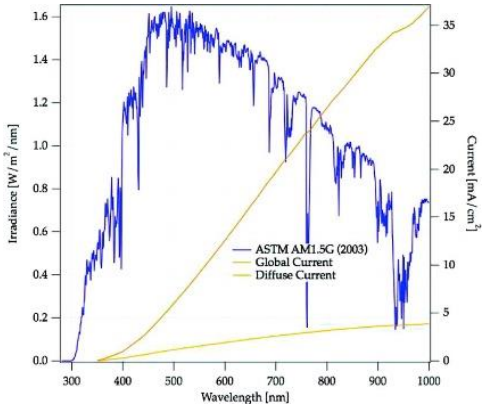

Figure 85. Spectral distribution of the intensity for AM 1.5G solar radiation (blue curves) and J_{SC} values for a device converting all incident photons bellow the absorption onset wavelength into electric current (yellow and brown curves).

2- ***The structure of the dye must include one or more anchoring groups*** (usually carboxylic acid groups) ***that guarantees its binding to the surface, avoiding desorption***.

[184] a) K. Hara, Y. Dan-oh, C. Kasada, Y. Ohga, A. Shinpo, S. Suga, K. Sayama, H. Arakawa, *Langmuir* **2004**, *20*, 4205; b) N. R. Neale, N. Kopidakis, J. van de Lagemaat, M. Grätzel, A. J. Frank, *J. Phys. Chem. B* **2005**, *109*, 23183; c) K. M. Lee, V. Suryanarayanan, K. C. Ho, K. R. Justin Thomas, J. T. Lin, *Sol. Energy Mater. Sol. Cells* **2007**, *91*, 1426.
[185] M. Urbani, M. Grätzel, M. K. Nazeeruddin, T. Torres, *Chem. Rev*. **2014**, *114*, 12330.

Furthermore, ***it should also allow the establishment of strong electronic communication with the TiO_2 orbitals*** to ensure an efficient electron injection of the excited dye into the semiconductor. Finally, the anchoring group should be chemically and photochemically stable under light exposure and heating over time. Besides the carboxyl, a variety of other groups have also been tested, such as phosphonic,[186] sulphonic or boronic acid,[187] sylanes,[188] pyridyl,[189] etc.

3- The redox and photophysical properties of the dye are also of crucial importance***: the LUMO energy level must be higher than the conduction band energy level of the semiconductor*** in order to be able to inject electrons into the TiO_2, and ***the HOMO energy level must be sufficiently low*** to enable fast electron regeneration by the electrolyte redox couple.

4- The spatial orientation and arrangement of the dyes on the surface also influences the performance of a DSSC. For instance, t***he magnitude and direction of the interfacial dipole moment of a dye*** (which originates from donor−acceptor within the dye molecule in the excited state) influence the shift of the CB of TiO_2, and impacts on both the V_{OC} and electron-injection rate. In addition, it also influences the electron recombination rate dye^+/e^-_{TiO2} depending on the proximity and orientation of the oxidised core of the dye to the surface.

5- ***The dye should be soluble in a volatile solvent to permit their adsorption onto the surface of the semiconductor, but should not be easily desorbed by the electrolyte solution***.

6- **The redox reactions involving the dyes must be reversible and the photosensitizers should be stable** enough to resist many oxidation/reduction cycles without decomposition of the molecules.

Several different classes of compounds have been investigated for solar cell applications during the past decades. They can be divided in three main groups: transition metal coordination complexes (mainly Ru(II)), metallated macrocycles (porphyrins and phthalocyanines) and metal-free all-organic dyes.

[186] G .J. Meyer, *Inorg. Chem*. **2001**, *40*, 6073.
[187] S. Altobello, C. A. Bignozzi, S. Caramori, G. Larramona, S. Quici, G. Marzanni, R. Lakhmiri, *J. Photochem. Photobiol. A* **2004**, *166*, 91.
[188] P. Ghosh, T. G. Spiro, *J. Am. Chem. Soc*. **1980**, *102*, 5543.
[189] a) D. Daphnomili, G. Landrou, S. Prakash Singh, A. Thomas, B. K. Yesudas, G. D. Sharma, A. G. Coutsolelos, *RSC Adv.* **2012**, *2*, 12899; b) D. Daphnomili, G. D. Sharma, S. Biswas, K. R. Justin Thomas, A. G. Coutsolelos, *J. Photochem. Photobiol. A: Chemistry* **2013**, *253*, 88.

2.2.2.3.1 Transition metal coordination complexes

The architecture of this family of photosensitizers is based on a central metal ion (usually Ru(II),[190] but also Os(II),[191] Pt(II),[192] Re(I),[193] Cu(I)[194] and Fe(II)[195]), coordinated by various ligands (typically polypyridyl) and having at least one anchoring group. Light absorption in the visible part of the solar spectrum is due to metal-to ligand charge transfer transitions with moderate absorption coefficients (typically $\varepsilon \approx 10{,}000–20{,}000\ cm^{-1}\cdot M^{-1}$). The central metal ion is a crucial part of the overall properties of the complexes. The utilization of different substituents (alkyl, aryl, heterocyclic, etc.) on the complex ligands, typically bipyridines or terpyridines, permit the tuning of its photophysical and electrochemical properties and therefore improve the photovoltaic performance and/or thermal and optical stability.

Among the transition metal coordination complexes, ruthenium (II) have shown the best photovoltaic properties: a broad absorption spectrum, appropriate excited and ground state energy levels, long excited-state lifetime and good electrochemical stability. Several ruthenium complexes used in DSSCs have exceeded 10% power conversion efficiency under standard conditions (AM1.5G). Among them, N3,[196] N719,[197] N749 (also called **"**black dye"),[198] and **CYC-**B11,[199] have shown the best reported efficiencies, over 11% (Figure 86). Ru(II) polypyridyl complexes have been for a long time the champion dyes in DSSC, and remain one of the most efficient class of sensitizers. However, the high cost of Ru metal and low extinction coefficients of Ru-based complexes have prompted the research on DSSCs to focus on other classes of ruthenium-free dyes.

[190] a) M. K. Nazeeruddin, S. M. Zakeeruddin, J. J. Lagref, P. Liska, P. Comte, C. Barolo, G. Viscardi, K. Schenk, M. Grätzel, *Coord. Chem. Rev.* **2004**, *248*, 1317; b) A. Reynal, E. Palomares, *Eur. J. Inorg. Chem*. **2011**, 4509.
[191] T. A. Heimer, C. A. Bignozzi, G. J. Meyer, *J. Phys. Chem*. **1993**, *97*, 11987
[192] A. Islam, H. Sugihara, K. Hara, L. P. Singh, R. Katoh, M. Yanagida, Y. Takahashi, S.Murata, H. Arakawa, G. Fujihashi, *Inorg. Chem*. **2001**, *40*, 5371.
[193] G. M. Hasselmann, G. J. Meyer, *J. Phys. Chem. B* **1999**, *103*, 7671.
[194] T. Bessho, E. C. Constable, M. Grätzel, A. Hernandez Redondo, C. E. Housecroft, W. Kylberg, M. K. Nazeeruddin, M. Neuburger, S. Schaffner, *Chem. Commun*. **2008**, 3717
[195] S. Ferrere, B. A. Gregg, *J. Am. Chem. Soc*. **1998**, *120*, 843.
[196] P. Persson, M. J. Lundqvist, *J. Phys. Chem. B* **2005**, *109,* 11918.
[197] M. K. Nazeeruddin, F. De Angelis, S. Fantacci, A. Selloni, G. Viscardi, P. Liska, S. Ito, B. Takeru, M. Grätzel, *J. Am. Chem. Soc*. **2005**, *127*, 16835.
[198] M. K. Nazeeruddin, P. Pechy, T. Renouard, S. M. Zakeeruddin, R. Humphry-Baker, P. Comte, P. Liska, L. Cevey, E. Costa, V. Shklover, L. Spiccia, G. B. Deacon, C. A. Bignozzi, M. Grätzel, *J. Am. Chem. Soc*. **2001**, *123*, 1613.
[199] C.-Y. Chen, M. Wang, J.-Y. Li, N. Pootrakulchote, L. Alibabaei, C.-h. Ngoc-le, J.-D. Decoppet, J.-H. Tsai, C. Grätzel, C.-G. Wu, S. M. Zakeeruddin, M. Grätzel, *ACS Nano* **2009**, *3*, 3103.

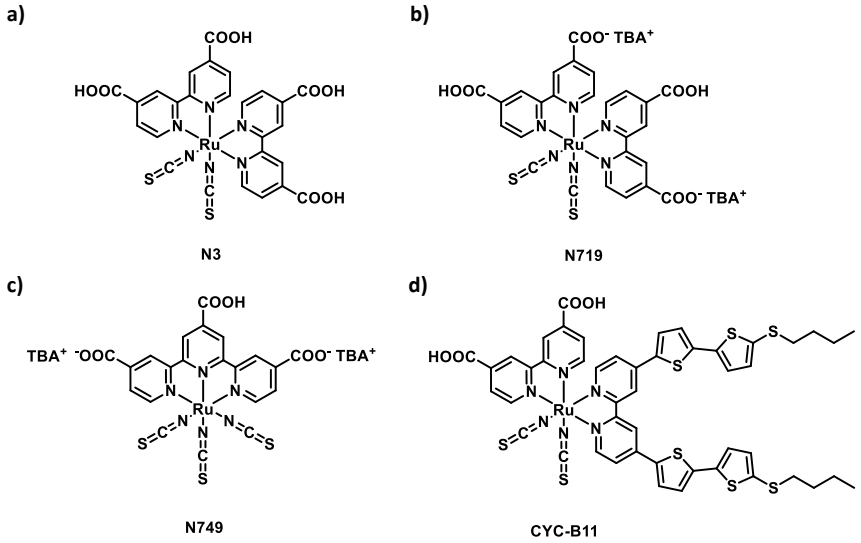

Figure 86. Chemical structure of Ru complexes N3 (a), N719 (b), N749 (c) and CYC-B11 (d)

2.2.2.3.2 Metallated macrocycles (porphyrins and phthalocyanines)

Some of the first examples of Ru-free sensitizers that researchers investigated were chlorophylls and porphyrins, probably attracted by their role in natural photosynthesis.[200] These molecules display strong tuneable absorptions between 400 and 500 nm as well as between 600 and 750 nm. Although the kinetics of charge injection and recombination are similar to those of Ru complexes, they present poor electronic interaction between the macrocyclic core and the anchor linker and molecular aggregation phenomena on the TiO_2 surface. During the last decades, many porphyrin structures have been studied to overcome those drawbacks.[185,201] First, charge transfer studies between tetrakis(4-carboxyphenyl)porphyrin) (ZnTCPP, Figure 87a) were carried out. Recently, a milestone has been achieved with the combination of donor-acceptor moieties that produces light absorbance in the complete visible spectrum, besides the use of long-chain alkoxy groups, which improve dye stability and block device dark current losses. Furthermore, the use of cobalt-based electrolytes show better results, as they minimize energy losses between the energy of the dye HOMO and the electrolyte redox potential, maximizing the V_{OC}. Following this strategy, porphyrin YD2-o-C8 (Figure 87b) reached 11.9% efficiency.[202]

[200] A. Kay, M. Grätzel, *J. Phys. Chem*. **1993**, *97*, 6272.
[201] Y. Tachibana, S. A. Haque, I. P. Mercer, J. R. Durrant, D. R. Klug, *J. Phys. Chem. B* **2000**, *104*, 1198.
[202] A. Yella, H.-W. Lee, H. N. Tsao, C. Yi, A. K. Chandiran, M. K. Nazeeruddin, E. W.-G. Diau, C.-Y. Yeh, S. M. Zakeeruddin, M. Grätzel, *Science* **2011**, *334*, 629.

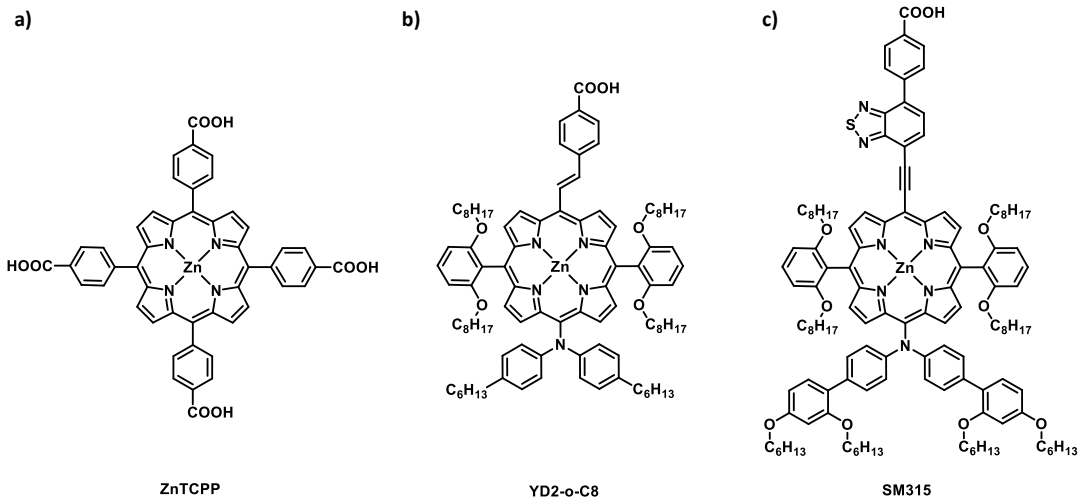

Figure 87. Chemical structure of porphyrins ZnTCPP (a), YD2-o-C8 (b) and SM315 (c).

Afterwards, another porphyrin named SM315 (Figure 87c), broke the DSSC efficiency record with a 13% overall power conversion efficiency.[143] This molecule possesses the same core as the YD2-o-C8 although it incorporates a benzothiadiazole moiety as acceptor/anchor group. This unit produces a broadening of the Soret and *Q* bands, increasing the light harvesting features in the regions between 500 and 800 nm.

Pcs have also attracted much attention in DSSCs thanks to their strong absorption in the far red/near-IR spectral region.[203] As it was the case with porphyrins, these molecules present aggregation on the TiO_2 surface that leads to deactivation of the excited states. The first breakthrough of this family of compounds PCH001,[204a] by Reddy *et al.*, and TT1,[204b] by Cid *et al.* (Figure 88). Both compounds incorporate *tert*-butyl groups at the peripheral positions to avoid aggregation but differed from each other in the number of carboxylic acid anchoring groups and their spacers.

The resulting efficiencies were 3.05% and 3.5% for PCH001 and TT1, respectively. The different spacers had an effect not only on the distance from the TiO_2 surface but also on the molecular orientation, which led to differences in the electron injection and recombination kinetics and, therefore, in the overall efficiencies.[204b] Apart from bulky peripheral substitution, aggregation can also be avoided either by the introduction of axial substituents at the central metal atom or using co-adsorbents like CHENO (up to a 100 equivalents), thus improving the photovoltaic devices performance.

[203] M. –E. Ragoussi, M. Ince, T. Torres, *Eur. J. Org. Chem.* **2013**, *29*, 6475.

[204] a) Y. Reddy, L. Giribabu, C. Lyness, H. Snaith, C. Vijaykumar, M. Chandrasekharam, M. Lakshmikantam, J. H. Yum, K. Kalyanasundaram, M. Grätzel, M. K. Nazeeruddin, *Angew. Chem.* **2007**, *119*, 377; b) J.-J. Cid, J.-H. Yum, S.-R. Jang, M. K. Nazeeruddin, E. Martínez- Ferrero, E. Palomares, J. Ko, M. Grätzel, T. Torres, *Angew. Chem.* **2007**, *119*, 8510.

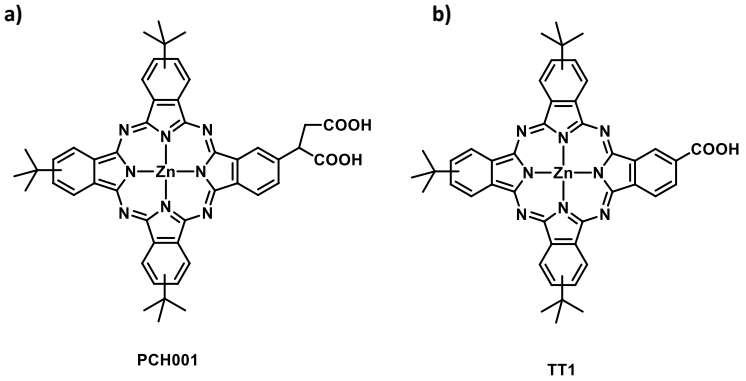

Figure 88. Chemical structure of phthalocyanines PCH001 (a) and TT1 (b).

Rational design of the peripheral substitution to obtain push-pull bulky structures led to PcS20[205] and TT40[205b] (Figure 89), which present the highest efficiencies reported with Pcs in DSSCs: 6.4 and 6.1 % respectively, without using co-adsorbents.

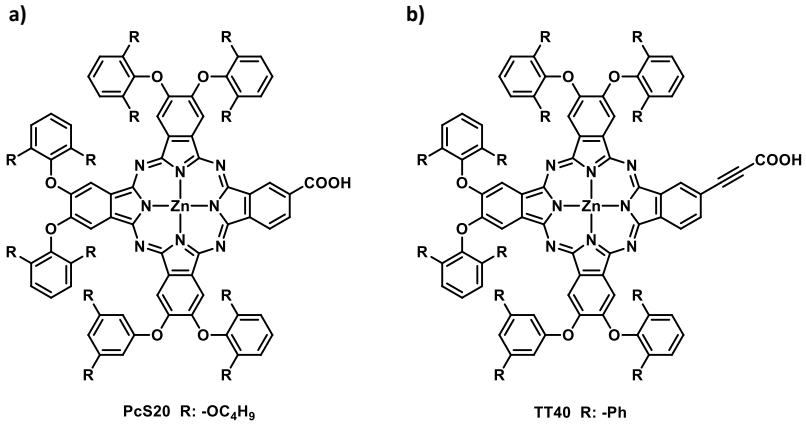

Figure 89. Chemical structure of phthalocyanines PcS20 (a) and TT40 (b).

As finding a single dye that strongly absorbs throughout the whole 350–940 nm range, co-sensitization with dyes that display complementary optical properties is one of the tactics that has been widely considered.[206] Quite often, though, a decrease instead of an increase in the efficiency is observed. This is attributed to intermolecular interactions between the dyes that

[205] a) T. Ikeuchi, H. Nomoto, N. Masaki, M. J. Griffith, S. Mori, M. Kimura, *Chem. Commun.* **2014**, *50*, 1941; b) M. -E. Ragoussi, J. -J. Cid, J. -H. Yum, G. de la Torre, D. Di Censo, M. Grätzel, M. K. Nazeeruddin, T. Torres, *Angew. Chem. Int. Ed*. **2012**, *51*, 4375.
[206] a) K. Sayama, S. Tsukagoshi, T. Mori, K. Hara, Y. Ohga, A. Shinpou, Y. Abe, S. Suga, H. Arakawa, *Sol. Energy Mater. Sol. Cells* **2003**, *80*, 47; b) T. Chen, Z. Zeng, C. Li, W. Wang, X. Wang, B. Zhang, *New J. Chem.* **2005**, *29*, 773; c) J.-H. Yum, S.-R. Jang, P. Walter, T. Geiger, F. Nüesch, S. Kim, J. Ko, M. Grätzel, M. K. Nazeeruddin, *Chem. Commun.* **2007**, 4680.

decrease the injection dynamics.[207] Nonetheless, there are some successful examples: a cocktail-type cell based on a mixture of the successful TT1 Pc dye (Figure 88) and the fully organic dye JK2 (Figure 90a),[208] yielded a 7.7% overall efficiency. This value is higher than those achieved with the single-dye devices (3.5 and 7 % respectively).

2.2.2.3.3 Metal free sensitizers

Although metal complexes have demonstrated outstanding performance in DSSCs, they present some non-desirable drawbacks, like is the use of costly metals such as Ru, but also due to their multistep synthesis and the need for complex purification methods.[164] For these reasons, organic dyes have been proposed as candidates to overcome the drawbacks of the metal complexes. They have lower cost of large-scale production due to their easier synthesis, higher molar extinction coefficient when compared with metal complexes, and the lack of dynamic exchange of ligands as for metal–organic bonds.[209]

A large number of organic dyes have been tested in DSSC with different outcomes: coumarins,[210] heteroantracenes,[211] perylenes,[212] indoles,[213] etc. The best efficiency was achieved by the latter family in 2008.[213b] Nonetheless, the best results found within the field of organic dyes have been achieved by using electron-donating and electron-withdrawing groups linked covalently through a π conjugate spacer (D-π-A structure, Figure 90).[214] This architecture enables the modulation of its properties by rational molecular design and, particularly, extension of the absorption spectra range, adjustment of the HOMO and LUMO levels and preparation of strong push-pull systems that assist the intramolecular charge separation. When a dye absorbs light, the intramolecular charge transfer occurs from subunit D to A mediated through the π- bridge. This "ballistic" configuration usually favours a longer charge separation state and hence a more efficient electron injection from the excited state of the photosensitizer into the TiO_2 conduction band.

---

[207] a) A. Ehret, L. Stuhi, M. T. Spitler, *J. Phys. Chem. B* **2001**, *105*, 9960; b) H. Otaka, M. Kira, K. Yano, S. Ito, H. Mitekura, T. Kawata, F. Matsui, *J. Photochem. Photobiol. A: Chem.* **2004**, *164*, 67; c) V. P. S. Perera, P. K. D. D. P. Pitigala, M. K. I. Senevirathne, K. Tennakone, *Sol. Energy Mater. Sol. Cells* **2005**, *85*, 91; d) C. Siegers, U. Würfel, M. Zistler, H. Gores, J. Hohl-Ebinger, A. Hinsch, R. Haag, *ChemPhysChem* **2008**, *9*, 793.

[208] S. Kim, J. K. Lee, S. O. Kang, J. Ko, J.-H. Yum, S. Fantacci, F. De Angelis, D. Di Censo, M. K. Nazeeruddin, M. Grätzel, *J. Am. Chem. Soc.* **2006**, *128*, 16701.

[209] L. Kloo, *Chem. Commun*. **2013**, *49*, 6580.

[210] K. Hara, T. Sato, R. Katoh, A. Furube, Y. Ohga, A. Shinpo, S. Suga, K. Sayama, H. Sugihara, H. Arakawa, *J. Phys. Chem*. *B* **2002**, *107*, 597.

[211] a) K. Hara, T. Horiguchi, T. Kinoshita, K. Sayama, H. Sugihara, H. Arakawa, *Sol. Energy Mater. Sol. Cells* **2000**, *64*, 115; b) K. Sayama, M. Sugino, H. Sugihara, Y. Abe, H. Arakawa, *Chem. Lett.* **1998**, *27*, 753; c) J.-H. Yum, P. Walter, S. Huber, D. Rentsch, T. Geiger, F. Nüesch, F. De Angelis, M. Grätzel, M. K. Nazeeruddin, *J. Am. Chem. Soc*. **2007**, 129, 10320.

[212] C. Li, J.-H. Yum, S.-J. Moon, A. Herrmann, F. Eickemeyer, N. G. Pschirer, P. Erk, J. Sch€oneboom, K. Müllen, M. Grätzel, M. K. Nazeeruddin, *ChemSusChem* **2008**, *1*, 615

[213] a)T. Horiuchi, H. Miura, S. Uchida, *Chem. Commun*. **2003**,3036; b) S. Ito, H. Miura, S. Uchida, M. Takata, K. Sumioka, P. Liska,P. Comte, P. Pechy, M. Grätzel, *Chem. Commun*. **2008**, 5194

[214] T. Kitamura, M. Ikeda, K. Shigaki, T. Inoue, N. A. Anderson, X. Ai, T. Lian, S. Yanagida, *Chem. Mater.* **2004**, *16*, 1806.

After light-absorption, the excited dye promotes an electron injection from its LUMO to the TiO_2 CB. In an efficient sensitizer, the LUMO is usually located at the electron-acceptor moiety, which also plays the role of the anchoring group, close to the semiconductor surface, in order to facilitate the electron injection process. In general, efficiencies consistently remain in the range of 6.0-8.0% with a few exceptions, and thus only few D-A organic dyes have overcome PCEs of 10.0% (C219[215a] and C257[215b] for instance, Figure 90b and c). The current efficiency record for pure organic dyes, 12.5%, has been achieved by an *N*-annulated indenoperylene electron-donor, decorated with an electron-acceptor benzothiadiazole moiety (C275, Figure 90d).[216]

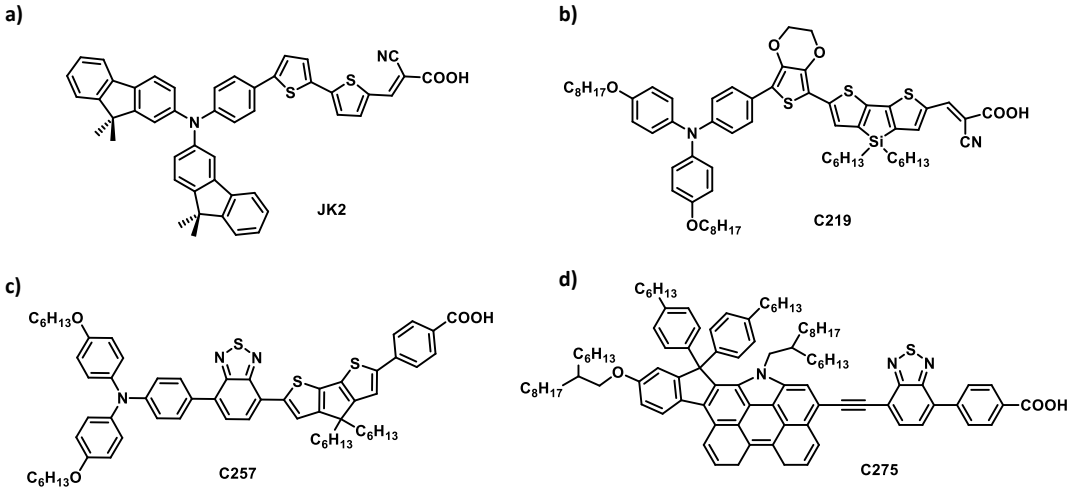

Figure 90. Chemical structure of organic dyes JK2 (a), C219 (b), C257 (c), and C275 (d).

[215] a) W. Zeng, Y. Cao, Y. Bai, Y. Wang, Y. Shi, M. Zhang, F. Wang, C. Pan, P. Wang, *Chem. Mater.* **2010**, *22*, 1915; b) M. Zhang, Y. Wang, M. Xu, W. Ma, R. Li, P. Wang, *Energy Environ. Sci.* **2013**, *6*, 2944.
[216] Z. Yao, M. Zhang, H. Wu, L. Yang, R. Li, P. Wang, *J. Am. Chem. Soc*. **2015**, *137*, 3799.

2.3 Specific objectives

The aim of this Chapter is the synthesis of unreported electron-donor photosensitizers based on porphyrazine derivatives for their application in dye sensitized solar cells (DSSCs). These new ligands will have a common structure consisting of three pyrrole units functionalized at the β-positions with electron-donor functions of different nature, and a fourth pyrrole unit containing the anchoring group which can anchor the dyes onto the TiO_2 surface. The effect of the diverse peripheral substitution of Pzs, as well as the anchoring motif in the performance of the Pzs in DSSCs, will be systematically studied.

The fabrication of the devices and the measurements of their performance will be carried out in the laboratory of Professors M. Grätzel and M. K. Nazeeruddin in the École Polytechnique Fédérale de Lausanne.

Specific objectives for this chapter are the following:

- Synthesis of a series of A_3B Pzs in which the B subunit is an isoindole containing a directly attached carboxylic acid function, like in TT-1.
- Assessment of the photovoltaic performances in TiO_2-DSSC, and selection of the best peripheral functionalization (nature of A)
- Synthesis of a second generation of Pzs by modification of subunit B. In particular, any anchoring motif in B will be directly attached to the β-positions of a pyrrole ring.

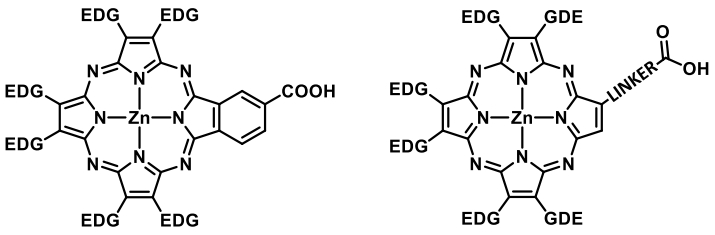

EDG = Electron donor group

2.4 Results and discussion

2.4.1 Synthesis of ZnPz derivatives containing an isoindole-4-carboxylic unit

The Zn porphyrazine derivatives synthesized in this Chapter possess a common basic structure consisting of three pyrrole units functionalized with electron donating functional groups, while the fourth unit is an isoindole-4-carboxylic moiety (Figure 91). This design provides the molecules with a push-pull structure that should facilitate the injection of an electron into the TiO_2 CB.

Pzs with heteroatoms with a lone pair directly attached to the β-carbon atom of the pyrrole system constitute extended–conjugated systems that exhibit relatively strong n→π* charge transfer bands. Therefore, these structures should, in principle, give rise to panchromatic electron-donor chromophores.

Taking into account the synthetic availability of maleonitrile precursors and their reactivity, macrocycles containing alkyl, thioether and amino- functions directly attached to the Pz periphery were envisioned (Pzs **33**, **34**, and **35**, Figure 91). Additionally, π-electron donor groups could be attached to the β-pyrrole positions through *p*-substituted phenyl linker. This kind of substitution has also provided Pz derivatives with electron-donor features[217] and could reduce aggregation phenomena owing to steric bulk. In this respect, Pzs **36**, **37**, and **38** were also designed (Figure 91).

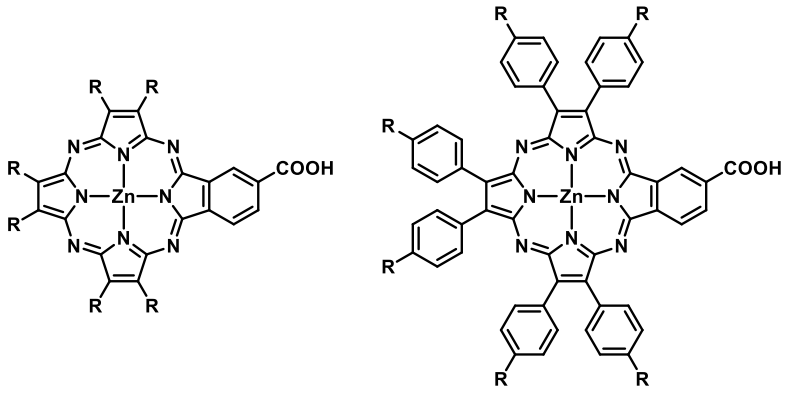

33 R = -C_3H_7
34 R = -SC_5H_{11}
35 R = -NMe_2

36 R = -*t*-Bu
37 R = -OMe
38 R = -NMe_2

Figure 91. Chemical structure of porphyrazines **33**-**38**.

[217]T. Higashino, S. Rodríguez-Morgade, A. Osuka, T. Torres, *Chem. Eur. J*. **2013**, *19*, 10353.

2.4.2 Synthesis of maleonitrile precursors

The preparation of 2,3-dipropylmaleonitrile **41** was carried out following the route described in Scheme 22.[218] Bromination of commercially available 4-octyne with a solution of bromine in AcOH provided 4,5-Dibromo-4*E*-octene **39**. Afterwards, substitution of the bromine groups by nitrile functions yielded 2,3-dipropylfumaronitrile **40**, which, after photoisomerization reaction by irradiation with a high-pressure Hg lamp, provided 2,3-dipropylmaleonitrile **41** in moderate yields.

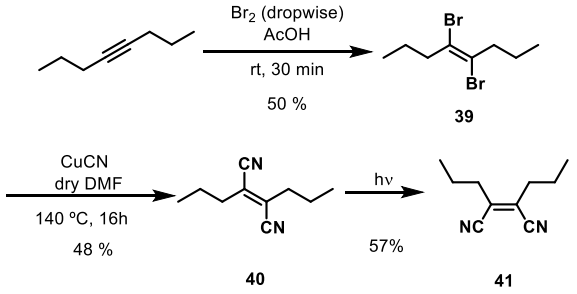

Scheme 22. Synthesis of maleonitrile **41**.

The preparation of thioalkylmaleonitrile **42a,b** started with the addition of sodium cyanide to carbon disulfide in DMF to afford sodium cyanodithioformate, which spontaneously dimerizes in distilled water to yield disodium maleonitrilebisthiolate (Scheme 23).[219] The bisthiolate was then alkylated by treating with the corresponding alkyl bromide, affording **42a,b**.

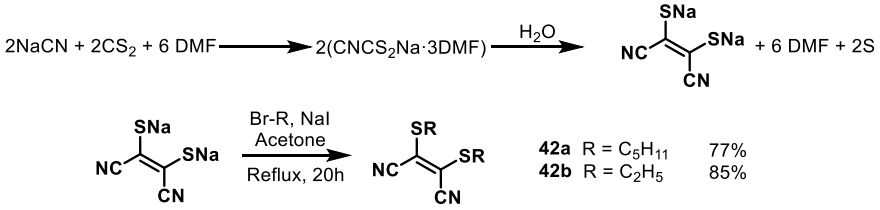

Scheme 23. Synthesis of maleonitriles **42a** and **42b**.

Dimethylaminomaleonitrile **43** was prepared in good yields by alkylation of diaminomaleonitrile with dimethylsulfate (Scheme 24).[220]

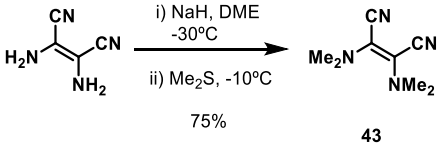

Scheme 24. Synthesis of maleonitrile **43**.

[218] S. J. Lange, H. Nie, C. L. Stern, A. G. M. Barrett, B. M. Hoffman, *Inorganic Chemistry* **1998**, *37,* 6435.
[219] a) G. Bahr, G. Schleitzer, *Chem. Ber*. **1957**, *90*, 438; b) P. Doppelt, S. Huille, *New J. Chem*. **1990**, *14*, 607.
[220] R. W. Begland, D. R. Hartter, F. N. Jones, D. J. Sam, W. A. Sheppard, O. W. Webster, F. J. Weigert, *J. Org. Chem.* **1974**, *39*, 2341.

The preparation of bisarylfumaronitriles **45**, **47** and **49** was carried out by dimerization reaction of the corresponding benzylcyanides (Schemes 25, 26, 27 and 28).

Reaction of 4-*tert*-butylbenzyl chloride with sodium cyanide generated (4-*tert*-butylphenyl)acetonitrile **44**, almost quantitatively (97%, Scheme 25).[221] Then, treatment of **44** with sodium methoxide and iodine[13] yielded the bis(4-*tert*-butylphenyl)-fumaronitrile **45** in 64% yield. Diphenyl substituted fumaronitriles cannot be photoisomerized into maleonitriles by irradiation, since side photocyclization reactions can take place.[222] Therefore, fumaronitrile **45** was converted into the corresponding 1,3-diiminopyrroline **46** to activate it. This was carried out by treating **45** with NH_3 gas in the presence of a refluxing solution sodium ethylene glycolate in ethylene glycol.[221]

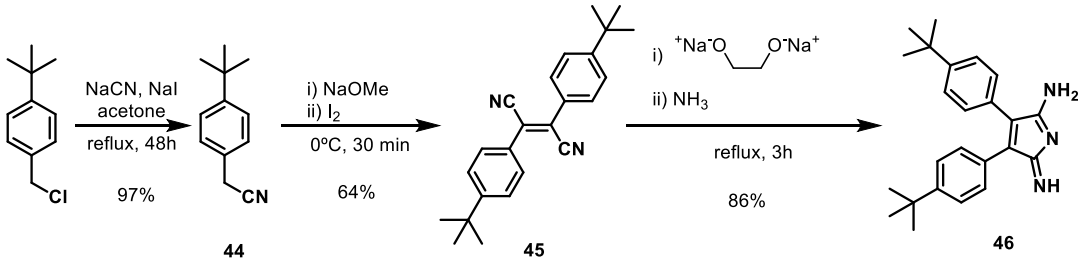

Scheme 25. Synthesis of 1,3-diiminopyrroline **46**.

Likewise, bis(4-methoxyphenyl)-1,3-diiminopyrroline **48** was obtained dimerizing (4-methoxyphenyl)acetonitrile e to yield fumaronitrile **47**.[223] Further reaction of **47** with NH_3 gas in the presence of a refluxing solution of sodium butoxide in butanol gave **48** in 68% yield (Scheme 26).[224]

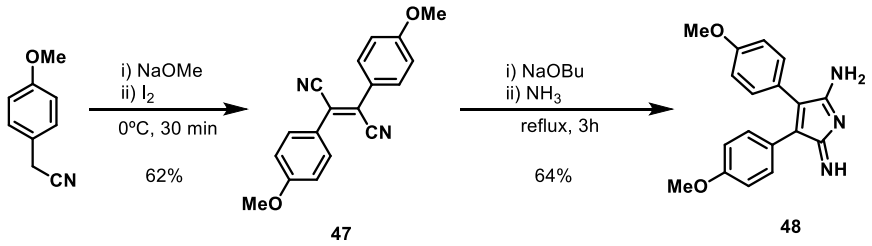

Scheme 26. Synthesis of 1,3-diiminopyrroline **48**.

[221] T. F. Baumann, A. G. M. Barrett, B. M. Hoffman, *Inorg. Chem.* **1997**, *36,* 5661.
[222] a) F. B. Mallory, C. W. Mallory, in *Photocyclization of Stilbenes and Related Molecules*. Organic Reactions. **2005**, *30*, 1; b) M. Yokoyama, H. Ohteki, M. Kurauchi, K. Hoshi, E. Yanagisawa,A. Suzuki, T. lmamoto, Yokoyama, *J. Chem. Soc*., *Perkin Trans.* ***1984,*** *1*, 2635.
[223] H.-C. Yeh, W.-C. Wu, Y.-S. Wen, D.-C. Dai, J.-K. Wang, C-T Chen, *J. Org. Chem.* **2004**, *69*, 6455.
[224] T. Furuyama, Y. Ogura, K. Yoza, N. Kobayashi, Angew. *Chem. Int. Ed*. **2012**, *51*, 11110.

The synthesis of *p*-dimethylaminophenylfumaronitrile **49** was carried out employing a different synthetic approach. Yokoyama *et al*. prepared compound **49** by reaction of 4-dimethylaminobenzaldehyde with methyl thiocyanate and tributylphosphine (Scheme 27).[222]

The proposed mechanism implies activation of methyl thiocyanate by tributylphosphine to generate a complex (M1, Scheme 28) which, in turn, attacks an arylaldehyde to form an intermediate M3 *via* M2 (Scheme 28). The intermediate M3 reacts with tributylphosphine rapidly to form M4, which can undergo two different reactions. It can either attack another molecule of M3 to give succinonitrile M5, or transform into a stable carbene (M6) that dimerizes affording fumaronitrile **49**.

Fumaronitrile **49** was converted into the corresponding 1,3-diiminopyrroline **50** by treatment with ammonia in butanol, in the presence of sodium butoxide (Scheme 27).

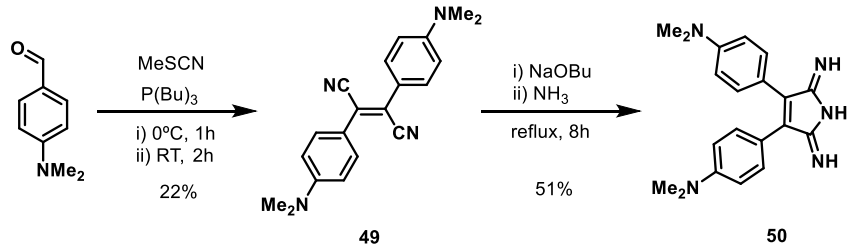

Scheme 27. Synthesis of 1,3-diiminopyrroline **50**.

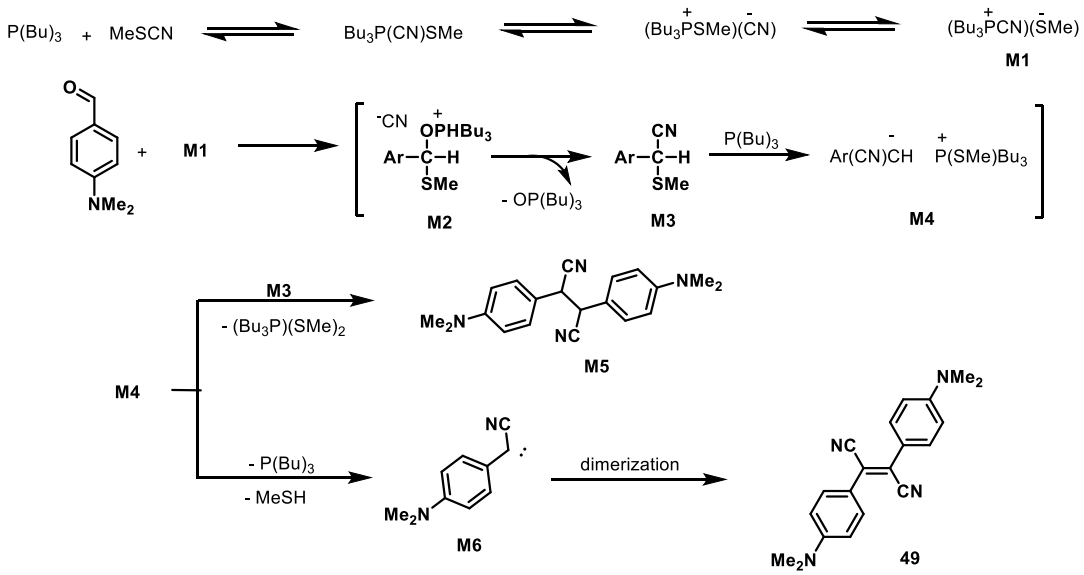

Scheme 28. Proposed mechanism of formation of 49 by Yokoyama *et al*.[222]

The preparation of phthalocyanines such as TT-1 bearing a carboxylic acid function is usually performed by consecutive oxidation reactions of the corresponding hydroxymethyl phthalocyanine (Scheme 29).[225] In the case of Pzs, the use of oxidants could lead to side reactions involving ring-cleavage, which generate seco-porphyrazines (Figure 92).[226] Therefore, we introduced the carboxylic function already in the phthalonitrile precursor.

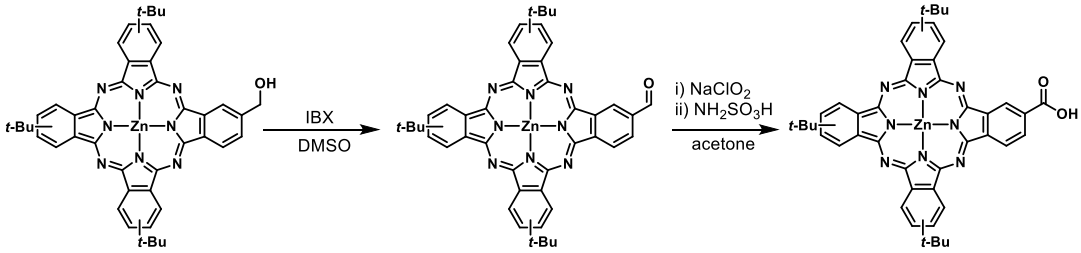

Scheme 29. TT-1 synthetic procedure.

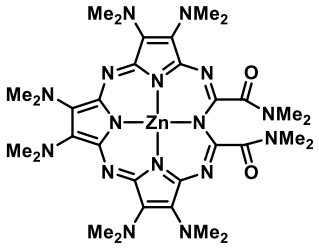

Figure 92. Chemical structure of a seco-porphyrazine

The synthesis of the phthalonitrile-4-methyl ester was carried out in two steps involving first iodination reaction of 4-iodobenzoic acid methyl ester with N-iodosuccinimide to yield methyl 3,4-diodobenzoate **51**. Further cyanation reaction of **51** with $Zn(CN)_2$ in the presence of $Pd_2(dba)_3$, dppf, and Zn powder led to obtaining phthalonitrile **52** in good yields (64 % overall, Scheme 30).[227]

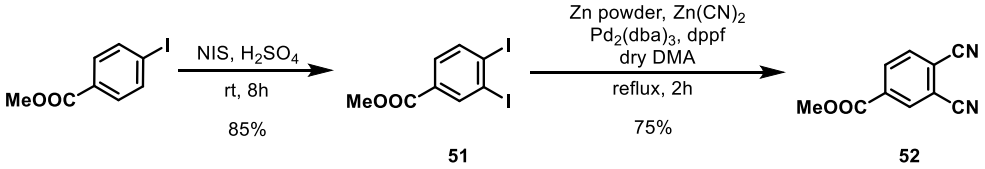

Scheme 30. Synthesis of phthalonitrile **52**.

[225]a) D. Díaz Díaz, J.-J. Cid, P. Vázquez, T. Torres, *Chem. Eur. J.* **2008**, *14*, 9261; b) L. Tejerina, M. V. Martínez-Díaz, T. Torres, *Org. Lett.* 2**015**, *17*, 552.

[226] A. G. Montalban, S. J. Lange, L. S. Beall, N. S. Mani, D. J. Williams, A. J. P. White, A. G. M. Barrett, B. M. Hoffman, *J. Org. Chem.* **1997**, *62,* 9284.

[227] G. Pozzi, S. Quici, M. C. Raffo, C. A. Bignozzi, S. Caramori , M. Orlandi, *J. Phys. Chem. C* **2011**, *115*, 3777.

2.4.3 Synthesis of A_3B porphyrazines bearing an isoindole carboxylic function

Porphyrazines bearing one isoindole carboxylic function were synthesized by crossover macrocyclizations of **52** and a maleonitrile or 1,3-diiminopyrroline, using Linstead macrocyclization conditions,[25] that is, in the presence of magnesium propoxide to template the formation of the MgPzs (Scheme 31). Under these conditions, the ester moiety always underwent a transesterification reaction and, consequently, propyl ester derivatives **53**-**58** were obtained (Figure 93). Afterwards, demetallation was carried out with TFA affording the free base macrocycles, except for $H_2(Me_2N)_6Pz$ **55**, in which acetic acid was used instead, to avoid the possible formation of seco-porphyrazines mentioned before.[226] Further metallation of the free base derivatives with $Zn(OAc)_2$ in a 1:1 mixture of DMF/PhCl provided ZnPz **59**-**64**. Under these macrocyclization conditions a mixture of differently substituted Pzs was obtained. The separation of the desired A_3B Pz from the statistical mixture of products was performed, depending on the solubility and polarity, at different stages of the synthetic route.

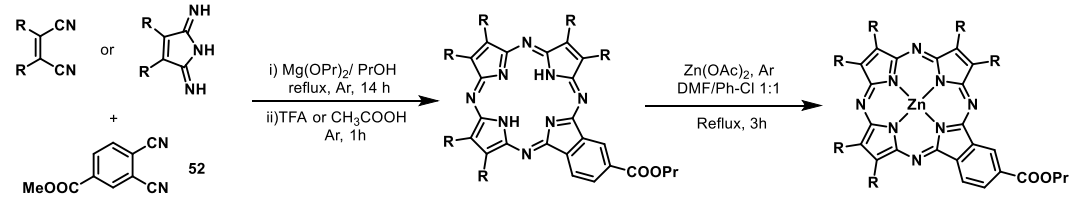

Scheme 31. Synthesis of ester ZnPzs.

The hydrolysis of the ester moiety to obtain the carboxylic acid was carried out by treating the corresponding ZnPzs **59**-**64** with a solution of KOH in *t*-BuOH followed by acidification with a diluted solution of HCl (Scheme 32). In the case of $Zn(NMe_2)_6Pz$ **61**, acidification of the potassium carboxylate $Zn(NMe_2)_6Pz$ salt **35K** (Scheme 32) led to decomposition of the compound. Since in principle the carboxylate can also anchor to the TiO_2, the potassium salt was precipitated and washed with water to remove any excess of KOH.

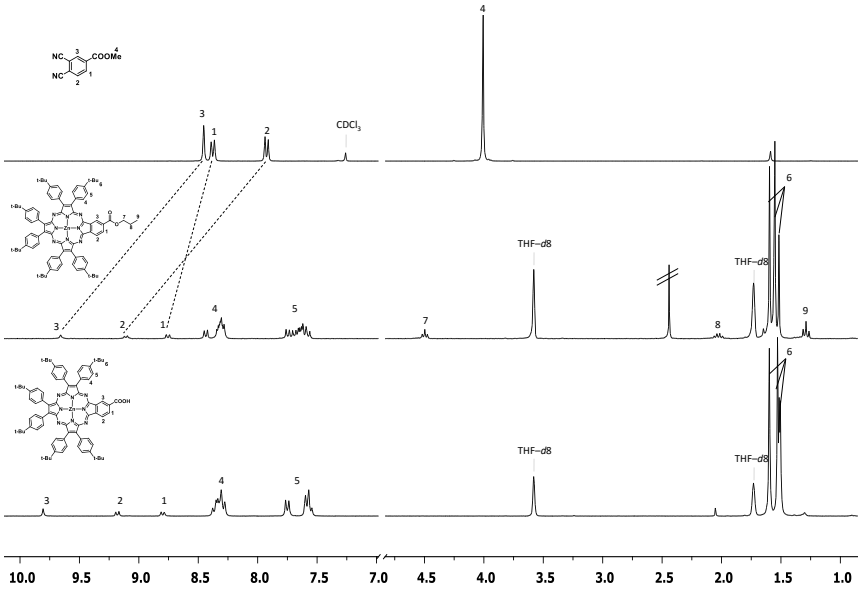

Figure 93. ^{1}H-NMR spectra of phthalonitrile **52** ($CDCl_3$, top), ester Zn(*t*-BuPh)$_6$Pz **62** (THF-d_8, middle), and acid Zn(*t*-BuPh)$_6$Pz **36** (THF-d_8, down).

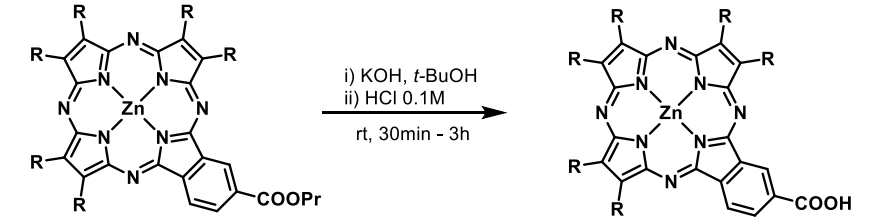

59 R = -C_3H_7 **62** R = -Ph-*t*-Bu

60 R = -SC_5H_{11} **63** R = -PhOMe

61 R = -NMe_2 **64** R = -$PhNMe_2$

33 R = -C_3H_7 **36** R = -Ph-*t*-Bu

34 R = -SC_5H_{11} **37** R = -PhOMe

35K R = -NMe_2 (potassium carboxylate) **38** R = -$PhNMe_2$

Scheme 32. Hydrolysis of ZnPzs **59**-**64** to prepare ZnPzs **33**-**38**.

2.4.4 Optical properties of Pzs 33-38

The absorption spectra of the synthesized Pzs is strongly influenced by the peripheral substitution and the coordination, metallated or free, of the central core. Figure 94a shows the absorption spectra of both the ester and acid hexapropylZnPzs (**59**, dashed line, and **33**, solid line). Both spectra are very similar and present a sharp *Q*-band at 615 nm, which indicates little aggregation, and a Soret band that appears at 350 nm. This spectra resemble that of TT-1, but with the absorption maxima shifted *ca.* 70 nm to the blue region of the visible spectrum.[204b]

Figure 93b shows thiopentyl substituted Pzs **54**, **60** and **34** absorption spectra. In this case, the *Q*- and Soret bands are bathocromically shifted around 65 and 25 nm, respectively, with respect with the propyl Pzs. This effect can be explained by the π-donor character of the thiopentyl substituents. Owing to the lower electronic symmetry that the push-pull structure produces, the *Q*-band splits, and this effect is even more pronounced in the case of the free base macrocycle **34** (dotted line, Figure 94b). This is in agreement with the usual reduction of symmetry when going from a metallated to a free base macrocycle. Also, a charge transfer band appears around 520 nm, confirming the π -donation of the thioether function (**54**, Figure 94b). This band decreases in intensity upon metalation.

Both $(NMe_2)_6$Pzs **61** and **35K** display an almost panchromatic absorption due to the wide broadening of the *Q*-band overlapping an also broad CT-band (Figure 94c). This CT-band is presumably due to n-π^* transitions that arise from the nonbonding electrons associated to the peripheral amine moieties.[228] The molar absorption coefficient is much lower than for alkyl and thioalkyl Pzs. The Soret band shows a 10 fold decrease, while the *Q*-band decreases approximately by a factor of 50. Due to the low solubility of this Pz in other organic solvents, the absorption spectrum of **35K** was measured in MeOH instead of THF.

Zn(*t*-BuPh)$_6$Pzs **62** and **36** (Figure 94d) display absorption spectra that resemble those of metallated thiopentylPzs (Figure 94b). The *Q*-band is better resolved, probably to less strong aggregation processes, and it shows the Q_x and Q_y components at 640 and 665 nm. The Soret band maximizes at 378 nm and a weak charge transfer band appears around 490 nm.

Regarding *para*-methoxyphenyl substituted Pzs **63** and **37**, again the optical spectre of the propyl ester resemble those of thiopentyl and *tert*-butylphenyl substituted Pz. However, upon hydrolysis of the ester to obtain the acid, splitting of the *Q*-band into 4 different bands is observed (Figure 94e). The Soret band also broadens significantly. All these phenomena lead to a decrease in the molar absorption coefficient.

Similarly to hexakis(dimethylamino)Pzs **61** and **35K**, Zn$(NMe_2Ph)_6$Pzs **64** and **38** exhibit a much broader *Q*-band that spans from 500 to 800nm, with the maxima at 690nm (Figure 94f). The Soret band is also broader, rendering also this molecules as panchromatic absorbers but,

[228]A. G. Montalban, W. Jarrell, E. Riguet, Q. J. McCubbin, M. E. Anderson, A. J. P. White, D. J. Williams, A. G. M. Barrett, B. M. Hoffman, *J. Org. Chem.* **2000**, *65,* 2472.

comparing with hexakis(dimethylamino)Pzs **61** and **35K**, the molar absorption coefficient are in the order of 4 x 10^4 $cm^{-1}·M^{-1}$.

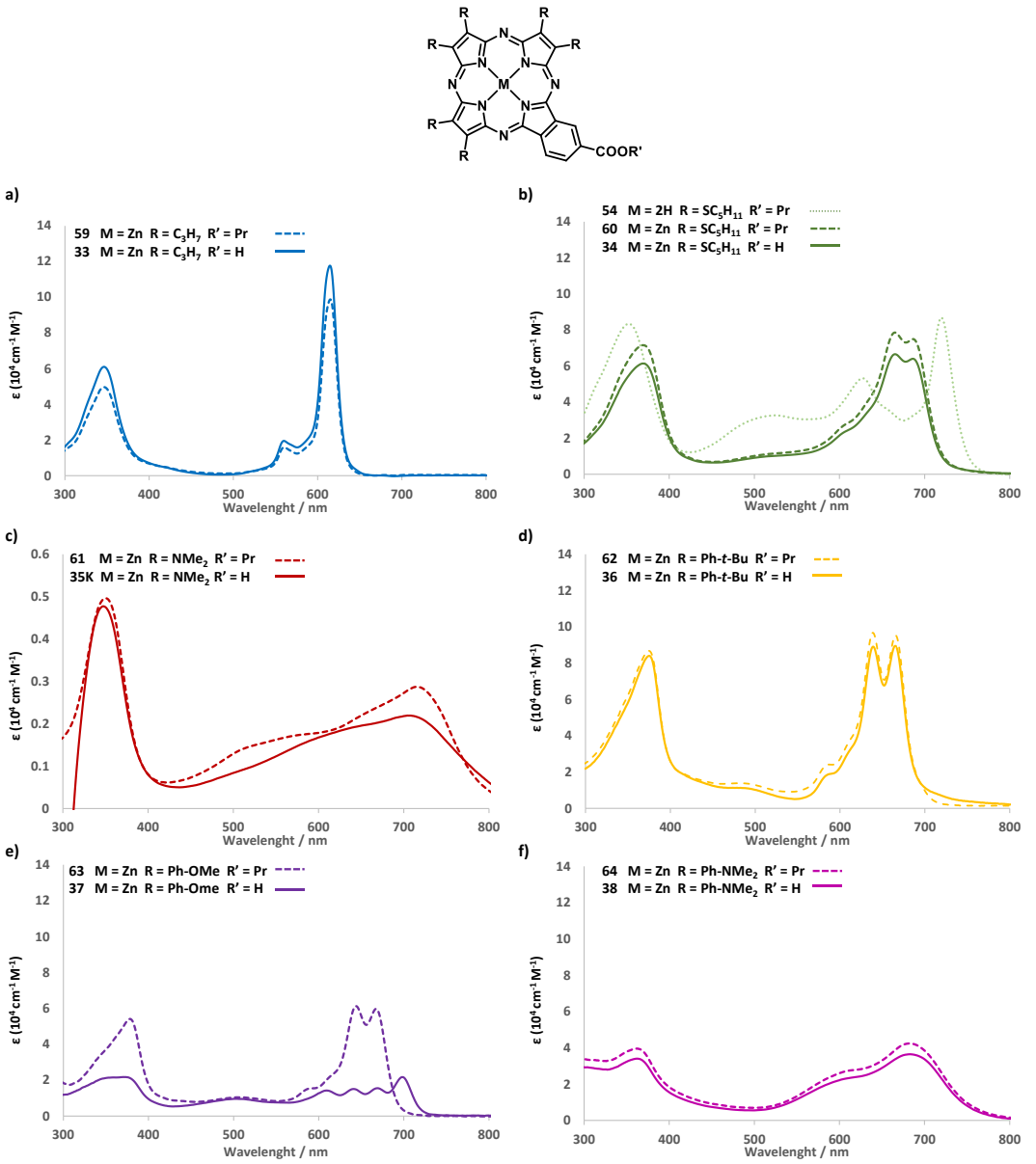

Figure 94. Absorption spectra of: a) $Zn(C_3H_7)_6$Pzs **59** (dashed line) and **33** (solid line) in THF, b) $(SC_5H_{11})_6$Pzs **54**, (dotted line), **60** (dashed line) and **34** (solid line) in THF, c) $Zn(NMe_2)_6$Pzs **61** (dashed line) in THF and **35K** (solid line) in MeOH, d) Zn(*t*-BuPh)$_6$Pzs **62** (dashed line) and **36** (solid line) in THF, e) Zn(MeOPh)$_6$Pzs **63** (dashed line) and **37** (solid line) in THF and f) $Zn(NMe_2Ph)_6$Pzs **64** (dashed line) and **38** (solid line) in THF.

The similar optical spectra of amino and aminophenyl-substituted Pzs indicates effective π-donation from the amino groups to the macrocyclic core through the peripheral phenyl linkers.

Regarding the emission spectra of ZnPzs **33**-**38**, only ZnPr$_6$Pz **31**, Zn(*t*-BuPh)$_6$Pz **35**, and in less extent, Zn(MeOPh)$_6$Pz **37** present fluorescence (Figure 95). The Stokes shift is of 12 nm for **33** and 15 nm for **36**. In the case of **37**, the fluorescence spectrum overlaps the absorption spectrum due to the splitting mentioned before.

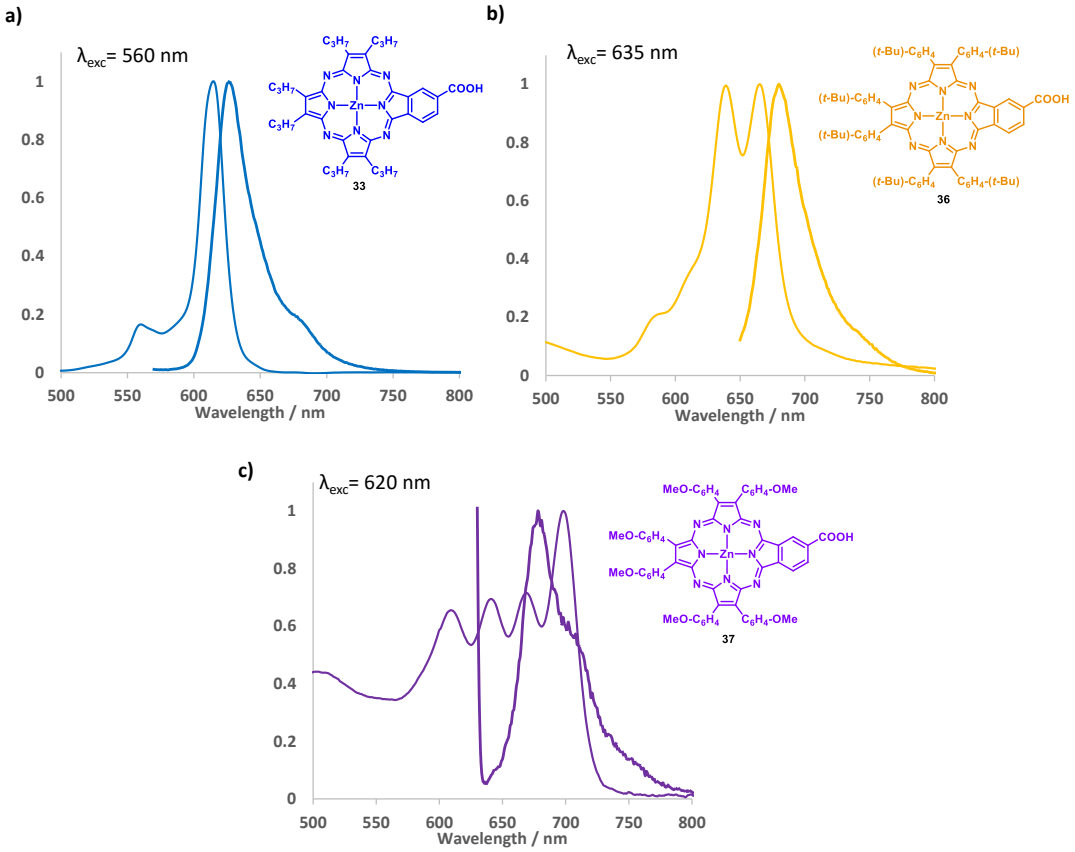

Figure 95. Absorption (solid line) and emission (dotted line) spectra of Pzs **33**, **36**, and **37**.

2.4.5 Electrochemical studies

Electrochemical experiments (cyclic voltammetry, square wave and differential pulse voltammetry (DPV)) were conducted to investigate the influence of the peripheral functionalization on the redox properties of the porphyrazines. The measurements were carried

out using a three electrode cell in Ar saturated THF solution containing 0.1 M $TBAPF_6$ supporting electrolyte. Due to its low solubility in THF, $Zn(NMe_2)_6Pz$ **35K** was measured in MeOH, and only in DPV was possible to observe redox processes. We used a glassy carbon working electrode, a Pt wire as counterelectode and $Ag/AgNO_3$ as reference electrode. Fc was used as an internal standard. All data are represented *vs* Fc/Fc^+.

Figure 96 shows the cyclovoltammograms of the different Pzs in the cathodic window. The number of reduction waves varies from 2 to 4 as a function of the peripheral substitution, and the processes are well defined in all cases except for Pz **35K**. $Zn(Pr)_6Pz$ **33** displays the most negative first reduction potential (Figure 96a). **33** shows two irreversible reductions centred at –1.71 and –2.39 V (ΔE > 200 mV). $Zn(SC_5H_{11})_6Pz$ **34**, on the other hand, shows four reduction waves, the first process being located at –1.09 V (Figure 96b). The low solubility even in MeOH of $Zn(NMe_2)_6Pz$ **35K** made the measurements more difficult. Even so, two reduction processes were found in DPV at –0.85 and –1.30 V (Figure 96c). *Tert*-butyl- and methoxy phenyl substituted Pzs **36** and **37** showed the first reduction wave at –1.16 V for **36** and –0.97 V for **37** and the second and third reduction waves appear for both compounds at –1.35 and –1.62 V (Figure 96d and e). $Zn(t\text{-}BuPh)_6Pz$ **36** showed an additional fourth wave at –1.90 V. Finally, $Zn(NMe_2Ph)_6Pz$ **38** exhibits 3 reduction processes, and is approximately 300 mV harder to reduce than $Zn(MeOPh)_6Pz$ **37**, but 250 mV easier than Pz **33** (Figure 96f).

The Pz/Pz^+ oxidation processes could not be identified in CV because they were overlapped by the end of the solvent oxidation window. Nonetheless, it was possible to observe them in DPV (Figure 97). All Pzs but the two bearing dimethylamino substituents display a single irreversible oxidation situated between 0.62 and 0.68 V. Dimethylamino Pz **35K** and dimethylaminophenyl Pz **38** present three and two oxidation processes respectively (Figures 97c and f) at values close to the Fc/Fc^+ reference that are attributed to oxidation of the amino functions. The multiple oxidation peaks denote effective electronic π-donation from the amino groups to the macrocycle for both aminoPz systems **35K** and **38**. In particular, Pz **35K** is easier to oxidize than the Fc/Fc^+ couple (**35K**: –0.01, –0.07 and –0.18 V, **38**: 0.12 and 0.22 V, Figures 97c and f). This is in agreement with the behaviour of free base and $MgNMe_2Pz$s described before.[228] All the electrochemical data are summarized in Table 13.

Table 13. Redox potentials ($E_{1/2}$ in V) *vs*. Fc/Fc^+ in THF (0.1 M $TBAPF_6$) at room temperature using a glassy carbon electrode.

Pz	E_{Red4}	E_{Red3}	E_{Red2}	E_{Red1}	E_{Ox1}	E_{Ox2}	E_{Ox3}
33	--	--	–2.39[a]	–1.71[a]	0.62[a]	--	--
34	–1.89	–1.52	–1.33[a]	–1.09[a]	0.65[a]	--	--
35K[b]	--	--	–1.30	–0.85	–0.18	–0.07	–0.01
36	–1.90	–1.61	–1.34[a]	–1.16[a]	0.68[a]	--	--
37	--	–1.62	–1.35	–0.97	0.64[a]	--	--
38	--	–2.03	–1.71	–1.47	0.12	0.22	--

[a] Irreversible. [b] Measured in MeOH

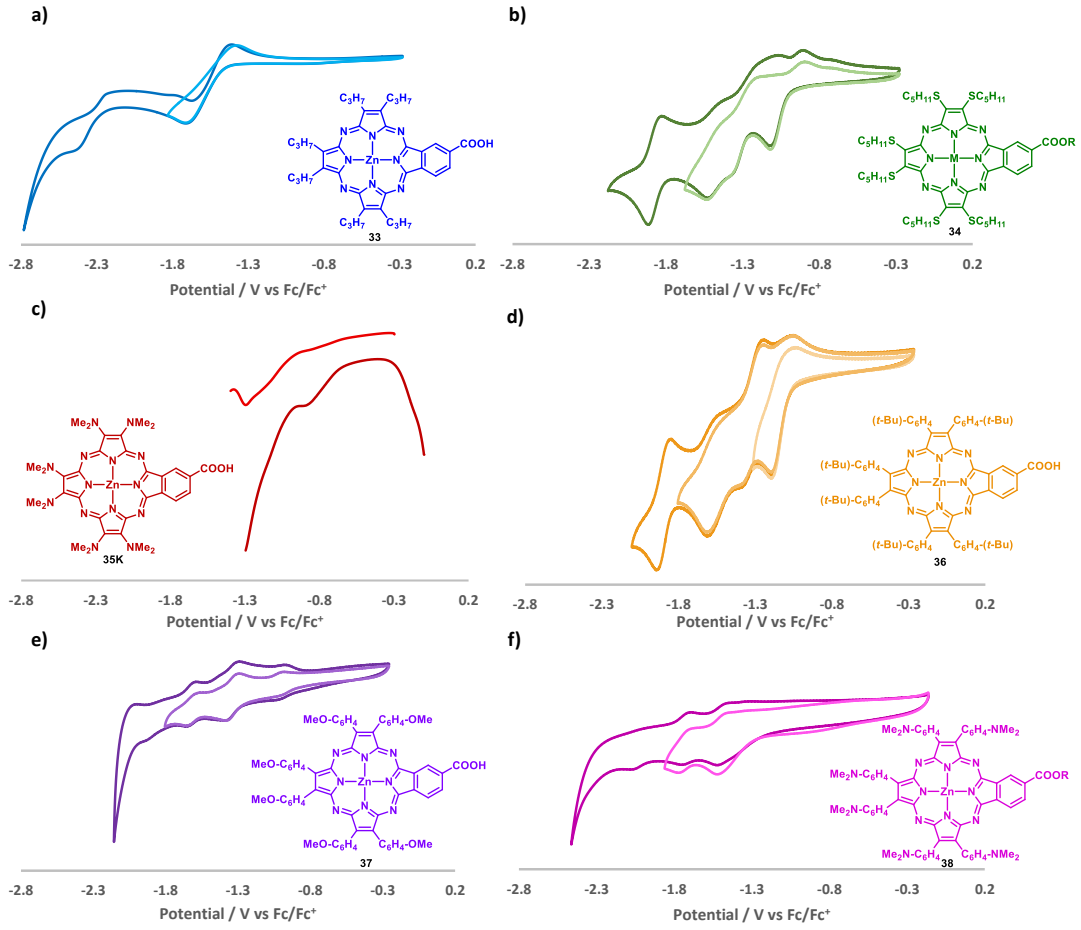

Figure 96. Cyclic voltammogram (anodic window) of compounds **33** (a), **34** (b), **36** (d), **37** (e) and **38** (f) in THF. c) Differential pulse voltammogram of **35K** in MeOH.

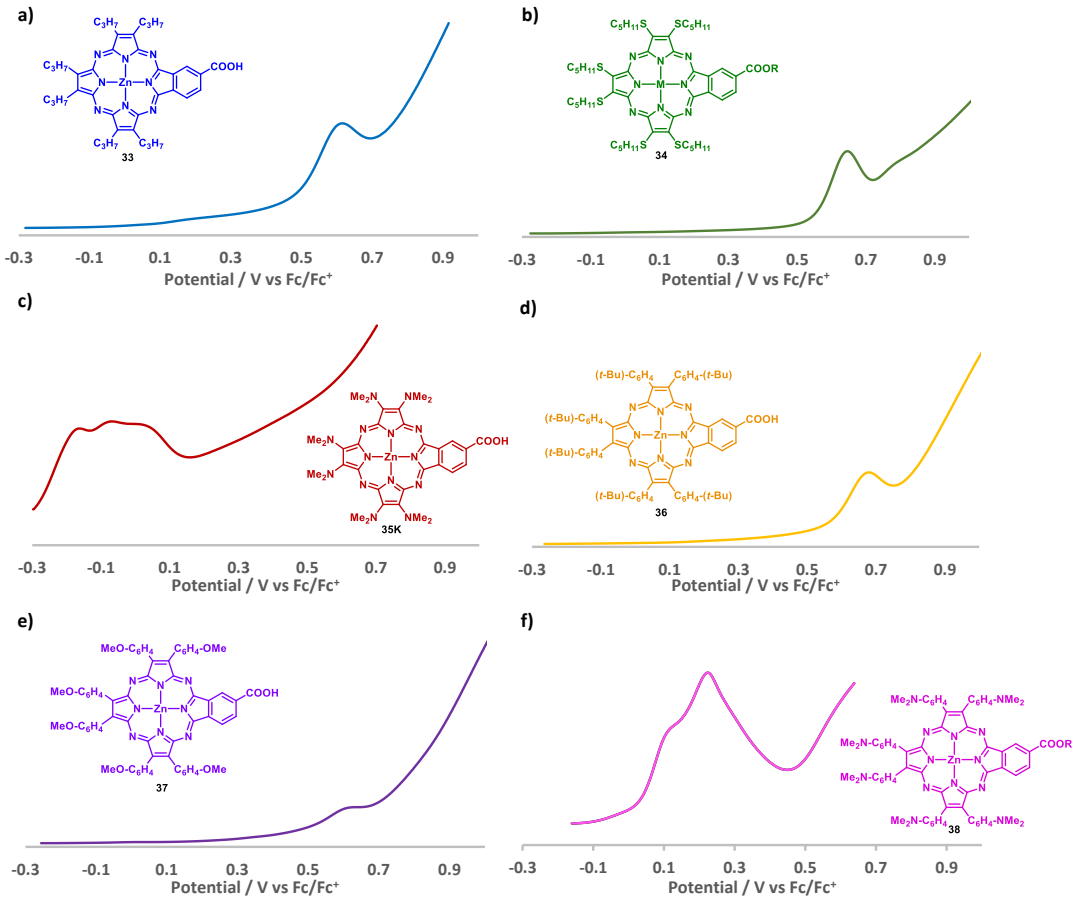

Figure 97. Differential pulse voltammogram (cathodic window) of compounds **33** (a), **34** (b), **36** (d), **37** (e) and **38** (f) in THF. c) Differential pulse voltammogram of **35K** in MeOH.

2.4.6 Calculation of HOMO-LUMO levels

For the electron injection process to be thermodynamically possible, the LUMO level of the dye must lie above the TiO_2 CB (E_{TiO2} = —4.00 eV), and the resulting overpotential satisfies a minimum value to make it efficient.[185,229] At the same time, the potential-energy difference between the HOMO level of the oxidized dye (e.g., porphyrazine dye cation) must lay lower in energy than the potential of the redox couple (I_3^-/I^-, E_{redox}= -4.75 eV). It is believed that a minimum potential difference of ~500 mV is necessary for the efficient dye regeneration when using a standard iodine-based liquid electrolyte.[140a]

The HOMO and levels (*vs* vacuum) of the porphyrazines **33**-**38** were calculated using the approximation depicted in Equation 22:[229,230]

$$E_{HOMO/LUMO} = -5.1 - E^1{}_{ox/red}\ (vs\ \mathrm{Fc/Fc^+})\ \text{(eV)} \qquad \text{(Eqn } \mathbf{22}\text{)}$$

Additionally, estimation of the HOMO-LUMO bandgap from the optical absorption allowed us to calculate the HUMO energy levels (*vs* vacuum) applying Equation 23:

$$E_{LUMO} = E_{HOMO} + E_{onset}\ \text{(eV)} \qquad \text{(Eqn } \mathbf{23}\text{)}$$

Where E_{onset} is the energy value of the onset of the *Q*-band of the absorption spectrum.

Finally, in order to further investigate the geometries and electronic properties of the dyes synthesized, computational studies were performed using GAUSSIAN 09 applying density functional theory (DFT) at the B3LYP/3-21G level for the geometry optimization and B3LYP/6-31G (d,p) for the calculation of the energy levels, both in vacuum and solvated with THF (or MeOH in the case of **35K**). Moreover, we also carried out computational studies of Pz **35** bearing the carboxylic acid to see if the potassium carboxylate induces substantial changes on the orbital energy levels.

All the data obtained about the HOMO-LUMO levels are summarized in Table 14 and is shown schematically in Figure 98.

[229] A. Aljarilla, J. N. Clifford, L. Pellejà, A. Moncho, S. Arrechea, P. de la Cruz, F. Langa, E.Palomares *J. Mater. Chem. A* **2013**, *1*, 13640.
[230] C. M. Cardona , W. Li , A. E. Kaifer , D. Stockdale , G. C. Bazan, *Adv. Mater.* **2011**, *23*, 2367.

Table 14. Experimental and theoretical HOMO-LUMO energy levels data (in eV) of dyes **33-38**.

Pz	Experimental			Computational studies[3]			
	HOMO[1]	LUMO[1]	LUMO[2]	HOMO	LUMO	HOMO (solv)	LUMO (solv)
33	–5.7	–3.4	–3.8 (630 nm)	–5.4	–3.0	–5.3	–2.9
34	–5.8	–4.0	–4.0 (719 nm)	–5.5	–3.3	–5.5	–3.3
35	--	--	--	–4.5	–2.4	–4.6[4]	–2.5[4]
35K	–4.9	–4.3	–3.4 (825 nm)	–4.0	–2.0	–4.4[4]	–2.4[4]
36	–5.8	–3.9	–4.0 (689 nm)	–5.3	–3.1	–5.4	–3.1
37	–5.7	–4.1	–4.0 (720 nm)	–5.2	–2.9	–5.3	–3.0
38	–5.2	–3.6	–3.7 (756 nm)	–4.4	–2.4	–4.6	–2.8

[1] Calculated applying Equation 22. [2] Calculated applying Equation 23. [3] Calculated using DFT B3LYP/6-31G (d,p) both in vacuum and solvated in THF. [4] Calculated solvated in MeOH.

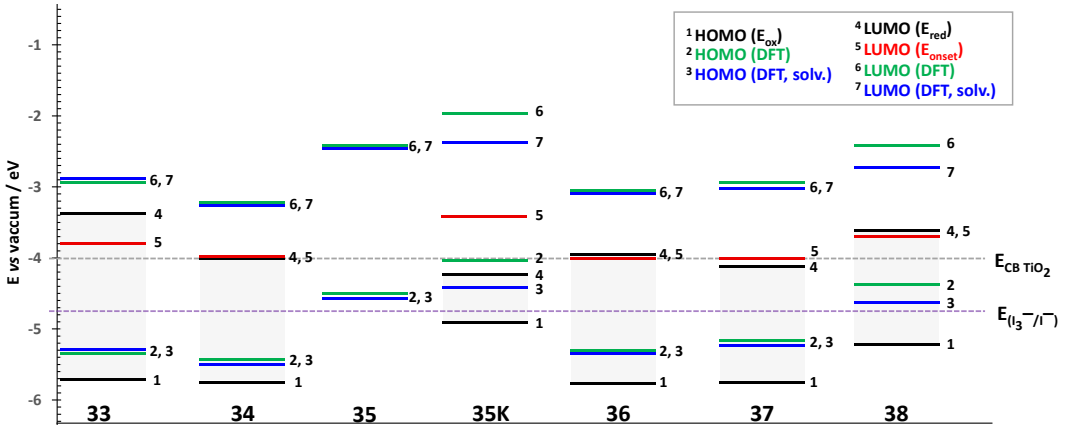

Figure 98. Schematic representation of the calculated HOMO and LUMO energy levels of Pzs **33**-**38**.

The LUMO levels calculated with the first reduction potential in Equation 22 and with the optical bandgap in Equation 23 almost match for all Pzs except for **33** and **35K**. For those**,** the LUMO levels calculated directly from the first reduction potential lies 0.4 eV higher in energy for the former and 0.9 eV lower in energy for the latter when compared to the value obtained from the optical bandgap. There is a big difference for all Pzs when comparing the experimental HOMO-LUMO data with the calculated with DFT. In all cases the HOMO-LUMO values coming from DFT calculation are higher in energy than the experimental data. The highest difference occurs for Pz **35K**, in which the experimental LUMO level differs from the theoretical one in more than 2 eV (Figure 98). The effect of solvation in the theoretical calculations is not remarkable except for Pzs **35K** and **38** that present a stabilization of the energy levels of 0.4 and 0.3 eV respectively. The structure of Pz **35** was optimized both in the carboxylic and carboxylate form to assess the effect that this change might have on the molecular orbital energy levels. In Pz **35** HOMO and

LUMO levels are not influenced by solvation, so there is an energy gap of approximately 0.5 eV. This difference in the energy levels almost disappears upon solvation of Pz **35K**.

The E_{HOMO} values indicate that for all dyes regeneration is feasible by the I_3^-/I^- electrolyte (E_{redox}= —4.75 eV). Nonetheless, the energy difference between redox potential of the electrolyte and E_{HOMO} of Pz **35K** (~0.2 eV), might not be large enough for efficient regeneration. On the other hands, even if the E_{LUMO} values calculated by DFT indicate that all the Pzs should be able to inject efficiently into the TiO_2 conduction band, the experimental E_{LUMO} values suggest that only Pzs **33** and **38** might be able to do so. Pz **35K** could also inject into the TiO_2 CB if we take into account the LUMO energy level calculated from the optical bandgap, but no if it is the electrochemical E_{LUMO} value the one we are considering. Pzs **34** and **36** E_{LUMO} values are too close to the TiO_2 conduction band (E_{TiO2} = —4.00 eV) to generate a driving force for the injection, and for Pzs **37**, the E_{LUMO} level is situated slightly below the TiO_2 conduction band.

Figures 99 and 100 show the HOMO and LUMO orbitals calculated by DFT. All porphyrazines except Zn(C_6H_4-NMe_2)$_6$Pz **38** have their HOMO delocalized through the macrocycle and some on the substituents, while in the case of **38** is situated exclusively over the dimethylaminophenyl substituents. No differences exist when comparing Pzs **35** and **35K** HOMO orbitals. Pzs **33**, **35** and **38** display their LUMO orbitals noticeably delocalized over the carboxylic functions, while the degree of delocalization on this function is lower for **36** and **37**, and inexistent for **34** and **35K**. Taking all into account, Pzs **33** and **38** should perform better in TiO_2 DSSCs.

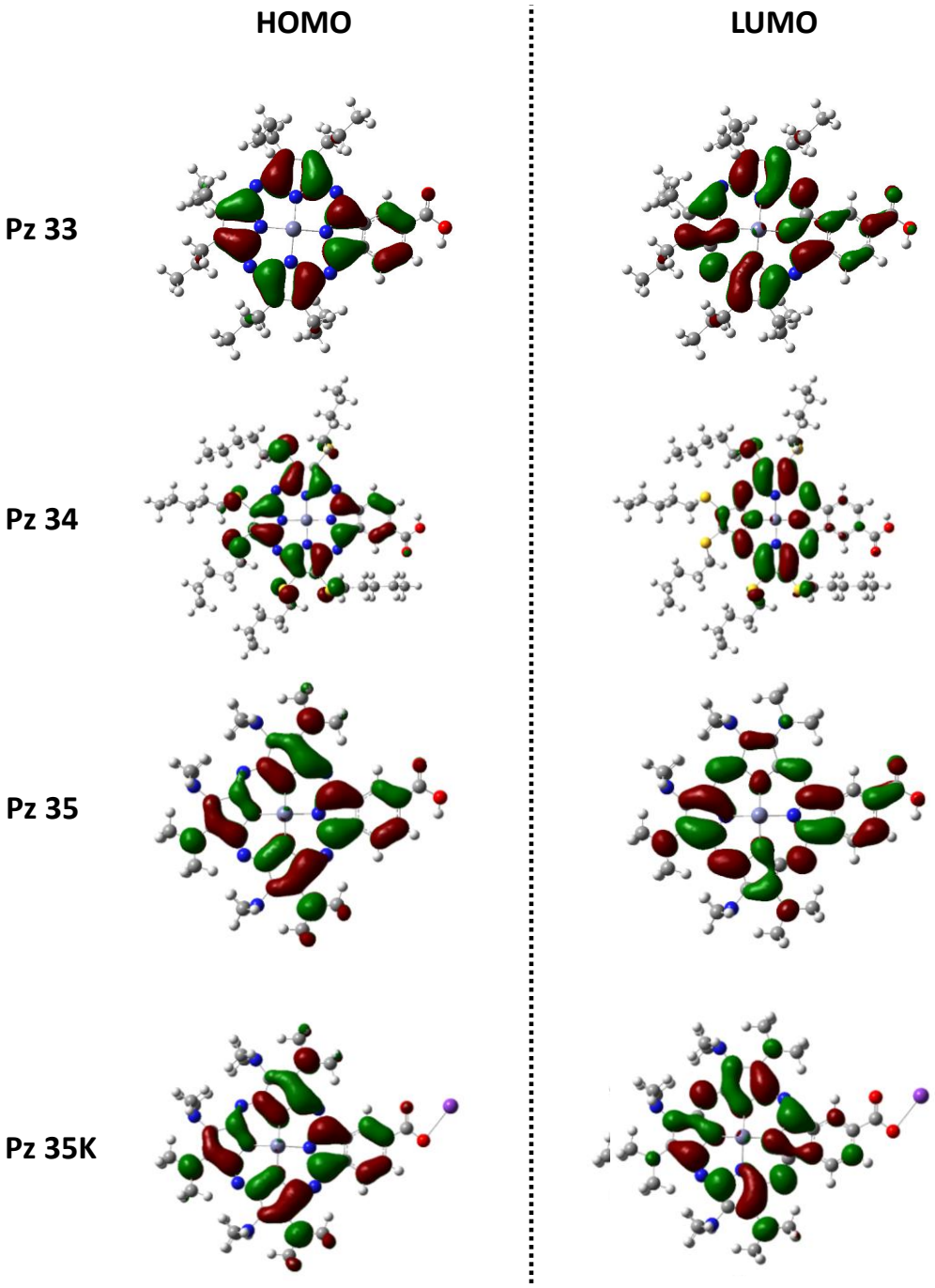

Figure 99. HOMO and LUMO orbitals of Pzs **33**, **34**, **35** and **35K**.

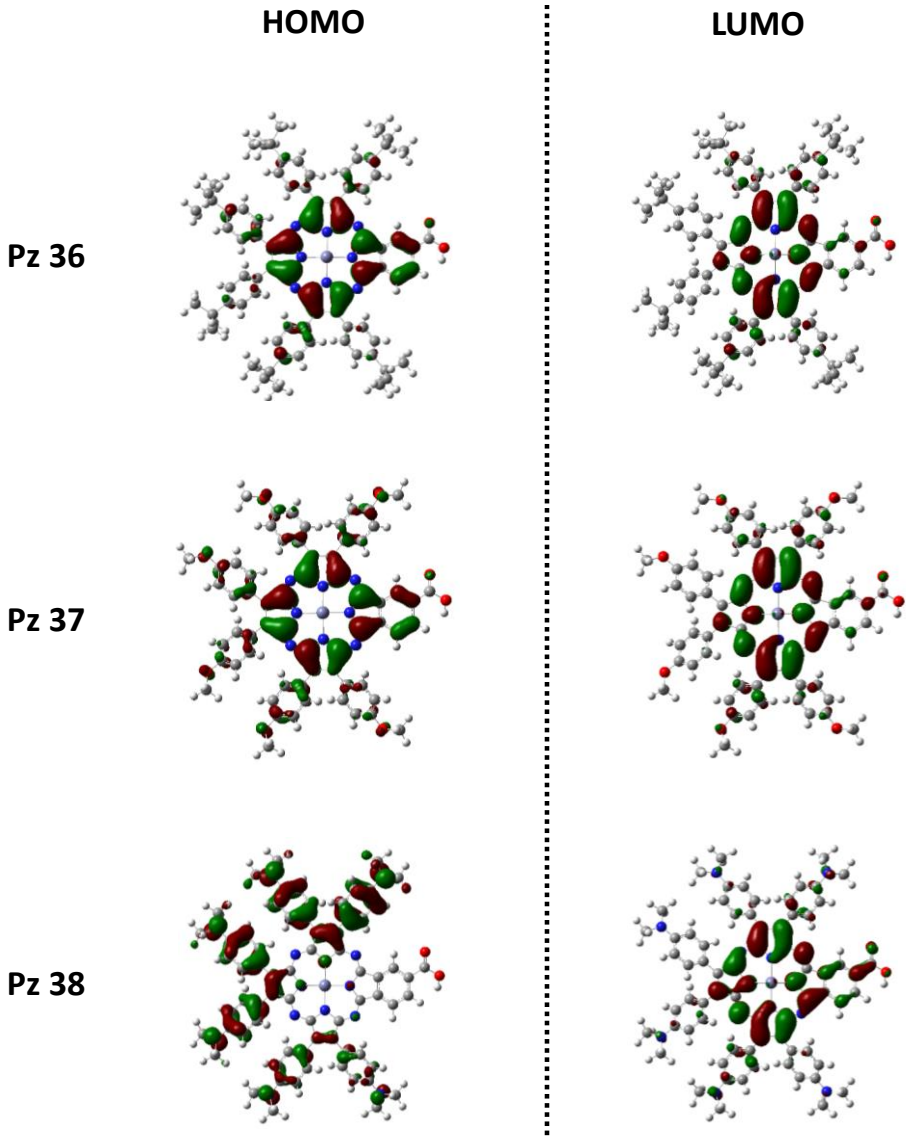

Figure 100. HOMO and LUMO orbitals of Pzs **36**, **37** and **38**.

2.4.7 Photovoltaic performances in TiO_2-DSSC

The study of the performance of the prepared dyes was carried out in the laboratory of Professors M. Grätzel and M. K. Nazeeruddin in the École Polytechnique Fédérale de Lausanne by Dr. Maxence Urbani.

2.4.7.1 Device fabrication

Photoanode preparation: A transparent FTO conducting glass (NSG10) was cleaned using ethanol and water followed by an ultrasonic cleaning in Deconnex™ solution for 30 min. The electrodes were then washed with water and ethanol. To remove the organics, a further thermal treatment was done at 500 °C for 30 min. The clean FTO glass were treated twice with TiCl4 (40 mM, 30 min, 75 °C). Two different TiO_2 pastes, transparent layer (20 nm particles with 32 nm pore size) and scattering layer (400 nm particles), were screen printed on to the $TiCl_4$ pretreated electrode and followed a series of sintering steps as described in the literature.[231]. The photoanodes were further treated with TiCl4 following the steps described above.

Device fabrication: The TiO_2 electrodes were dried at 500°C for 30 min prior to the sensitization in the dye solution. The dye solutions were composed of 0.1 mM of the porphyrazines either in EtOH or in a mixture of THF and EtOH in different proportions (usually 2:3). When indicated, coadsorbent (CHENO) was incorporated into the dye solution at different concentrations. After 14–18h of dipping, the electrodes were washed with EtOH to remove the loosely bounded dye molecules. The counter electrodes were made by drop casting of an isopropanolic solution of H_2PtCl_6 (5 mM) onto a pre-cleaned FTO glass (TEC7, Solaronix, Switzerland) and the electrodes were heated by flame at 410 °C for 30 min. The sensitized photoanode and counter electrode were melt sealed using a 25 µm polymeric spacer (Surlyn™, Dupont, USA). The electrolyte in acetonitrile was then injected by the vacuum backfilling process through a hole drilled at the side of the counter electrode. The cell fabrication was completed by melt sealing the hole with a glass and soldering the metal solder to make contacts. Figure 101 shows the schematic structure of a DSSC device and a photo of real studied devices.

Photovoltaic characterization: A 450W xenon lamp (Oriel, USA) was used as a light source. The spectral output of the lamp was filtered using a Schott K113 Tempax sunlight filter (Präzisions Glas & Optik GmbH, Germany) to reduce the mismatch between the simulated and actual solar spectrum to less than 2%. The current-voltage characteristics of the cell were recorded with a Keithley model 2400 digital source meter (Keithley, USA). The photo-active area of 0.159 cm^2 was defined by a black metal mask. The values reported are for the best devices obtained in each configuration. Two cells were made for each condition.

[231] S. Ito, T. N. Murakami, P. Comte, P. Liska, C. Grätzel, M. K. Nazeeruddin, M. Grätzel, *Thin Solid Films* **2008**, *516*, 4613.

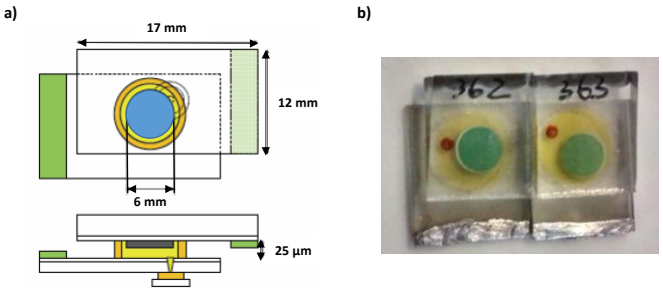

Figure 101. Sketch (left) and pictures (right) of the DSSC device made with dye **35K**.

2.4.7.2 DSSC test results of sensitizers Pz 33-38

The photovoltaic performances of the six Pzs were tested in TiO_2-DSSC employing different thick films and electrolytes (Table 15). Besides, two devices of equal quality were made for each configuration. The values obtained for the best device are presented in Table 15, where we can observe that the device made with $Zn(Pr)_6Pz$ **33** produced larger V_{OC} values (568 mV) and significantly larger J_{SC} (4.64 mA·cm^{-2}) than those prepared with the other sensitizers. Specifically, **33** achieved an overall efficiency of 2.11 %, approximately nine times the efficiency obtained by Pz **36**, which was the second highest. A higher extinction coefficient and more favourable HOMO-LUMO, situated at energetic levels that allow injection in the TiO_2 CB and dye regeneration, as well as being delocalized over the carboxylic group, should explain the larger observed J_{SC}. Pzs **34**, **35K** and **38** show efficiencies that are situated below the noise range of the apparatus (0.1 %): Pz **34** was unstable under illumination, Pz **35K** decomposed upon addition of the acidic coadsorbent CHENO, and Pz **38**, which showed promising HOMO and LUMO characteristics, performed poorly in DSSC devices. Pzs **36** and **37**, which have higher efficiencies, also present very low current densities, probably due to low orbital energy levels and poor injection.

Table 15. Photovoltaic data of the devices made with Pz dyes on TiO_2 films using an iodine-based liquid electrolyte, under simulated one sun illumination (AM1.5G) and active area of 0.159 cm^{-2}.

Dye	Electrolyte[1]	Coadsorbent	Film thickness[2]	J_{SC} (mA.cm^{-2})	V_{OC} (mV)	FF	η
33	0.025 M LiI	CHENO 10 mM	[10+5]	4.64	568.30	0.772	2.11 %
34	0.5 M LiI	CHENO 9 mM	[9+4]	0.07987	273.47	0.648	0.015 %
35K	0.1 M LiI	CHENO 10 mM	[9+4]	0.25498	423.46	0.713	0.08 %
36	0.5 M LiI	CHENO 9 mM	[9+4]	0.84448	393.95	0.688	0.24 %
37	0.1 M LiI	--	[5+5]	0.46931	430.65	0.744	0.15 %
38	0.1 M LiI	CHENO 20 mM	[5+5]	0.29006	427.40	0.73	0.09 %

[1] Electrolyte A is composed of the indicated molarity of LiI, 0.6 M (except for Pz **33**, 0.9 M) DMII, 0.28 M TBP, 0.04 M I_2 and 0.05M guanidinium thiocyanate, in AcCN. [2] The TiO_2 film thickness [x + y] consists of an x µm thick TiO_2 active layer and an additional y µm of scattering layer.

As the results obtained for Pz **33** were significantly better than for the rest of Pz dyes, we focused on optimizing its DSSC devices, modifying the film thickness and the electrolyte, varying the proportions of the components of electrolyte A, and using also a cobalt based electrolyte. In the end, seven devices using iodine-based electrolytes and three with cobalt-based electrolytes (and at least two identical cells for each) were fabricated. The results of the best obtained for each configuration are summarized in Table 16.

First, keeping constant the electrolyte used before, the film thickness was modified, observing that the best efficiency was obtained with 6 μm active layer + 3 μm scattering layer (entries 1, 2 and 3, Table 16). Regarding the iodine electrolyte, the focus was first on optimizing the amount of LiI. A higher content of LiI produces a downshift of the TiO_2 CB, which can improve the electron-injection for dyes that have a low-lying LUMO, and hence produce larger J_{SC}. As a drawback, lowering the TiO_2 CB concurrently decreases the $V_{OC.}$ Furthermore, the small-radius Li^+ cation can deeply penetrate deep into the mesoporous TiO_2 film. Thus, it can combine with the electrons in the conduction band of TiO_2 to form an ambipolar $Li^+–e^–$. This produces an increase of the transport speed of electrons and enhances the J_{SC} of DSSCs. The negative influence of the small cations in the TiO_2 film is that the cations easily combine with triiodide species leading to recombination losses and the decrease of V_{OC}.[152] The amount of LiI was increased from 0.025 M up to 0.5 M, finding the best results at a concentration of 0.1 M (entry 4, Table 16). Finally, the concentration of dimethylimidazolium iodide was also varied and found optimum at a value of 0.6 M (entries 5 and 6, Table 16). This type of additive contributes to the enhancement of conductivity of $I_3^–/I^–$ electrolyte and their multilayer adsorption on the TiO_2 surface, increasing the electron diffusion coefficient.[152,232] On the other hand, a high concentration can cause reduction of the dye molecules, which cannot then effectively inject electrons into the semiconductor.[152] Finally, when using the cobalt-based electrolyte greater V_{OC} was observed (630 mV), but much lower J_{SC} was obtained, resulting in much lower overall efficiency of only η = 0.59% in the best case (entries 8, 9 and 10, Table 16).

Therefore, the performance of Pz **33** was optimized up to an efficiency of η = 3.42 %, with J_{sc} = 7.58 mA·cm^{-2}, V_{OC} = 572 mV and a fill factor FF = 0.764 (Figure 102). This efficiency value is comparable to those obtained with phthalocyanine TT-1 (η = 3.65 %), measured in the same conditions as a reference. Although J_{sc} of Pz **33** is lower than that of TT-1 (J_{sc} = 8.61 mA·cm^{-2}), V_{OC} and FF are higher.

[232] V. Suryanarayanan, K. –M. Lee, J.-G. Chen, K. –C. Ho, *J. Electroanal. Chem.* **2009**, 146.

Table 16. Photovoltaic data of the devices made with dye Pz **33** using different configurations under simulated one sun illumination (AM1.5G) and active area of 0.159 cm^{-2}.

Pz 33	Electrolyte (M)					Coadsorbent	Film thickness	J_{SC} ($mA.cm^{-2}$)	V_{OC} (mV)	FF	η
Entry	LiI	DMII	TBP	I_2	GuNCS						
TT1[1]	0.1	0.6	0.28	0.04	0.05	CHENO 10 mM	[9+4]	8.61	564.64	0.722	3.65 %
1	0.025	0.9	0.28	0.04	0.05	CHENO 10 mM	[10+5]	4.64	568.30	0.772	2.11 %
2	0.025	0.9	0.28	0.04	0.05	CHENO 10 mM	[6+3]	5.53	609.77	0.778	2.72 %
3	0.025	0.9	0.28	0.04	0.05	CHENO 10 mM	[5+5]	4.91	593.55	0.776	2.34 %
4	0.1	0.6	0.28	0.04	0.05	CHENO 10 mM	[6+3]	7.58	572.41	0.764	**3.42 %**
5	0.2	0.6	0.28	0.04	0.05	CHENO 10 mM	[6+3]	7.21	553.01	0.760	3.11 %
6	0.2	0.9	0.28	0.04	0.05	CHENO 10 mM	[5+5]	4.66	499.93	0.734	1.80 %
7	0.5	0.6	0.28	0.04	0.05	CHENO 10 mM	[6+3]	6.78	451.44	0.713	2.50 %
8	Cobalt electrolyte[2]					CHENO 10 mM	[5+5]	0.95	545.50	0.639	0.35 %
9	Cobalt electrolyte[2]					CHENO 10 mM	[9+4]	0.93	622.47	0.712	0.43 %
10	Cobalt electrolyte[2]					CHENO 10 mM	[4+4]	1.20	630.24	0.756	0.59 %

[1] Pc TT-1 is measured in the same conditions as entry 4 as reference. [2] The cobalt electrolyte consists of: 0.06 M $Co(Bipy)_3(PF_6)_3$, 0.25 M $Co(Bipy)_3(PF_6)_2$, 0.1 M LiTFSI, and 0.5 M TBP in AcCN.

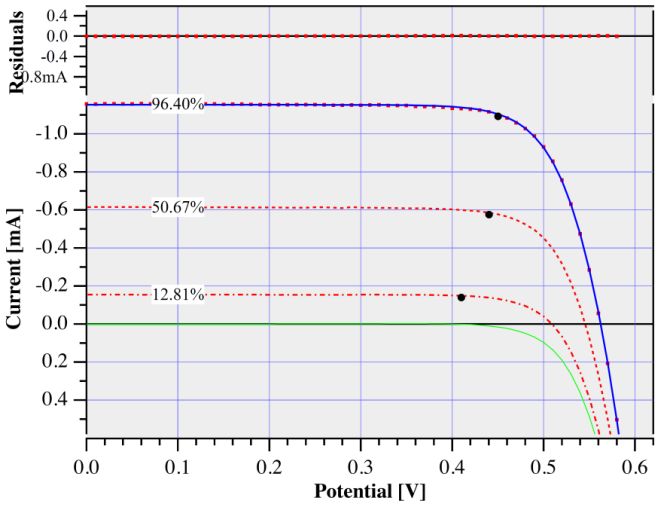

Figure 102. I-V curve of Pz **33** entry 4. Each curves show the performance at a different percentage of illumination, being 100% = 1 Sun = 100 $mW{\cdot}cm^{-2}$. Green line represents the dark current.

$Zn(Pr)_6Pz$ **33** show an IPCE that maximizes at 620 nm with a value of 60% (Figure 103). The shape of the IPCE curve is in agreement with the absorption spectrum of the dye shown in Figure 93, *vide supra*.

Finally, aging experiments were carried out to assess the stability of the device under illumination (Figure 104). Under ambient light illumination, the overall efficiency of the tested device decreases from η = 3.05 % to η = 2.53 % in 3 days. On the other hand, under 1 sun illumination (AM1.5G), the drop in the device performance sharpens and after one more day it goes down to η = 1.68 %. After a total of 6 days of illumination (3 under ambient light and 3 under 1 sun illumination), the efficiency of the device has dropped by a 65% from η = 3.05 % to η = 1.08 %

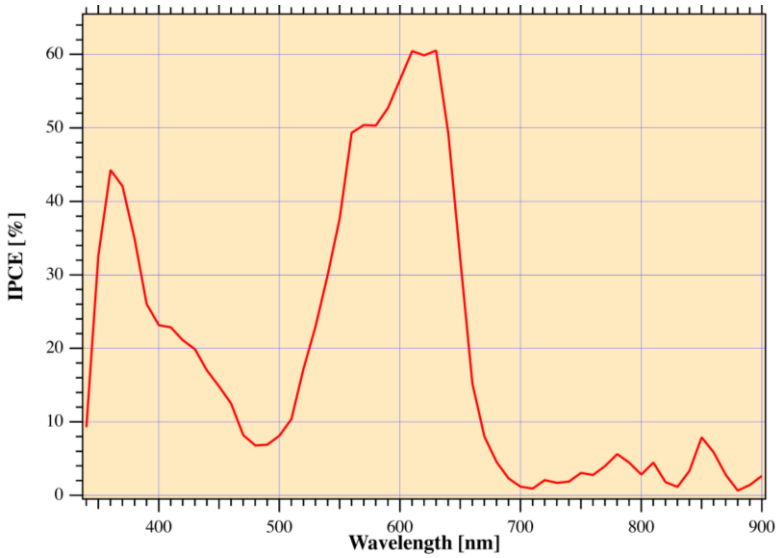

Figure 103. Incident photon-to-electron conversion efficiency of the photovoltaic device sensitized with Pz **33**.

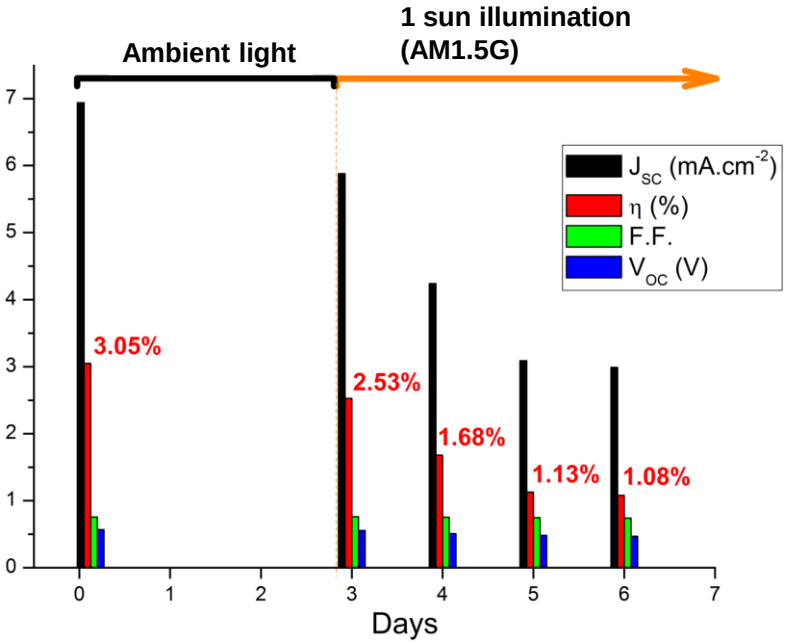

Figure 104. Aging experiment of a photovoltaic device sensitized with Pz **33**.

2.5 Synthesis of new Pzs by modification of the anchoring group

Several studies have been carried out that have demonstrated that the introduction of different spacers in the anchoring group of a dye can greatly influence its performance on light harvesting devices.[203] On this behalf, we decided to modify the spacer between the porphyrazine macrocyclic core and the carboxylic acid anchoring group. Three different A_3B porphyrazines were designed. All of them contained propyl groups directly attached to the pyrrole β-positions, as in **33**, while the fourth subunit was a pyrrole containing a carboxylic acid function attached directly or through different linkers (Figure 105). In Pz **65**, the carboxylic acid is directly linked to pyrrolic unit and, in Pzs **66** and **67**, the anchoring function is separated from the macrocycle by either a double or a triple bond, respectively. The direct attachment to the pyrrole ring could provide the dye with better injection into the semiconductor, and the inclusion of different spacers should modify the orientation of the molecule in the mesophase and enhance the directionality in the excited state.

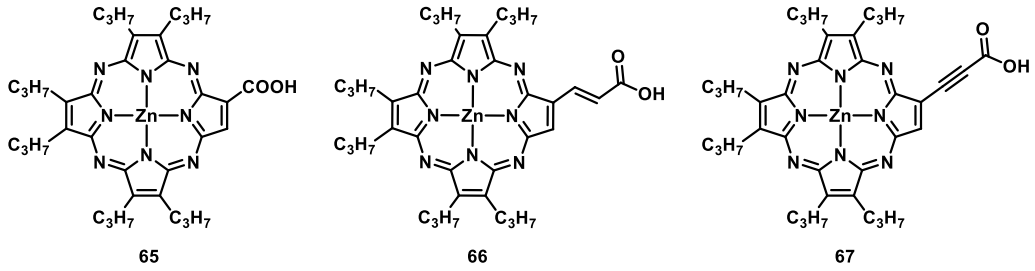

Figure 105. Chemical structure of Pzs **65**-**67**.

The synthetic route devised for the three new derivatives was based on a methodology developed by Liebeskind and Srogl, consisting in the palladium-catalysed, copper(I) thiophene-2-carboxylate (CuTC)-mediated coupling of boronic acids with heteroaromatic thioethers.[233] In our case, we would need to synthesize the hexapropylmonothioethylPz precursor (Pz **69**, Retrosynthetic Scheme 33) and perform the coupling reactions with the corresponding alkenyl- or alkynylboronic acid derivatives.

The oxidative cleavage of a vinyl Pz **70** to yield an aldehyde, followed by a second oxidation to the acid would lead to Pz **65**.[234]. Porphyrazines **66** and **67** would be the product of the hydrolysis of the methyl esters of Pzs **72** and **73**.

[233] L. S. Liebeskind, J. Srogl, Org. Lett. 2002, 4, 979
[234] A. Gouloumis, S. –G. Liu, A. Sastre, P. Vázquez, L. Echegoyen, T. Torres, *Chem. Eur. J*. **2000**, *6*, 3600.

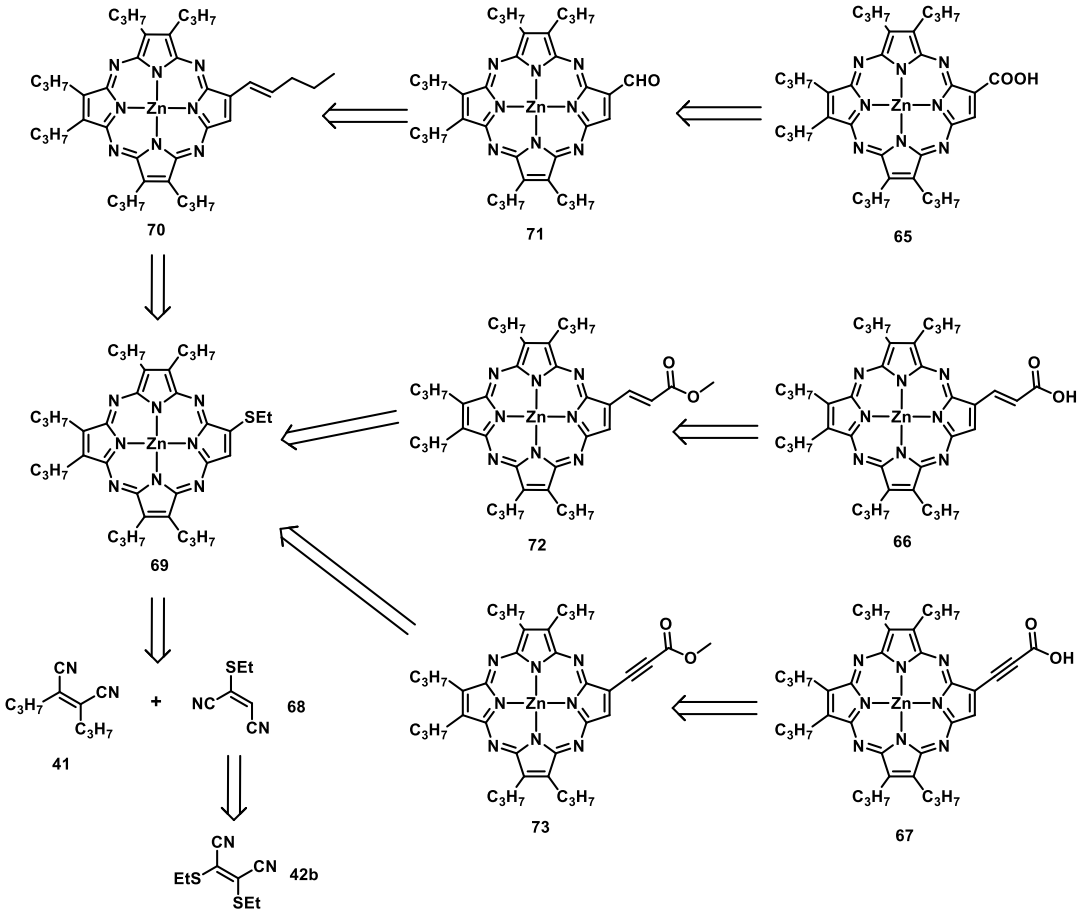

Scheme 33. Retrosynthetic analysis of Pzs **65**-**67**.

2.5.1 Synthesis of the maleonitrile precursors

Monothioethylmaleonitrile **68** was prepared by controlled desulfuration reaction of one of the thioethyl groups in maleonitrile **42b**, using a variation of the Liebeskind-Srogl cross-coupling conditions described by Arroyo *et al*. (Scheme 34).[235] Treatment of bis thioethylmaleonitrile with 1.5 equivalents of CuTC and triethylsilane afforded a mixture of the starting material, the monothioethyl and the unsubstituted maleonitrile. After separation by column chromatography, monothioethylmaleonitrile **68** was obtained in a fair 45 % yield as a yellow oil.

[235]I. J. Arroyo, R. Hu, G. Merino,B. Z. Tang, E. Peña-Cabrera, *J. Org. Chem*. **2009**, *74*, 5719.

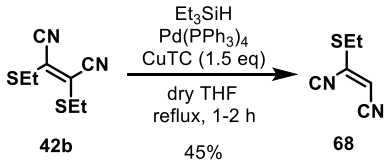

Scheme 34. Synthesis of maleonitrile **68**.

The next step was the synthesis of the boronic acid precursors. The synthesis of [(1*E*)-3-Methoxy-3-oxoprop-1-en-1-yl]boronic acid **74** was carried out following a reported procedure, that consists in the hydroboration reaction of methylpropiolate, affording the desired product in excellent yields (Scheme 35).[236]

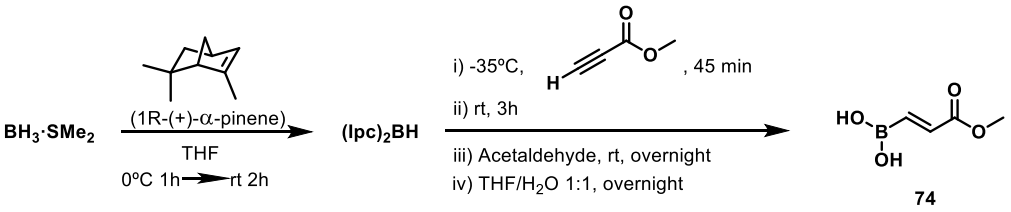

Scheme 35. Synthesis of boronic acid **74**.

The synthesis of the corresponding alkynylboronic ester was also attempted through dehydrogenative borylation of methyl propiolate following a reported procedure (Scheme 36).[237] However, purification of the compound was not possible by distillation as the product darkened, probably due to polymerization side reactions.[237a] Furthermore, the lability of the B–C_{sp} bond made impossible any attempt of hydrolysis or purification by column chromatography. This compound, and therefore the synthesis of Pz **67** was discarded.

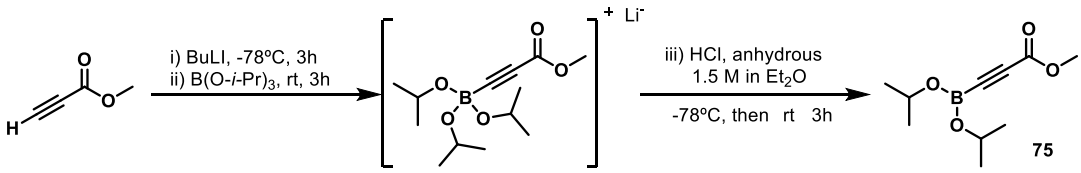

Scheme 35. Unsuccessful synthesis of the alkynylboronate **75**.

The Liebeskind-Srogl cross-coupling copper mediator, CuTC, was synthesized as depicted in Scheme 36, following a reported procedure.

[236]a) F. Berrée, A. Debache, Y. Marsac, B. Collet, P. Girard-Le Bleiza, B. Carboni, *Tetrahedron* **2006**, *62,* 4027; b) M. V. Chelliah *et al*. *J. Med. Chem.* **2007**, *50,* 5147.

[237] a)H. C. Brown, N. G. Bhat, M. Srebnik, *Tetrahedron Lett*. **1988**, *29*, 2631; b) R. Morita, E. Shirakawa, T. Tsuchimoto, Y. Kawakami, *Org. Biomol. Chem*. **2005**, *3*, 1263.

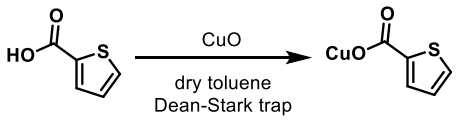

Scheme 36. Synthesis of CuTC.

2.5.2 Synthesis of the porphyrazines

Monothioethylporphyrazine **69** was prepared by crossover Lindstead macrocyclization of a 3:1 mixture of maleonitriles **41** and **68**, in the presence of freshly prepared magnesium propoxide. This led to a mixture of MgPzs, which was subsequently demetallated with TFA. Further reaction of the free-base mixture of Pzs with $Zn(OAc)_2$ in a refluxing 1:1 mixture of DMF/PhCl, followed by column chromatography on silica gel, yielded the desired A_3B Pz **69** (Scheme 37) in 7% yield.

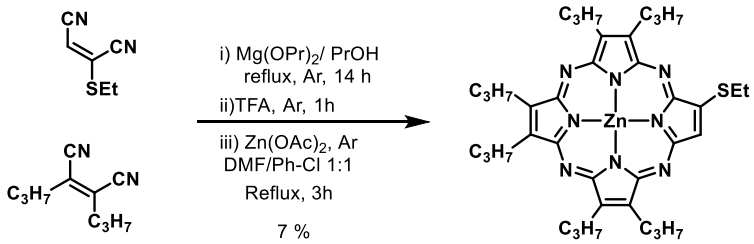

69

Scheme 37. Synthesis of ZnPz **69**.

A monocrystal of ZnPz **69** was obtained by diffusion of MeOH in a DCM solution of the porphyrazine overnight. The structure was determined by X-Ray diffraction. Figure 105 shows the Zn atom situated above the macrocycle and coordinating a MeOH molecule. The porphyrazine rings are arranged into head-to-head *J*-aggregates, the head being the macrocyclic face to which the axial ligand is attached. The porphyrazines present π-π interactions with the molecules directly above and below in the same row, and Van der Waals interactions between the different rows.

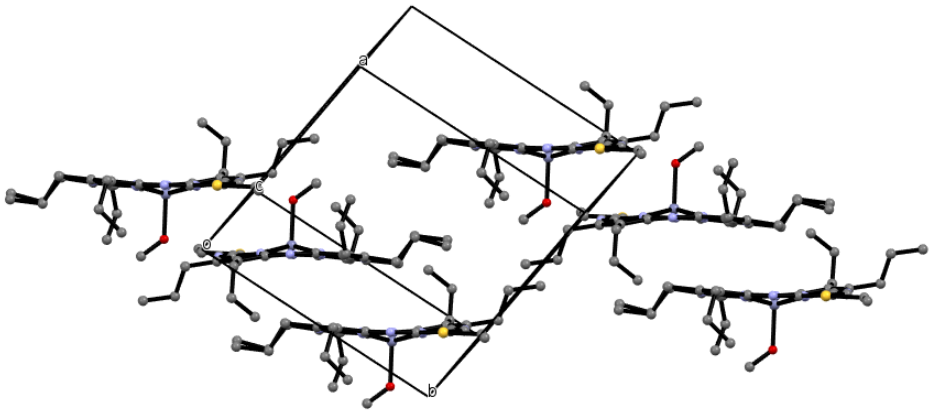

Figure 106. X-Ray structure of ZnPz **69**, including the unity cell.

The synthesis of Pz **70** was first essayed from the commercially available 1-penten-1-ylboronic acid, by applying the reaction conditions previously described in our group, that is, using three equivalents of arylboronic acid and CuTC, and 10 % mol of palladium catalyst per thioether unit.[217] Under these conditions, we also detected by mass spectroscopy the transmetallated CuPz **70b** accompanying ZnPz **70** (Figure 106). Attempts to remove the copper atom from the central cavity with TFA were unsuccessful. In order to minimize the transmetallation reaction, we reduced the amount of CuTC added to 1.2 equivalents (Scheme 38). Under these conditions, we were able to isolate **70** in good yields.

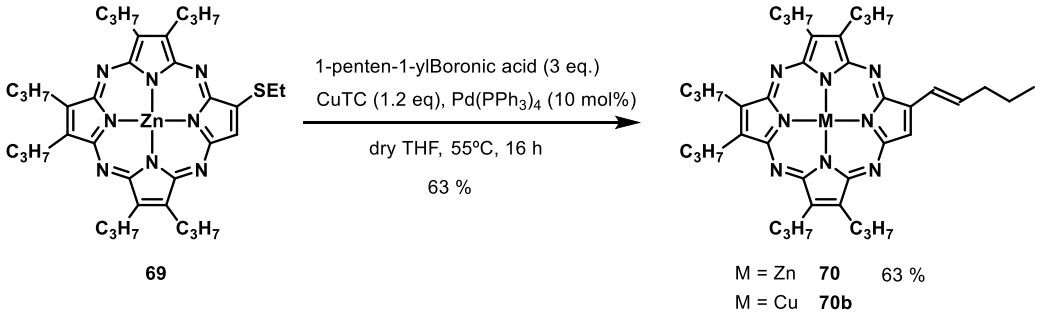

Scheme 38. Synthesis of Pz **70**.

Conversely the same coupling reaction conditions using the boronic acid **74** led to the formation almost exclusively of the copper Pz **72**. Some other coloured products were spotted on the TLC but none of them could be identified as the desired ZnPz **72**. Furthermore, once again any attempts to remove the Cu from the Pz core was ineffective.

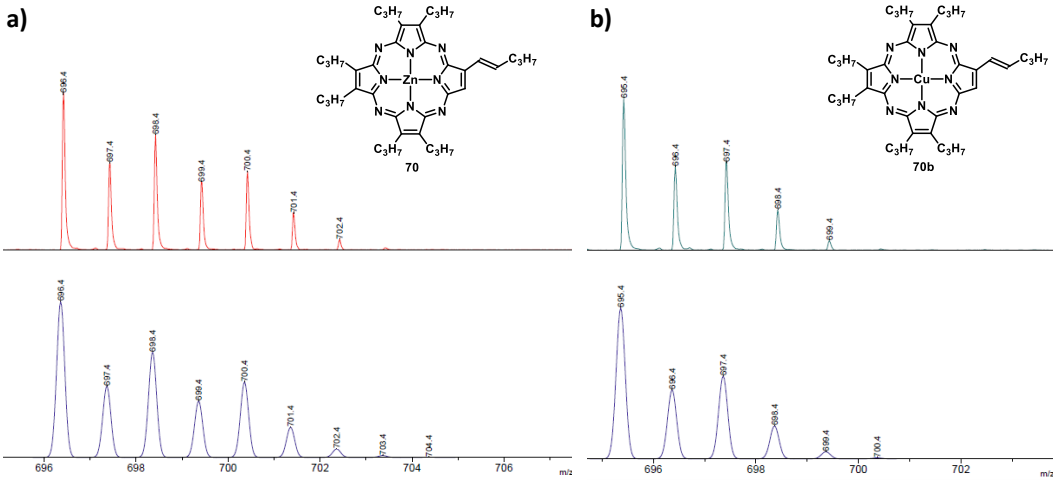

Figure 107. Experimental (top) and simulated (down) isotopic distribution of the main peak of the mass spectra of ZnPz **70** (a) and CuPz **70b**.

We focused then, on the synthesis of ZnPz **65**. Oxidation of the vinyl double bond of ZnPz **70** was performed by reaction of the macrocycle with OsO_4 and $NaIO_4$ (Scheme 39).[234] ZnPz **71** was thus obtained in 85 % yield. Further oxidation of ZnPz **71** with $NaClO_2$ and sulfamic acid produced the carboxylic acid **65** in 63 % yield.

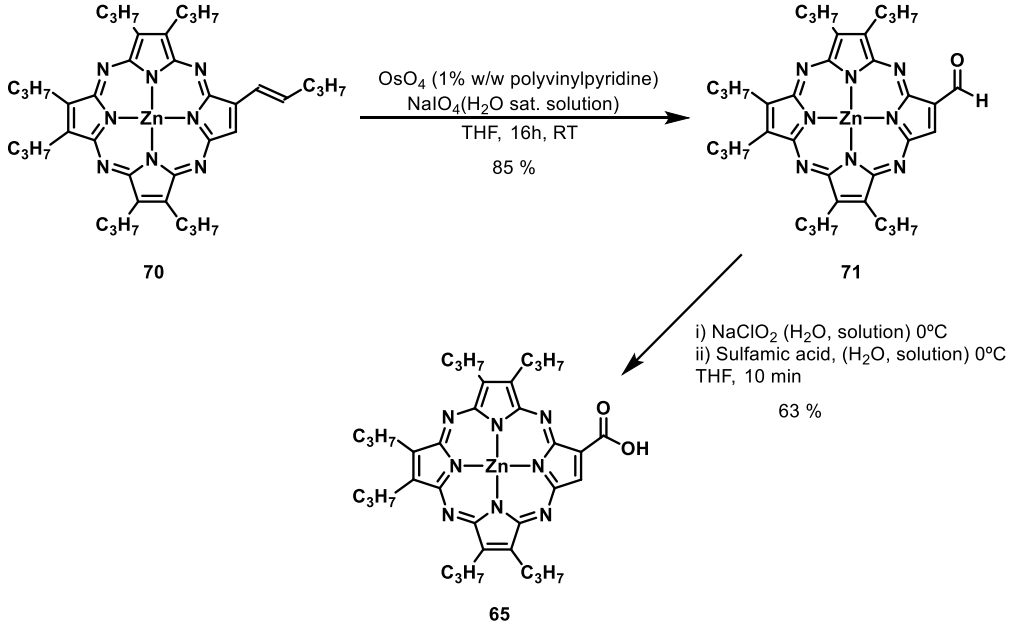

Scheme 39. Synthesis of ZnPz **65**.

Figure 107 shows the ^{1}H-NMR spectra of Pzs **70**, **71** and **65**. All of them display similar aliphatic signals corresponding to the peripheral propyl groups. In addition, the signals corresponding to the aliphatic part of the pentenyl chain in the spectrum of Pz **70** overlap with those of the peripheral propyl groups, while the signals assigned to the vinyl protons appear at δ = 8.0 ppm, very much influenced by the anisotropic Pz current. Furthermore, a signal at δ = 9.0 ppm accounts for the pyrrolic H^{β}. Ongoing from **70** to **71** the electron-withdrawing aldehyde produces a downfield shift on the H^{β}, and the effect is even more pronounced in the case of **65**, owing to the presence of the carboxylic acid (δ = 9.5 ppm and δ = 9.65 ppm, respectively). Finally, the signals corresponding to the protons of the aldehyde and the acid are found at around 12 and 15 ppm.

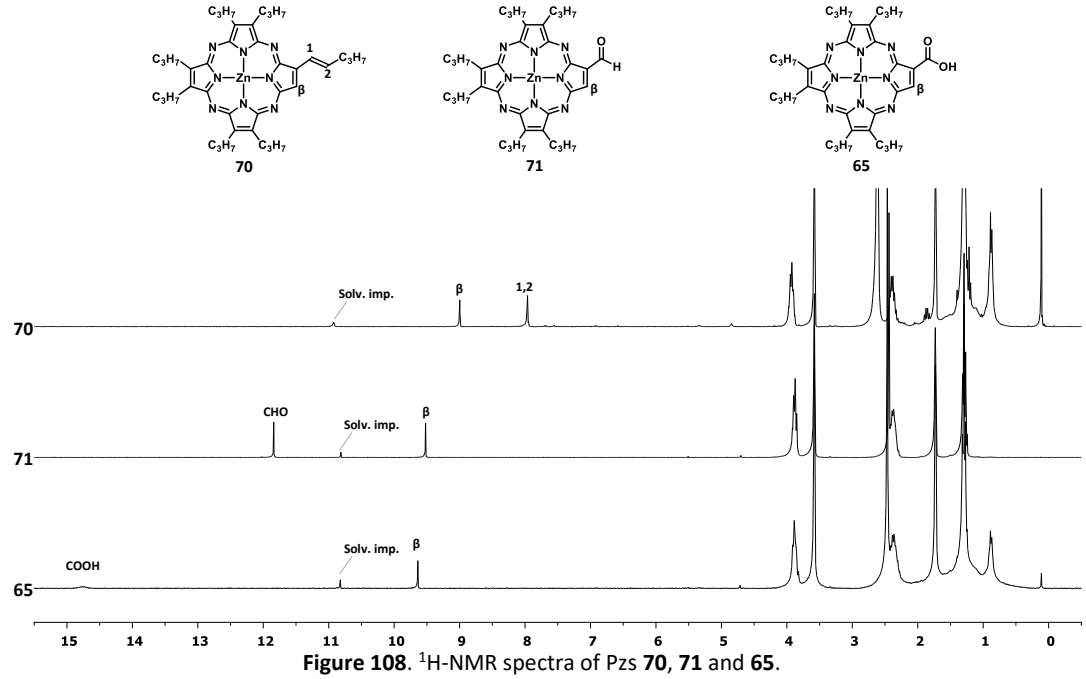

Figure 108. ^{1}H-NMR spectra of Pzs **70**, **71** and **65**.

2.5.3 Optical properties

The Pz series **69**-**71** and **65** exhibit lower molar absorption coefficients in their absorption spectra than Pzs **33**-**38**, probably owing to the decrease in the π-conjugation produced by the removal of the fused benzene ring (Figure 108). The conversion of the thioether in Pz **69** into the acid in Pz **65** produces a reduction of symmetry in the Pz, which is reflected by a splitting of the *Q*-band that is already manifest for pentenylPz **70** (~20 nm), maximizes for Pz **71** (~55 nm) and decreases again for Pz **65** (~35 nm). The lowest energy absorption appears in all cases in a range between 615 and 625 nm. The *B*-band also splits in the spectra of Pzs **71** and **65**, and is centred at ~350 nm for all Pzs.

All the Pzs are fluorescent and their emission maxima display small Stokes shifts (less than 10 nm). Figure 110 presents the normalized absorption and emission spectra of Pz **65**. The intersection point of the curves is situated at 621 nm.

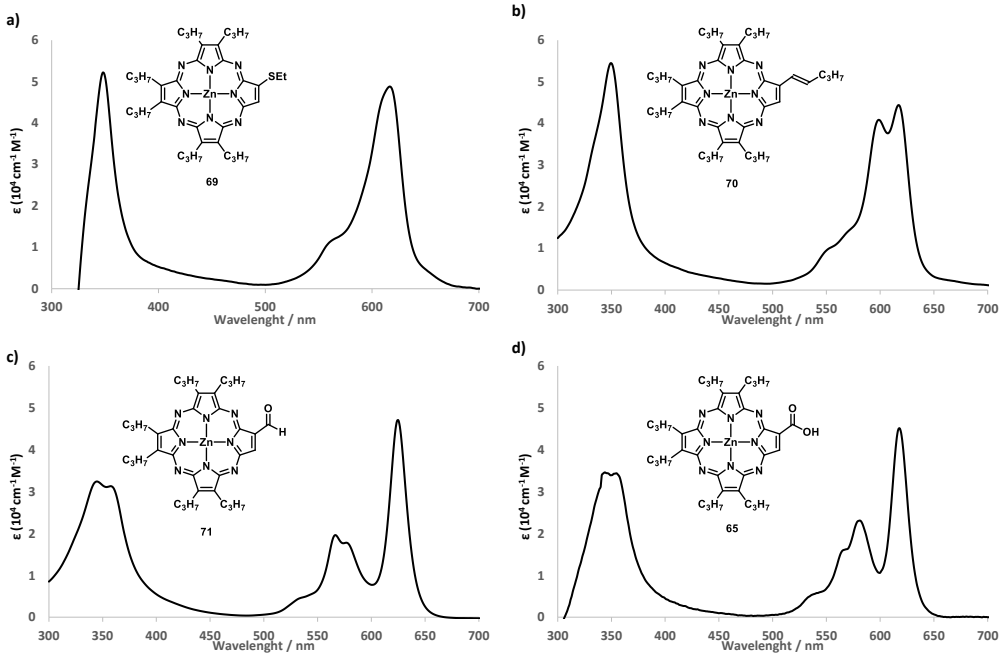

Figure 109. Absorption spectra of Pzs **69**, **70**, **71** and **65**.

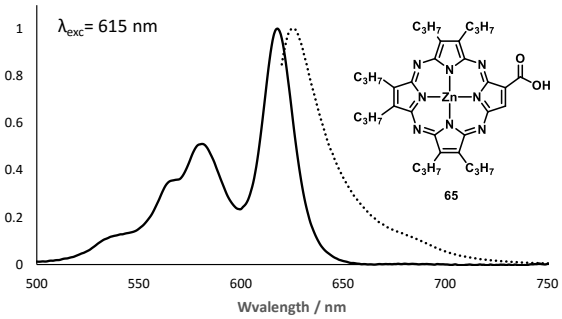

Figure 110. Normalized absorption and emission spectra of Pz **65**.

2.5.4 Electrochemical studies

Electrochemical experiments (cyclic voltammetry, square wave and differential pulse voltammetry (DPV)) were conducted in the same experimental conditions as Pzs **33**-**38**.

Similarly to porphyrazines **33**-**38**, the first oxidation of the macrocycle takes place at +0.56 V, 60 mV lower than Pz **33**. This was only detectable in square wave voltammetry (Figure 109b, dashed line). In the cathodic window (Figure 109a), the first reduction process appears at –1.08 V, that is, 63 mV more positive than for Pz **33**. Two more reduction waves can be located in square wave, appearing at –1.57 V and –2.36 V. The data are summarized in Table 17.

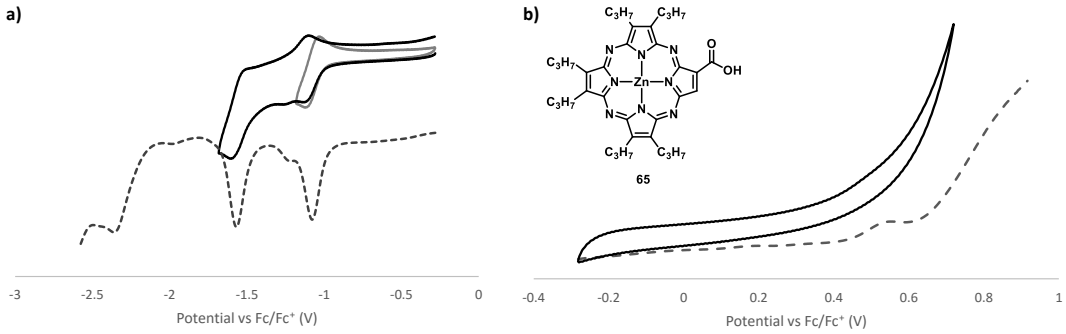

Figure 111. Cyclic (solid line) and square wave (dashed line) voltammogram of Pz **65**.a) Anodic window. b) Cathodic window.

Table 17. Redox potentials ($E_{1/2}$ in V) *vs*. Fc/Fc^+ in THF (0.1 M $TBAPF_6$) of Pzs **33** and **65** at room temperature using a glassy carbon electrode.

Pz	E_{Red3}	E_{Red2}	E_{Red1}	E_{Ox1}
33		–2.39[a]	–1.71[a]	0.62[a]
65	–2.36[a]	–1.57	–1.08	0.56[a]

[a] Irreversible.

2.5.5 Calculation of HOMO-LUMO levels

The experimental HOMO and LUMO energy levels of the molecule were calculated applying Equations 22 (directly from the first reduction and oxidation values) and 23 (applying the absorption onset value). Also, DFT studies were carried out to optimize the geometry of **65** (B3LYP/3-21G) and calculate the energy levels at the same level (B3LYP/6-31G (d,p)). The results are presented in Table 18 and graphically in Figure 112.

Experimental values place the HOMO level of Pz **65** at –5.7 eV and the LUMO at –4.0 and –3.7 eV when calculating it from the first reduction potential or from the absorption onset, respectively. The theoretical calculations rendered the HOMO at –5.6 and LUMO at –3.1 eV. All

the values are very similar to those found for Pz **33** except for the LUMO calculated from the first reduction potential, which is much lower in energy and might indicate some problems for injection into the TiO_2 conduction band. Nonetheless, when calculating the LUMO by using other procedures such as equation 23, the value comes very close to that obtained for Pz **33**.

Table 18. Experimental and theoretical HOMO-LUMO energy levels data (in eV) of dyes **33** and **65**.

Pz	Experimental			Computational studies[3]			
	HOMO[1]	LUMO[1]	LUMO[2]	HOMO	LUMO	HOMO (solv)	LUMO (solv)
33	–5.7	–3.4	–3.8 (630 nm)	–5.4	–3.0	–5.3	–2.9
GAP	2.3		1.9	2.42		2.40	
65	–5.7	–4.0	–3.7 (634 nm)	–5.6	–3.1	–5.6	–3.1
GAP	1.7		2	2.5		2.5	

[1] Calculated applying Equation 22. [2] Calculated applying Equation 23. [3] Calculated using DFT B3LYP/6-31G (d,p) both in vacuum and solvated in THF.

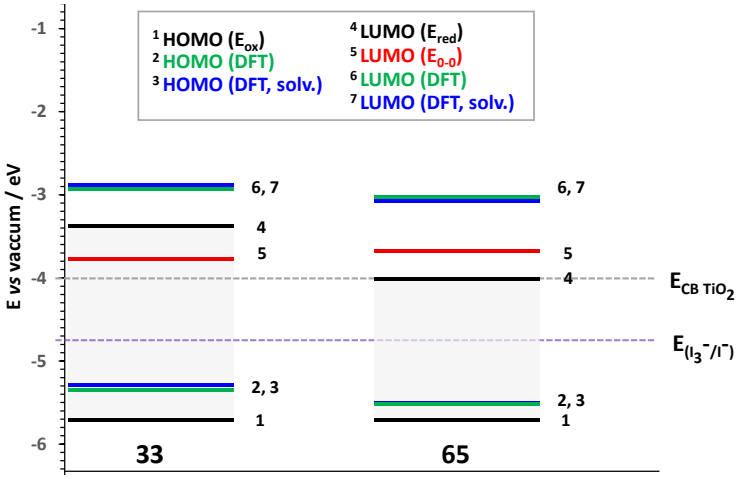

Figure 112. Representation of the HOMO and LUMO levels of Pzs **33** and **65**.

Figure 113 shows the theoretical distribution of the HOMO and the LUMO of Pzs **31** and **65**. The HOMO of **65** is located over the macrocycle while the LUMO orbitals are also extended to the carboxylic functions for both Pzs **33** and **65**

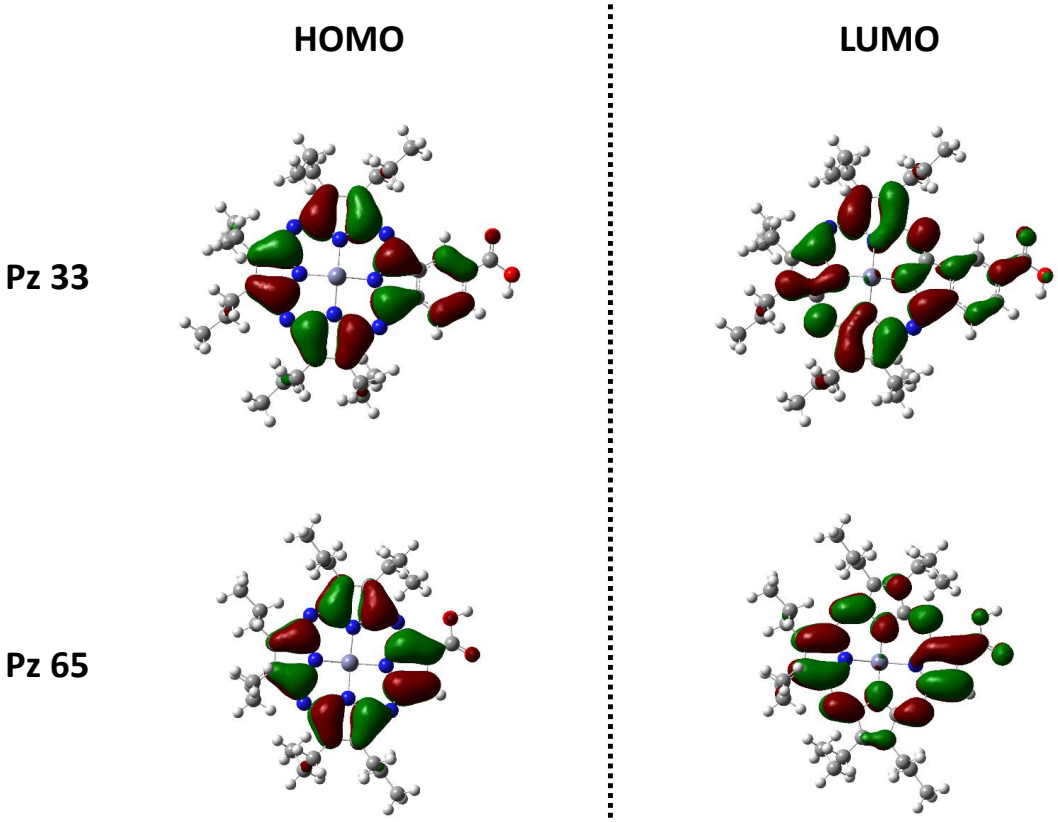

Figure 113. HOMO and LUMO orbitals of Pzs **33** and **65**.

2.5.6 Photovoltaic performances in TiO_2-DSSC

The performance of Pz **65** will also be determined in the laboratory of Professors M. Grätzel and M. K. Nazeeruddin the École Polytechnique Fédérale de Lausanne in the near future.

2.6 Summary and conclusions

We have designed and synthesized a series of six porphyrazine derivatives of A_3B type, in which unit B is an isoindole 4-carboxylic acid similar to that of TT-1, while unit A has been functionalized with a variety of groups, namely, alkyl, thioether, amino and *p*-substituted aryl groups. We have studied the electronic and redox properties of the Pz dyes and estimated the HOMO and LUMO energy levels based in experimental data and in DFT calculations. As expected, the direct attachment of different chemical functions to Pz periphery produces strong perturbation on the electronic and redox properties of the dyes.

Measurements of the performance of the dyes revealed efficiencies over 2% for porphyrazine endowed with six peripheral propyl groups. Optimization of the parameters of the cell such as film thickness or electrolyte composition raised this value up to 3.42 %, close to that observed for Pc TT-1 under the same conditions.

In the second part of this Chapter we have started to modify unit B, containing the anchoring group. We have prepared a new Pz based photosensitizer containing the anchoring group, namely a carboxylic acid function, directly attached to the pyrrole β-position. This unprecedented dye could provide an enhanced electronic communication with the semiconductor, related to TT-1.

As a general conclusion to this chapter, we have tested for the first time in DSSCs several photosensitizers based in porphyrazines. Although the efficiencies are not as high as those observed for porphyrins or Ru-complexes, they are promising results taking into account that only six compounds have been tested so far, and there is plenty of room for structural modification and optimization.

2.7 Experimental section

2.7.1 Synthesis of ZnPz derivatives containing an isoindole-4-carboxylic unit

2.7.1.1 Synthesis of the maleonitrile precursors.

4,5-Dibromo-4E-octene (39)[218]

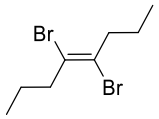

A solution of bromine (32.6 mL, 0.64 mol) in acetic acid (175 mL) was added dropwise to 4-octyne (70.5 g, 0.64 mol) dissolved in an equal amount of AcOH (175 mL) at such rate as not to develop an orange colour in the flask. After the addition was complete the solution was stirred 30 min and then poured into ice water (2 L). A yellow oil separated under the aqueous layer and was collected. The oil was extracted in CH_2Cl_2 (750 mL), and the resulting solution was washed with saturated aqueous $NaHCO_3$ (3 times, 150 mL), water (2 times, 150 mL), and dried ($MgSO_4$). The solvent was removed by rotary evaporation to yield a yellow oil (crude 85 g, 50%) which was used without further purification.

Dipropylfumaronitrile (40)[218]

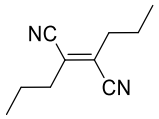

A suspension of CuCN (23.3 g, 0.26 mol) in anhydrous DMF (310 mL) was heated to 145°C for approximately 1 h, then it was cooled to 130°C and 4,5-dibromo-4E-octene (35 g, 0.13 mol) was added all at once. The solution turned dark brown, and it was still heated for 14 h. After this time the solution was allowed to cool down to room temperature and carefully poured into concentrated ammonium hydroxide (0.5 L). The solution was stirred for approximately 30 min, and portions (100 mL) were extracted three times each with hexane (100 mL). The large volume of hexanes was reduced to approximately 150 mL and washed with water and brine to remove any residual DMF. The organic layer was dried ($MgSO_4$), and the solvent was removed by rotary evaporation. The resulting brown oil was purified by vacuum distillation to give a yellow oil (10 g, 48%).

^{1}H NMR (300 MHz, $CDCl_3$) δ (ppm) = 2.51 (t, *J* = 7.5 Hz, 4H), 1.65 (m, *J* = 7.4 Hz, 4H), 0.96 (t, *J* = 7.4 Hz, 6H).

2,3-Dipropylmaleonitrile (41)[218]

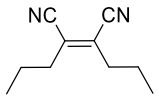

Fumaronitrile **40** (13 g) was dissolved in dry acetonitrile (300 mL) in a quartz photochemical reactor fitted with a magnetic stirrer. Nitrogen was bubbled through the solution for a minimum of 20 min before the solution was irradiated at 253 nm (*λ*max) with a 250W Hg lamp, keeping the reaction at rt. After approximately 60 h the reaction reached a photostationary state and was stopped. The solvent was removed by rotary evaporation, and the cis and trans isomers were separated by fractional distillation under high vacuum. The trans isomer distilled first, at about 40°C lower than the desired cis isomer (7.3 g, 57% cis isolated).

^{1}H NMR (300 MHz, $CDCl_3$) δ (ppm) = 2.29 (t, *J* = 7.5 Hz, 4H), 1.56 (m, *J* = 7.5 Hz, 4H), 0.92 (t, *J* = 7.4 Hz, 6H).

2,3-Dithioetylmaleonitrile (42)[219b]

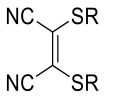

3a: R=C_2H_5
3b: R=C_5H_{11}

To a suspension of finely grounded NaCN (29.4 g, 0.6 mol) in 180 mL of dry DMF, carbon disulfide (36.5 mL, 0.6 mol) was added dropwise at 0°C. When the addition is over the solution is vigorously stirred at rt for 30 min before adding 500 mL of *i*-BuOH and heating the mixture to reflux for 10 min. The solution was filtered while hot and then cooled in an ice-salt bath, upon which a brown precipitate appears, that is filtered and washed thoroughly with Et_2O, obtaining 130 g of a yellow solid. The solid is dissolved in 1 L of distilled water and left for 1 day. The sulphur formed was eliminated by filtration and the water eliminated in the rotary evaporator. Ethanol (400 mL) is added to the remaining oil and heated up to its boiling point and filtered while hot. When the solution cools down again to rt, Et_2O was added until a yellow precipitate appears, which corresponds to the maleonitrile dication (30 g).

42a: To a suspension of this solid (10.5 g, 0.056 mol) in acetone (260 mL), bromopentane (18 g, 0.119 mol) and a spoon of NaI were added, and the mixture was stirred at rt for 72h. After this time, the solvent was eliminated at reduced pressure. Water was added to the residue and it was extracted three times with hexane. The organic phase is washed again with water and dried over $MgSO_4$ before eliminating the solvent. The yellow oil is purified by column chromatography on silica gel using hexane as eluent to yield the compound as a yellow oil (12.2 g, 77%).

^{1}H NMR (300 MHz, $CDCl_3$) δ(ppm) = 3.08 (t, 4H), 1.78 – 1.61 (m, 4H), 1.47 – 1.22 (m, 8H), 0.88 (t, *J* = 7.0 Hz, 6H).

42b: To a suspension of this solid (20 g, 0.107 mol) in acetone (550 mL), bromoethane (25 g, 0.229 mol) and a spoon of NaI were added, and the mixture was heated to reflux for 20h. After this time the solution was filtered hot and the solvent eliminated in the rotary evaporator. The orange oily residue was purified by column chromatography on silica gel (eluent: hexane/AcOEt 3:1) to yield the compound as a yellow oil (18.07 g, 85%).

^{1}H NMR (300 MHz, $CDCl_3$) δ (ppm) = 3.12 (q, *J* = 7.4 Hz, 4H), 1.39 (t, *J* = 7.4 Hz, 6H).

2,3-bis(dimethylamino)maleonitrile (43)[220]

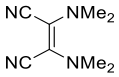

A solution of diaminomaleonitrile (10 g, 0.1 mol) in 60 mL of dimethoxyethane was added dropwise to a suspension of NaH (60% in mineral oil, 20 g, 0.5 mol) in 200mL of dimethoxyethane at -30°C. Then the reaction mixture was heated to -10°C, and dimethylsulfate (48 mL, 0.5 mol) was also added dropwise over 2 h. The precipitate of unreacted NaH and dimethylsulfate was washed with THF (100 mL) and the solvent of the combined filtrate and wash evaporated at rt, and to eliminate the excess of dimethylsulfate, the residue was diluted in diethylether and washed with 30% NH_3 (aq). The aqueous phase was discarded and the organic solvent was eliminated, yielding the compound as a brown oil (mixture of maleo/fumaronitrile 15:85, 11.4 g, 75%)

^{1}H NMR (300 MHz, $CDCl_3$) δ(ppm) = 2.66 (s, 12H)
^{13}C NMR (75.5 MHz, $CDCl_3$): δ(ppm) = 117.45, 114.71, 41.94.

(4-*tert*-Butylphenyl)acetonitrile (44)[221]

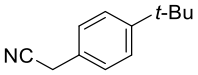

4-*tert*-Butylbenzyl chloride (25 g, 0.137 mol), finely-grounded NaCN (10.1 g, 0.205 mol), and NaI (3.0 g, 0.02 mol) were suspended in acetone (30 mL), and the mixture was heated to reflux for 48 h. The reaction mixture was filtered hot, and the filtrate was concentrated under vacuum. The residue was extracted in $CHCl_3$, washed with hot water twice, and dried ($MgSO_4$). The $CHCl_3$ was eliminated under reduced pressure yielding a yellow oil. The product was distilled under vacuum at 110 °C to yield a clear oil (22.96 g, 97%).

^{1}H NMR (300 MHz, $CDCl_3$) δ(ppm) = 7.43 (m, 2H), 7.28 (m, 2H), 3.73 (s, 2H), 1.35 (s, 9H).

Bis(4-*tert*-butylphenyl)fumaronitrile (45)[221]

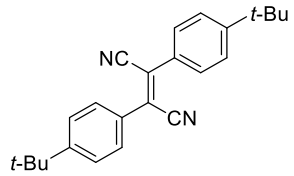

Freshly-cut Na (5.7 g, 0.246 mol) was added to MeOH (80 mL) at 0 °C. The sodium methoxide solution was added dropwise over 30 min to a solution of **44** (21.2 g, 0.123 mol) and I_2 (31.2 g, 0.123 mol) dissolved in diethyl ether (500 mL) at 0 °C. The dark red color of the solution cleared, and a white precipitate formed, which was collected, washed with MeOH, and dried under vacuum. The filtrate volume was reduced by half and was placed in freezer overnight. A second crop of product was filtered out, washed, and dried under vacuum. In the end, 13.5 g of the product were obtained (64%).

^{1}H NMR (300 MHz, $CDCl_3$): δ(ppm) = 7.80 (m, 4H), 7.55 (m, 4H), 1.37 (s, 18H).

3,4-Bis(4-*tert*-butylphenyl)pyrroline-2,5-diimine (46)[220]

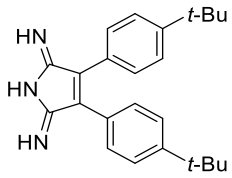

Compound **45** (3.5 g, 0.01 mol) was suspended in ethylene glycol (600 mL) and heated to 115 °C and then it was allowed to cool back to rt. Na (60 mg) was added to the reaction, and when it was completely dissolved, a strong current of gaseous NH_3 was bubbled through the solution during 30 min. The suspension was then heated to 120 °C keeping a small NH_3 current. After 3 h, the solution was filtered hot and the filtrate was poured over ice water (700 mL). A yellow precipitate formed which was collected by filtration and washed with water and a 2:1 water/MeOH mixture. The product was isolated as a yellow powder (3.15 g, 86%).

^{1}H NMR (300 MHz, $CDCl_3$)): δ(ppm) = 7.75 (m, 4H), 7.51 (m, 4H), 3.51 (br. s, 3H), 1.37 (s, 18H).

Bis(4-methoxyphenyl)fumaronitrile (47)[223]

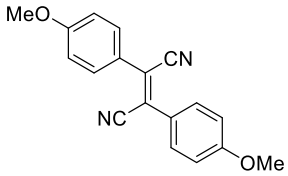

Freshly-cut Na (3.2 g, 0.113 mol) was added to MeOH (40 mL) at to 0 °C. The sodium methoxide solution was added dropwise over 30 min to a solution of 4-methoxyphenyl acetonitrile (10 g, 0.068 mol) and I_2 (17.4 g, 0.068 mol) dissolved in diethyl ether (250 mL) at 0 °C, upon which a yellow precipitate formed, which was collected, washed with $Na_2S_2O_3$, H_2O, MeOH and hexane. The filtrate volume was reduced by half and was placed in freezer overnight. A second crop of product was filtered out, washed, and dried under vacuum. Finally. 6.1 g of the product were obtained (62%).

^{1}H NMR (300 MHz, $CDCl_3$): δ(ppm) = 7.80 (d, J_o = 8.9 Hz, 4H), 7.02 (d, J_o = 8.9 Hz, 4H), 3.89 (s, 6H).

3,4-Bis(4-methoxyphenyl)pyrroline-2,5-diimine (48)[224]

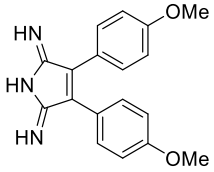

Compound **47** (2 g, 6.89 mmol) was added to a solution of sodium butoxide in butanol (40 mg of Na in 300 mL) and heated to 60 °C. When it was completely dissolved, a strong current of gaseous NH_3 was bubbled through the solution during 30 min. The suspension was then heated to 120 °C keeping

a small NH_3 current. After 3 h, the solution was poured over ice water (300 mL). A yellow precipitate was collected by filtration and purified by column chromatography on silica gel (eluent: CH_2Cl_2/MeOH 95:5). The product was isolated as a yellow powder (1.35 g, 64%).

^{1}H NMR (300 MHz, $CDCl_3$): δ(ppm) = 7.16 (d, J_o = 8.7 Hz, 4H), 6.87 (d, J_o = 8.7 Hz, 4H), 3.80 (s, 6H).

Bis(4-dimethylaminophenyl)fumaronitrile (49)[222b]

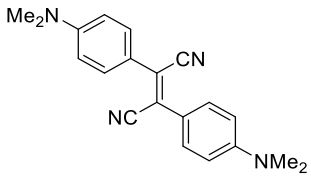

To an ice-cold mixture of 4-dimethylaminobenzaldehyde (1 g, 6.70 mmol) and tributylphosphine (0.921 ml, 3.69 mmol) was added methyl thiocyanate (0.233 ml, 3.35 mmol) dropwise with a syringe, under argon. After the addition was complete, the mixture was stirred for 1 h at 0°C and for an additional 2 h at rt. The reaction crude is dissolved completely in CH_2Cl_2 and then hexane was added until an orange precipitate appears, which was collected by filtration and washed with hexane and methanol. The product was isolated as an orange-reddish powder (230mg, 22%).

^{1}H NMR (300 MHz, $CDCl_3$): δ(ppm) = 7.74 (d, J_o = 9.1 Hz, 4H), 6.72 (d, J_o = 9.1 Hz, 4H), 3.06 (s, 12H).

3,4-Bis(4-dimethylaminophenyl)pyrroline-2,5-diimine (50)

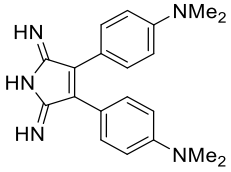

A solution of compound **49** (2 g, 6.89 mmol) in dry DMF was added to a solution of sodium butoxide in butanol (40 mg of Na in 300 mL). A strong current of gaseous NH_3 was then bubbled through the solution during 30 min. The suspension was then heated to 140 °C keeping a small NH_3 current. After 8 h, the solvent was eliminated under reduced pressured and the residue was then dissolved in $CHCl_3$ and washed three times with water. The solvent was eliminated again and the residue was purified by column chromatography on silica gel (eluent: $CHCl_3$/MeOH 95:5). The product was isolated as a brown powder (160 mg, 51%).

^{1}H NMR (300 MHz, $CDCl_3$): δ(ppm) = 7.14 (d, J_o = 8.8 Hz, 2H), 6.67 (d, J_o = 8.8 Hz, 2H), 2.97 (s, 12H).
^{13}C NMR (75.5 MHz, $CDCl_3$): δ(ppm) = 166.99, 150.48, 130.55, 117.87, 112.32, 40.32.
MS (FAB, *m*-NBA): *m/z* = 334.2 $[M+H]^+$
HRMS: *m/z* Calcd for $[C_{20}H_{25}N_5]$: 334.2032; Found: 334.2040.

Methyl 3,4-Diodobenzoate (51)[227]

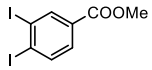

To a suspension of 4-iodobenzoic acid methyl ester (1.31 g, 5.00 mmol) in 96% H_2SO_4 (7mL), N-iodosuccinimide (1.13 g, 5.00 mmol) was added. The black mixture was stirred at rt for 8 h, then it was poured into ice-water. The dark oil formed on the bottom was dissolved in AcOEt and the solution was washed with H_2O, 5% aqueous $NaHCO_3$, brine and dried over MgSO4. After removal of the solvent at reduced pressure, the crude product was purified by column chromatography on silica gel (eluent: petroleum ether/AcOEt 95:5), affording the product as a white solid (1.64 g, 85% yield).

^{1}H NMR (300 MHz, $CDCl_3$): δ (ppm) = 8.46 (d, J_m = 2.0 Hz, 1H), 7.94 (d, J_o = 8.2 Hz, 1H), 7.63 (dd, J_o = 8.2, J_m = 2.0 Hz, 1H), 3.90 (s, 3H).

Methyl 3,4-Dicyanobenzoate (52)[227]

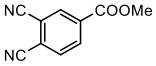

Methyl 3,4-diodobenzoate **51** (0.50 g, 1.29 mmol) $Pd_2(dba)_3$ (47 mg, 0.05 mmol), dppf (60 mg, 0.08 mmol), Zn powder (16 mg, 0.24 mmol) and $Zn(CN)_2$ (0.18 g, 1.54 mmol) were transferred under nitrogen into a flame-dried Schlenk flask. Dry N,N-dimethylacetamide (10 mL) was added and the resulting mixture was heated at 120 °C and stirred for 2 h, then cooled to room temperature, and partitioned between H_2O and AcOEt. The resulting biphasic system was filtered through Celite, the organic layer was separated and the aqueous layer was extracted with AcOEt. The combined organic extracts were washed with H_2O and brine, and dried over $MgSO_4$. After removal of the solvent at reduced pressure, the crude product was purified by column chromatography (silica gel, hexane/AcOEt 7:3) affording the compound as a white solid (0.18 g, 75% yield).

^{1}H NMR (300 MHz, $CDCl_3$): δ (ppm) = 8.45 (s, 1H), 8.38 (d, J = 8.1 Hz, 1H), 7.92 (d, J = 8.1 Hz, 1H), 4.01 (s, 3H).

2.7.1.2 Synthesis of A_3B porphyrazines bearing an isoindole carboxylic function

General procedure to obtain free base Pz-Pc hybrids. Method A

An oven-dried 50 mL flask was charged with 25 mL of dry propanol, Mg turnings (3 equiv.) and a catalytic amount of I_2 under Ar. After flushing Ar through the system for 5 min, the mixture was heated to 140 ^oC during 4-6 h until the Mg is completely dissolved and a whitish suspension was observed. After this, the maleonitrile (or the 1,3-diiminopyrroline) (3 equiv.) and methyl 3,4-cyanobenzoate (1 equiv.) were added and the mixture was stirred at 140^oC for 14h. After letting the mixture cool down to rt, the solvent was eliminated under reduced pressure, and 15 mL of TFA was added to the residue and stirred at rt in absence of light for 1h. The solution was then carefully poured into a 1:1 ice-water/NH_3 (30% ac.) mixture, and the resulting precipitate was filtered and washed with water and a 1:1 water/MeOH mixture. Pzs bearing propyl, thiopentyl and dimethylamino groups were separated at this point by column chromatography as indicated below for each particular case. Pzs bearing *tert*-butylphenyl, methoxyphenyl and dimethylaminophenyl groups were used at the next step without further purification.

General procedure to obtain Zn Pz-Pc hybrids. Method B

The purified free base hybrid or crude mixture was dissolved in 10 mL of a 1:1 DMF/PhCl mixture and $Zn(OAc)_2$ (2 equiv.) was added and the resulting solution was heated to 140^oC for 3h. Afterwards the solvent was eliminated under reduced pressure. The purification process was subsequently performed as indicated below for each particular case. Generally, it involves column chromatography on silica gel. The separation of the products generated during the statistical tetramerization was separated by column chromatography at different points of the synthesis, depending on the difficulty of achieving a good separation:

General procedure for the hydrolysis of the ester group. Method C

A 25 mL round bottom flask was charged with the Pz (0.01 mmol, 1 equiv.), KOH 85% (0.20 mmol, 20 equiv.) and 10 mL of *t*-BuOH. The reaction was monitored by TLC until no more starting material was observed. 10 mL of HCl 0.1 M were added to the reaction mixture, which was then extracted three times with DCM or chloroform, and the organic phase washed two times with H_2O. The solvent was eliminated under reduced pressure. The purification process was subsequently performed as indicated below for each particular case. Generally it involved recrystallization or column chromatography on silica gel.

2,3,7,8,12,13-Hexapropyl-17,18-(4'-propyloxycarbonylbenzo)porphyrazine (53)

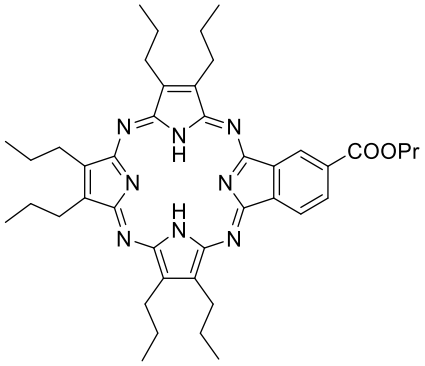

Method A. Starting material: dipropylmaleonitrile **41** (523 mg, 3.22 mmol). The crude was purified by column chromatography on silica gel (eluent: Toluene/MeOH 97:3). Yield: 12%.

Mp > 250 °C.

^{1}H-NMR (300 MHz, $CDCl_3$): δ (ppm) = 9.84 (s, 1H), 9.21 (d, J_o = 7.9 Hz, 1H), 8.77 – 8.71 (m, 1H), 4.58 (t, J = 6.6 Hz, 2H), 4.09 – 3.88 (m, 9H), 3.80 (t, J = 7.5 Hz, 3H), 2.32 (m, 12H), 2.06 (q, J = 7.1 Hz, 2H), 1.39 – 1.17 (m, 18H), 0.84 (m, 3H), -2.42 (s, 2H).
UV-vis (THF): λ_{max} (nm) (log ε (dm^3 mol^{-1} cm^{-1})) = 644 (4.39), 615, (3.69), 573 (4.33), 536 (sh), 342 (4.32).
MS (MALDI-TOF, DCTB): *m/z* = 702.5 [M^+].
HRMS: *m/z* Calcd for [$C_{42}H_{54}N_8O_2$]: 702.4364; Found: 702.4355.

[2,3,7,8,12,13-Hexapropyl-17,18-(4'-propyloxycarbonylbenzo)porphyrazinate]Zn(II) (59)

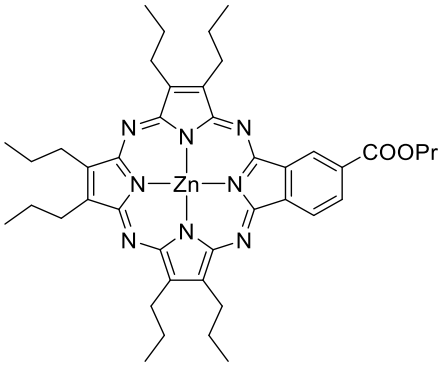

Method B. Starting material: Pz **53** (70 mg, 0.09 mmol). The crude was purified by column chromatography on silica gel (eluent: chloroform). Yield: 88%.

Mp > 250 °C.

^{1}H-NMR (300 MHz, THF-d_8): δ(ppm) = 10.01 (s, 1H), 9.42 (d, J_o = 8.0 Hz, 1H), 8.80 (dd, J_o = 8.0, J_m =1.4 Hz, 1H), 4.55 (t, J = 6.6 Hz, 2H), 4.15 – 3.72 (m, 12H), 2.43 (m, 12H), 2.02 (m, 2H), 1.48 – 1.05 (m, 21H).
^{13}C-NMR (75.5 MHz, THF-d_8): δ (ppm) = 167.17, 159.72, 159.42, 158.54, 158.40, 158.31, 154.70, 154.15, 145.42, 145.34, 144.68, 144.62, 144.51, 144.33, 143.48, 140.33, 132.31, 130.87, 124.96, 123.35, 29.25, 29.18, 29.08, 26.71, 26.6, 23.44, 15.31, 15.27, 11.17.
UV-vis (THF): λ_{max} (nm) (log ε (dm^3 mol^{-1} cm^{-1})) = 615 (4.99), 560, (4.20), 347 (4.69).
MS (MALDI-TOF, DCTB): *m/z* = 764.4[M$^+$].
HRMS: *m/z* Calcd for [$C_{42}H_{52}N_8O_2Zn_1$]: 764.3499; Found: 764.3494.

[2,3,7,8,12,13-Hexapropyl-17,18-(4'-carboxylbenzo)porphyrazinate]Zn(II) (33)

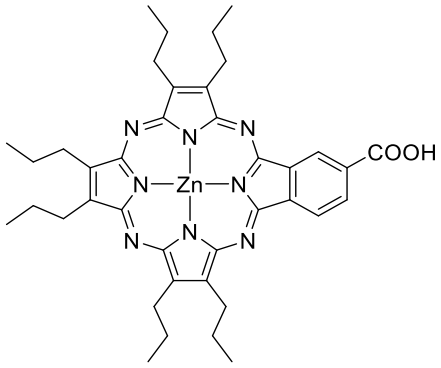

Method C. Starting material: Pz **59** (55 mg, 0.076 mmol). The crude was purified by column chromatography on silica gel (eluent: chloroform with 0.5% MeOH) Yield: 64%.

Mp > 250 °C.
^{1}H-NMR (300 MHz, THF-d_8): δ(ppm) = 10.04 (s, 1H), 9.45 (d, J_o = 7.8 Hz, 1H), 8.86 – 8.77 (m, 1H), 3.99 (m, 12H), 2.49 – 2.29 (m, 12H), 1.48 – 1.04 (m, 18H).
^{13}C-NMR (75.5 MHz, THF-d_8): δ (ppm) = 168.30, 159.82, 159.51, 158.52, 158.35, 155.05, 154.46, 145.47, 145.35, 144.62, 144.49, 144.31, 143.50, 140.45, 132.85, 131.32, 125.27, 123.26, 29.25, 29.17, 29.09, 28.97, 26.68, 15.24.
FT-IR (KBr): ν (cm^{-1}) = 3450.4 (br), 3072.3, 2958.2, 2930.2, 2836.3, 2655.7, 2531.6, 1733.2, 1691.9, 1615.7, 1579.1, 1463.8, 1438.5, 1416.1, 1374.9, 1341.0, 1287.2, 1259.4, 1235.1, 1155.9, 1124.1, 1110.7, 1095.1, 1039.5, 1023.0, 951.3, 932.5, 917.7, 892.5, 861.5, 848.0, 798.1, 758.9, 731.6, 714.8, 688.5, 557.2, 503.5, 484.5, 443.6, 422.1.
UV-vis (THF): λ_{max} (nm) (log ε (dm^3 mol^{-1} cm^{-1})) = 615 (5.07), 560 (4.25), 346 (4.78).
MS (MALDI-TOF, DCTB): *m/z* = 722.4
HRMS: *m/z* Calcd for [$C_{39}H_{46}N_8O_2Zn$]: 722.3030; Found: 722.3028.

2,3,7,8,12,13-Hexathiopentyl-17,18-(4'-propyloxycarbonylbenzo)porphyrazine (54)

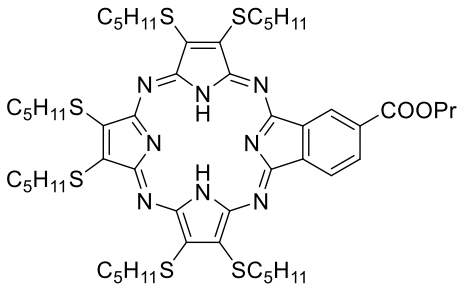

Method A. Starting material: dithiopentylmaleonitrile **42a** (910 mg, 3.22 mmol). The crude was purified by column chromatography on silica gel (eluent: DCM/Heptane 1:1). Yield: 20%.

Mp > 250 °C.

^{1}H-NMR (300 MHz, $CDCl_3$) δ = 9.47 (s, 1H), 8.83 (d, J_o = 7.8 Hz, 1H), 8.69 (dd, J_o = 7.9, J_m = 1.4 Hz, 1H), 4.61 (t, J = 6.7 Hz, 2H), 4.35 – 3.84 (m, 12H), 2.09 (m, 2H), 2.01 – 1.83 (m, 12H), 1.65 (m, 12H), 1.50 – 1.33 (m, 12H), 1.29 (m, 3H), 0.93 (s, 18H), -2.21 (s, 2H).

^{13}C-NMR (75 MHz, $CDCl_3$) δ = 166.62, 142.31, 141.67, 141.46, 139.24, 139.09, 138.94, 137.57, 136.98, 132.07, 131.39, 124.05, 122.37, 67.30, 35.48, 35.45, 35.35, 35.29, 32.08, 31.41, 31.41, 31.32, 31.30, 30.32, 30.31, 30.30, 30.23, 29.85, 29.81, 29.52, 22.85, 22.63, 22.58, 22.54, 14.27, 14.20, 14.15, 14.11, 10.91.

UV-vis (THF): λ_{max} (nm) (log ε (dm^3 mol^{-1} cm^{-1})) = 720 (4.94), 689 (sh), 660 (sh), 631 (4.72), 525 (br, 4.51), 353 (4.92).

MS (MALDI-TOF, DCTB): *m/z* = 1062.4[M^+].

HRMS: *m/z* Calcd for [$C_{54}H_{78}N_8O_2S_6$]: 1062.4566; Found: 1062.4546.

[2,3,7,8,12,13-Hexathiopentyl-17,18-(4'-propyloxycarbonylbenzo)porphyrazinate]Zn(II) (60)

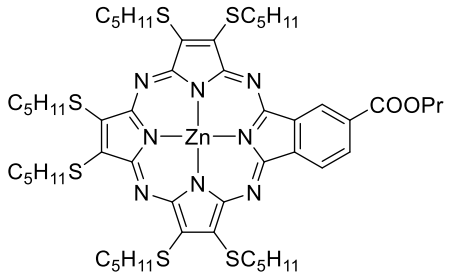

Method B. Starting material: Pz **54** (150 mg, 0.141 mmol). The crude was purified by column chromatography on silica gel (eluent: DCM with 0.5% MeOH). Yield: 98%.

Mp > 250 °C.

^{1}H-NMR (300 MHz, $CDCl_3$) δ = 9.40 (s, 1H), 8.76 (d, J_o = 7.9 Hz, 1H), 8.65 (d, J_o = 8.0 Hz, 1H), 4.57 (t, J = 6.7 Hz, 2H), 3.86 – 3.61 (m, 10H), 3.49 – 3.36 (m, 2H), 2.04 (m, 2H), 1.76 – 1.55 (m, 12H), 1.55 – 1.38 (m, 14H), 1.38 – 1.16 (m, 15H), 0.94 – 0.72 (m, 18H).
^{13}C-NMR (75 MHz, $CDCl_3$) δ = 166.51, 157.26, 156.64, 155.86, 155.40, 155.32, 155.23, 155.17, 154.89, 154.38, 142.12, 141.01, 140.04, 139.63, 138.93, 136.93, 131.81, 124.31, 67.29, 34.98, 32.08, 31.36, 31.32, 31.30, 31.15, 31.12, 30.09, 30.07, 29.98, 29.87, 29.85, 29.65, 29.51, 22.84, 22.60, 22.59, 22.57, 22.53, 22.49, 22.41, 14.26, 14.17, 14.14, 14.05, 14.04, 10.88.
UV-vis (THF): λ_{max} (nm) (log ε (dm^3 mol^{-1} cm^{-1})) = 687 (4.88), 665 (4.90), 610 (sh), 523 (br, 4.06), 369 (4.86).
MS (MALDI-TOF, DCTB): *m/z* = 1126.4 [M^+].
HRMS: *m/z* Calcd for [$C_{54}H_{78}N_8O_2S_6Zn_1$]: 1126.3686; Found: 1126.3709.

[2,3,7,8,12,13-Hexathiopentyl-17,18-(4'-carboxylbenzo)porphyrazinate]Zn(II) (34)

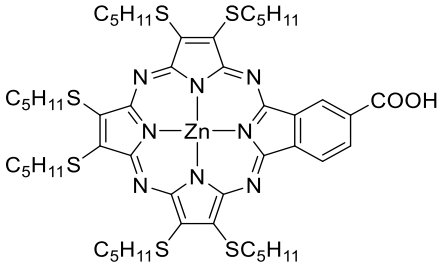

Method C. Starting material: Pz **60** (140 mg, 0.124 mmol). The crude was purified by recrystallization from DCM/acetonitrile. Yield: 60%.

MP > 250 °C.
^{1}H-NMR (300 MHz, THF-d_8) δ = 9.92 (s, 1H), 9.33 (d, J_o = 7.9 Hz, 1H), 8.83 (dd, J_o = 7.9, J_m = 1.4 Hz, 1H), 4.23 (m, 12H), 1.90 (m, 12H), 1.69 – 1.55 (m, 12H), 1.48 – 1.21 (m, 12H), 0.96 – 0.78 (m, 18H).
^{13}C-NMR (75 MHz, THF-d_8) δ = 167.87, 158.97, 158.66, 156.61, 156.59, 156.45, 156.44, 156.33, 156.13, 156.11, 143.37, 141.99, 141.46, 141.30, 140.79, 140.42, 132.23, 125.42, 123.55, 36.00, 35.94, 35.86, 32.28, 32.23, 31.51, 31.44, 23.47, 14.54.
FT-IR (KBr): ν (cm^{-1}) = 2956.6, 2922.4, 2852.0, 1685.1, 1617.6, 1581.5, 1465.8, 1417.5, 1340.4, 1295.0, 1235.6, 1115.4, 1061.0, 1026.8, 881.8, 843.1, 785.1, 738.6, 557.6, 509.6.
UV-vis (THF): λ_{max} (nm) (log ε (dm^3 mol^{-1} cm^{-1})) = 686 (4.81), 665 (4.82), 610 (sh), 523 (br, 4.01), 369 (4.79).
MS (MALDI-TOF, DCTB): *m/z* = 1082.4[M^+].
HRMS: *m/z* Calcd for [$C_{51}H_{70}N_8O_2S_6Zn_1$]: 1082.3232; Found: 1082.3212.

2,3,7,8,12,13-Hexakis(dimethylamino)-17,18-(4'-propyloxycarbonylbenzo)porphyrazine (55)

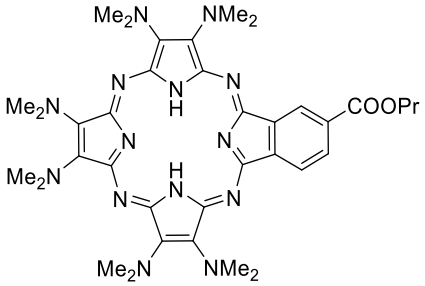

Method A. Starting material: bis(dimethylamino)maleonitrile **43** (300 mg, 1.827 mmol). The demetallation step was carried out with glacial acetic acid instead of trifluoroacetic acid to avoid possible formation of secoporphyrazine derivatives. The crude was purified by column chromatography on silica gel (eluent: Toluene with 3% MeOH). Yield: 22%.

Mp > 250 °C.

^{1}H-NMR (300 MHz, $CDCl_3$): δ (ppm) = 9.61 (s, 1H), 8.96 (d, J_o = 8.0 Hz, 1H), 8.53 (dd, J_o = 7.9, J_m =1.4 Hz, 1H), 4.44 (t, J = 6.6 Hz, 2H), 3.99 (m, 12H), 3.69 – 3.62 (m, 24H), 2.06 – 1.80 (m, 2H), 1.15 (m, 3H), -0.74 (s, 2H).
MS (MALDI-TOF, DCTB): *m/z* = 708.5 [M^+].
HRMS: *m/z* Calcd for [$C_{36}H_{48}N_{14}O_2$]: 708.4079; Found: 708.4079.

[2,3,7,8,12,13-Hexakis(dimethylamino)-17,18-(4'-propyloxycarbonylbenzo)-porphyrazinato]Zn(II) (61)

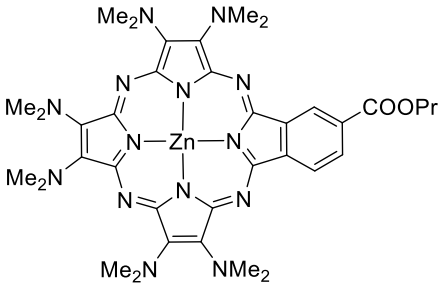

Method B. Starting material: Pz **55** (65 mg, 0.092 mmol).The crude was purified by column chromatography on silica gel (eluent: Toluene with 2% MeOH). Yield: 91%.

Mp > 250 °C.

^{1}H-NMR (500 MHz, THF-d_8): δ (ppm) = 9.83 (s, 1H), 9.19 (d, J_o = 7.9 Hz, 1H), 8.63 (d, J_o = 9.4 Hz, 1H), 4.48 (t, J = 6.6 Hz, 2H), 4.04 (s, 6H), 4.02 (s, 6H), 3.84 (s, 6H), 3.82 (s, 6H), 3.74 (s, 6H), 3.73 (s, 6H), 1.97 (m, 2H), 1.20 (m, 3H).
^{13}C-NMR (126 MHz, THF-d_8): δ (ppm) = 44.36, 44.17, 43.40, 31.88, 29.70 , 22.57 , 13.43.
UV-vis (THF): λ_{max} (nm) = 714 (3.46), 584 (sh), 529 (sh), 350 (3.70), 277 (sh), 247 (3.48).

MS (MALDI-TOF, DCTB): *m/z* = 770.4
HRMS: *m/z* Calcd for $[C_{36}H_{46}N_{14}O_2Zn]$: 770.3214; Found: 770.3223.

[2,3,7,8,12,13-Hexakis(dimethylamino)-17,18-(4'-carboxylbenzo)-porphyrazinato]Zn(II) (35K)

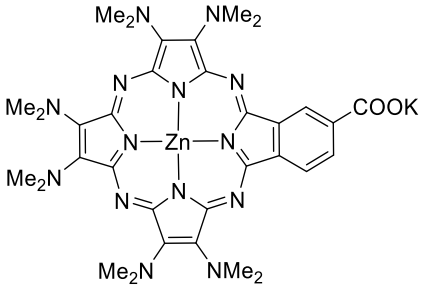

Method C. Starting material: Pz **61** (50 mg, 0.065 mmol).The product decomposed if it was acidified, so it was isolated as the potassium carboxylate. The reaction mixture was extracted with DCM before adding the HCl and washed with H_2O two times. Hexane was then added to the organic phase until a precipitate appeared, which was filtered and washed with more hexane. Yield: 45%

Mp > 250 °C.
^{1}H-NMR (500 MHz, DMSO-d_6): δ (ppm) = 9.6-9.2 (broad, 2H), 8.6 – 8.2 (br, 1H), 3.92 (d, 12H), 3.75 (s, 12H), 3.70 (d, 12H).
^{13}C-NMR (126 MHz, DMSO-d_8): δ (ppm) = 184.26, 152.28, 152.09, 152.04, 151.94, 151.88, 151.53, 151.43, 150.95, 150.83, 139.43, 139.24 (s), 138.02, 137.88, 137.84, 135.218, 134.86, 129.593, 119.97, 44.87, 44.85, 44.75, 44.34, 44.24.
FT-IR (KBr): ν (cm^{-1}) = 3422.1 (br), 2922.2, 2209.5, 1577.9, 1373.5, 106.9, 1083.5, 878.5, 795.4, 747.6, 580.5.
UV-vis (MeOH): λ_{max} (nm) (log ε (dm^3 mol^{-1} cm^{-1})) = 707 (br, 3.35), 635 (br, sh), 347 (3.68).
MS (MALDI-TOF, DCTB): *m/z* = $[M\text{-}K+H]^+$: 728.2
$[M]^+$: 766.2
HRMS: *m/z* Calcd for $[C_{33}H_{40}N_{14}O_2Zn_1]$: 728.2745; Found: 728.2758
m/z Calcd for $[C_{33}H_{39}K_1N_{14}O_2Zn_1]$: 766.2303; Found: 766.2279

[2,3,7,8,12,13-Hexakis(4-*tert*-butylphenyl)-17,18-(4'-propyloxycarbonylbenzo)-porphyrazinate]Zn(II) (62)

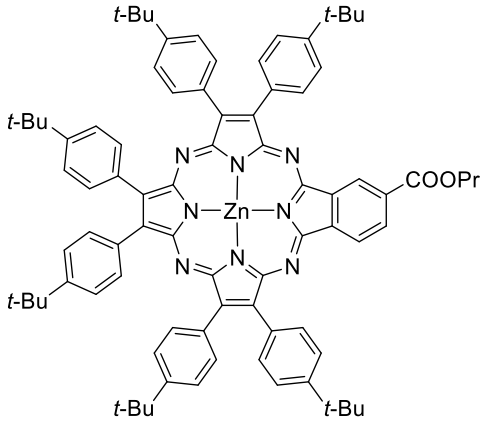

Method B. Starting material: Bis(4-*tert*-butylphenyl)pyrroline-2,5-diimine **46** (276 mg, 0.806 mmol). The crude was purified by column chromatography on silica gel (eluent: chloroform) and posterior recrystallization from DCM/MeOH. Yield: 17%.

Mp > 250°C.

^{1}H-NMR (300 MHz, THF-d_8) δ = 9.66 (s, 1H), 9.11 (d, J_o = 7.9 Hz, 1H), 8.76 (dd, J_o = 7.9, J_m =1.4 Hz, 1H), 8.44 (d, J_o = 8.2 Hz, 3H), 8.38 – 8.23 (m, 9H), 7.82 – 7.50 (m, 12H), 4.50 (t, J = 6.5 Hz, 2H), 2.03 (m, 2H), 1.56 (m, 54H), 1.29 (t, J = 7.4 Hz, 3H).

^{13}C-NMR (75 MHz, THF-d_8) δ = 163.85, 143.35, 148.29, 148.06, 130.79, 130.69, 130.06, 129.91, 129.72, 122.84, 122.75, 32.66, 29.21.

UV-vis (THF): λ_{max} (nm) (log ε (dm^3 mol^{-1} cm^{-1})) = 665 (4.98), 639 (4.99), 614(sh), 587 (4.38), 495 (br, 4.13), 374 (4.94).

MS (MALDI-TOF, DCTB): *m/z* = 1304.6 [M$^+$].

HRMS: *m/z* Calcd for [$C_{84}H_{88}N_8O_2Zn$] : 1304.6316; Found: 1304.6294.

[2,3,7,8,12,13-Hexakis(4-*tert*-butylphenyl)-17,18-(4'-carboxylbenzo)-porphyrazinate]Zn(II) (36)

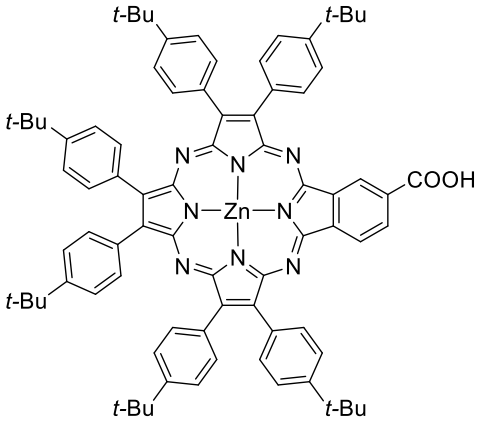

Method C. Starting material: Pz **62** (40 mg, 0.031 mmol).The crude was purified by recrystallization from DCM/MeOH. Yield: 68%.

Mp > 250 °C.

^{1}H-NMR (300 MHz, THF-d_8) δ = 9.80 (s, 1H), 9.18 (d, J_o = 7.9 Hz, 1H), 8.80 (d, J_o = 7.9 Hz, 1H), 8.33 (m, 12H), 7.75 (d, J_o = 8.0 Hz, 3H), 7.57 (m, 9H), 1.54 (m, 54H).

^{13}C-NMR (75 MHz, THF-d_8) δ = 167.98, 159.09, 158.80, 157.17, 156.95, 156.80, 156.68, 156.51, 156.06, 151.35, 151.22, 151.19, 151.00, 143.75, 142.76, 142.62, 142.13, 141.77, 141.62, 140.67, 133.80, 133.79, 133.75, 133.69, 133.29, 133.07, 132.97, 132.94, 132.70, 132.62, 131.89, 125.90, 125.87, 125.83, 125.78, 123.71, 35.69, 35.61, 32.27, 32.18.

FT-IR (KBr): ν (cm^{-1}) = 3442.9 (br), 3036.6, 2959.0, 2903.3, 2866.4, 2594.5, 2338.4, 1907.7, 1687.6, 1612.0, 1582., 1471.5, 1436.8, 1393.3, 1363.7, 1336.5, 1268.1, 1196.9, 115039, 1101.4, 1016.8, 979.2, 880.2, 837.8, 796.5, 773.4, 758.5, 744.4, 694.9, 648.1, 631.4, 597.2, 562.8, 507.5.

UV-vis (THF): λ_{max} (nm) (log ε (dm^3 mol^{-1} cm^{-1})) = 665 (4.95), 639 (4.95), 614(sh), 590 (sh), 495 (br, 4.03), 375 (4.92).

MS (MALDI-TOF, DCTB): *m/z* = 1262.6 [M$^+$].

HRMS: *m/z* Calcd for [$C_{81}H_{82}N_8O_2Zn$]: 1262.5847; Found: 1262.5828.

[2,3,7,8,12,13-Hexakis(4-methoxyphenyl)-17,18-(4'-propyloxycarbonylbenzo)-porphyrazinate]Zn(II) (63)

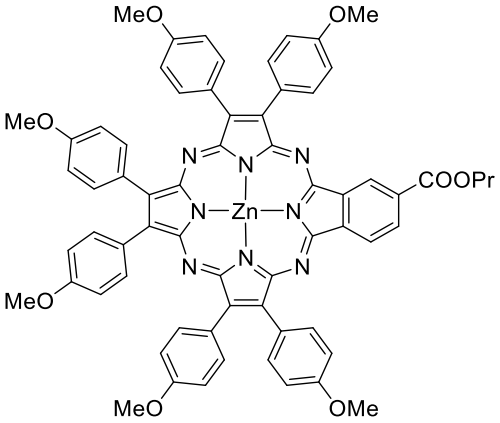

Method B. Starting material: Bis(4-methoxyphenyl)pyrroline-2,5-diimine **48** (250 mg, 0.713 mmol). The crude was purified by column chromatography on silica gel (eluent: DCM with 1% THF). Yield: 9%.

Mp > 250°C.

^{1}H-NMR (300 MHz, THF-d_8) δ = 9.86 (s, 1H), 9.26 (d, J_o = 8.0 Hz, 1H), 8.77 (d, J_o = 6.7 Hz, 1H), 8.35 (m, 12H), 7.51 – 6.81 (m, 12H), 4.52 (t, J = 6.4 Hz, 2H), 4.01 (d, J = 1.6 Hz, 6H), 3.99 (d, J = 1.7 Hz, 12H), 2.02 (m, 2H), 1.29 (t, J = 7.4 Hz, 3H).

^{13}C-NMR (75 MHz, THF-d_8) δ = 165.80, 159.80, 159.72, 159.63, 159.60, 159.53, 157.88, 157.64, 156.71, 156.34, 156.07, 155.93, 154.78, 149.32, 140.83, 140.00, 139.95, 139.56, 139.53, 139.33, 133.97, 133.92, 133.84, 133.78, 131.53, 130.20, 127.03, 126.97, 126.81, 124.03, 122.53, 113.58, 113.48, 54.54, 22.26, 10.26.

UV-vis (THF): λ_{max} (nm) (log ε (dm^3 mol^{-1} cm^{-1})) = 667 (4.77), 644 (4.78), 592 (sh), 504 (4.01), 378 (4.73).

MS (MALDI-TOF, DCTB): *m/z* = 1148.3 [M$^+$].

HRMS: *m/z* Calcd for [$C_{66}H_{52}N_8O_8Zn$]: 1486.3194; Found: 1148.3177.

[2,3,7,8,12,13-Hexakis(4-methoxyphenyl)-17,18-(4'-carboxylbenzo)-porphyrazinate]Zn(II) (37)

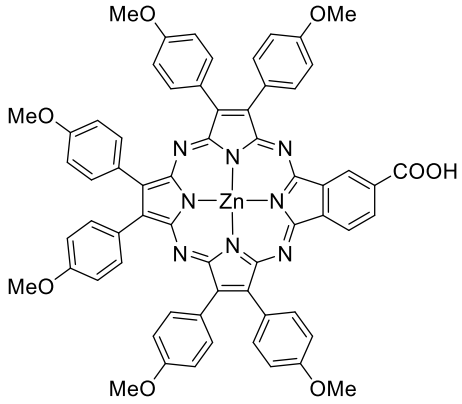

Method C. Starting material: Pz **63** (20 mg, 0.018 mmol). The crude was purified by washing the precipitate with hexane. Yield: 95%.

Mp > 250°C.

^{1}H-NMR (300 MHz, THF-d_8) δ = 9.66 (s, 1H), 9.23 (d, J_o = 7.8 Hz, 1H), 8.75 (d, J_o = 7.8 Hz, 1H), 8.35 – 8.14 (m, 12H), 7.40-7.18 (m, 12H), 4.00-3.92 (m, 18H).

^{13}C-NMR (75 MHz, THF-d_8) δ = 188.39, 158.96, 158.87, 158.77, 133.55, 133.47, 126.68, 126.55, 114.00, 113.87, 55.26, 55.18.

FT-IR (KBr): ν (cm^{-1}) = 3443.0 (br), 3298.7, 2997.1, 2930.8, 2833.2, 2541.4, 2032.8, 1688.8, 1606.3, 1515.9, 1492.8, 1439.1, 1389.8, 1339.3, 1292.8, 1250.5, 1176.7, 1034.3, 970.6, 954.4, 878.33, 830.9, 783.7, 764.9, 753.1, 726.6, 640.8, 623.6, 574.7, 529.7.

UV-vis (THF): λ_{max} (nm) (log ε (dm^3 mol^{-1} cm^{-1})) = 698 (4.33), 669 (4.19), 641 (4.17), 609 (4.15), 504 (3.98), 373 (4.33), 353 (4.33).

MS (MALDI-TOF, DCTB): *m/z* = 1106.3 [M$^+$].

HRMS: *m/z* Calcd for [$C_{63}H_{46}N_8O_8Zn$]: 1106.2725; Found: 1106.2739.

[2,3,7,8,12,13-Hexakis(4-dimethylaminophenyl)-17,18-(4'-propyloxycarbonylbenzo)-porphyrazinate]Zn(II) (64)

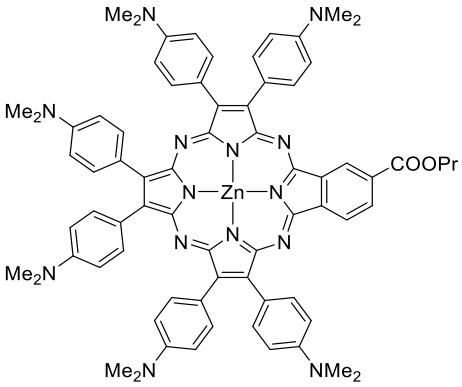

Method B. Starting material: Bis(4-*tert*-butylphenyl)pyrroline-2,5-diimine **50** (270 mg, 0.774 mmol). The crude was purified by column chromatography on silica gel (eluent: chloroform/acetone 19:1). Yield: 7%.

Mp > 250°C.

^{1}H-NMR (300 MHz, THF-d_8): δ(ppm) = 9.95 (s, 1H), 9.32 (d, J_o = 7.7 Hz, 1H), 8.76 (d, J_o = 7.8 Hz, 1H), 8.50 – 8.32 (m, 12H), 7.15 – 6.92 (m, 12H), 4.52 (m, 2H), 3.18 (m, 36H), 2.04 (m, 2H), 1.30 (m, 3H).
DEPT 135 NMR (75.5 MHz, THF-d_8): δ(ppm) = 134.46, 134.26, 130.60, 124.66, 123.17, 112.74, 40.49, 30.46, 23.09, 11.19, 10.89, 10.86.
UV-vis (THF): λ_{max} (nm) (log ε (dm^3 mol^{-1} cm^{-1})) = 683 (4.63), 618(sh), 361 (4.60), 262 (4.60).
MS (MALDI-TOF, DCTB): *m/z* = 1226.5 [M$^+$].
HRMS: *m/z* Calcd for [$C_{72}H_{70}N_{14}O_2Zn$]: 1226.5061; Found: 1226.5092.

[2,3,7,8,12,13-Hexakis(4-dimethylaminophenyl)-17,18-(4'-carboxylbenzo)-porphyrazinate]Zn(II) (38)

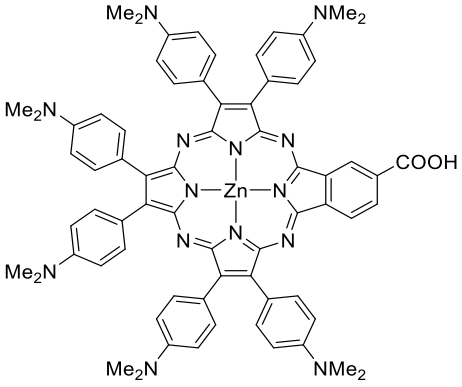

Method B. Starting material: Pz **64** (10 mg, 0.008 mmol).The crude was purified by column chromatography on silica gel (eluent: chloroform/MeOH 19:1). Yield: 67%.

Mp > 250°C.

^{1}H-NMR (300 MHz, DMSO-d_6): δ (ppm) = 13.52 (br, 1H), 9.71 (s, 1H), 9.26 (d, J_o = 7.7 Hz, 1H), 8.77 (d, J_o = 7.8 Hz, 1H), 8.37 – 7.99 (m, 12H), 7.15 – 6.92 (m, 12H), 3.21 – 2.98 (m, 36H).
FT-IR (KBr): ν (cm^{-1}) = 3393.2 (br), 2934.3, 1720.8, 1610.4, 1435.2, 1359.7, 1205.6, 1124.5, 1097.5, 1057.4, 679.7, 625.7.
UV-vis (THF): λ_{max} (nm) (log ε (dm^3 mol^{-1} cm^{-1})) = 683 (4.56), 618(sh), 363 (4.53), 260 (4.57).
MS (MALDI-TOF, DCTB): *m/z* = 1184.5 [M^+].
HRMS: *m/z* Calcd for [$C_{69}H_{64}N_{14}O_2Zn$]: 1184.4623; Found: 1184.4596.

2.7.2 Synthesis of new Pzs by modification of the anchoring group.

2.7.2.1 Synthesis of the precursors.

Thioethylmaleonitrile (68)

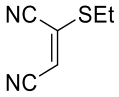

And oven dry, degassed Schlenk tube was charged with dithioethylmaleonitrile **42b** (300 mg, 1.5 mmol), triethylsilane (0.24 mL, 1.5 mmol), and 8 mL of dry THF under Ar. After a few minutes, copper thiophenecarboxylate (289 mg, 1.5 mmol) and $Pd(PPh_3)_4$ (45mg, 2.5 mol%) were added under Ar. The reaction mixture was then heated to 55°C. The reaction was monitored by TLC (Heptante/EtOAc 2:1) and small portions of triethylsylane, and $Pd(PPh_3)_4$ were added until formation of unsubstituted maleonitrile was observed. Rhe mixture was allowed to reach rt and filtered over a Celite pad. The filtrate was then washed three times with saturated $NaHCO_3$ and two times with H_2O. The solvent was eliminated under reduced pressure and the residue purified by column chromatography on silica gel (eluent: Heptane/EtOAc 2:1) to yield a yellowish oil (94 mg, 45%).

Mp > 250°C.

^{1}H-NMR (300 MHz, $CDCl_3$): δ (ppm) = 5.80 (s, 1H), 3.02 (q, *J* = 7.4 Hz, 2H), 1.37 (t, *J* = 7.4 Hz, 3H).
^{13}C-NMR (75.5 MHz, $CDCl_3$): δ (ppm) = 134.06, 114.31, 111.87, 104.79, 28.23, 13.71.
MS (GC-EI): *m/z* = 138.0 [M^+].
HRMS: *m/z* Calcd for [$C_6H_6N_2S$]: 138.0252; Found: 138.0248.

[(1E)-3-Methoxy-3-oxoprop-1-en-1-yl]boronic acid (74)[236]

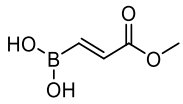

Borane dimethylsulfide complex (5.82 mL, 1.05 equiv) was dissolved in THF and cooled to 0 °C. (1*R*)-(+)-R-Pinene (22.56 mL, 2.32 equiv) was added dropwise, and the mixture was stirred at 0 °C for 1 h and at rt for 2 h. The mixture was cooled to -35 °C and ethyl propiolate (6.2 mL, 1 equiv) was added dropwise; the mixture was stirred at -35 °C for 45 min and rt for 3 h. Acetaldehyde (48 mL) was added, and the mixture was heated at rt overnight. The volatile organic components were carefully removed under reduced pressure to give 29 g of a mixture of the product and R-pinene. A mixture of THF/water (5 mL/5 mL) was added. The mixture was stirred overnight. After removing most of the solvent under reduced pressure, 30 mL of pentane were added give a solid, which was filtered and washed several times with pentane.

^{1}H-NMR (300 MHz, MeOD): δ(ppm) = 6.87 (d, *J* = 17.8 Hz, 1H), 6.52 (d, *J* = 17.8 Hz, 1H), 3.78 (s, 3H).

Copper (I) thiophene-2-carboxylate (CuTC)

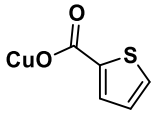

A 50mL round-bottomed flask was charged with thiophene-2-carboxylic acid (10g, 78 mmol), Cu_2O (2.8 g, 19.6 mmol) and dry toluene (30 mL). The flask was then outfitted with Dean-Stark trap and a condenser and the mixture was refluxed overnight with azeotropic removal of water. The yellow/grey suspension was cooled to 60 °C the product was collected by filtration. The solid was washed by methanol (30 mL) to remove excess acid, and with ether until the eluent was colourless, then with a small amount of hexane. The product was dried under vacuum. The product was obtained as a tan powder (5.56 g, 75%).

2.7.2.2 Synthesis of the porphyrazines

[2,3,7,8,12,13-Hexapropyl-17-thioethylporphyrazinate]Zn(II) (69)

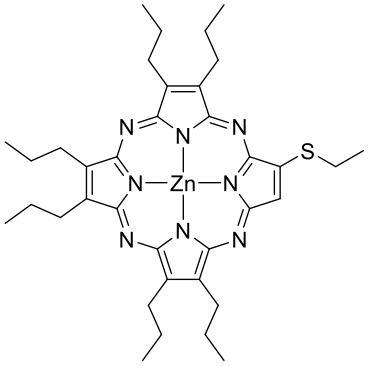

An oven-dried, 250 mL flask was charged with 100 mL of dry propanol, Mg turnings (120 mg, 4.94 mmol) and a catalytic amount of I_2 under Ar. After flushing Ar through the system for 5 min, the mixture was heated to 140 °C during 4-6 h until the Mg was completely dissolved and a whitish suspension was observed. After this, dipropylmaleonitrile **41** (704 mg, 5.79 mmol) and monothioethylmaleonitrile **68** (200 mg, 1.45 mmol) were added and the mixture was stirred at 140 °C for 14 h. After letting the mixture cool down to rt, the solvent was eliminated under reduced pressure, and 15 mL of TFA was added to the residue and stirred at rt in the dark for 1 h. The solution was then carefully poured into a 1:1 ice-water/NH_3 (30% ac.) mixture, and the resulting precipitate was filtered and washed with water and a 1:1 water/MeOH mixture. The precipitate was then dissolved in 40 mL of a 1:1 DMF/PhCl mixture and $Zn(OAc)_2$ (650 mg, 3.6 mmol) was added and the resulting solution was heated to 140 °C until no more starting material was observed. Afterwards, the solvent was eliminated under reduced pressure. The residue was purified by column chromatography on silica gel (Toluene with 1% THF) to yield a blue solid (65 mg, 7%)

Mp > 250°C.

^{1}H-NMR (300 MHz, THF-d_8): δ (ppm) = 8.75 (s, 1H), 3.99 – 3.85 (m, 12H), 3.72 (q, J = 7.4 Hz, 2H), 2.38 (m, 12H), 1.79 (t, J = 7.4 Hz, 3H), 1.28 (m, 18H).

^{13}C-NMR (75.5 MHz, THF-d_8): δ (ppm) = 159.46, 159.37, 159.05, 158.94, 158.38, 155.70, 149.09, 145.21, 145.03, 144.84, 144.71, 124.91, 67.57, 30.80, 29.16, 29.03, 27.89, 26.62, 26.55, 15.22, 14.75.

FT-IR (KBr): ν (cm^{-1}) = 2958.3, 2930.3, 2870.5, 1724.0, 1633.4, 1490.7, 1464.7, 1371.1, 1315.2, 1264.1, 1235.2, 1154.1, 1117.5, 1085.7, 1071.6, 1036.6, 1015.3, 950.7, 890.0, 861.1, 794.5, 770.4, 757.9, 730.7, 573.7.

UV-vis (THF): λ_{max} (nm) (log ε (dm^3 mol^{-1} cm^{-1})) = 619 (4.69), 567(sh), 350 (4.72).

MS (MALDI-TOF, DCTB): *m/z* = 688.4 [M^+].

HRMS: *m/z* Calcd for [$C_{36}H_{48}N_8SZn$]: 688.3009; Found: 688.3001.

XRD: monocrystalls of a Pz **68** structure were obtained by slow diffusion of methanol in DCM. Crystallographic data and some refining details are summarized in the following table

Formula	$C_{37}H_{52}N_8OSZn$
M	722.30
Volume/ Å^3	1878.92(14)
Z	2
Density/ g cm^{-3}	1.277
Crystalline system	Triclinic
Spatial group	P -1
a/ Å	11.1803(5)
b/ Å	12.5793(5)
c/ Å	13.9769(6)
α/ °	81.136(2)
β/ °	76.267(2)
γ/ °	82.893(3)
R	0.0505

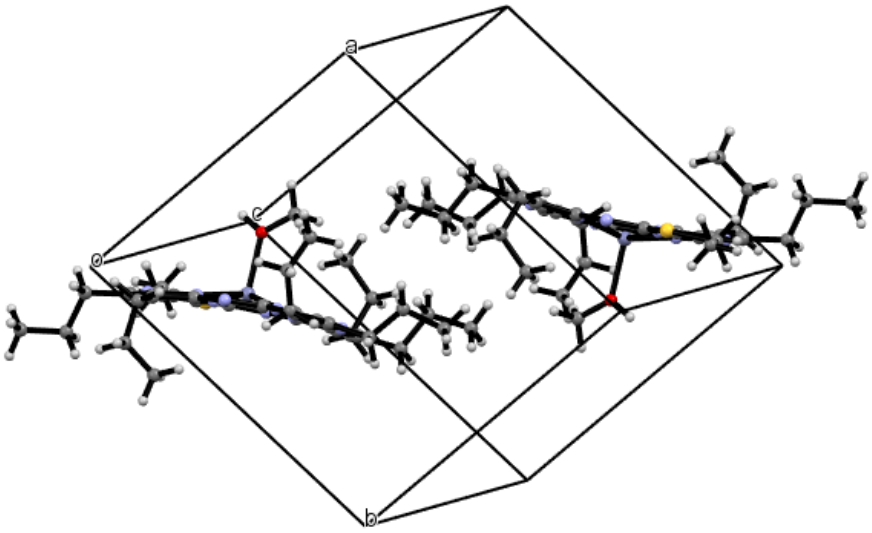

Figure 114. Unity cell and crystalline packing of Pz **68**.

[2,3,7,8,12,13-Hexapropyl-17-pent-1enylporphyrazinate]Zn(II) (70)

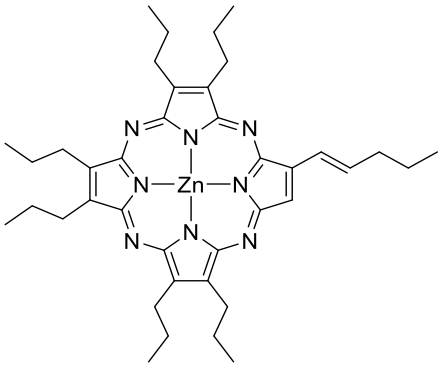

An oven-dried flask containing Pz **69** (40 mg, 0.058 mmol), 1-pent-1-enylboronic acid (20 mg, 0.176 mmol), $[Pd(PPh_3)_4]$ (7 mg, 0.006 mmol;), and CuTC (14.6 mg, 0.076 mmol) was purged with Ar, then charged with dry THF (2 mL). The mixture was stirred at 60 °C for 20 h under Ar atmosphere. The reaction mixture was cooled to room temperature and passed through a short silica gel column using THF as eluent. After the solvent was removed, the residue was purified by silica gel column chromatography (eluent Toluene/THF 99:1). The products were recrystallized from CH_2Cl_2 and n-hexane.

Mp > 250°C.

^{1}H-NMR (300 MHz, THF-d_8): δ (ppm) = 9.00 (s, 1H), 7.96 (m, 2H), 4.20 – 3.77 (m, 12H), 2.47 – 2.17 (m, 12H), 1.88 (m, 2H), 1.25 (m, 23H).
^{13}C-NMR (75.5 MHz, THF-d_8): δ (ppm) = 159.99, 159.88, 159.70, 159.45, 159.15, 158.74, 158.45, 156.73, 145.37, 145.15, 145.03, 144.87, 144.67, 138.67, 127.68, 124.56, 37.55, 33.03, 30.80, 30.47, 29.17, 29.06, 23.94, 23.73, 15.26, 15.21, 14.60.
FT-IR (KBr): ν (cm^{-1}) = 2961.3, 2934.3, 2870.5, 1717.4, 1663.3, 1447.2, 1261.7, 1207.7, 1122.2, 876.7, 673.6, 619.4.
UV-vis (THF): λ_{max} (nm) (log ε (dm^3 mol^{-1} cm^{-1})) = 617 (4.64), 599 (4.60), 570 (sh), 555 (sh), 350 (4.73).
MS (MALDI-TOF, DCTB): *m/z* = 696.4 [M^+].
HRMS: *m/z* Calcd for [$C_{39}H_{52}N_8Zn$]: 696.3601; Found: 696.3609.

[2,3,7,8,12,13-Hexapropyl-17-vinylporphyrazinate]Zn(II) (71)

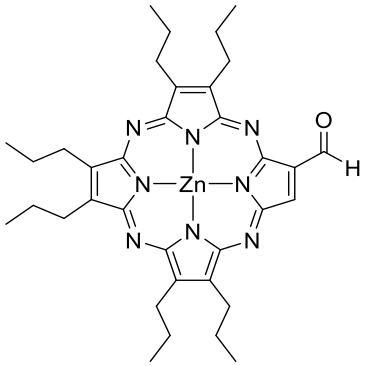

To a suspension of OsO_4 (364 mg, 1% wt of polyvinylpyridine) and Pz **70** (10 mg, 0.014 mmol) in 15 mL of THF was added dropwise a saturated aqueous solution of $NaIO_4$ (5 mL) at rt. The reaction mixture was stirred for 16h at that temperature, then filtered over Celite, and after the solvents were evaporated under reduced pressure, the crude product was purified by flash column chromatography (eluent: Toluene/THF 98:2), obtaining Pz **71** as a blue solid (8 mg, 85%).

Mp > 250^{o}C.
^{1}H-NMR (300 MHz, THF-d_8): δ (ppm) = 11.84 (s, 1H), 9.52 (s, 1H), 3.87 (m, 12H), 2.38 (m, 12H), 1.30 (m, 18H).
^{13}C-NMR (75.5 MHz, THF-d_8): δ (ppm) = 188.42, 163.57, 163.38, 163.22, 162.87, 159.09, 158.94, 154.70, 154.10, 147.13, 146.78, 146.68, 145.39, 145.09, 138.88, 132.16, 29.05, 28.97, 26.46, 26.40, 26.37, 15.21, 15.14.
FT-IR (KBr): ν (cm^{-1}) = 2961.3, 2935.0, 2866.3, 1718.4, 1664.2, 1516.4, 1448.2, 1273.5, 1205.5, 1124.2, 1097.2, 775.7, 673.6, 627.5.
UV-vis (THF): λ_{max} (nm) (log ε (dm^3 mol^{-1} cm^{-1})) = 625 (4.67), 577 (4.25), 567 (sh), 539 (4.29), 358 (4.50), 345 (4.51).
MS (MALDI-TOF, DCTB): *m/z* = 656.4 [M^+].
HRMS: *m/z* Calcd for [$C_{35}H_{44}N_8OZn$]: 656.2924; Found: 656.2918.

[2,3,7,8,12,13-Hexapropyl-17-carboxyporphyrazinate]Zn(II) (65)

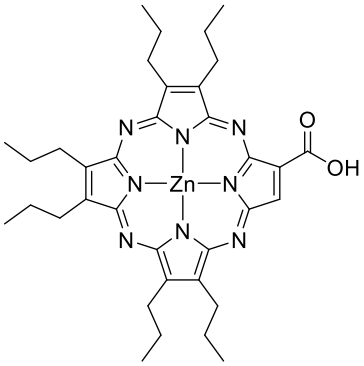

A $NaClO_2$ (27 mg, 0.024mmol) solution in water (0.5 mL, Milli-Q grade) was added dropwise over a solution of vinylPz **71** (8 mg, 0.012 mmol) in THF (2 mL) that had been previously cooled down to 0 ^oC. Then, a solution of sulfamic acid (3 mg, 0.03 mmol) in water (0.6 mL, Milli-Q grade) was added in one portion. After the starting compound disappeared (ca. 10 min), the solution was poured into aqueous HCl (5 mL, 1 M) and a greenish solid precipitated. The solid was dissolved in DCM, washed with water and dried with $MgSO_4$ before eliminating the solvent. The crude product was purified by flash column chromatography (eluent: Toluene/THF 2:1), obtaining Pz **65** as a blue solid (5 mg, 63%).

Mp > 250^oC.

^{1}H-NMR (300 MHz, THF-d_8): δ (ppm) = 14.75 (br s, 1H), 9.64 (s, 1H), 3.87 (m, 12H), 2.37 (m, 12H), 1.30 (m, 18H).

^{13}C-NMR (75.5 MHz, THF-d_8): δ (ppm) = 163.87, 163.45, 162.99, 162.77, 162.59, 159.50, 157.97, 154.42, 152.43, 147.25, 147.01, 146.77, 146.13, 145.53, 136.81, 132.58, 33.03, 30.79, 30.46, 29.07, 15.21, 15.14, 14.58.

FT-IR (KBr): ν (cm^{-1}) = 3383.6 (br), 2968.4, 2928., 2860.5, 1713.3, 1665.3, 1097.2, 885.6, 777.5, 615.2.

UV-vis (THF): λ_{max} (nm) (log ε (dm^3 mol^{-1} cm^{-1})) = 618 (4.65), 581 (4.36), 570 (sh), 544 (3.83), 355 (4.54), 344 (4.54).

MS (MALDI-TOF, DCTB): *m/z* = 672.4 [M^+].

HRMS: *m/z* Calcd for [$C_{35}H_{44}N_8O_2Zn$]: 672.2873; Found: 672.2846.

Resumen y Conclusiones

La presente Tesis Doctoral titulada “Synthesis and properties of photo- and electroactive tetraazaporphyrins and their performance in dye-sensitized solar cells” tiene como objetivo general la síntesis de nuevos complejos basados en derivados de tetraazaporfirinas para su aplicación en tecnologías solares.

El primer objetivo de este trabajo es la preparación de sistemas fotosintéticos artificiales que, imitando a los naturales, generen estados de separación de cargas de tiempos de vida largos. Durante el proceso de la fotosíntesis en organismos, la luz es convertida en combustibles químicos en forma de carbohidratos a partir de CO_2 y agua. Los sistemas fotosintéticos contienen pigmentos que actúan como antenas luminosas, absorbiendo luz para transformarla en energía electroquímica a través de un gradiente de transferencias electrónicas sucesivas, que se utiliza para generar ATP y NADPH (Figura 115). Estos combustibles moleculares se utilizan posteriormente durante la fase biosintética, donde se generan los carbohidratos. Durante este proceso, la excitación producida por la absorción de fotones genera estados de separación de carga de tiempo de vida media aproximada de 1 s.

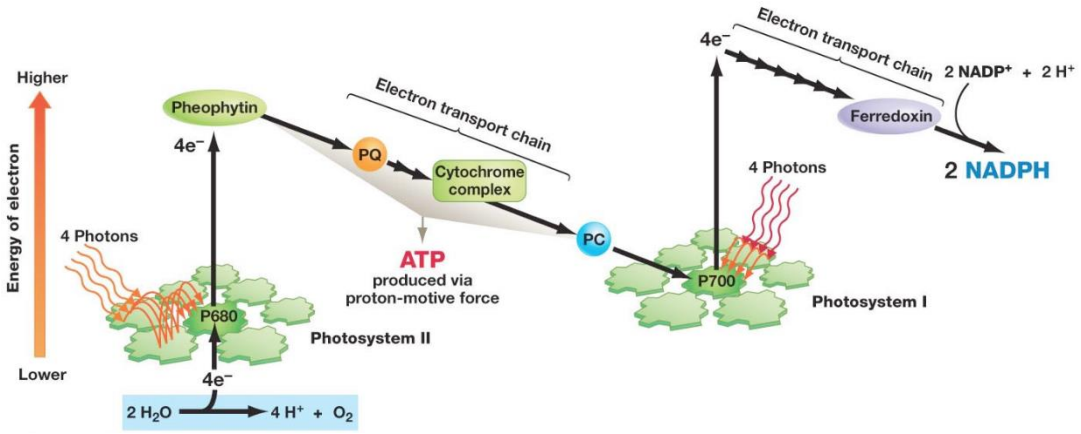

Figura 115. Proceso fotosintético de obtención de ATP y NADPH.

La fotosíntesis artificial utiliza versiones simplificadas, habitualmente compuestas de una unidad dadora (D) y otra aceptora (A) unidas mediante un conector, ya sea covalentemente o mediante interacciones supramoleculares. La fotoexcitación de cualquiera de las unidades produce una transferencia electrónica bien desde el orbital LUMO del dador al LUMO del aceptor, si es el dador el que se ha excitado, o bien desde el orbital HOMO del dador al HOMO del aceptor, si por el contrario ha sido este último el que ha sido excitado.

Una de las estrategias más comunes para aumentar los tiempos de vida de los estados de separación de carga se basa en la introducción de una segunda unidad dadora, capaz de rellenar el hueco generado después de la transferencia electrónica fotoinducida. De esta manera, las

cargas están más separadas espacialmente y se ralentiza el proceso de recombinación (Figura 116).

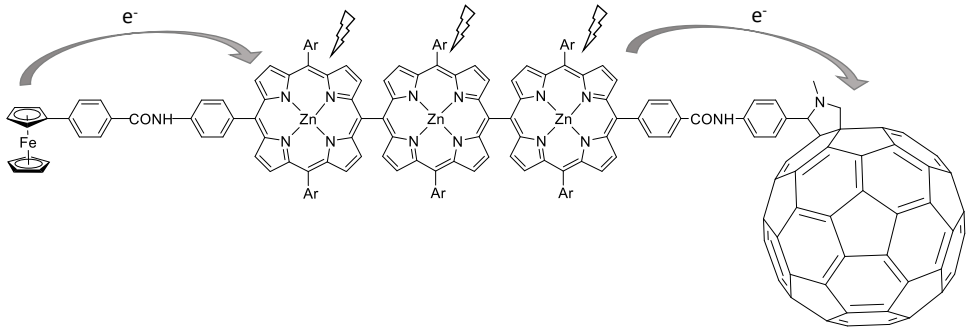

Figura 116. Estructura de una péntada con tres moléculas antena y dos transferencias electrónicas.

Nuestro grupo de investigación había descrito un sistema dador-aceptor de tipo **18a** formado por dos ftalocianinas de rutenio unidas mediante coordinación metálica a una unidad de perilenodiimida, con un tiempo de vida del estado de separación de cargas de 115 ns. En este trabajo, nos propusimos optimizar la respuesta fotofísica del sistema mediante la introducción de unidades de ferroceno como dador secundario. Así, en el capítulo 1 se prepararon cuatro ftalocianinas sustituidas en la periferia con cuatro y ocho unidades de ferroceno, respectivamente, y conteniendo Zn(II) o Ru(II) en su cavidad central. Estas ftalocianinas se obtuvieron mediante reacciones de ciclotetramerización de derivados de ftalonitrilo adecuadamente funcionalizados con una o dos unidades de ferroceno. En una segunda etapa, se prepararon los complejos dador-aceptor "rueda de carro" mediante coordinación del metal central a la unidad de perilenodiimida (Figura 117).

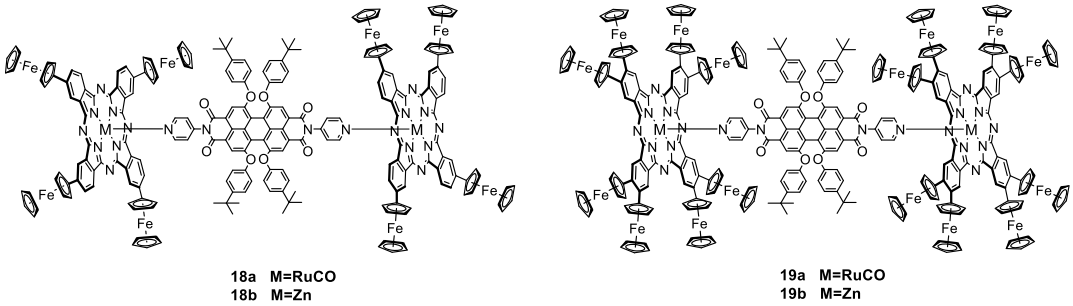

Figura 117. Estructura química de los sistemas dador-aceptor sintetizados.

El espectro de absorción de las ftalocianinas revela una fuerte interacción electrónica del macrociclo con las unidades de ferroceno periféricas. Así, se observa como al aumentar el número de unidades de ferroceno se produce un desplazamiento batocrómico de la banda Q además de un aumento de su coeficiente de extinción molar. Además, se observan bandas de transferencia de carga intervalente que son debidas a la comunicación electrónica existente

entre las distintas unidades de ferroceno a través del sistema aromático. Esto se confirma mediante estudios electroquímicos de voltametría cíclica, donde se observan varios picos correspondientes a la oxidación de los ferrocenos. Cabe destacar además que ninguna de las ftalocianinas presenta emisión, debido a una rápida desactivación de su estado excitado singlete hacia el triplete, favorecida por las unidades de ferroceno.

Los complejos formados RuPc-PDI son suficientemente estables como para ser aislados y caracterizados. Sin embargo, y debido a la menor fortaleza del enlace Zn-piridina, los complejos ZnPc-PDI se estudiaron en disolución mediante valoraciones por RMN. Los valores de las constantes de asociación para los sistemas 1:1 fueron de $8.5 \cdot 10^2$ y $6.7 \cdot 10^3$ M^{-1}, para los tetra y octasustituidos respectivamente. El valor de K_a obtenido para el sistema $PcFc_8$-PDI fue aproximadamente de un orden de magnitud superior al obtenido para $PcFc_4$-PDI. Para los sistemas 1:2 no fue posible obtener un buen ajuste de los datos experimentales que nos llevasen a una estimación de K1 y K2. El cálculo de las constantes de asociación se llevó a cabo en este caso mediante valoraciones monitorizadas por espectrofotometría de fluorescencia, ya que se produce una reducción de la intensidad de la emisión del PDI al añadir las Pcs. Las constantes de asociación obtenidas para los complejos formados van desde 10^5 a 10^7 M^{-1}. En esta ocasión no se observan diferencias importantes en los valores de k_a entre los sistemas con ftalocianinas tetra- y octasustituidos. Sin embargo, el cambio del metal central sí provoca variaciones importantes en los valores de las constantes de asociación, llegando a ser hasta dos órdenes de magnitud superior en el caso de las ftalocianinas de Ru.

Se llevaron a cabo estudios de espectroscopía de absorción transitoria en el laboratorio del profesor Guldi en Erlangen, Alemania. Las ftalocianinas sustituidas con ferroceno mostraron cruces intersistémicos rápidos desde el estado singlete excitado al triplete en el orden de los picosegundos, que seguidamente se desactivaban hasta el estado fundamental en nanosegundos. Este comportamiento se explica por la presencia de ferrocenos directamente unidos a los macrociclos. En el caso de los complejos supramoleculares de Zn, se observaron procesos de transferencia de energía al excitar la PDI, mientras que la excitación de las Pcs produce únicamente un rápido decaimiento al estado fundamental. Los complejos RuPc-PDI-RuPc generaron, mediante fotoexcitación, estados de separación de cargas con tiempos de vida de 1.2 y 2.3 nanosegundos respectivamente. En este caso, la presencia de ferrocenos como segundo dador produce un efecto contrario al esperado, reduciendo los tiempos de vida de separación de cargas del sistema, debido a una aceleración del proceso de recombinación. Este resultado podría deberse a la rápida desactivación de los estados excitados de las ftalocianinas debido una fuerte interacción entre las unidades debido a su proximidad. No se han realizado estudios para confirmar esta hipótesis.

El segundo objetivo del primer capítulo se centra en la funcionalización periférica de subftalocianinas con tres y seis unidades de ferroceno, con el propósito de obtener sistemas curvos dadores de electrones, que podrían utilizarse para reconocimiento molecular de moléculas con una curvatura complementaria, como es el fullereno C_{60}.

Las subftalocianinas Fc_3SubPc y Fc_6SubPc se prepararon mediante acoplamiento del ácido ferrocenil borónico con triyodo- o hexayodosubftalocianina, respectivamente. Las propiedades ópticas de las subftalocianinas preparadas muestran también una fuerte interacción electrónica entre las unidades de ferroceno y los macrociclos, que se manifiesta mediantedesplazamiento hacia la zona del infrarrojo, al aumentar el número de unidades de Fc. La emisión típica de la subftalocianinas también desaparece con este tipo de funcionalización. Los estudios electroquímicos muestran un potencial de reducción más negativo para las subftalocianinas hexasustituidas, con respecto a las trisustituidas, lo que concuerda con el carácter dador del metaloceno. Por último, la fotoexcitación del macrociclo genera el estado excitado singlete que evoluciona rápidamente al triplete, para seguidamente desactivarse al estado fundamental. En ningún caso se observaron signos de transferencia electrónica hacia el fullereno en disolución. Tampoco se observaron interacciones entre la SubPc y el fullereno C_{60} mediante valoraciones en UV-Vis y fluorescencia. Sin embargo, hemos obtenido un cocristalato del sistema SubPcFc_6/C_{60} con estequiometría 1:1, poniendo de manifiesto cierto grado de interacción entre la cara cóncava del macrociclo y el fullereno, al menos en el estado sólido (Figura 118).

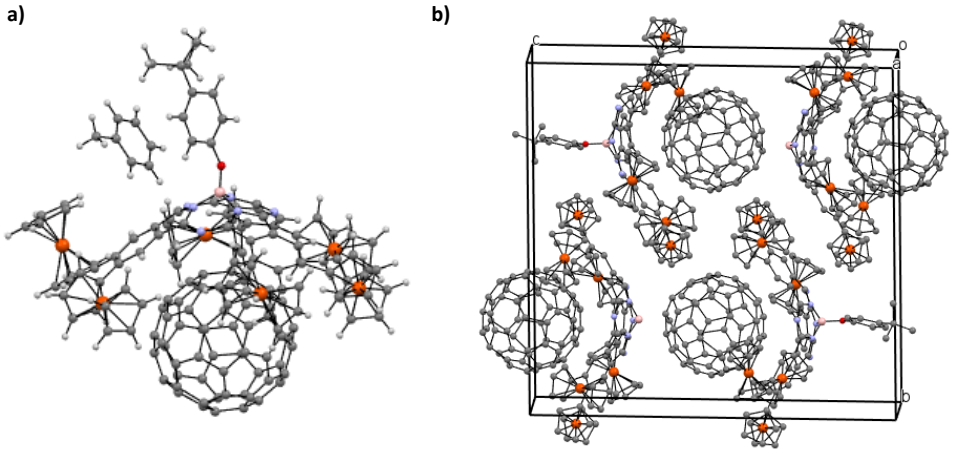

Figure 118. a) Estructura molecular del sistema SubPcFc_6-C_{60}, determinada mediante difracción de Rayos-X. b) Vista de la celdilla unidad.

El segundo capítulo de esta tesis se centra en el desarrollo de nuevos colorantes basados en derivados de porfirazinas para su aplicación en células solares sintetizadas por colorante (DSSC) o células de Grätzel. Este tipo de dispositivos pertenece al grupo de las células solares híbridas, que combinan materiales inorgánicos y orgánicos, obteniendo de esta manera ventajas asociadas a cada tipo de material. Por ejemplo, las células híbridas se benefician de las excelentes propiedades transportadoras de carga de los materiales inorgánicos, así como de los altos coeficientes de absorción molar y los bajos costes de procesado de los materiales orgánicos. De hecho, el alto coste de las células solares basadas en silicio monocristal, que son

las que actualmente dominan el mercado, es su mayor desventaja, y es lo que hace tan atractivas a las células solares híbridas y de las completamente orgánicas.

Actualmente, la mayor parte del interés investigador está centrado en un tipo específico de dispositivos híbridos, los basados en perovskitas. Esto es debido a que son de fácil fabricación y, sobre todo, a que las eficiencias obtenidas han pasado de apenas un 4% en 2009 hasta un más de un 20% a finales de 2015. Sin embargo, aunque las DSSCs no han alcanzado nunca eficiencias tan altas (el record está situado en un 13%), poseen ciertas ventajas frente a las células solares de perovskitas, ya que éstas utilizan Pb, un elemento tóxico, y requieren un encapsulamiento debido a su alta inestabilidad frente a la humedad, lo cual encarece su fabricación.

La estructura típica de una célula del tipo Grätzel (Figura 119) se basa en: (a) un cristal transparente cubierto con un óxido conductor como el FTO, sobre el que se deposita (b) una capa de un óxido mesoporoso, normalmente TiO_2, formando el fotoánodo, (c) una monocapa de colorante adsorbida sobre el óxido mesoporoso del fotoánodo, (d) un electrolito que sea capaz de regenerar el colorante y (e) un contraelectrodo de ITO, recubierto por un catalizador de Pt, capaz de catalizar la regeneración del par redox del electrolito.

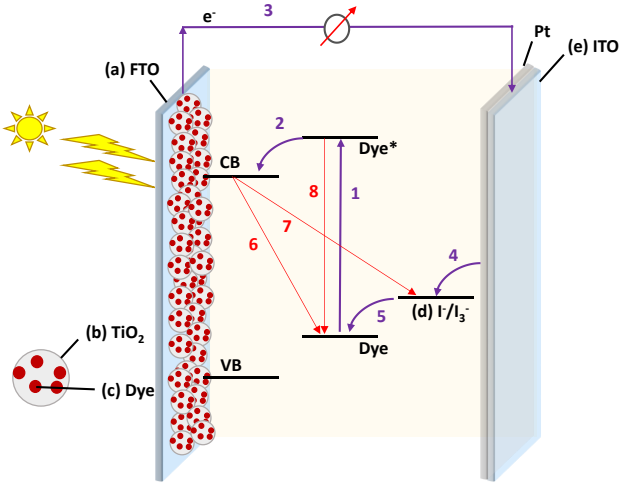

Figura 119. Representación esquemática de los componentes y los procesos de una DSSC.

El funcionamiento de la célula es el siguiente: la luz incidente es absorbida por el colorante, lo que provoca el salto de un electrón del estado fundamental al excitado (proceso 1, Figura 119). El electrón excitado es inyectado desde el colorante a la banda de conducción del óxido de titanio (proceso 2), que se difunden a través del mismo hasta llegar al contacto, desde donde fluyen hasta el contraelectrodo generando la corriente eléctrica (proceso 3). Desde el contraelectrodo, los electrones son transferidos a la forma oxidada del par redox del electrolito, recuperando la forma reducida (proceso 4), que, por último, regenera la forma neutra del colorante (proceso 5). Aparte de éstos, también existen procesos no deseados que tienen lugar

en la célula solar y que disminuyen su eficiencia, como son la recombinación del electrón inyectado con la forma oxidada del colorante (proceso 6), o con el par redox (proceso 7), o que el electrón excitado del colorante regrese al estado fundamental mediante decaimiento no radiativo (proceso 8).

En este trabajo nos hemos centrado en la preparación de nuevos colorantes derivados de porfirazina, que hasta la fecha, nunca habían sido probados en DSSCs. En la primera parte del capítulo hemos estudiado el efecto de la sustitución periférica en porfirazinas del tipo A_3B, en las que B es una unidad de isoindol con un grupo de anclaje carboxílico, y A es un pirrol disustituido con diferentes grupos funcionales (Figura 120). Estas porfirazinas se prepararon mediante ciclotetramerización cruzada de un derivado de maleonitrilo o pirrolidina adecuadamente funcionalizado (unidad A) y el 4-metoxicarbonilftalonitrilo. La última etapa de la síntesis de estas Pzs A_3B consiste en una hidrólisis del grupo éster. Las unidades A se dotaron de grupos muy diferentes desde el punto de vista electrónico, como son las aminas, tioéteres, grupos alquilo, arilo y éter.

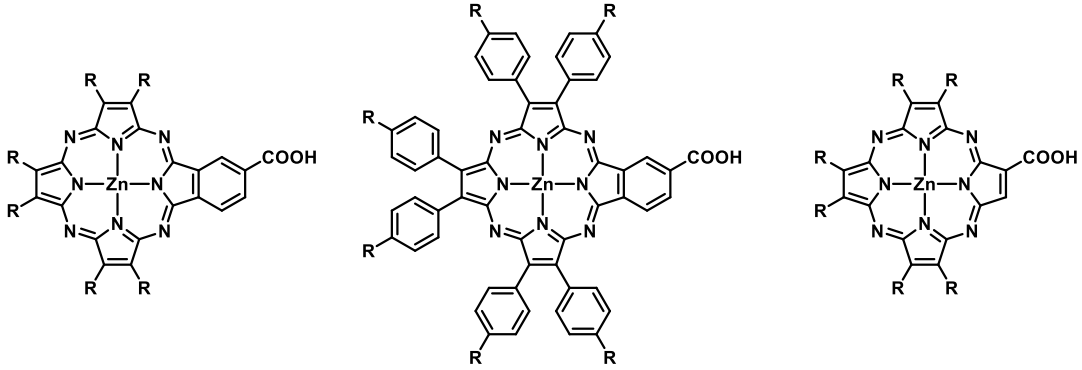

33 R = -C_3H_7
34 R = -SC_5H_{11}
35 R = -NMe_2
36 R = -*t*-Bu
37 R = -OMe
38 R = -NMe_2
65 R = -C_3H_7

Figura 120. Estructura química de las porfirazinas **33**-**37**.

Se estudiaron las propiedades ópticas y electroquímicas de todas las porfirazinas y se estimaron los niveles energéticos de los orbitales HOMO y LUMO. Además, se realizaron cálculos computacionales que, aparte de proveer valores teóricos de los mismos orbitales, mostraron la distribución de los orbitales HOMO y LUMO en las porfirazinas (Figura 121).

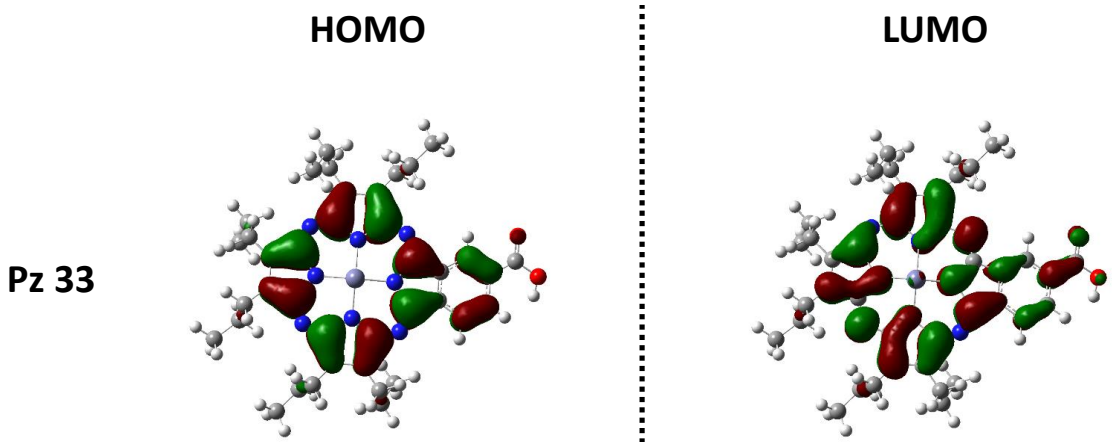

Figura 121. Distribución de los orbitales HOMO y LUMO en la porfirazina **33**.

Las medidas del rendimiento de los colorantes en dispositivos solares fue llevado a cabo en el laboratorio de los profesores M. Grätzel and M. K. Nazeeruddin en Lausanne. De las 6 moléculas, sólo la Pz **33**, sustituida con cadenas alquílicas, obtuvo una eficiencia de conversión superior al 2% en las primeras pruebas. El resto no supero el 0.2%. Los esfuerzos se centraron entonces en la optimización de los dispositivos basados en este colorante, y mediante modificaciones en el grosor de las películas de óxido de titanio así como de los componentes del electrolito, la eficiencia de estos dispositivos aumentó hasta un 3.42%, un valor prometedor bastante próximo al descrito para la ftalocianina TT-1 en las mismas condiciones.

En una segunda etapa, se llevó a cabo la modificación de la Pz **33** en la unidad B, modificando así las características del grupo de anclaje al semiconductor. Con este fin se preparó una porfirazina sustituida con seis cadenas propilo (unidades A) y una función ácido carboxílico directamente unida al pirrol que constituye la unidad B. Esta función ácida se generó mediante ruptura oxidante de un grupo vinilo directamente unido al pirrol B. Las propiedades ópticas y electroquímicas de la nueva Pz (**65**, Figura 120) son parecidas a las de la Pz **33**,al igual que los niveles energéticos de sus orbitales HOMO y LUMO, pero la proximidad del grupo carboxílico al macrociclo modifica la distribución del orbital LUMO (Figura 122).

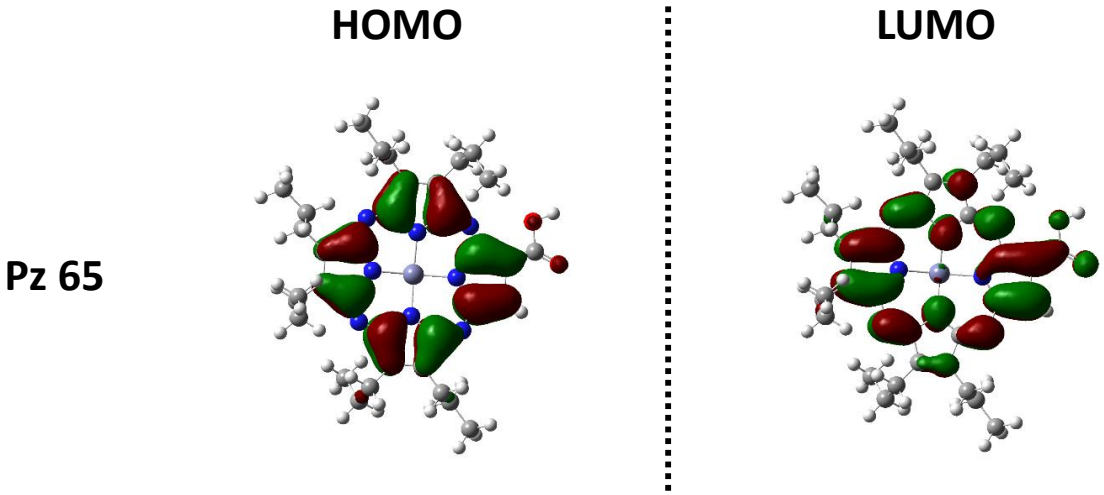

Figura 122. Distribución de los orbitales HOMO y LUMO en la porfirazina **65**.

El rendimiento en células solares de esta nueva porfirazina se estudiará en Lausanne en los próximos meses.